Modeling of Thermofluid Phenomena in Segmented Network Simulations of Loop Heat Pipes

by

Nirmalakanth Jesuthasan

Department of Mechanical Engineering

McGill University
Montréal, Québec, Canada

August 2011

A thesis submitted to McGill University
in partial fulfillment of the requirements for the degree of
Doctor of Philosophy

© Nirmalakanth Jesuthasan, Montréal, Canada, 2011

Abstract

The overarching goal of the work presented in this thesis is to formulate, implement, test, and demonstrate cost-effective mathematical models and numerical solution methods for computer simulations of fluid flow and heat transfer in loop heat pipes (LHPs) operating under steady-state conditions.

A segmented network thermofluid model for simulating steady-state operation of conventional LHPs with cylindrical and flat evaporators is proposed. In this model, the vapor-transport line, condenser pipe, and liquid-transport line are divided into longitudinal segments (or control volumes). Quasi-one-dimensional formulations, incorporating semi-empirical correlations for the related single- and two-phase phenomena, are used to iteratively impose balances of mass, momentum, and energy on each of the aforementioned segments, and collectively on the whole LHP. Variations of the thermophysical properties of the working fluid with temperature are taken into account, along with change in quality, pressure drop, and heat transfer in the two-phase regions, giving the proposed model enhanced capabilities compared to those of earlier thermofluid network models of LHPs. The proposed model is used to simulate an LHP for which experimental measurements are available in the literature: The predictions of the proposed model are in very good agreement with the experimental results.

In earlier quasi-one-dimensional models of LHPs, the pressure drop for vapor flow through the grooves in the evaporator is computed using a friction-factor correlation that applies strictly only in the fully-developed region of fluid flows in straight ducts with impermeable walls. This approach becomes unacceptable when this pressure drop is a significant contributor to the overall pressure drop in the LHP. A more accurate correlation for predicting this pressure drop is needed. To fulfill this need, first, a co-located equal-order control-volume finite element method (CVFEM) for predicting three-dimensional parabolic fluid flow and heat transfer in straight ducts of uniform regular- and irregular-shaped cross-section is proposed. The methodology of the proposed CVFEM is also adapted to formulate a simpler finite volume method (FVM), and this FVM is used to investigate steady, laminar, Newtonian fluid flow and heat transfer in straight vapor grooves of rectangular cross-section, for parameter ranges representative of

typical LHP operating conditions. The results are used to elaborate the features of a special fully-developed flow and heat transfer region (established at a distance located sufficiently downstream from the blocked end of the groove) and to propose novel correlations for calculating the overall pressure drop and also the bulk temperature of the vapor. These correlations are incorporated in the aforementioned quasi-one-dimensional model to obtain an enhanced segmented network thermofluid model of LHPs.

Sintered porous metals of relatively low porosity (0.30 – 0.50) and small pore diameter (2.0 – 70 micrometers) are the preferred materials for the wick in LHPs. The required inputs to mathematical models of LHPs include the porosity, maximum effective pore size, effective permeability, and effective thermal conductivity of the liquid-saturated porous material of the wick. The determination of these properties by means of simple and effective experiments, procedures, and correlations is demonstrated using a sample porous sintered-powder-metal plate made of stainless steel 316.

Finally, the capabilities of the aforementioned enhanced segmented network thermofluid model are demonstrated by using it to simulate a sample LHP operating under steady-state conditions with four different working fluids: ammonia, distilled water, ethanol, and isopropanol. The results are presented and comparatively discussed.

Sommaire

L'objectif principal de cette thèse consiste à formuler, mettre en œuvre, tester et démontrer des modèles mathématiques et des méthodes numériques pour réaliser la simulation d'écoulements de fluide et de transfert de chaleur dans des boucles fluides diphasiques [Loop Heat Pipes (LHPs) en anglais], opérant en régime permanent.

Un modèle de réseau segmenté thermofluide pour simuler le fonctionnement en régime permanent des LHPs conventionnelles avec des évaporateurs cylindriques et plats est proposé. Dans ce modèle, la ligne de transport de la vapeur, le tuyau du condenseur et la ligne de transport du liquide sont divisés en segments longitudinaux (ou volumes de contrôle). Des formulations quasi-unidimensionnelles, intégrant des corrélations semi-empiriques pour les phénomènes multiphasiques sont utilisées pour assurer la conservation de la masse, de la quantité de mouvement et de l'énergie sur chacun des segments individuels, puis sur l'ensemble du LHP. Les variations des propriétés thermophysiques du fluide en fonction de la température sont prises en compte, ainsi que le changement dans le titre en vapeur, la chute de pression, et le transfert de chaleur dans les régions diphasiques, améliorant ainsi les capacités du modèle proposé par rapport aux modèles précédents de réseaux de LHPs. Le modèle proposé est utilisé pour simuler un LHP pour lequel des mesures expérimentales sont disponibles dans la littérature: les prédictions du modèle proposé sont en très bon accord avec les résultats expérimentaux.

Dans les modèles quasi-unidimensionnels précédents de LHPs, la chute de pression pour un débit de vapeur à travers les gorges de l'évaporateur est calculée en utilisant une corrélation faisant intervenir un facteur de friction s'appliquant uniquement dans la région pleinement développé de conduits avec des murs imperméables. Cette approche est inacceptable quand cette baisse de pression devient significative devant la chute de pression globale du LHP. Une corrélation plus précise pour prédire cette chute de pression est alors nécessaire. Pour répondre à ce besoin, une méthode de volumes éléments finis (CVFEM) est proposée pour prédire l'écoulement en trois dimensions du fluide et le transfert de chaleur dans différents conduits à section uniforme régulière et irrégulière. La méthodologie du CVFEM est également adaptée pour formuler une méthode plus simple en volumes finis (FVM). Cette approche est utilisée pour étudier

l'écoulement laminaire de fluides newtoniens et le transfert de chaleur dans des cannelures de vapeur à section rectangulaire, pour des conditions typiques de fonctionnement d'un LHP. Les résultats sont utilisés pour élaborer les caractéristiques d'une région pleinement développé (particulière aux LHPs) et de proposer de nouvelles corrélations pour le calcul de la chute de pression globale et des températures de vapeur. Ces corrélations sont incorporées dans le modèle quasi-unidimensionnel pour obtenir un modèle amélioré de réseau segmenté thermofluide pour les LHPs.

Les métaux poreux, fabriqués à partir de poudre de métaux sintérisées, ayant une faible porosité (0.30 - 0.50) et un diamètre de pores de petite taille (2.0 à 70 micromètres), sont les matériaux idéals pour la mèche des LHPs. Les paramètres d'entrées des modèles mathématiques de LHPs incluent la porosité, la taille effective maximale des pores, la perméabilité effective et la conductivité thermique effective de la mèche saturée d'un liquide. La détermination de ces propriétés par des expériences simples est réalisée en utilisant un échantillon poreux fritté de poudre de métal en acier inoxydable 316.

Enfin, les capacités du modèle améliorée du réseau segmenté thermofluide discuté ci-dessus sont démontrées en l'utilisant pour simuler un LHP opérant en régime permanent avec quatre fluides différents: l'ammoniac, l'eau distillée, l'éthanol et l'isopropanol. Les résultats sont présentés et discutés comparativement.

Acknowledgements

I wish to express my heartfelt thanks to my thesis advisor and mentor, Professor B. Rabi Baliga, whose teachings, guidance, support, suggestions, and encouragements during the course of this research work were plentiful and unprecedented. He always knew how to make the apparently complicated into the ridiculously simple, and the humility, care, patience and good humour with which he shared his thoughts and ideas have made my experience at McGill University especially memorable and rewarding.

I would like to thank the Natural Sciences and Engineering Research Council of Canada (NSERC), the Fonds québécois de la recherche sur la nature et les technologies (FQRNT), the Canadian Space Agency (CSA), and McGill University for their financial support through Doctoral fellowships during my graduate studies.

A special note of thanks to Mr. Juan Vasquez and Mr. Ariel Kemer of Arsal Industries, and the staff of the Machine Tool Laboratory [Antonio (Tony) Micozzi, Sam Minter, and J. Roy Wesgate], for their exquisite craftsmanship in machining various elements of the experimental setups designed and used in this work. I am grateful to Dr. Marcia Huber of the National Institute of Standards and Technology (NIST) for her invaluable help and inputs in accessing thermofluid property data of LHP working fluids.

I also wish to thank the Mechanical Engineering Department staff (George Tewfik and Mario Iacobaccio) for their technical support. Special thanks are due to Joyce Nault and Professor David Frost for their help with the paperwork and administration details.

Many thanks are due to my colleagues and friends from the Heat Transfer Laboratory, Dave Scott, Nima Atabaki, Eric Duplain, Alexandre Lamoureux, Adam Samuel, Samer Afarah, James Medvescek, Raul Palacios Gamez and Jeffrey Poissant, and my officemates and friends, Hossein Ghiasi, Zouya Zarei, Peter Gerontakos, and Sudarshan Martins whose fellowship I have treasured.

Finally, I would like to thank my dear wife, Sobana, and son, Aiden, for their love, and for their never-ending encouragement and patience in seeing me through this long process. The support of my parents, sister and in-laws is also appreciated.

Ivan Turgenev said that “Time sometimes flies like a bird, sometimes crawls like a snail; but a man is happiest when he does not even notice whether it passes swiftly or slowly” and this is how I would like to remember my time at McGill University.

Table of Contents

List of Figures

List of Tables

Nomenclature

a	Width of the vapor groove
AR	Aspect ratio (AR = a/b)
A_{c-s}	Cross-sectional area of duct
$A_{surf,\,wick}$	Surface area of the wick structure normal to the flow
b	Height of the vapor groove
c_p	Specific heat at constant pressure
d_p	Diameter of pore size ($d_p = 2r_p$)
D_h	Hydraulic diameter
$\left(dP/dz\right)_g^s$	Axial gradient of the static pressure for the gas-phase flowing alone inside the pipe with its own mass flow rate
$\left(dP/dz\right)_l^s$	Axial gradient of the static pressure for the liquid-phase flowing alone inside the pipe with its own mass flow rate
$\Delta P_{cap,\,max}$	Maximum capillary head available in the wick
$\Delta P_{cd}^{2\varphi}$	Liquid-vapor mixture pressure drop in the two-phase part of the condenser
ΔP_{cd-sc}	Liquid pressure drop in the subcooled region of the condenser (single-phase part)
$\Delta P_f^{2\phi}$	Pressure drops caused by the wall friction force (and also bends and fittings)
ΔP_{grav}	Pressure drops caused by the gravity force
$\Delta P_{l,wick}$	Friction pressure drop for the liquid phase of the working fluid flowing through the wick inside the evaporator
ΔP_{ll}	Liquid pressure drop through the liquid-transport line
ΔP_{mom}	Pressure drops caused by momentum changes during the condensation process
ΔP_{tot}	Total (sum of all the pressure drops) in the LHP
ΔP_{vg}	Friction pressure drop total static pressure drop in these vapor grooves
ΔP_{vl}	Vapor pressure drop through the vapor-transport line
e	Roughness (rms) of the internal surface of the pipe
f	Darcy friction factor
f_{app}	Apparent friction factor; Eq. (4.12)
$f_{Fanning}$	Fanning friction factor; Eq. (4.12)
$f\,\mathrm{Re}_{D_h}$	Product of Darcy friction factor and Reynolds number
F_{so}	Modified Froude number [Soliman (1982)]
F_{TD}	Modified Froude number [Taitel and Duklet (1976)]; Eq. (2.12)
g	Gravitational acceleration
G	Mass flux
Ga	Galileo number; Eq. (5.24)

h	Heat transfer coefficient
h_{cap}	Capillary height
H_g	Adverse elevation of condenser unit with respect to evaporator
i_{fg}	Enthalpy of evaporation
Ja_l	Jacob number for the liquid
k,	Thermal conductivity
k_{eff}	Effective thermal conductivity of the liquid-saturated wick
k_l , k_s	Average values of the thermal conductivities of the liquid and the solid (material of the porous medium) in the wick, respectively
K_{TD}	Modified Froude number [Taitel and Dukler (1976)]; Eq. (2.12)
K_{wick}	Permeability of the wick
L	Longitudinal length of vapor groove
$L_{cd}^{2\phi}$	Length of condenser pipe required to fully condense the vapor
L_{vg}	Length of the vapor groove
L_{sc}	Length of the subcooled (single-phase) region of the condenser pipe
l_{wick}	Thickness of the rectangular wick
$\dot{m}_{tot}$	Total mass flow rate in the LHP
Nu	Nusselt number in the two-phase annular flow regime
p	Reduced perturbation pressure (static pressure minus hydrostatic pressure)
P	Reduced pressure (static pressure minus hydrostatic pressure)
$\overline{P}(\mathrm{z})$	Reduced cross-sectional averaged pressure (static pressure minus hydrostatic pressure)
$Peri$	Perimeter
Pr	Prandtl number
q_{app}	Rate of heat transfer applied to LHP evaporator (cylindrical or flat),
q_{cc-amb}	Rate of heat loss from the fluid in the compensation chamber to the ambient environment
$q_{cd-loss,\,tot}^{2\phi}$	Rate of heat transfer (total) required to fully condense the vapor in the condenser unit
q_{fg}	Rate of heat transfer associated with the evaporation process at the liquid-vapor interface
q_{hl}	Rate of heat leak through the wick
q_{sc}	Rate of heat rejection (total) from the liquid in the subcooled part of the condenser
$q_{vl-gain,\,i}$	Rate of heat gain in segment *i* of the vapor-transport line
$q_{vl-loss,\,i}$	Rate of heat loss in segment *i* of the vapor-transport line
q_{vsh}	Rate of heat transfer to the saturated vapor during its passage through the grooved channels
r_c	Mean radius of curvature
r_i , r_o	Inner and outer radii of the cylindrical wick, respectively

r_p	Effective pore radius
Re_{D_h}	Reynolds number based on hydraulic diameter
Re_{inj}	Injection Reynolds number, $\mathrm{Re}_{inj} = \rho v_{inj} \mathrm{b} / \mu$; Eq. (4.12)
$R'_{th\_inside,\, i}$	Thermal resistance (per unit length) for internal convection in a generic transport line
$R'_{th\_wall-outside,\, i}$	Sum of thermal resistance (per unit length) associated with the pipe wall, insulating material, and the external heat transfer
$\mathrm{Re}_{L_{vg}}$	Reynolds number, at the end of the vapor groove
Re_{vo}	Vapor-only Reynolds number
T_{amb}	Ambient temperature
$T_{cc,\, in}$	Bulk temperature of the subcooled fluid entering the compensation chamber
$T_{cd-exit}$	Bulk temperature of the fluid exiting the condenser unit
T_{cd-in}	Temperature of the saturated vapor entering the condenser unit
T_{inj}	Uniform injection temperature of vapor along bottom lateral surface of the vapor groove
T_{sat}	Saturation temperature at the liquid-vapor interface in the wick structure
$T_{sat,\, cc}$	Saturation temperature of the two-phase mixture in the compensation chamber
T_{sink}	Temperature of the sink
T_w	Vapor groove uniform wall temperature
$T_{wick,\, ent}$	Saturated temperature of the liquid entering the wick structure
U	Overall heat transfer coefficient
$(UA')_i$	Overall thermal conductance per unit length of segment i
v_{inj}	Uniform injection velocity of vapor along bottom lateral surface of the vapor groove
w_{av}	Cross-sectional averaged axial velocity
x	Vapor quality
X	Lockhart-Martinelli (1949) parameter

Greek Symbols

α	Vapor void fraction
α_{con}	Porous material consolidation parameter
β	Pipe inclination angle (measured from horizon)
ε	Porosity of the wick material
θ	Dimensionless temperature, $\theta = (T - T_{inj}) / (T_w - T_{inj})$
θ_c	Contact angle at static equilibrium
θ_{eff}	Effective contact angle of the liquid-vapor interface inside the representative pore
μ	Fluid dynamic viscosity

ρ_v	Mass density of the vapor-phase
ρ_l	Mass density of the liquid-phase
σ	Liquid-vapor surface tension
φ_l^2	Two-phase pressure drop multiplier based on the liquid-phase

Superscripts

amb	Ambient
b	Bulk
cap	Capillary
cc	Compensation chamber
cd	Condenser
e	Elliptic
f	Friction
F.D.	Hydrodynamically or thermally fully-developed region
g	Gas-Phase
grav	Gravity
i	Refers to segment (or cell) *i*
inj	Injection
l	Liquid-phase
ll	Liquid-transport line
mom	Momentum
p	Parabolic
sat	Saturation condition
sc	Subcooled
tot	Total
v	Vapor-phase
vg	Vapor groove
vl	Vapor-transport line

Superscripts

2ϕ	Two-Phase

Chapter 1:
Introduction

This research work is primarily concerned with the modeling of fluid flow and heat transfer phenomena occurring in loop heat pipes (LHPs) under steady operating conditions. LHPs are devices in which capillary forces in a wick and liquid-vapor phase-change phenomena are used to achieve continuous transfer of thermal energy from a heat source to a heat sink. The phase-change phenomena and the capillary-driven circulation of the fluid within LHPs allow them to transfer heat over long distances with relatively small temperature drops, no mechanical moving parts, and no special external power inputs. In addition, the rates of heat transfer achievable with LHPs are usually one to three orders of magnitude larger than those possible with either single-phase convection systems or solid thermal conductors for corresponding thermal boundary conditions.

Owing to fewer restrictions and greater flexibility in applications than conventional heat pipes (HPs) [Silverstein (1992)], LHPs have received much attention in the space community. LHPs are currently emerging as the baseline design for the thermal management of several commercial communication satellites and NASA spacecrafts, including ICESAT, AURA, SWIFT, and GOES [Wang et al. (2008)]. There is also an on-going Canadian effort to use LHPs in the Polar Communication and Weather (PCW) mission led by the Canadian Space Agency (with the participation of Environment Canada and Canada's Department of National Defense), which has two PCW satellites scheduled for launch in 2016 [Trishchenko and Garand (2011)]. LHPs have also found numerous applications on earth: In electronics cooling, gas turbine engines, avionics, cryogenics, solar energy devices, and heating, ventilating and air-conditioning (HVAC) systems, for instance. In these applications, the allure of LHPs is directly related to their passive nature, in that they do not necessitate any external motive devices (such as pumps), and, as was stated above, their ability to continuously transport heat over long distances with relatively small temperature drops. However, LHPs have not been as intensively researched as HPs, and, currently, the manufacturing costs of LHPs are about an order of magnitude higher than HPs for comparable applications. Thus, in recent years, there has been a great deal of interest in further developing LHPs [Maydanik

(2005); Launay et al. (2007a); Vasiliev et al. (2009)], and new and challenging research needs have been identified. This research work represents an effort to fulfill some of these needs.

In this chapter, succinct discussions of the background, motivation, and overall goals of this research work are presented. Following that, a concise review of the pertinent literature is provided. Next, the specific objectives of this research work are put forward. Finally, the organization of the thesis is summarized.

1.1 Background, Motivation and Overall Goals

Loop heat pipes (LHPs) chronologically follow heat pipes (HPs) and capillary pumped loops (CPLs), and many of the underlying concepts and principles of operation of these two-phase, capillary-driven, devices are similar [Stenger (1966); Chi (1976); Dunn and Reay (1982); Faghri (1995); Nikitkin and Cullimore (1998)].

LHPs were first developed in the former Soviet Union in the early 1970s [Maydanik (2005)]. The primary components of a conventional (cylindrical-type) LHP are shown schematically in Figure 1.1, consisting of an evaporator, a compensation chamber, a vapor-transport line, a condenser, and a liquid-transport line. In LHPs, the evaporator and the compensation chamber are integrated, and linked together both hydrodynamically and thermally. Typically, the evaporator is composed of an internally-grooved metal pipe and an annular wick (usually made of sintered powder metal) with a liquid pool of the working fluid at its center (core). A variety of working fluids such as ammonia, ethanol, isopropanol, acetone, water, and liquid metals have been used in LHPs, to achieve a high level of operational versatility, with applications ranging from cryogenics to metallurgy.

In steady-state operation of LHPs, the heat input to the evaporator is conducted through its metallic grooved wall to the adjoining wick surface. This causes the saturated liquid in the wick to evaporate at its outer surface, and the resulting vapor flows into the grooves (vapor channels), as is schematically illustrated in Figure 1.2. The depletion of the liquid in the evaporator causes the liquid-vapor interface to enter the wick, which, in turn, creates a capillary pressure head: the pressure in the vapor phase at the interface is higher than that of the liquid on the other side, by an amount equal to the capillary pressure jump. The vapor collected in the grooves then flows through a smooth pipe

(vapor-transport line) and reaches the condenser. In the condenser, the vapor is first condensed, and then, if the condenser is long enough (as the one shown is Figure 1.1), the condensed liquid is subcooled. The liquid collected in the condenser flows through the liquid-transport line and reaches the compensation chamber. Upon entering the compensation chamber, this liquid is heated, due to a "heat leak" from the evaporator [Kaya and Hoang (1999)], and also experiences heat exchange with the ambient environment. After passing through the compensation chamber, the liquid reaches the inner surface of the wick, and then flows through the wick back to the liquid-vapor interface. The static pressure drops as the liquid flows through the wick, and its temperature rises due to heat conducted through the grooved walls of the evaporator to the wick. At the liquid-vapor interface, the liquid temperature reaches that of the saturated vapor on the other side. Furthermore, as the saturated vapor is at a higher pressure than the adjoining liquid at the interface, due to the capillary pressure jump, the liquid at the liquid-vapor interface is in a superheated state.

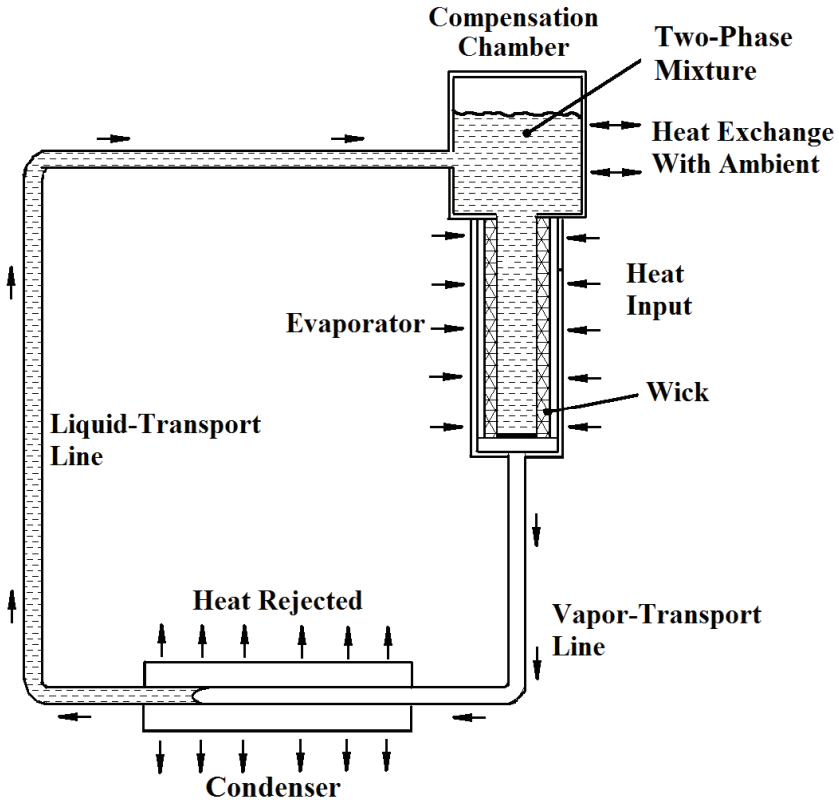

Figure 1.1: Schematic representation of a conventional (cylindrical-type) loop heat pipe.

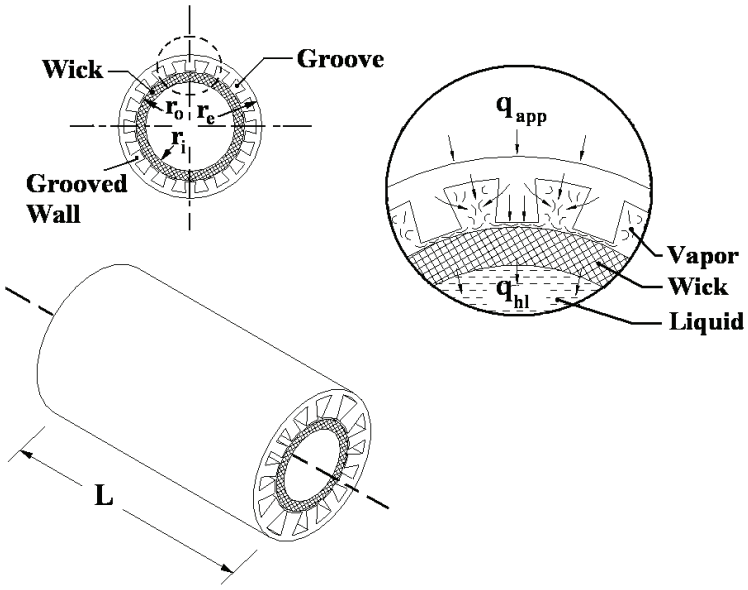

Figure 1.2: Schematic representation of the evaporator of a typical loop heat pipe.

As was mentioned previously in this section, LHPs chronologically follow HPs and CPLs, and some of the underlying concepts and principles of operation of these capillary-driven heat transfer devices are similar [Stenger (1966); Chi (1976); Dunn and Reay (1982); Faghri, A. (1995); Nikitkin and Cullimore (1998)]. Therefore, it is useful to ascertain the evolutionary advantages of LHPs over HPs and CPLs.

LHPs, as well as CPLs, use separate smooth tubing for both the vapor- and liquid-transport lines, and a wick is only needed in the evaporator section of the loop. Therefore, the pressure drop associated with the liquid flow through the wick is significantly reduced in comparison to that in HPs (where the wick covers the entire length of the pipe) for the same overall mass flow rate of the working fluid [Chi (1976); Dunn and Reay (1982); Faghri, A. (1995)]. As a result, LHPs and CPLs are usually capable of higher maximum rates of heat transfer than HPs, over longer distances. Moreover, the pore sizes of the wicks used in LHPs and CPLs can be finer than those of wicks used in HPs: The corresponding increase in capillary head allows LHPs and CPLs to more effectively accommodate adverse gravitational effects. In addition, in LHPs and CPLs, the evaporator and the condenser can be installed at a greater distance from one another, which facilitates the applications of these devices by providing flexibility in the

positioning of the heat source and the heat sink [Ku (1999); Maydanik (2005); Launay and Vallée (2011)].

Another advantage of LHPs and CPLs over HPs is that the vapor- and liquid-flow paths are completely separated. In HPs, the vapor and the returning liquid (condensate) flow in opposite directions, and a shear force exists at the corresponding liquid-vapor interface. At a high vapor velocity, liquid droplets can detach from the surface of the wick and get entrained in the vapor flow leading to a dry-out of the wick in the evaporator. This counter flow (vapor-liquid) arrangement in HPs imposes an entrainment limit on these devices: The entrainment limit dictates a maximum vapor velocity that can be sustained within a HP, which, in turn, limits the rate of heat transport that the HP can provide (more so than in LHPs and CPLs) [Silverstein (1992)].

LHPs and CPLs also allow the possibility of cooling multiple heat sources and rejecting the collected heat to single or multiple thermal sinks: This can be achieved by installing multiple evaporators in a hydrodynamically parallel configuration, and rejecting the total heat input via a single- or multi-condenser arrangement. Multi-evaporator LHPs and CPLs, with and without multiple condensers, are discussed in papers by Ku (1998, 1999), Yun et al. (1999), Goncharov et al. (2000), Hoang and Ku (2005), Ku et al. (2009), and Anderson et al. (2010). The main distinction between LHPs and CPLs resides in the location of the two-phase reservoir (or compensation chamber) in the loop. As discussed earlier, the two-phase reservoir in LHPs is an integral part of the evaporator body, whereas in CPLs, this reservoir is a separate chamber that is connected via a relatively short pipe to the liquid-transport line, at a point that is usually quite close to the evaporator [Ku (1998, 1999); Nikitkin et al. (1998)]. This seemingly minute difference has a noticeable impact on the start-up characteristics of LHPs and CPLs: In most instances, it is easier to start and maintain the steady-state operation of LHPs than that of CPLs. CPLs typically require preconditioning, where the reservoir is heated incrementally a few degrees (roughly 5 – 15 ^{o}C) above the evaporator temperature. On the other hand, LHPs do not necessitate any such preconditioning, and can begin operating as soon as the temperature difference between the compensation chamber and the evaporator is sufficient to establish the corresponding pressure difference required to

initiate circulation of the working fluid [Bienert and Wolf (1995); Nikitkin et al. (1998); Maydanik (2005)]

The main source of motivation for the work reported in this thesis is a strong desire and sense of commitment, on the part of both the author and his supervisor, to contribute to ongoing international efforts to ameliorate the design or enhance the operating efficiency of energy exchange, storage, and conversion systems.

As was mentioned earlier, this work pertains to the modeling of thermofluid phenomena encountered in loop heat pipes (LHPs). The overarching goal is to formulate, implement, and demonstrate cost-effective mathematical models and numerical solution methods for computer simulations of LHPs. The intention here is to propose improved models and numerical solution methods that are suitable for the design and optimization of LHPs, to illustrate the use of simple experimental procedures and correlations to effectively calculate the properties of the porous material (sintered powder metal) used as wicks in LHPs that are needed as inputs to the mathematical models, and also contribute to the understanding of the thermofluid processes that occur within these devices.

1.2 LITERATURE REVIEW

This section is divided into five subsections as follows: 1) textbooks, handbooks, and review articles that provide historical and comprehensive discussions of heat pipes (HPs), capillary pumped loops (CPLs), and loop heat pipes (LHPs); 2) textbooks, handbooks, and review articles that provide detailed discussions of the thermofluid phenomena that occur in LHPs; 3) publications on numerical methods for the prediction of fluid flow and heat transfer; 4) publications related to the properties of liquid-saturated porous materials; and 5) published works on the transient and steady-state operations of LHPs.

A comprehensive review of the vast number of published works on each of the above-mentioned topics is not intended in this section. Rather, only works that were used in and/or are directly relevant (or closely related) to the research presented in this thesis are reviewed here.

1.2.1 Books and Review Articles

Excellent reviews and discussions of the underlying theory, modeling, design, construction, and operation of HPs, CPLs (both chronologically preceding LHPs), and LHPs are available in books by Chi (1976), Dunn and Reay (1982), Silverstein (1992), Petersen (1994), and Faghri (1995). Review articles (on these devices) that were found to be particularly informative and useful in this work include the contributions of Ochterbeck and Peterson (1997), Ku (1999), Garimella and Sobhan (2001), Maydanik (2005), Launay et al. (2007), and Launay and Vallée (2011).

1.2.2 Thermofluid Phenomena in LHPs

The following thermofluid phenomena are encountered in LHPs: Single- and two-phase (vapor-liquid) fluid flow and heat transfer in passages (of circular and noncircular cross section) and fittings; fluid flow and heat transfer in porous media (wick materials); boiling; and condensation.

There are numerous textbooks related to single-phase Newtonian fluid flow and heat transfer in ducts: Examples include the works of Batchelor (1967), Eckert and Drake (1971), Landau and Lifshitz (1987), Tritton (1988), White (1991), Kays and Crawford (1993), Bejan (1995), Fox and McDonald (1998), Oosthuizen and Naylor (1999), Kaviany (2001), Incropera and DeWitt (2002), Bird et al. (2002), Currie (2003), and Munson et al. (2008). Classical research works in this area are reviewed in Kays and Perkins (1973). Single-phase laminar flow and heat transfer in ducts have been discussed comprehensively by Shah and London (1978). Detailed discussions of single-phase turbulent flow and heat transfer in ducts are available in the works of Tennekes and Lumley (1972), Hinze (1975), Wilcox (1993), Pope (2000), Launder and Sandham (2002), Davidson (2004), and Durbin (2010). For comprehensive reviews of the rheology of non-Newtonian flows, the reader is referred to books by Dealy and Wissbrun (1990), Macosko (1994), Tanner (2000), and Chhabra et al. (2008). Details of single-phase fluid flow and heat transfer topics of particular relevance to this research are covered in the works of Colebrook (1939), Sparrow and Patankar (1977), Gnielinski (1976, 1983), White (1991), and Kays and Crawford (1993), and are also elaborated in Chapters 2, 3, and 4 of this thesis.

Authoritative discussions of the basic and more advanced aspects of fluid flow and heat transfer in porous materials are available in books by Dullien (1992), Kaviany (1999), Nield and Bejan (2006), and Smirnov (2009). For comprehensive derivations of volume-averaged equations that govern these phenomena and related topics, the reader is referred to the contributions of Beavers and Sparrow (1969), Crapiste et al. (1973), Scheidegger (1974), Slattery (1981), Whitaker (1999), Kaviany (1999), Minkowycz et al. (1999), Alazmi and Vafai (2000), Nield and Bejan (2006), Clark (2009), and Civan (2011). Specific details of fluid flow and heat transfer in the wicks of LHPs are provided in Chapters 2 and 5 of this thesis.

For extensive discussions of two-phase (vapor-liquid) fluid flow and heat transfer in ducts, boiling, and condensation, the reader is referred to books by Wallis (1969), Collier (1972), Carey (1992), Whalley (1996), Tong and Tang (1997), Levy (1999), Klienstreuer (2003), Brennen (2005), Kolev (2007), and Ishii and Hibiki (2010). Reviews of these topics are available in articles by Bouré and Delhaye (1982), Drew (1983), Rohsenow (1985), Griffith (1985), Rose (1998), Ghajar (2005), Cheng and Mewes (2006), and Cheng et al. (2008). Pioneering works related to flow regime maps, pressure drops, and heat transfer coefficients for two-phase flows in horizontal and slightly inclined tubes include the contributions of Lockhart and Martinelli (1949), Baker (1954), Chato (1962), Mandhane et al. (1974, 1977), Taitel and Dukler (1976), Jaster and Kosky (1976), Soliman (1982, 1986), Dobson (1994), Dobson and Chato (1998), Ould Didi et al. (2002), El-Hajal et al. (2003), Thome (2003), Kim and Ghajar (2006), Lee et al. (2010), and Ong and Thome (2011). Some details of these works are provided in Chapter 2 of this thesis.

The *Handbook of Single-Phase Convective Heat Transfer* edited by Kakac et al. (1987), *Handbook of Heat Transfer* edited by Rohsenow et al. (1998), *Handbook of Phase Change: Boiling and Condensation* edited by Kandlikar et al. (1999), *ASHRAE Fundamentals* (2005), *Handbook of Porous Media* edited by Vafai (2005), and *Multiphase Flow Handbook* edited by Crowe (2006) are rich sources of information on the above-mentioned thermofluid phenomena that occur in LHPs. Comprehensive reviews of these topics can also be found in Vols. 1 – 42 of the series *Advances in Heat Transfer* edited by Hartnett et al. (1964 – 2010).

1.2.3 Numerical Methods for Fluid Flow and Heat Transfer

Numerical methods for the prediction of fluid flow and heat transfer phenomena are usually grouped into the following five main categories: finite difference methods, finite volume methods, finite element methods, boundary element methods, and spectral methods. Hybrid numerical methods that combine the attractive features of the aforementioned categories of methods have also been proposed, and examples include: Spectral element methods, finite analytic methods, and control-volume finite element methods. The fundamentals of these numerical methods are discussed in books authored by Patankar (1980), Tannehill et al. (1997), Roache (1998), Ferziger and Peric (1999), Reddy and Gartling (2000), Gresho and Sani (2000), Zienkiewicz and Taylor (2000), Peyret (2002), Gaul et al. (2003), Jaluria and Torrance (2003), Karniadakis and Sherwin (2005), and Wendt and Anderson (2009), among others. Comprehensive reviews of control-volume finite element methods for fluid flow and heat transfer are available in the works of Baliga (1997), Baliga and Atabaki (2006), and Jesuthasan and Baliga (2009b). For authoritative and useful discussions of the numerical modeling of turbulent flow and heat transfer in ducts, the reader is referred to the works of Wilcox (1993), Pope (2000), and Launder and Sandham (2002). The contributions of Leonard (1979, 1997) are also recommended for reviews of upwind procedures. The *Handbook of Numerical Heat Transfer* edited by Minkowycz et al. (2006) and Vols. 1 and 2 of the series *Advances in Numerical Heat Transfer* edited by Minkowycz and Sparrow (1997, 2000), provide comprehensive reviews and overviews of various aspects of computational fluid dynamics and heat transfer.

1.2.4 Properties of Liquid-Saturated Porous Materials

As was mentioned previously in this chapter, the wicks of LHPs are liquid-saturated porous materials. Therefore, key inputs to the design and mathematical models of LHPs include the porosity, the maximum effective pore size, the effective permeability, and the effective thermal conductivity of liquid-saturated wicks.

The seminal contributions of Maxwell (1954), Kunii and Smith (1960), Chen and Tien (1973), Batchelor and O'Brien (1977), Ogniewicz and Yovanovich (1978), Sangani and Acrivos (1983), Hadley (1986), Bauer (1993), Kaviany (1999), Hsu (2000),

Bonnefoy et al. (2004), Bahrami et al. (2004, 2006), and Nield and Bejan (2006) provide extensive discussions of many of the available analytical, semi-analytical, and numerical correlations for effective properties of porous materials made of uniformly sized, regularly spaced, and packed (unconsolidated or consolidated) spherical particles. Reviews of some of the aforementioned and additional analytical correlations are available in the works of Tsotsas and Martin (1987), Tavman (1996), Gusarov and Kovalev (2009), and Antwerpen et al. (2010).

The above-mentioned analytical correlations are inapplicable to the wicks typically used in LHPs, as they are made from sintered metal powders or fibers. Furthermore, for the sintering of metal powders, particles of angular rather than spherical shapes are preferred, and these particles are not necessarily uniformly sized or regularly spaced [Goring and Churchill (1961), Batchelor (1974), Hadley (1986); Leong et al. (1997); Mo et al. (2006)]. The sintering process creates excellent joints (solid-to-solid contact zones) between the particles or fibers; and most of the available analytical correlations do not properly account for this effect of the sintering process [Kunii and Smith (1960); Hadley (1986); Leong et al. (1997); Mo et al. (2006)].

Analytical and experimental investigations to determine the effective properties of sintered metal powders and fibers have been conducted and reported by Kunz et al. (1967), Soliman et al. (1970), Alexander (1972), Singh et al. (1973), Van Sant and Malet (1975), Hadley (1986), Peterson and Fletcher (1987), Chang (1990), Mantel and Chang (1991), Bonnefoy et al. (2004), Atabaki and Baliga (2007), Petrasch et al. (2008), and Yu et al. (2011).

Details of some of the aforementioned and other contributions on this topic are presented in Chapters 2 and 5 of this thesis.

1.2.5 Loop Heat Pipes

The main focus of this thesis is on the steady-state operation of loop heat pipes (LHPs). However, there have been some recent efforts aimed at better understanding of the transient operations of LHPs, including their temperature overshoots and oscillations during startup. In this subsection, first, papers that deal with the startup and transient

operations of LHPs are reviewed. Following that, attention is then devoted to works on modeling and experimental investigations of the steady-state operation of LHPs.

1.2.5.1 Startup and Transient Operations of LHPs

Ku and Rodriguez (2003) and Ku (2003) have outlined the existence of what are essentially three types of temperature oscillations in LHPs: (i) An ultra-high-frequency temperature oscillation with a period of the order of a few seconds that is associated with the inherent two-phase flow characteristics in LHPs; (ii) a high-frequency, low-amplitude, temperature oscillation with a period of the order of seconds to minutes, and an amplitude of the order of 1 K (this type of oscillation is attributed to the inability of the vapor front to find a stable position inside the condenser); and (iii) a low-frequency, high-amplitude, temperature oscillation with a period of the order of hours and an amplitude of the order of tens of Kelvin.

Ku and Rodriguez (2003) have reported experimental results of low-frequency, high-amplitude temperature oscillations for their LHP operating with propylene, with power inputs in the range of 15 – 75 W and sink temperatures between 243 K and 273 K. The authors first described the two most common conditions associated with this type of temperature oscillation in LHPs: (i) a constant power input to the evaporator linked with an oscillating sink temperature; and (ii) a constant sink temperature coupled with an oscillating power input to the evaporator. Ku and Rodriguez (2003) then presented a third, more subtle, condition for the aforementioned temperature oscillation: A large thermal mass attached to the evaporator can absorb and store energy during an increase in the compensation chamber temperature, and can also release energy during a decrease in the temperature of the latter. As a result, the large thermal mass can modulate the constant power applied to the evaporator into what is essentially an oscillating power input. This subsequent oscillation of the power input to the evaporator is the main source of the low-frequency and high-amplitude temperature oscillations in LHPs.

Ku (2003) has also performed an analytical and experimental investigation of the high-frequency and low-amplitude temperature oscillations in LHPs. As was mentioned earlier, this type of temperature oscillation is commonly associated with the inability of the vapor front to find a suitable, stable, position inside the condenser. Ku (2003) has used three different LHPs (all working with ammonia) to investigate the motion of the

vapor front. The experimental results of Ku (2003) showed the occurrence of high-frequency, low-amplitude temperature oscillations in the LHPs corresponding to the following locations of the vapor front: (i) near the condenser inlet; and (ii) near the condenser outlet. Thus, when the vapor front moves near the inlet or outlet of the condenser, it is unable to find a suitable stable location and moves back-and-forth in the vicinity of these locations. As a result of this movement of the vapor front in the condenser, a temperature fluctuation is induced in the liquid line leading to a corresponding oscillation in the temperature of the compensation chamber in LHPs.

Chen et al. (2006) have conducted an experimental investigation of the steady-state and transient performance of a miniature loop heat pipe under different orientations (one horizontal and four vertical) for sink temperatures ranging from 5 – 50 ^{o}C. The LHP had a cylindrical evaporator with an outer diameter of 5 mm and a length of 29 mm. The working fluid consisted of ammonia, and the maximum evaporator temperature was limited to 80 ^{o}C. Chen et al. (2006) have presented steady-state and transient results of their LHP for the following orientations: (i) Horizontal (the evaporator and condenser are located on a single horizontal plane with respect to the gravitational acceleration vector); (ii) condenser above evaporator; (iii) evaporator above condenser; (iv) compensation chamber above evaporator; and (v) evaporator above compensation chamber. The authors claimed that startup of the LHP was possible with a power input as low as 5 W. Generally, a small temperature overshoot was observed during startup, which was attributed to the slow movement of the cold liquid from the condenser into the compensation chamber. The thermal resistance of the LHP decreased with increasing sink temperature and power input to the evaporator. Chen et al. (2006) reported that for a sink temperature of 25 ^{o}C and a power input of 70 W, the resulting thermal resistance of the loop approached a minimum value of 0.2 ^{o}C/W for the first four orientations described earlier; whereas for the prescribed sink temperature, the LHP did not work under the fifth (evaporator above compensation chamber) orientation.

Launay et al. (2007b) have formulated a mathematical model for the prediction of the transient behavior of LHPs. In this model, the LHP is first divided into the following four subsystems: (i) the fluid in the compensation chamber; (ii) the evaporator and compensation chamber wall; (iii) the fluid in the condenser; and (iv) the fluid in the

vapor- and liquid-transport lines. The conservation of mass, momentum and energy are then imposed on each subsystem and also on the overall LHP. Launay et al. (2007b) compared the predictions of their model with the experimental results of Wrenn et al. (1999): Their model qualitatively predicted the experimental data despite an inherent time lag of about 100 s between the model predictions and experimental results. The model also under-predicted the temperature of the evaporator saddle and compensation chamber by less than 2 K, and the liquid-line temperature variation by nearly 3.5 K. Nevertheless, the model predictions of Launay et al. (2007b) are in qualitative agreement with the experimental findings of Wrenn et al. (1999).

Launay et al. (2007b) also used their transient model of LHPs to study the occurrence of (i) low-frequency, high-amplitude, temperature oscillations; and (ii) high frequency, low amplitude, temperature oscillations.

As reported earlier by Ku and Rodriguez (2003), low frequency, high amplitude, temperature oscillations are related to the evaporator thermal mass, which modulates the net heat input to the evaporator by storing energy when the compensation chamber temperature is increasing, and releasing energy when the compensation chamber temperature is decreasing. Consequently, the net heat load on the evaporator is oscillatory. In order to investigate low-frequency and high-amplitude temperature oscillations, a heat input of 25 W was imposed on the LHP by Launay et al. (2007b). In addition, the sink and ambient temperatures were maintained constant with a temperature difference of 35 K, and the thermal mass attached to the evaporator was increased to a value of 10 kg, similar to the experimental study of Ku and Rodriguez (2003). The model of Launay et al. (2007b) qualitatively predicted the low-frequency, high-amplitude, temperature oscillations in the LHP. The oscillation period was around 140 minutes, and the maximum temperature variation at the evaporator was equal to 8 K.

The high-frequency, low-amplitude, temperature oscillations, on the other hand, are caused by the inability of the vapor front to find a stable position at the condenser outlet (or inlet for low power input) [Ku (2003)]. In order to simulate this type of temperature oscillations, Launay et al. (2007b) imposed two heat inputs on the LHP: one varying from 20 to 800 W at time 1000 s, and another varying from 800 to 450 W at time 4000 s. The sink and ambient temperatures were also maintained constant, with a temperature

difference of 15 K. The model then predicted a temperature oscillation at a heat input of 800 W with a frequency equal to 1.8 x 10^{-3} Hz. The maximum amplitude of the temperature oscillation reported was about 5 K.

Li et al. (2010) conducted an experimental study on the startup and transient behavior of a compact copper LHP with a flat evaporator operating with de-ionized distilled water (claimed to be most environmental-friendly and compatible with copper wick) as the working fluid. The authors further underlined the extensive international interest of both academic and industrial circles in high performance LHPs, as well as the on-going research efforts being conducted to provide a well-accepted physical model capable of describing the mechanisms behind the transient and steady-state operations of LHPs.

The compact LHP designed and used by Li et al. (2010) consisted of a flat square evaporator with a dimension of 30 mm (L) x 30 mm (W) x 15 mm (H). The vapor- and liquid-transport lines each had an internal pipe diameter of 5 mm and a length of 120 mm. No additional information was provided regarding the size of the condenser, compensation chamber, or the characteristics of the porous wick (porosity, permeability, maximum pore size, and effective thermal conductivity) used in this work. This LHP was tested under a vertical configuration with the evaporator placed below the condenser. Li et al. (2010) noticed repeated transient temperature oscillations during the startup process of their LHP for heat loads of 30 W, 50 W, and 100 W. During the startup process, they monitored the evaporator-bottom temperature, and observed an initial temperature rise followed by a sudden temperature drop (with a magnitude between 5 – 10 ^{o}C). Following this rapid drop, the evaporator temperature oscillated over time in a regular and periodic manner.

Li et al. (2010) hypothesized that the oscillations with different characteristics arise mainly from the following three effects: (i) original liquid blocking along the vapor flow passage; (ii) alternative turn-out of menisci and flooding in the wick; and (iii) two-phase flow instability in the condenser. Based on their experimental findings and earlier work on high-speed visualization of boiling and evaporation of water on micro-porous-media, the authors proposed the existence of two main modes associated with the startup of LHPs to explain how vapor is first generated in the evaporator, and how it ultimately displaces liquid from the vapor flow passage in the evaporator, vapor-transport line, and a

portion of the condenser. These modes are referred to in their work as (i) a boiling-triggered startup at comparatively low temperatures, and (ii) an evaporation-triggered startup at comparatively high temperatures.

Li et al. (2010) inferred from their experiments that at very low heat loads the LHP startup can be initiated in an unstable manner. The observed irregular oscillations in the LHP temperature at very low heat loads were associated with the discontinuous bubble generation and collapse, combined with the two-phase flow instability in the condenser. This represents the so-called boiling-triggered startup of the LHP. If this boiling process is unable to maintain the appropriate heat balance in the LHP with increasing heat loads, the LHP temperature increases and the liquid-vapor interface starts to retreat into the wick, meaning that the circulation of the fluid in the LHP from the evaporator back to the compensation does not fully occur at this boiling stage due to the lack of sufficient driving force. Once the liquid-vapor interface (and related menisci) is established in the wick, the capillary force drives the circulation of the fluid in the LHP, and evaporation becomes the dominant heat transfer mechanism: this is the so-called evaporation-triggered startup of the LHP.

Li et al. (2010) also noticed the occurrence of temperature oscillations when the startup mode switched from the boiling-triggered to the evaporation-triggered mode. A probable explanation was put forward: The heat load was still comparatively low at this stage, and therefore immediately after the establishment of the liquid-vapor interface in the wick and the proper fluid circulation inside the loop, the extensive evaporation heat transfer process resulted in a sudden cooling of the evaporator. The temperatures of the compensation chamber and the rest of the LHP also decrease correspondingly. Consequently, the vapor pressure at the liquid-vapor interface reduces causing the collapse of the menisci, and results in the temporary re-flooding of the wick. This repeated process of the menisci formation and re-flooding of the wick is the suggested mechanism behind the temperature oscillations during the evaporation-triggered startup mode.

1.2.5.2 Steady-State Operation and Models of LHPs

Bienert and Wolf (1995) presented an analytical model and some experimental results for an LHP. However, full details of the experimental setup were not provided. The proposed analytical model was focused on pressure and energy balances on each component of the LHP. The energy balances are resolved using a combined lumped parameter and nodal network approach: Specifically, the evaporator and compensation chamber are treated as lumped parameters, whereas the rest of the loop was modeled using a nodal network approach. The authors presented experimental results for the steady-state performance of an LHP operating in both variable- and fixed-conductance modes. They also indicated that these two modes of operation may not be fully prevalent in every test case. Furthermore, one mode may be inhibited by the other, depending on the thermal connection to the ambient environment.

Bienert and Wolf (1995) also discussed the concept of using an active thermal control in the operations of LHPs. In their experiments, the thermostatic control (heating) of the compensation chamber of their LHP was operated at temperatures higher than that of the ambient environment. This approach allowed for active control of the steady-state operating temperatures in the LHP, but only until the condenser could no longer accommodate the rejection of the total power input: Simply put, for a given sink temperature using this method, the control range was constrained by the heat rejection capability of the condenser. Therefore, increasing the set-point, for the given sink temperature, allowed for a higher heat rejection capability and more precise thermal control over a broader spectrum of the overall power input to the evaporator-compensation-chamber assembly.

Wirsch and Thomas (1996) have conducted experimental, analytical, and numerical studies of the performance of an LHP constructed of stainless steel and operated with ammonia as the working fluid. The evaporator was equipped with a cylindrical sintered nickel-powder wick fitted in a flat aluminum saddle. To keep the temperature of the fluid in the vapor-transport line stable at a pre-established set-point temperature, the condenser's cooling rate was modified by increasing or reducing the flow-rate of the refrigerant. Wirsch and Thomas (1996) performed two tests for vapor-transport-line temperatures of 40 ^{o}C and 50 °C, and through these tests were able to discern the

maximum power inputs that could be sustained by the LHP: A maximum power input of 337 W was achieved with a vapor-transport-line temperature of 50 ^{o}C. However, at this point, there was insufficient amount of liquid to maintain the wick wet, the evaporator temperature increased suddenly, and the evaporator eventually dried out. Wirsch and Thomas (1996) then found conditions that limited the power input and kept the evaporator sufficiently wet: This corresponded to a 40 °C vapor-transport-line temperature and an approximate condenser limit (the highest heat-rejection capability) of 260 W. From these results, the authors were able to calculate an effective thermal resistance using the input power and temperature difference between the average steady-state temperatures of the evaporator and condenser. This effective thermal resistance decreased when the power input was increased, and attained a minimal sustainable value of 0.085 ^{o}C/W.

Wirsch and Thomas (1996) used a finite-element analysis to model the steady-state heat conduction in the evaporator assembly (aluminum saddle, thermal grease, and stainless steel evaporator shell). Their model focused on the transfer of heat from a strip heater to the aluminum saddle of the evaporator, which was then directed to and conducted through the stainless steel wall of the evaporator, and ultimately dissipated at the inner radius of the evaporator wall through an evaporative boundary condition. Based on their experimental results, the authors computed values of the evaporative heat transfer coefficient as a function of the power input and difference in the average temperatures of the vapor-transport line and the evaporator. Their predictions of the outer-surface temperature of the evaporator were in agreement with the corresponding experimental data.

Kaya and Hoang (1999) proposed a mathematical model for LHPs, built on steady-state energy conservation equations and pressure drop calculations. The predictions they obtained using this model were compared to experimental data from two different LHPs (the GLAS-LHP and the NRL-LHP). NASA designed the GLAS-LHP to facilitate thermal control of the Geoscience Laser Altimeter System (GLAS), while the NRL was designed and built for U.S. Naval Research Laboratory (NRL). Good agreements (within 5%) were reached between corresponding computational and experimental results. The model proposed by Kaya and Hoang (1999) assumed that the LHP compensation

chamber would always be filled with a two-phase (liquid and vapor) fluid mixture. This condition guaranteed that the mass and phase distribution requirements in the LHP were automatically satisfied. It also ensured that there was enough room in the compensation chamber to absorb excess fluid forced into it from the condenser, while also maintaining the fluid inside it in a two-phase condition. Kaya and Hoang (1999) also assumed that any subcooled liquid entering the compensation chamber from the liquid-transport line would be heated to the same temperature as the liquid absorbed into the inner surface of the wick, with the required energy coming from the heat transfer from the ambient environment (conducted through the compensation chamber envelope) and heat leak from the evaporator. The heat rejection in the condenser was divided into a two-phase and a subcooled part. However, the details for the calculation of the two-phase pressure drop in this region were not provided. The condenser tube was attached on one side to a plate with embedded pipes through which a coolant (a refrigerant) was circulated to simulate a uniform-temperature thermal sink, and the other side of the condenser pipe was exposed to the ambient environment. In the model of this condenser, the heat exchange with the ambient environment (the so-called "parasite heat transfer") was included. However, details of how the heat transfer surface of the condenser tube was partitioned to take into account heat transfer to and/or from the ambient environment and to the sink (cooling plate) are not provided in this paper.

Kaya and Hoang (1999) reported that the GLAS-LHP performed in a variable-conductance mode when the power input to the evaporator was less than 100 W. The operating temperature (saturation temperature in the vapor grooves of the evaporator) in this mode decreases to a minimum with increasing power input, up to 100 W. For power inputs above 100 W, the LHP operated in the fixed-conductance mode: This was demonstrated by the linear rise in the operating temperature with increase in the power input. The experimental results reported in Kaya and Hoang (1999) were used, in Chapter 2 of this thesis, to validate the proposed segmented network thermofluid model of LHPs. The predictions obtained with this computational model were in very good qualitative agreement with the reported experimental data of Kaya and Hoang (1999).

Maydanik (2005) has provided a review of LHPs, including a short historical background, description of the theory, and presented some recent developments and test

results concerning LHPs. In particular, he presented elements of a mathematical model of LHPs, widely adopted by many researchers, based on steady-state energy conservation equations and pressure drop calculations akin to Kaya and Hoang (1999).

As a condition of LHP operability, Maydanik (2005) stated that the capillary pressure jump across the liquid-vapor interface located in the wick must sustain all the associated vapor and liquid pressure drops in the overall LHP system. However, he explicitly asserted that the pressure drop in the condenser section of LHPs was negligible. This definitive statement is too restrictive. Indeed, many of the available mathematical models of LHPs do not properly account for the single- and two-phase pressure drops in the condenser portion of LHPs. As will be shown in this thesis (Chapter 6), the pressure drop in the condenser of LHPs can make up a significant portion of the overall pressure drop in the loop for certain operating conditions.

Maydanik (2005) also described the importance of vapor removal channels in LHPs, especially for LHPs with high heat flux (great than 0.70 MW/m^2) capability. The evaporation of the working fluid takes place in a relatively thin layer of the wick immediately adjacent to the wall of the evaporator, towards which the evaporating menisci are turned. To provide effective heat exchange in this evaporation zone, it is necessary to create a special system of vapor-removal channels located at the wall-wick boundary to facilitate the vapor flow into the vapor-transport line. The simplest vapor-removal channels are straight grooves cut into the metal wall of the evaporator, adjacent to the wick. A two-step vapor-removal system incorporates small azimuthal grooves cut into the evaporator wall, and larger longitudinal channels cut into the wick itself. Although Maydanik (2005) discussed the importance of the vapor-removal channels for achieving high heat exchange in the evaporation zone, he did not discuss the importance of adequately accounting for the associated increase in pressure drop in these vapor channels due to the corresponding increase in the rate of evaporation in high-heat flux LHPs. Furthermore, to the knowledge of the author, no currently available mathematical model of LHPs provides for accurate and reliable calculations of the pressure drop in the vapor-removal channels of LHPs. A suitable numerical method for the computation of the pressure drop and also heat transfer in the vapor-removal channels of LHPs is put forward, implemented, tested, and used in Chapters 3, 4, and 6 of this thesis.

Singh et al. (2007) presents an experimental investigation of a miniature LHP made of copper, and with a flat-disk shaped evaporator (30 mm in diameter and 10 mm thick) designed for thermal control of computer microprocessors. The inner face of the evaporator was machined with 15 vapor channels of rectangular cross-section (1 mm deep and 0.50 mm wide), which provided an efficient vapor-removal mechanism. The evaporator was also equipped with a nickel wick, of thickness 3 mm, mean pore radius between 3 - 5 μm, and porosity 0.75. The condenser of the LHP was provided with external fins measuring 20 mm x 10 mm with a thickness of 0.20 mm. Cooling of the condenser was achieved by forced convection, provided using a cooling fan and ambient air with inlet temperature of about 24 °C. Tests were conducted using water as the working fluid. The reported LHP design was able to transport a maximum heat load of 70 W over a distance of 150 mm. The flat-evaporator design was preferred due to its lower interface resistance and ease of integration inside the limited space of notebook PCs.

In the above-mentioned paper, Singh et al. (2007) reported that the LHP achieved reliable startup with a power input as low as 20 W, and was able to attain steady-state operation for every 5 W step-increases in the input power. The LHP operated in the variable-conductance mode for power inputs less than 30 W, and in the constant-conductance mode of operation for power inputs greater than 30 W. The minimum value of the overall thermal resistance of the LHP was 0.17 °C/W. Singh et al. (2007) stated that the maximum heat capacity of miniature LHPs in electronics cooling is essentially dictated by the maximum permissible temperature at the heat source (chip surface, for example), which is generally estimated as 100 °C. They also stated that water is an ideal candidate for the working fluid of LHPs designed for ground based electronics cooling applications, where stringent restrictions are in place concerning the use of high-pressure, toxic, or inflammable working fluids such as ammonia, acetone, or different grades of alcohol. In this regard, water was selected as a suitable option, and for its highly-effective heat transfer characteristics in the 50 - 100 °C temperature range.

More recently, Singh et al. (2009) presented a mathematical model of a miniature LHP operating under steady-state conditions. In this work, the pressure drop associated with the flow of liquid in the wick is modelled using Darcy's law, and the pressure drops in the vapor- and liquid-transport lines are computed based using correlations for the

Darcy friction factor for fully-developed (laminar or turbulent) flows in circular and non-circular pipes. However, Darcy friction-factor correlations that are strictly applicable only for fully-developed (laminar or turbulent) flows in ducts of circular and non-circular cross-sections and impermeable walls were also used to calculate the pressure drop in the vapor-removal channels of rectangular cross section (based on the hydraulic diameter of the channel and vapor flow-rate at the exit of the channel). This approach is inherently invalid as it fails to account for injection of vapor into the vapor-removal channels, along their surface adjacent to the wick, as a result of the vaporization process at the liquid-vapor interface located in the wick. Furthermore, the mathematical model of Singh et al. (2009) does not account for the single- and two-phase pressure drops in the condenser section of the LHP. Instead, single-phase flow correlations were used to determine the overall pressure drop in the entire condenser unit. In addition, the calculation of the two-phase heat transfer in the condenser was simplified and assumed to be equal to the rate of heat transfer required for evaporation of the saturated liquid in the wick. These shortcomings of this and other similar mathematical models of LHPs are addressed further (along with ways to overcome them) in Chapters 2, 3, and 4 of this thesis.

Most recently, Li and Peterson (2011) presented a quasi three-dimensional computational model of a specific flat-evaporator design used in their earlier LHP experiments [Li et al. (2010)]. The special features of this evaporator design pertained to construction of the sintered-powder-copper wick structure, in which (i) the wick was mounted on top of a copper substrate; (ii) vapor-removal channels of rectangular cross-section were directly machined in the wick structure; and (iii) the compensation chamber was attached on top of the wick, keeping it in a fully-saturated condition. The heat input to the evaporator occurred at the base of the copper substrate, and evaporation took place at the liquid-vapor interface located near the wick-substrate boundary.

In the above-mentioned paper, Li and Peterson (2011) computationally investigated the fluid flow and heat transfer mechanisms, but only within the wick structure and compensation chamber. In particular, attention was focused on understanding the heat transfer mechanism along the liquid-vapor interface inside the wick. They adapted suitable liquid and vapor boundary conditions in the wick, based on works of Demidov and Yatsenko (1994), and Kaya and Goldak (2008). Li and Peterson (2011) observed that

the highest heat flux occurred at the wick-substrate boundary where there is excellent metal-to-wick contact. When moving further from the metal-to-wick contact region and closer to the open cavity region representing the vapor-removal channel (or groove), the heat flux decreased. This provided support to the earlier work of Demidov and Yatsenko (1994), which claimed that the evaporation from the meniscus formed in the vicinity of the metal-to-wick contact region between the wick and evaporator body was much higher than that occurring at the interface between the wick and the open vapor-channel.

It should also be noted that Li and Peterson (2011) proposed the use of a detailed evaporator model in conjunction with a network model (based on steady-state energy conservation equations and pressure-drop calculations) for the accurate predictions of LHP performance. However, details concerning the heat transfer in the rest of the LHP were not provided. Furthermore, despite aiming to provide a detailed model of the LHP evaporator, Li and Peterson (2011) used a fully-developed Darcy friction-factor correlation strictly applicable only to ducts of rectangular cross-section and impermeable walls for the calculation of the pressure drop in the vapor-removal channels. A full three-dimensional conjugate fluid flow and heat transfer model of the LHP evaporator is needed to properly account for the details of the heat transfer across the liquid-vapor interface in the wick and the associated pressure-drop mechanisms in the evaporator section of LHPs. However, this approach could potentially become computationally intensive, and would not be readily adaptable within the framework of a simple and cost-effective thermofluid model for the reliable design and optimization of LHPs.

Considering the aforementioned shortcomings in past models of LHPs, the work reported in this thesis was directed towards the formulation of novel correlations for predicting pressure drops and the associated heat transfer within the vapor-removal channels, and the incorporation of these correlations within enhanced quasi-one-dimensional network thermofluid models. The overall goal in this work was to propose cost-effective mathematical models and numerical solution methods that could serve as useful tools for the design and optimization of LHPs.

1.3 OBJECTIVES

The objectives of the research work reported in this thesis are summarized below:

- To formulate, implement, test, and apply a segmented network thermofluid model for the simulation of conventional LHPs with cylindrical and flat evaporators operating under steady-state conditions. The aim is to illustrate the main steps in the formulation of a segmented network model of LHPs that is, at the least, capable of generating qualitatively accurate predictions of the associated thermofluid phenomena. In addition, the model is intended to serve as a cost-effective tool for the design and optimization of LHPs. In this context, the capabilities of the proposed model are assessed by using it to simulate an LHP akin to that illustrated in Figure 1.1, and comparing its predictions against experimental measurements in the available literature.
- To put forward a co-located equal-order control-volume finite element method (CVFEM) for predicting three-dimensional parabolic fluid flow and heat transfer in straight ducts of uniform *regular*- and *irregular*-shaped cross-section. The methodology of the proposed CVFEM is also adapted to formulate a simpler finite volume method (FVM). The aim here is to use this simpler FVM to investigate steady, laminar, Newtonian fluid flow and heat transfer in straight vapor grooves of rectangular cross-section, for parameters ranges representative of typical LHP operating conditions.
- To propose novel correlations for accurate, reliable, and cost-effective predictions of the overall pressure drop, and also the bulk temperature, of the vapor flowing in straight grooves of rectangular cross-section machined in the metallic body of the evaporator of LHPs. The aim is to develop correlations that could be easily incorporated into thermofluid models of LHPs. These correlations are incorporated in the aforementioned quasi-one-dimensional model to obtain an enhanced segmented network thermofluid model of LHPs.
- To illustrate the use of simple and effective experiments, procedures, and correlations for determining the following properties of sintered powder-metal porous materials that are used as wicks in LHPs:
    - Porosity

- Maximum effective pore size
- Effective permeability
- Effective thermal conductivity when fully saturated with a liquid

These properties of the porous wick material are required for the design of LHPs and are needed as inputs in mathematical models of these devices. The intension here to illustrate the determination of these properties for a sample porous sintered-powder-metal plate made of stainless steel 316, and present and discuss the results.

- To demonstrate the capabilities of the enhanced network thermofluid model by applying it to simulate a sample LHP operating with four different working fluids: Ammonia, distilled water, ethanol and isopropanol.
- To present and comparatively discuss the model predictions of the above demonstration problem and to illustrate the significance of incorporating in accurate correlations for the predictions of the overall pressure drop in the vapor-grooves of LHP evaporators into thermofluid models of LHPs.

1.4 ORGANIZATION OF THE THESIS

In earlier sections of this chapter (Chapter 1), some background discussions (of HPs, CPLs, and LHPs), the motivation for this work, a review of the literature relevant to this research, and its objectives were presented.

In Chapter 2, a segmented network thermofluid model for simulating steady-state operation of conventional LHPs with cylindrical and flat evaporators is presented. Suitable quasi-one-dimensional formulations, incorporating semi-empirical correlations for the related multiphase phenomena, are presented and discussed. The proposed model is used to simulate an LHP for which experimental measurements are available in the literature, and comparisons of the predicted results to the experimental data are presented and discussed.

In Chapter 3, a three-dimensional, parabolic numerical method based on a control-volume finite element method (CVFEM) is first put forward. This CVFEM is designed for predicting steady developing fluid flow and heat transfer in straight ducts of irregular cross-section. Next, this three-dimensional parabolic CVFEM is adapted to formulate a

simpler finite volume method (FVM) designed for predicting developing fluid flow and heat transfer in straight ducts of *regular* rectangular cross-section, akin to the geometry of vapor grooves (or vapor-removal channels) used in the LHPs considered in this work.

In Chapter 4, the FVM formulated in Chapter 3 is used to investigate steady, laminar, Newtonian fluid flow and heat transfer in straight vapor grooves of rectangular cross-section. Some novel results corresponding to a special fully-developed flow and heat transfer region (particular to LHPs) are systematically presented and discussed, and suitable new correlations are developed for predictions of the overall pressure drop and the bulk temperature of the vapor flowing in the vapor grooves.

In Chapter 5, the use of simple and effective experiments, procedures, and correlations for the determination of the porosity, maximum effective pore size, effective permeability, and effective thermal conductivity of liquid-saturated, porous-sintered-powder-metal wicks in LHPs is demonstrated. This demonstration exercise is conducted using a sample porous sintered-powder-metal plate made of stainless steel 316, and the results are presented and discussed.

In Chapter 6, the capabilities of the proposed enhanced thermofluid network model (comprised of the segmented network thermofluid model presented in Chapter 2, coupled with the correlations developed from the detailed numerical analysis of the flow and heat transfer in the vapor grooves, as outlined in Chapter 4) are illustrated through a demonstration problem, that involves an LHP operating with four different working fluids. In this work, ammonia, distilled water, ethanol, and isopropanol are used as the working fluids, and the obtained results are comparatively discussed.

In Chapter 7 (the concluding chapter), the contributions of this thesis are reviewed and some suggestions are presented for extensions of this work.

Chapter 2:

A Segmented Network Thermofluid Model of Loop Heat Pipes

A segmented network thermofluid model for the simulation of loop heat pipes (LHPs) operating under steady-state conditions is presented in this chapter. This model was formulated by borrowing, extending, and amalgamating key ideas from Atabaki (2006) and Atabaki et al. (2007). The extensions have been reported in Jesuthasan et al. (2008) and Jesuthasan and Baliga (2009a). The proposed model also sets the stage for important contributions of this thesis (presented in Chapters 3 and 4) related to modeling and computer simulations of fluid flow and heat transfer in the vapor grooves of the evaporators of LHPs. The focus here is on cost-effective modeling of thermofluid phenomena in LHPs with one evaporator, a vapor-transport line, one condenser, a liquid-transport line, and a compensation chamber, akin to those illustrated in Figure 2.1.

In this segmented network thermofluid model, the vapor-transport line, the condenser pipe, and the liquid-transport line are divided into longitudinal control volumes or cells (segments). Quasi-one-dimensional formulations, incorporating semi-empirical correlations for the related single-phase and multiphase phenomena, are used to impose balances of mass, momentum, and energy on each of the aforementioned cells. Variations of thermophysical properties of the working fluid with temperature are taken into account, along with change in quality, pressure drop, and heat transfer in the two-phase regions, giving the proposed model enhanced capabilities compared to those of earlier thermofluid network models of LHPs, such as those of Bienert and Wolf (1995), Kaya and Hoang (1999), Maydanik (2005), Singh et al. (2007). In these earlier models, balances of mass, momentum, and energy are imposed on the full elements (rather than segmented portions) of the LHP, and the variations of quality and pressure drops in the liquid-vapor two-phase regions are overlooked.

After the presentation of the aforementioned segmented network thermofluid model, its capabilities are demonstrated by using it to simulate an LHP similar to one investigated experimentally by Kaya and Hoang (1999). This chapter provides details of this

simulation, including comparisons of the predicted results and with the experimental results of Kaya and Hoang (1999).

Chapters 3 and 4 are devoted to the presentation of multidimensional mathematical models, numerical solution methods, and the development of accurate correlations for predicting the pressure drop and bulk temperature of the vapor flowing in the vapor-removal channels cut in the metallic walls of the evaporators of LHPs. These correlations are used to enhance the segmented network thermofluid model proposed in this chapter. In Chapter 6, the capabilities of this enhanced model are demonstrated by using it to simulate an LHP operated with four different working fluids.

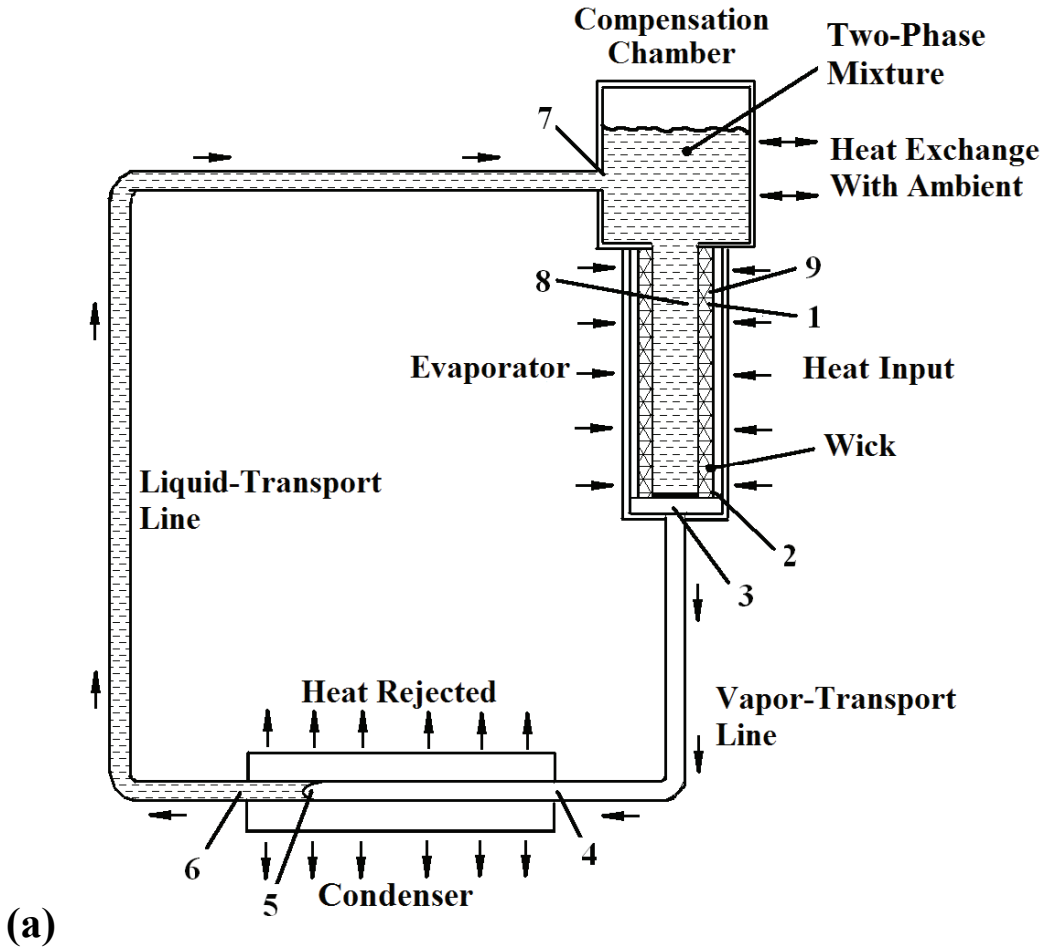

(a)

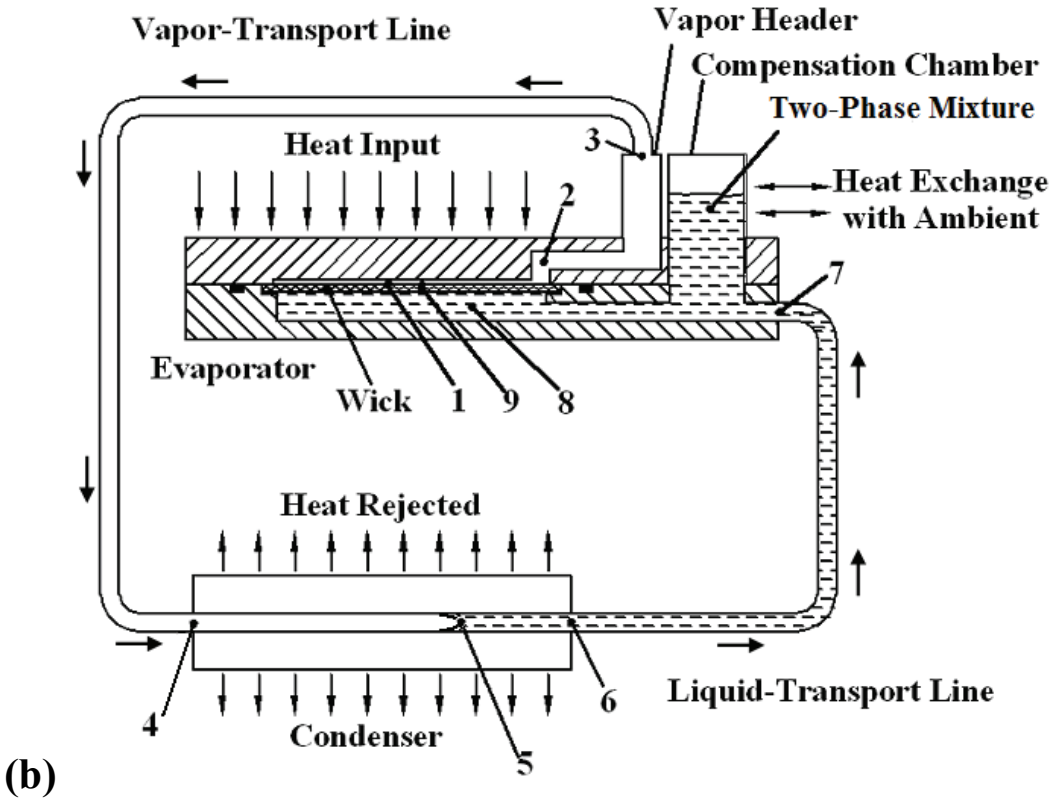

Figure 2.1: Schematic representations (not to scale) of loop heat pipes with (a) a cylindrical-evaporator and (b) a flat-evaporator.

2.1 OVERVIEW OF LHP THERMODYNAMICS

The pressure-temperature (*P*-*T*) diagram given in Figure 2.2 illustrates the thermodynamic states of the working fluid at each of the numbered points shown in Figure 2.1. In the *P*-*T* diagram given in Figure 2.2, it is assumed that the evaporator and condenser sections are at comparable elevations (so the effect of gravity is negligible), mainly for ease of presentation.

At point 1, which corresponds to the liquid-vapor interface located inside the rectangular wick very close to its outer surface, the fluid is vaporized at $T_1 = T_{sat}$ and $P_1 = P_{sat}$ (on the vapor side of the liquid-vapor interface). P_1 is the highest thermodynamic (static) pressure in the loop. The vapor flows through the grooves in the wall of the evaporator to the entrance of a collector (vapor exit header) at point 2, and then reaches point 3 at the entrance to the vapor-transport line. A rate of heat input, q_{app}, is applied to the evaporator. A part of q_{app} superheats the vapor as it flows in the grooves

cut into the metallic body of the evaporator, from point 1 to point 2, and this process is also accompanied by a pressure drop. In the collector of the evaporator, there is some heat loss from the vapor to the ambient environment and a small pressure drop: here, the vapor at point 3 is assumed to be saturated ($x = 1$). However, it should be noted that vapor leaving the evaporator and entering the vapor-transport line could be superheated, as discussed by Maydanik (2005).

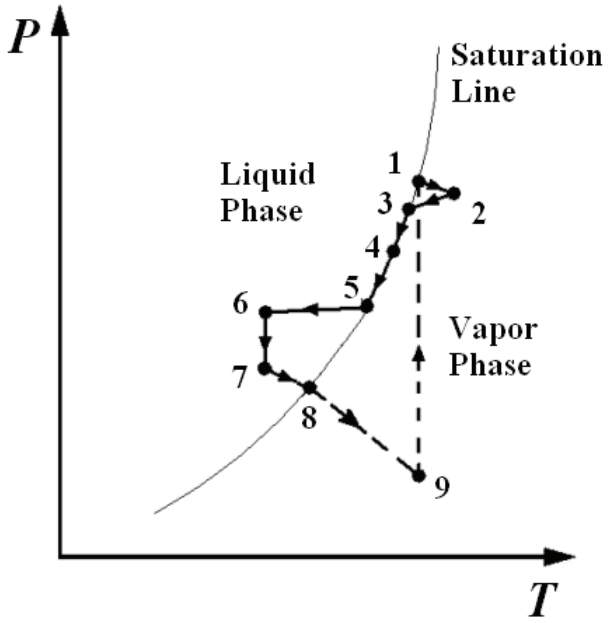

Figure 2.2: Pressure-temperature (*P*-*T*) diagram for the LHP (not to scale).

The process 3-4 corresponds to the flow of the working fluid through the vapor-transport line: it is assumed here that this process is accompanied by a very small rate of heat loss, just enough to keep the vapor essentially saturated, with an exit quality between $x = 0.98 - 1.0$. Again, in some LHPs, the vapor exiting this transport line could be superheated [Maydanik (2005)].

The saturated vapor that enters the condenser unit cools to a saturated liquid (quality $x = 0$) in the process 4-5, and experiences a pressure drop (needed to drive the momentum changes and overcome the shear stresses at the wall) and a corresponding temperature drop. If the condenser is sufficiently long (which is the case for the conditions depicted in Figure 2.1), then in the process 5-6, the liquid is subcooled and there is a slight pressure

drop. The fluid flow in the liquid-transport line is assumed to be essentially adiabatic, with a small pressure drop and negligible viscous dissipation. Thus, the process 6-7 in Figure 2.12 is an essentially isothermal process. In practice, there could be some heat exchange between the liquid-transport line and the external environment, which is accounted for in the proposed thermofluid model.

The subcooled liquid (at T_7) enters the compensation chamber, and then mixes with the warmer two-phase (saturated liquid-vapor) mixture in this chamber. The two-phase mixture inside the compensation chamber could either gain or lose heat to the outside (ambient) environment, depending on whether its temperature is lower or higher, respectively, than the ambient temperature. Furthermore, a part of the rate of heat input to the evaporator goes into heating up the fluid in the compensation chamber by means of conduction through the wick material: this heat transfer is referred to as heat leak [Kaya and Hoang (1999)]. The saturation temperature (and the corresponding saturation pressure) of the two-phase mixture inside the compensation chamber ($T_8 = T_{sat,\,cc}$) is determined by an energy balance on this element of the LHP. In Figure 2.2, the related path 7-8 is shown as a heating process accompanied by a pressure drop.

The saturated liquid from the compensation chamber enters the wick (it is assumed here that $T_{wick,\,ent} = T_8 = T_{sat,\,cc}$) and then moves up through it to the liquid-vapor interface. During this passage through the wick, the temperature of the liquid rises and its pressure drops. At the liquid-vapor interface, the temperature of the liquid (T_9) equals that of saturated vapor (T_1), but P_1 is greater than P_9 because of the capillary jump across the liquid-vapor interface in the wick. Therefore, the liquid at point 9 is in a superheated (metastable) state. The processes 8-9 and 9-1 are thus plotted as dashed lines in the vapor region of the *P-T* diagram in Figure 2.2. Due to heat input at the interface, the superheated liquid at the liquid-vapor interface evaporates along a constant-temperature process (9-1). Point 9 has the lowest absolute pressure in the loop. The pressure difference ($P_1 - P_9$) is sustained by the capillary jump across the liquid-vapor interface, and the assumption of local thermodynamic equilibrium at this interface gives $T_9 = T_1$.

In practice, the difference between the saturation temperatures in the evaporator and the condenser ($T_1 - T_5$) and the overall pressure drop in the entire loop ($P_1 - P_9$) would typically be relatively small compared to the absolute values of the saturation temperature

and pressure in the evaporator, T_1 and P_1, respectively: these values are depicted in Figure 2.2 in an exaggerated manner (not to scale) to aid the presentation.

2.2 SEGMENTED NETWORK THERMOFLUID MODEL

As was noted earlier, this model is intended for cost-effective simulations of the steady-state operation of LHPs akin to those shown schematically in Figure 2.1. Variations of the thermophysical properties of the working fluid with temperature, and multiphase phenomena, such as the change in quality, pressure drops and heat transfer in the two-phase regions, are taken into account. The model can handle any suitable working fluid for which the required thermophysical properties can be provided as inputs. In the energy balances on the various elements of the LHP, the rates of viscous dissipation and changes in the kinetic energy of the fluid are assumed to be negligible (as the related values of Eckert number are all much less than one). The details of this model are concisely presented in the remainder of this section.

2.2.1 Evaporator Section

In conventional LHPs, the evaporator unit is typically constructed of an internally grooved cylindrical-pipe of circular cross section, with an annular wick installed on its inner surface, akin to that illustrated schematically in Figure 2.3. The wick is usually made of a sintered powder metal. However, cylindrical evaporators generally require a special saddle (a kind of cylindrical-planar reducer) to properly attach them to a flat surface. This saddle design creates an additional thermal resistance and increases the total mass of the LHP.

LHPs with a flat-evaporator design are less susceptible to the above-mentioned difficulties or inconveniences, and can be easily integrated into compact spaces. A typical flat-evaporator design, schematically illustrated in Figure 2.4, consists of the following parts: An upper piece with vapor-transport grooves (or vapor-removal channels) of rectangular cross section cut into its metallic body, adjacent to its interface with the wick; a lower piece with a cavity of rectangular cross section that serves as the liquid pool in the evaporator; and a sintered powder-metal rectangular wick sandwiched between the upper and lower pieces, as shown in Figure 2.4.

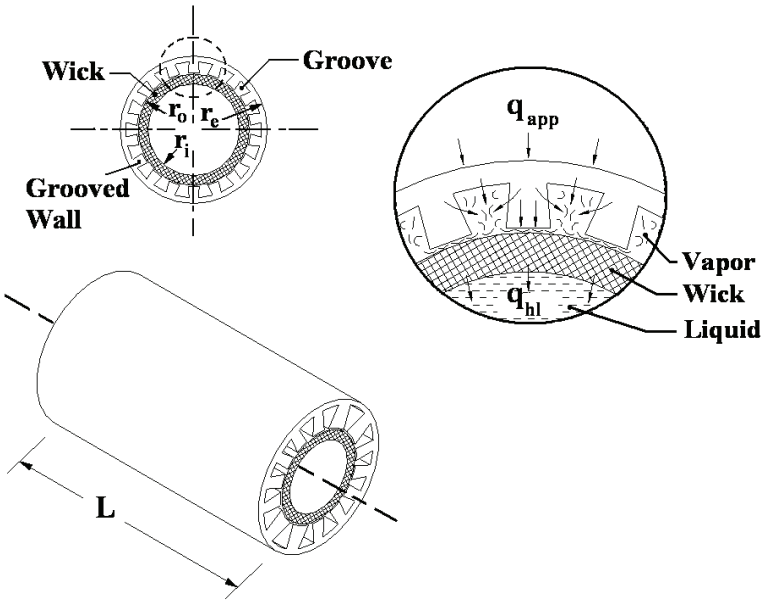

Figure 2.3: Details of a cylindrical-evaporator section of a conventional LHP design.

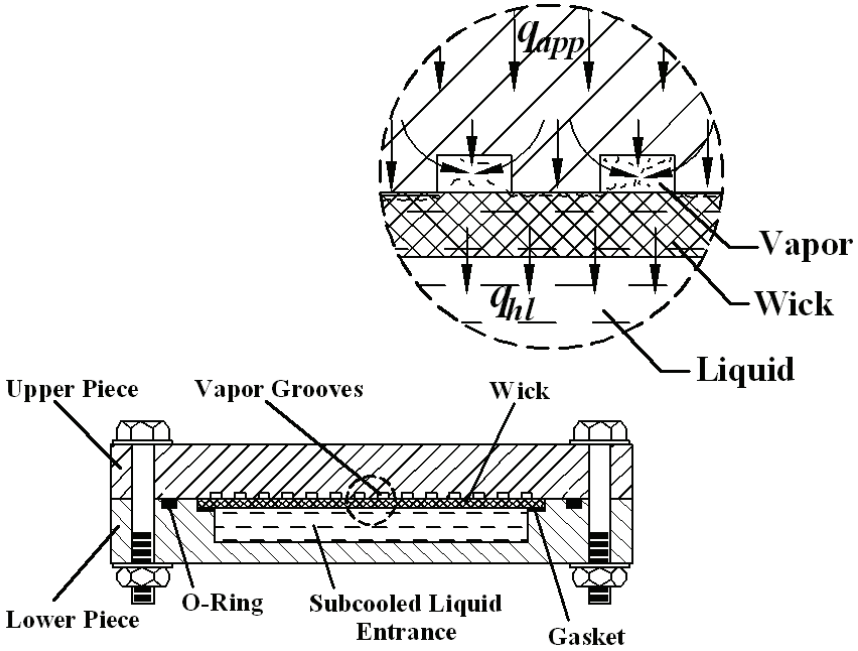

Figure 2.4: Details of a flat-evaporator section of an LHP.

Under steady-state conditions, the rate of heat transfer applied to LHP evaporator (cylindrical or flat), q_{app}, can be expressed as follows:

$$q_{app} = q_{vsh} + q_{fg} + q_{hl} \tag{2.1}$$

In the above equation, q_{vsh} is the rate of heat transfer to the saturated vapor during its passage through the grooved channels (causing the vapor to superheat), q_{fg} is the rate of heat transfer that is associated with the evaporation process at the liquid-vapor interface, and q_{hl} is the rate of heat leak through the wick. The rate of heat loss from the exit header to the ambient is denoted as q_{exhd}. In the proposed model and in many practical applications of LHPs, the following conditions apply: $[\{(q_{vsh} - q_{exhd})/(\dot{m}_{tot} c_{p,v})\}/T_{sat}] << 1$; $(q_{vsh}/q_{app}) << 1$; and the sum of pressure drops in the grooves and the exit header is very small compared to the absolute value of P_1. Under these conditions, for all practical purposes, $T_3 = T_1 = T_{sat}$.

2.2.2 Liquid-Vapor Interface Inside the Porous Wick

The location of the liquid-vapor interface is assumed to be near the outer surface of the cylindrical and rectangular wicks shown in Figures 2.3 and 2.4, respectively. A momentum balance in a direction normal to this interface in a representative pore inside the wick, paired with the assumption that the corresponding net normal viscous stress is negligible, yields the following equation:

$$\left(P_1 - P_9\right) = \frac{2\sigma\cos\theta_{eff}}{r_p} - \left(\frac{\dot{m}_{tot}}{\varepsilon A_{surf,\,wick}}\right)^2 \left(\frac{1}{\rho_v} - \frac{1}{\rho_l}\right) \tag{2.2}$$

Here, σ is the surface tension at the vapor-liquid interface, r_p is the effective pore radius, ε is the porosity of the wick material, $A_{surf,\,wick}$ is the outer surface area of the wick structure normal to the flow, θ_{eff} is the effective contact angle of the liquid-vapor interface inside the representative pore, and $\dot{m}_{tot}$ is the total mass flow rate in the LHP. During steady-state operation of the LHP, θ_{eff} self-regulates to meet the requirement stipulated by Eq. (2). For successful operation of the LHP, (P_1 – P_9) should not exceed the maximum capillary pressure associated with the chosen porous wick material and working fluid combination: This is the well-known capillary limit [Chi (1976); Silverstein (1992)].

2.2.3 Pressure Drop and Heat Leak Across the Porous Wick

The liquid flow through the wick is modeled using the Darcy law for a homogenous porous medium [Kaviany (1999); Nield and Bejan (2006)]. The rate of heat transfer inside the liquid-saturated wick is, however, assumed to be conduction-dominated, as the related values of the effective Peclet number are very small [Kaya and Hoang (1999); Maydanik (2005)]. Invoking these assumptions, the pressure *drop* in the liquid, $\Delta P_{l,wick}$, and the rate of heat leak, q_{hl}, across the cylindrical and rectangular wick geometries (as illustrated in Figures 2.3 and 2.4) are given by the following expressions:

Cylindrical wick geometry:

$$\Delta P_{l,wick} = \frac{\dot{m}_{tot}\mu_l}{2\pi L\rho_l K_{wick}} \ln\left(\frac{r_o}{r_i}\right);\ q_{hl} = 2\pi L k_{eff} \frac{\left(T_{sat} - T_{wick,\,ent}\right)}{\ln\left(r_o / r_i\right)} \tag{2.3}$$

Rectangular wick geometry:

$$\Delta P_{l,wick} = \frac{l_{wick}}{A_{surf,\,wick}} \frac{\dot{m}_{tot}}{K_{wick}} \frac{\mu_l}{\rho_l};\ q_{hl} = \frac{k_{eff} A_{surf,\,wick}}{l_{wick}} \left(T_{sat} - T_{wick,\,ent}\right) \tag{2.4}$$

In these equations, K_{wick} refers to the permeability of the wick; l_{wick} denotes the thickness of the rectangular wick; L is the length of the cylindrical wick structure; and r_i and r_o denote the inner and outer radii of the cylindrical wick, respectively.

The effective thermal conductivity, k_{eff}, of the liquid-saturated sintered powder-metal wick was calculated using the following model proposed by Atabaki and Baliga (2007):

$$\begin{aligned}\frac{k_{eff}}{k_l} = &\left(1-\alpha_{con}\right)\left[\frac{\varepsilon f_0 + \left(k_s/k_l\right)\left(1-\varepsilon f_0\right)}{1-\varepsilon\left(1-f_0\right)+\left(k_s/k_l\right)\varepsilon\left(1-f_0\right)}\right] \\ &+ \alpha_{con}\left[\frac{2\left(k_s/k_l\right)^2\left(1-\varepsilon\right)+\left(1+2\varepsilon\right)\left(k_s/k_l\right)}{\left(2+\varepsilon\right)\left(k_s/k_l\right)+1-\varepsilon}\right]\end{aligned} \tag{2.5}$$

$$\begin{aligned}&f_{o,\min} = \frac{2}{3}\ ;\ f_{o,\max} = \frac{2(k_s/k_l)}{2(k_s/k_l)+1} \\ &f_o = f_{o,\min}\varepsilon + f_{o,\max}(1-\varepsilon)\end{aligned} \tag{2.6}$$

$$\alpha_{con} = 1 - \exp\left\{ -\Lambda \left(\frac{1-\varepsilon}{\varepsilon} \right)^{m} \Big/ \left[1 - \left(\frac{k_s}{k_l} \right)^{-n} \right] \right\} \qquad (2.7)$$

$$\Lambda = 0.148 \quad ; \quad m = 0.283 \quad ; \quad n = 0.04$$

In these equations, k_{eff} is the effective thermal conductivity of the liquid-saturated wick; k_l and k_s denote the average values of the thermal conductivities of the liquid and the solid (material of the porous medium) in the wick, respectively; and ε represents the porosity of the wick material. Additional details of this and other effective thermal conductivity models are presented and discussed in Chapter 5 of this thesis.

2.2.4 Vapor-Removal Channels in the Evaporator

Here, it is assumed that the evaporator has N grooves of essentially rectangular cross-section. The vapor generated from the evaporation process at the liquid-vapor interface (located near the outer surface of the wick) is injected at a uniform velocity, v_{inj}, into the vapor grooves from the bottom lateral surface. The vapor then flows along the length of the vapor groove, as illustrated schematically in Figure 2.5.

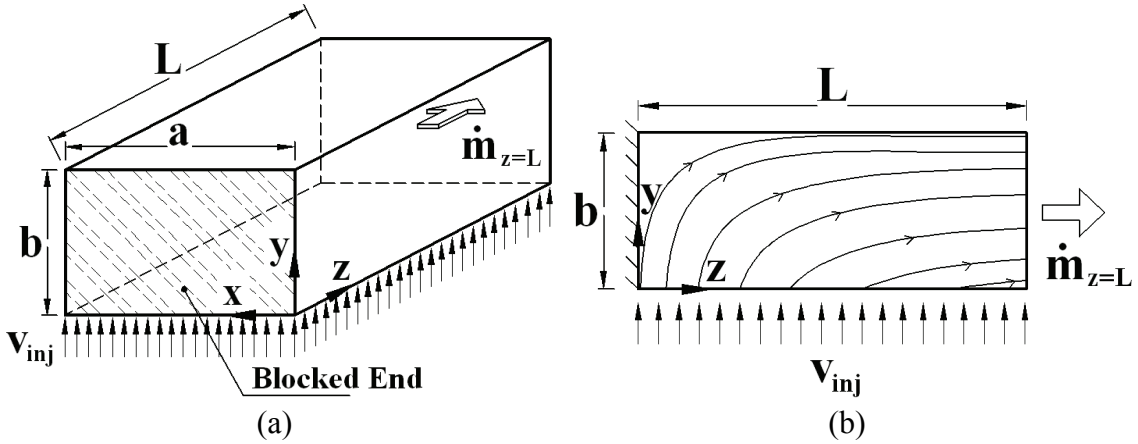

Figure 2.5: (a) schematic representation of vapor flow in straight rectangular grooves cut in the evaporator body of an LHP; (b) cross-sectional (y-z plane) view of this flow.

The flow of vapor in each of the grooves (or channels) could be either laminar or turbulent, depending on the local running Reynolds number along the length of the

channel. The total static pressure *drop* in these vapor grooves, ΔP_{vg}, is computed in available quasi-one-dimensional models of LHPs using correlations for a Darcy friction factor that strictly applies only in the fully-developed region of flows in straight ducts of circular and non-circular cross-sections with impermeable walls [Kaya and Hoang (1999); Ghajar and Darabi (2005); Maydanik (2005); Atabaki et al. (2007); Launay et al. (2007); Jesuthasan et al. (2008); Jesuthasan and Baliga (2009a); Singh et al. (2009)], as follows:

$$\Delta P_{vg} = \frac{\left(f \operatorname{Re}_{L_{vg}}\right)}{2}\left(\frac{\dot{m}_{tot}}{N}\right)\frac{L_{vg}}{A_{c-s,\,\mathrm{vg}} D_{h,\,\mathrm{vg}}^2}\frac{\mu_v}{\rho_v} \tag{2.8}$$

The hydraulic diameter of the groove, $D_{h,\,\mathrm{vg}}$, the Darcy friction factor, f, and the Reynolds number, $\operatorname{Re}_{L_{vg}}$, at the end of the channel (L_{vg}) are defined as follows:

$$D_{h.\,\mathrm{vg}} = \frac{4A_{c-s,\,\mathrm{vg}}}{Peri_{vg}} \;;\quad f = \frac{\left(\Delta P_{vg} / L_{vg}\right) D_{h,\,\mathrm{vg}}}{0.5\rho_v w_{av}^2};\; \operatorname{Re}_{L_{vg}} = \frac{\dot{m}_{tot} D_{h,\,\mathrm{vg}}}{N A_{c-s,\,\mathrm{vg}} \mu_v} \tag{2.9}$$

In this analysis, it is assumed that the product $f \operatorname{Re}_{L_{vg}}$ is a constant and corresponds to its fully developed value. For $\operatorname{Re}_{L_{vg}} \le 2300$, the flow is considered laminar, and for fully-developed flow $f \operatorname{Re}_{L_{vg}}$ is set equal to 64.0. For $\operatorname{Re}_{L_{vg}}$>2300, the flow is considered turbulent, and the Colebrook and White correlation [Colebrook (1939); White (1991)] is used to estimate the friction factor (using an iterative procedure). Thus,

$$f = 64 / \operatorname{Re}_{L_{vg}} \text{ when } \operatorname{Re}_{L_{vg}} \le 2300$$

$$\frac{1}{\sqrt{f}} = -2.0 \log_{10}\left[\frac{e / D_{h,\,\mathrm{vg}}}{3.7} + \frac{2.51}{\operatorname{Re}_{L_{vg}}\sqrt{f}}\right] \text{ when } \operatorname{Re}_{L_{vg}} > 2300 \tag{2.10}$$

This approach is inapplicable or ad hoc, at best, with respect to the vapor flows illustrated in Figure 2.5. The resulting errors can become serious if the pressure drop in the vapor grooves is a significant contributor to the overall pressure drop in the LHP. Consequently, to enhance the capabilities of current quasi one-dimensional models of LHPs, more accurate correlations for the calculation of the above-mentioned vapor-channel pressure drop are needed. It is within this context that a computational method is formulated in Chapter 3 and applied in Chapter 4 to develop accurate and cost-effective

correlations for the prediction of the pressure drop in the vapor-removal channels of LHPs. The development and incorporation of these novel correlations, and their incorporation into the proposed segmented network thermofluid model of LHPs, are important contributions of this thesis. The capabilities of the resulting enhanced model are demonstrated in Chapter 6.

In this work, the effects of the compressibility of the vapor in the grooves and also the rest of the LHP are assumed to be negligible (as the values of the associated Mach number are all much less than 0.1). If necessary, the effects of vapor compressibility could be accounted for by using recommendations available in Chi (1976).

The specific enthalpy, *i*, of the vapor is assumed to be only a function of temperature ($di = c_{p,v} dT$). Thus, the vapor temperature (T_3) at the exit of the evaporator, just before it enters the vapor-transport line, can be expressed as follows:

$$T_3 = T_{sat} + (q_{vsh} - q_{exhd}) / (c_{p,v} \dot{m}_{tot}) \tag{2.11}$$

As was mentioned earlier, it is assumed that $[\{(q_{vsh} - q_{exhd})/(\dot{m}_{tot} c_{p,v})\} / T_{sat}] << 1$ and the sum of pressure drops in the grooves and the exit header is very small compared to the absolute value of P_1, although not necessarily negligible with respect to the overall pressure drop in the LHP. Therefore, for all practical purposes, $T_3 \simeq T_1 = T_{sat}$.

2.2.5 Vapor-Transport Line

The vapor-transport line connects the exit of the evaporator section of the LHP to the entrance of the condenser unit, as shown schematically in Figure 2.1. A segmented quasi-one-dimensional model is used to simulate the thermofluid phenomena in the vapor-transport line. The vapor-transport line is first discretized (segmented) into control volumes or cells of *equal length* ($\Delta z = L_{vapor-transport\ line} / M_{vl} = \text{const.}$). The number of cells ($M_{vl}$) that is suitable is determined heuristically: M_{vl} is increased until the differences in the results obtained are negligibly small. A schematic illustration of this segmentation is given in Figure 2.6 with reference to a general fluid-transport line.

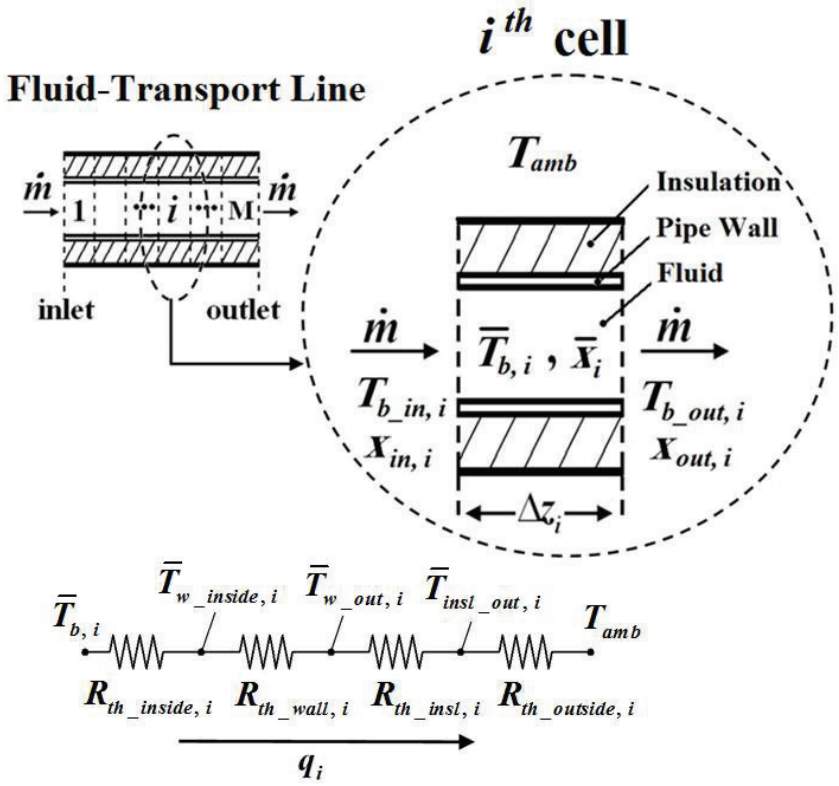

Figure 2.6: Segmentation of a general fluid-transport line into cells.

The principles of conservation of mass, momentum, and energy are applied over each of the aforementioned control volumes or cells. Quasi-one-dimensional formulations and semi-empirical correlations are used to calculate the corresponding single- and two-phase heat transfer and pressure drops over each cell. In each cell, the fluid properties, and also the heat transfer and pressure drop calculations, are based on the arithmetic mean values of the inlet and outlet temperatures and quality ($\overline{T}_{b,i}$ and $\overline{x}_i$). These particular features of the segmented network model allow it to accurately account for the influences of the variation of fluid properties and of the quality (in two-phase regions). Depending on the values of the loop operating temperature (T_{sat}) and the ambient environment temperature (T_{amb}), the vapor flowing through the vapor-transport line could either undergo a heat loss or a heat gain. The related pressure drops and heat transfer calculations for these two cases are presented next.

2.2.5.1 Case 1: $T_{sat} > T_{amb}$

In this case, the vapor loses heat to the ambient and partially condenses in the vapor-transport line. This two-phase flow also involves a pressure drop.

Segmented Pressure Drop Calculations in the Two-Phase Region

In this work, following the recommendations of Rouhani and Sohal (1983) and Dobson and Chato (1998), the two-phase flow regimes were determined using a map proposed by Taitel and Dukler (1976) for horizontal and slightly inclined gas-liquid flows. This map requires the values of the following parameters:

$$\dot{m}_l = (1-\mathrm{x})\dot{m}_{tot}\,;\dot{m}_v = \mathrm{x}\dot{m}_{tot}\,;G_l = \dot{m}_l/(\pi D^2/4)$$

$$G_v = \dot{m}_v/(\pi D^2/4)\,;Re_l^s = G_l D/\mu_l\,;Re_v^s = G_v D/\mu_v$$

$$X^2 = \frac{C_l (Re_v^s)^m \rho_v (\dot{m}_l)^2}{C_v (Re_l^s)^n \rho_l (\dot{m}_v)^2} = \frac{|\left(dP/dz\right)_l^s|}{|\left(dP/dz\right)_v^s|}$$

$$F_{TD} = \left(\frac{\rho_v \left(G_v/\rho_v\right)^2}{g\left(\rho_l-\rho_v\right)D\cos\beta}\right)^{\frac{1}{2}} \tag{2.12}$$

$$K_{TD} = \left(\frac{\rho_l \rho_v (G_l/\rho_l)\left(G_v/\rho_v\right)^2}{\mu_l g\left(\rho_l-\rho_v\right)\cos\beta}\right)^{\frac{1}{2}}$$

$$T_{TD} = \left(\frac{\left|(dP/dz)_l^s\right|}{\left(\rho_l-\rho_v\right)g\cos\beta}\right)^{1/2}$$

In this equation, C_l, C_v, m, and n are constants; ρ is the mass density; μ is the dynamic viscosity; D is the internal diameter of the fluid transport line (vapor-transport line here); dP/dz is the axial gradient of the static pressure; G_l and G_v denote the superficial liquid and vapor mass fluxes; Re_l^s and Re_v^s are the superficial liquid and vapor Reynolds numbers; X is a parameter introduced by Lockhart and Martinelli (1949); β is the angle between the axis of the fluid transport line and the horizontal (in the demonstration problem considered in this work, $\beta = 0$); F_{TD} is a modified Froude number (ratio of inertia to gravity forces); $K_{TD} = F_{TD}\sqrt{Re_l^s}$; and T_{TD} is the ratio of turbulent to gravity forces acting on the gas phase. The values of the constants C_l, C_v, m, and n depend on the

four possible particular combinations of laminar and turbulent flows of the liquid and vapor phases. The recommendations of Taitel and Dukler (1976) are given in the Tables 2.1 and 2.2.

Table 2.1: Laminar and turbulent combinations of the liquid and vapor phases [Taitel and Dukler (1976)].

Liquid-Phase	Vapor-Phase	Symbol	Re_l^s	Re_v^s
Turbulent	Turbulent	$t-t$	> 2000	> 2000
Laminar	Turbulent	$l-t$	< 1000	> 2000
Turbulent	Laminar	$t-l$	> 2000	< 1000
Laminar	Laminar	$l-l$	< 1000	< 1000

Table 2.2: Constants in the Lockhart-Martinelli parameter [Taitel and Dukler (1976)].

Constants	$t-t$	$l-t$	$t-l$	$l-l$
n	0.2	1	0.2	1
m	0.2	0.2	1	1
C_l	0.046	16	0.046	16
C_v	0.046	0.046	16	16

In the two-phase flows encountered in LHPs, the liquid flow is typically laminar, but the vapor flow could become turbulent in some cases. Thus, conservatively, the laminar-liquid/turbulent-vapor combination can be assumed, as was done in this work, and then the following values of the constants in Eq. (2.12) apply: n = 1.0; m = 0.2; C_l = 16.0; and C_v = 0.046. The corresponding Taitel and Dukler (1976) map is shown schematically in Figure 2.7: The parameter F_{TD} is used to distinguish between the stratified and annular flow regimes, whereas K_{TD} is used to specify two subclasses of the stratified flow, namely, stratified-smooth and stratified-wavy; T_{TD} is used to separate the intermittent and dispersed bubble flow regimes; and the Lockhart and Martinelli (1949) parameter X_{lt} (conservatively assumed here to correspond to the laminar-liquid/turbulent-vapor

condition) is calculated using Eq. (2.12), and used to delineate between the annular and dispersed bubble regimes.

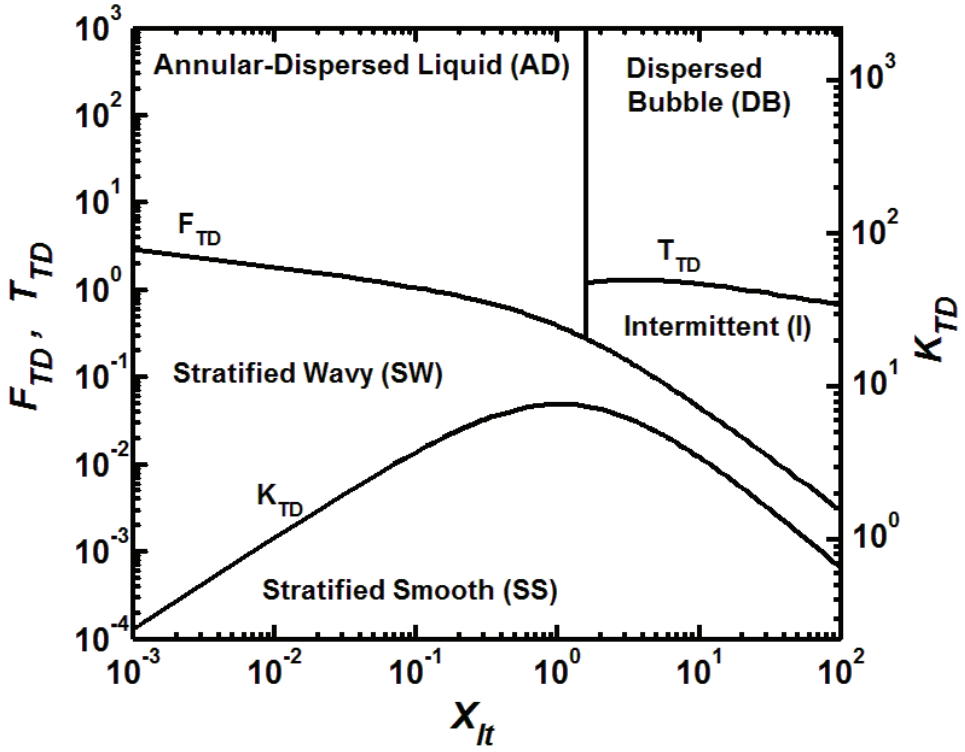

Figure 2.7: The Taitel and Dukler (1976) flow regime map for laminar-liquid/turbulent-vapor flow.

For a fixed mass flow rate, the pressure drop in the two-phase flow is needed to overcome the wall friction (shear) and gravity forces, and sustain the momentum changes during the condensation process [Griffith (1985); Ould Didi et al. (2002); Thome (2003); Quibén and Thome (2007a); Quibén and Thome (2007b)]. Furthermore, if fittings and/or bends are used, additional pressure drops are needed to overcome the associated losses: these losses are assumed to be minor in comparison to the pressure drops in the straight portions of the fluid-transport line, and are thus neglected. The two-phase pressure *drop* in the i^{th} cell of the vapor-transport line, $\left(\Delta P_{vl}^{2\phi}\right)_i$, is then expressed as follows:

$$\left(\Delta P_{vl}^{2\phi}\right)_i = \left(\Delta P_f^{2\phi}\right)_i + \left(\Delta P_{mom}\right)_i + \left(\Delta P_{grav}\right)_i \tag{2.13}$$

In the above expression, the terms $\Delta P_f^{2\phi}$, ΔP_{mom}, and ΔP_{grav} denote pressure *drops* caused by the wall friction force, momentum changes during the condensation process, and

gravity force, respectively: These pressure drops are referred to in this thesis as the friction pressure drop, momentum pressure drop, and gravity pressure drop, respectively.

Baker (1954) has proposed different correlations for the calculation of two-phase pressure drops in each of the aforementioned flow regimes. However, Dukler et al. (1964) recommended the Lockhart and Martinelli (1949) pressure-drop correlations over that proposed by Baker (1954), based on an extensive assessment against experimental data. Thus, for each segment in the straight portions of the vapor-transport line, the two-phase friction pressure drop was computed using the approach proposed by Lockhart and Martinelli (1949). The parameter X given in Eq. (2.12), is first calculated, using the laminar-turbulent combinations of the liquid-gas flows and the corresponding constants given in Tables 2.1 and 2.2. Then, a two-phase multiplier, φ_l^2, (based on the liquid phase) is calculated using the following equation [Chisholm (1967)]:

$$\varphi_l^2 = 1 + \frac{C}{X} + \frac{1}{X^2} \tag{2.14}$$

The value of the coefficient C in this equation also depends on the laminar-turbulent combinations of the liquid-gas flows [Collier (1972)], and is given in Table 2.3.

Table 2.3 Values of the coefficient, *C*, in the two-phase multiplier.

Liquid-phase	Gas-phase	Symbol	C
Turbulent	Turbulent	$t-t$	20
Laminar	Turbulent	$l-t$	12
Turbulent	Laminar	$t-l$	10
Laminar	Laminar	$l-l$	5

Once φ_l^2 is obtained, the two-phase friction pressure drop for each segment in straight portions of the vapor-transport line is calculated using the following equation:

$$\left(\Delta P_f^{2\phi}\right)_i = \varphi_l^2 \left(\Delta P_{f,l}\right)_i \tag{2.15}$$

In this equation, $\Delta P_{f,l}$ is the single-phase friction pressure drop with the liquid-phase flowing alone in the pipe at *its* mass velocity. For laminar fully-developed flow of the

liquid, the following equation yields the single-phase frictional pressure drop over the i^{th} cell:

$$\left(\Delta P_{f,l}\right)_i = \left[-\left(\frac{dP}{dz}\right)_{f,l}\right]_i \Delta z = \left[\left(\frac{32}{Re_l^s}\right)\left(\frac{G_l^2/\rho_l}{D}\right)\right]_i \Delta z \tag{2.16}$$

As was stated earlier, in this work, a conservative approach is taken, and the laminar-liquid/turbulent-vapor combination is assumed to prevail.

The pressure drop needed to sustain the momentum changes due to condensation in the segment of interest, $\left(\Delta P_{mom}\right)_i$, is obtained as follows:

$$\left(\Delta P_{mom}\right)_i = G^2 \left\{\left[\frac{(1-x)^2}{\rho_l(1-\alpha)} + \frac{x^2}{\rho_g \alpha}\right]_{out,\,i} - \left[\frac{(1-x)^2}{\rho_l(1-\alpha)} + \frac{x^2}{\rho_g \alpha}\right]_{in,\,i}\right\} \tag{2.17}$$

Here, α denotes the void fraction. It is calculated using a correlation proposed by Zivi (1964):

$$\frac{1}{\alpha} = 1 + \frac{1-\mathrm{x}}{\mathrm{x}}\left(\frac{\rho_v}{\rho_l}\right)^{2/3} \tag{2.18}$$

Next, the gravitational pressure drop in the i^{th} cell is calculated using the following equation:

$$\left(\Delta P_{grav}\right)_i = \left[\alpha\rho_g + (1-\alpha)\rho_l\right]_i \left[g\left(\sin\beta\right)\right]_i \Delta z \tag{2.19}$$

In this equation, β denotes the angle between the axis of the transport-line segment *i* and the horizontal, and g is the gravitational acceleration. In this work, only horizontal or slightly inclined (< 5°) transport lines are considered.

The total pressure drop, $\left(\Delta P_{vl}\right)_{tot}$, in the vapor-transport line is then computed as follows:

$$\left(\Delta P_{vl}\right)_{tot} = \sum_{i=1}^{M_{vl}} \left(\Delta P_{vl}^{2\phi}\right)_i = \sum_{i=1}^{M_{vl}} \left[\Delta P_f^{2\phi} + \Delta P_{mom} + \Delta P_{grav}\right]_i \tag{2.20}$$

Segmented Heat Transfer Calculations in the Two-Phase Region

Following the thermodynamic description of the LHP provided earlier in this chapter, the vapor at the entrance of the vapor-transport line is assumed to be saturated and thus

has a quality of one. It is assumed here that the vapor only partially (not completely) condenses in the vapor-transport line. Therefore, based on the *equal length* segmentation ($\Delta z = L_{vapor-transport\ line} / M_{vl} = \text{const.}$) of the vapor-transport, the rate of heat *loss* from the i^{th} cell (refer to Figure 2.6) is calculated as follows:

$$q_{vl-loss,\,i} = \left(UA'_{vl}\right)_i \Delta z \left(\overline{T}_{sat-vl,\,i} - T_{amb}\right) = \dot{m}_{tot}\, \Delta x_{vl,i} i_{fg}\big|_{\overline{T}_{sat-vl,\,i}} \tag{2.21}$$

In this expression, $(UA'_{vl})_i$ is the i^{th} cell overall thermal conductance *per unit length* based on the inside area of the vapor-transport line; $\overline{T}_{sat-vl,\,i}$ is the average saturation temperature for segment i (Note: In the two-phase fluid region, the fluid bulk temperature corresponds to the saturation temperature); $i_{fg}\big|_{\overline{T}_{sat-vl,\,i}}$ is the latent heat of vaporization based on the average saturation temperature for segment i; and $\Delta x_{vl,i} = \left(x_{vl,\,in} - x_{vl,\,out}\right)_i$ is the change in the quality over the segment i.

The i^{th} cell overall thermal conductance *per unit length*, $(UA'_{vl})_i$, takes the following factors into account: The convective *two-phase* heat transfer inside the vapor-transport line, the radial heat conduction in the pipe wall and the insulation (if present), and the external heat transfer (free convection, forced convection, radiation, or a combination of all three). This overall cell thermal conductance (refer to Figure 2.6) can be expressed as follows:

$$(UA'_{vl})_i = 1/(R'_{th\_inside,\,i} + R'_{th\_wall-outside,\,i}) = 1/(R'_{th\_inside,\,i} + R'_{th\_wall,\,i} + R'_{th\_insl,\,i} + R'_{th\_outside,\,i}) \tag{2.22}$$

In this equation, $R'_{th\_inside,\,i}$ and $R'_{th\_wall-outside,\,i}$ are, respectively, the *per unit length* thermal resistance for the internal two-phase convection in the vapor-transport line segment *i*; and the external thermal resistance (sum of the thermal resistances associated with the pipe wall, insulating material, and the external heat transfer). Here, it is assumed that the rate of axial heat conduction through the pipe wall and the insulation are negligible compared to the heat transfer in the radial direction. It is also assumed that the convective heat transfer inside the pipe is fully developed. In this context, the two thermal resistances in Eq. (2.22) are defined as follows:

$$R'_{th\_inside,\,i} = \frac{1}{\pi D_{vl} h_i^{2\phi}} \text{ and } R'_{th\_wall-outside,\,i} = \frac{1}{\left(UA'_{vl,\,wall\text{-}outside}\right)_i} \tag{2.23}$$

In the above expression, $h_i^{2\phi}$ is the internal two-phase heat transfer coefficient in the i^{th} cell of the vapor-transport line based on its inside surface area; $\left(UA'_{vl,\,wall\text{-}outside}\right)_i$ is the overall conductance *per unit length* between the inside surface area of the vapor-transport line segment *i* and the outside external environment; and D_{vl} is the internal diameter of the vapor-transport line. The internal heat transfer coefficient $h_i^{2\phi}$ for the condensing vapor inside segment i of the vapor-transport line depends on the two-phase flow regime and needs to be properly determined for accurate heat transfer calculations.

The method used for the two-phase heat transfer calculations in the proposed segmented network model is based on the average vapor and liquid properties as well as the average quality over each cell. These average cells attributes are based on estimates from the previous iteration of the overall solution procedure, or initial estimates of the dependent variables. In this work, the stratified- (wavy/smooth) and annular-flow regimes are considered for LHP applications, and the corresponding two-phase heat transfer coefficients on the inside surface of the vapor-transport line are calculated using the following correlations proposed by Dobson and Chato (1998):

$$\begin{aligned}
&Ga = g\rho_l\left(\rho_l - \rho_g\right)D^3 / \mu_l^2 \;;\; G = \dot{m}_{tot} / (\pi D^2 / 4) \\
&Re_l = \left(1-\mathrm{x}\right)GD / \mu_l \;;\; Re_{vo} = GD / \mu_v;\; Pr_l = \mu_l c_{p,l} / k_l \\
&Ja_l = c_{p,l}(\overline{T}_{sat-vl} - \overline{T}_{wall}) / i_{fg};\; Fr_l = G^2 / (\rho_l^2 g D) \\
&X_{tt} = \left(\frac{\rho_v}{\rho_l}\right)^{0.5}\left(\frac{\mu_l}{\mu_v}\right)^{0.1}\left(\frac{1-\mathrm{x}}{\mathrm{x}}\right)^{0.9} \;;\; \varphi_l = \sqrt{1.376 + \frac{c_1}{X_{tt}^{c_2}}}
\end{aligned} \tag{2.24}$$

$$\begin{aligned}
&Nu_{forced} = 0.0195 Re_l^{0.8} Pr_l^{0.4} \varphi_l;\; (1-\theta_l/\pi) \cong \frac{\arccos\left(2\alpha - 1\right)}{\pi} \\
&Nu_{\substack{stratified \\ wavy}} = \frac{h_{segment}^{2\phi} D}{k_l} = \frac{0.23 Re_{vo}^{0.12}}{1 + 1.11 X_{tt}^{0.58}}\left[\frac{GaPr_l}{Ja_l}\right]^{0.25} + (1 - \frac{\theta_l}{\pi}) Nu_{forced} \\
&Nu_{annular} = \frac{h_{segment}^{2\phi} D}{k_l} = 0.023 Re_l^{0.8} Pr_l^{0.4}\left[1 + \frac{2.22}{X_{tt}^{0.89}}\right]
\end{aligned} \tag{2.25}$$

These correlations involve the following dimensional and dimensionless parameters: Galileo number, *Ga*; total mass flux, G; superficial liquid Reynolds number, Re_l;

quality, x; vapor-only Reynolds number, Re_{vo}; Jacob number for the liquid, Ja_l; liquid Prandtl number, Pr_l; liquid Froude number, Fr_l; turbulent-turbulent Lockhart-Martinelli (1949) parameter, X_{tt}; and the angle subtended at the center of the tube cross-section by the portion of the inner wall that is above the liquid level, θ_l. The constants c_1 and c_2 in the above-mentioned equations are determined using the following expressions:

$$\begin{aligned}&\text{For } 0 < Fr_l \le 0.7\\ &c_1 = 4.172 + 5.48Fr_l - 1.56Fr_l^2 \;;\; c_2 = 1.773 - 0.169Fr_l\\ &\text{and for } Fr_l > 0.7\\ &c_1 = 7.242 \;;\; c_2 = 1.655\end{aligned} \tag{2.26}$$

It is important to note that the Dobson and Chato (1998) correlation for the stratified-wavy flow contains the average temperature of the inner surface of the transport-line wall, $\overline{T}_{wall}$, which is not known *a priori*. However, using the resistance analogy, the following relation can be used to relate $\overline{T}_{\text{wall}}$ to $\overline{T}_{sat-vl}$ and T_{amb}, which are known:

$$\frac{\left(\overline{T}_{sat-vl} - \overline{T}_{wall}\right)_i}{R'_{th\_inside,\,i}} = \frac{\left(\overline{T}_{sat-vl} - T_{amb}\right)_i}{R'_{th\_inside,\,i} + R'_{th\_wall-outside,\,i}} \tag{2.27}$$

In the heat transfer calculations, a Froude number, Fr_{so}, proposed by Soliman (1982) is used to distinguish the transition between the stratified-wavy and annular flow regimes:

$$\begin{aligned}Fr_{so} &= 0.025Re_l^{1.59}\left(\frac{1+1.09X_{tt}^{0.039}}{X_{tt}}\right)^{1.5}\frac{1}{Ga^{0.5}} \quad \text{for } Re_l \le 1250\\ Fr_{so} &= 1.260Re_l^{1.04}\left(\frac{1+1.09X_{tt}^{0.039}}{X_{tt}}\right)^{1.5}\frac{1}{Ga^{0.5}} \quad \text{for } Re_l > 1250\end{aligned} \tag{2.28}$$

While Soliman (1982) sets the transition from stratified-wavy to annular flow at $Fr_{so} = 7$, Dobson and Chato (1998) obtained better correlation of their experimental data by setting $Fr_{so} = 20$. Thus, in this work, the transition value is set at $Fr_{so} = 20$, and the two-phase heat transfer coefficient is selected as follows:

$$\begin{aligned}&G > 500 \text{ [kg/m}^2\text{s]} && : Nu_{annular}\\ &G < 500 \text{ [kg/m}^2\text{s] and } Fr_{so} > 20 && : Nu_{annular}\\ &G < 500 \text{ [kg/m}^2\text{s] and } Fr_{so} < 20 && : Nu_{\substack{stratified\\wavy}}\end{aligned} \tag{2.29}$$

The correlations proposed by Dobson and Chato (1998) for the stratified-wavy and annular flow regimes matched their experimental data very well with a mean deviation of 6.6% and 11.8%, respectively. Therefore, these correlations are used in this work to compute the appropriate value of the internal two-phase heat transfer coefficient, $h_i^{2\phi}$, inside each segment *i* of the vapor-transport line (and also the two-phase portion of the condenser pipe as will be discussed later in this section). This exercise is required to compute the overall thermal conductance *per unit length* and the associated rate of heat loss for each segment of the discretized vapor-transport line as per Eq. (2.21).

The total rate of heat loss from the vapor-transport line is determined by adding together the rates of heat loss from all of the segments:

$$q_{vl-loss,\,tot} = \sum_{i=1}^{M_{vl}} q_{vl-loss,\,i} = \sum_{i=1}^{M_{vl}} \left(UA'_{vl}\right)_i \Delta z \left(\overline{T}_{sat-vl,\,i} - T_{amb}\right) = \dot{m}_{tot} \sum_{i=1}^{M_{vl}} \Delta x_{vl,\,i} i_{fg}\Big|_{T_{sat-vl,\,i}} \qquad (2.30)$$

Finally, the saturation temperature at the exit of segment *i,* $\left(T_{sat-vl,\,out}\right)_i$, (which corresponds to the temperature at the inlet of segment *i*+1) is obtained from the saturation temperature at the inlet of segment *i,* $\left(T_{sat-vl,\,in}\right)_i$, using the slope of the liquid-vapor saturation curve (P-T diagram) of the working fluid and the associated pressure drop $\left(\Delta P_{vl}^{2\phi}\right)_i$ in segment *i* computed from Eq. (2.20):

$$\left(T_{sat-vl,\,out}\right)_i = \left(T_{sat-vl,\,in}\right)_i - \left(\Delta P_{vl}^{2\phi}\right)_i \Big/ \left(\frac{dP_{sat}}{dT_{sat}}\right)_{\overline{T}_{sat-vl,\,i}} \qquad (2.31)$$

At the entrance of the first segment in the vapor-transport line, $i = 1$, the saturation temperature is T_{sat}, which corresponds to the saturation temperature at the exit of the evaporator. The average temperature in segment *i*, $\overline{T}_{sat-vl,\,i}$, is initially assumed to be its inlet temperature, $\left(T_{sat-vl,\,in}\right)_i$. All vapor and liquid properties, as well as the average quality, are then based on this temperature. Once the temperature at the exit of segment *i,* $\left(T_{sat-vl,\,out}\right)_i$, is calculated from Eq. (2.31), the average temperature in segment *i* is re-computed based on the arithmetic mean of the inlet and exit temperatures: $\overline{T}_{sat-vl,\,i} = \left[\left(T_{sat-vl,\,in}\right)_i + \left(T_{sat-vl,\,out}\right)_i\right] / 2$. Following that, another iteration of the aforementioned pressure drop and heat transfer calculations is conducted for segment *i*

using the newly calculated value of $\overline{T}_{sat-vl,\,i}$. This process is repeated for segment *i* until subsequent changes in $\overline{T}_{sat-vl,\,i}$ are within a user-specified tolerance (all absolute relative changes < 10^{-4} was used in this work). A similar iterative procedure is then conducted on the next *i*+1 segment for the corresponding pressure drops and heat transfer calculations in the vapor-transport line (and so, until $i = M_{vl}$ is reached).

2.2.5.2 Case 2: $T_{sat} < T_{amb}$

In this case, heat is transferred from the ambient environment to the vapor (heat gain), there is no condensation (vapor is superheated, and single-phase flow prevails), and the static pressure drops as the vapor flows through the vapor-transport line.

Segmented Pressure Drop Calculations in the Single-Phase Region

As mentioned earlier, the vapor-transport line is segmented into control-volumes or cells of equal *lengths*, Δz_i. The single-phase, static-pressure drop is calculated in each segment *i* of the vapor-transport line as follows (for the flow of superheated vapor, gravitational effects are assumed to be insignificant):

$$\Delta P_{vl,i} = \frac{\dot{m}_{tot}}{2}\left[f\,\mathrm{Re}_{vl}\,\frac{\mu_g}{\rho_g A_{vl} D_{vl}^2}\right]_i \Delta z \tag{2.32}$$

The Reynolds number is defined as follows:

$$\mathrm{Re}_{vl} = \left[\frac{\dot{m}_{tot} D_{vl}}{\mu_g A_{vl}}\right] \tag{2.33}$$

For Re_{vl} <2300, the flow is considered to be laminar and fully-developed, and the Darcy friction factor, *f*, is calculated using the analytical solution $f\,\mathrm{Re}_{vl} = 64.0$ [Kays and Crawford (1993)].

For Re_{vl} >2300, the flow is considered to be turbulent and fully developed, and the Colebrook-White correlation [Colebrook (1939); White (1991)] is used to estimate the Darcy friction factor:

$$\frac{1}{\sqrt{f}} = -2.0\log_{10}\left[\frac{e/D_{vl}}{3.7} + \frac{2.51}{\mathrm{Re}_{vl}\sqrt{f}}\right] \tag{2.34}$$

Note that the Re_{vl}, f, the related fluid properties, and $\Delta P_{vl,i}$ are computed in a segment-by-segment manner based on the average fluid temperature in each segment of the vapor-transport line. The overall pressure drop in the complete (or total) vapor-transport line is then obtained as follows:

$$\left(\Delta P_{vl}\right)_{tot} = \sum_{i=1}^{M_{vl}} \left(\Delta P_{vl}\right)_i \tag{2.35}$$

Segmented Heat Transfer Calculations in the Single-Phase Region

A steady-state energy balance over segment *i* of the vapor-transport line yields the following relation for the corresponding heat gain $q_{vl-gain,\,i}$:

$$q_{vl-gain,\,i} = \dot{m}_{tot}\left(c_{p,v}\right)_i \left(T_{vl,\,out} - T_{vl,\,in}\right)_i \text{ , where}$$
$$\left(T_{vl,\,out}\right)_i = T_{amb} - \left[T_{amb} - \left(T_{vl,\,in}\right)_i\right] \exp\left[-\left(\frac{UA'_{vl}}{c_{p,v}}\right)_i \frac{\Delta z}{\dot{m}_{tot}}\right] \tag{2.36}$$

In the above expressions, $\left(UA'_{vl}\right)_i$, is the cell overall thermal conductance *per unit length* akin to the one introduced earlier, and takes into account the following considerations: the convective *single-phase* heat transfer inside the vapor-transport line; the radial heat conduction in the pipe wall and the insulation (if present); and the external heat transfer (free convection, forced convection, radiation, or a combination of them). In Eq. (2.36), $\left(T_{vl,\,\mathrm{in}}\right)_i$ and $\left(T_{vl,\,out}\right)_i$ are, respectively, the bulk fluid temperature at the inlet and exit of segment *i*; and $\left(c_{p,v}\right)_i$ is the specific heat at constant pressure of the vapor in the i^{th} cell.

In a manner similar to that used in ***Case 1***, $(UA'_{vl})_i$ is expressed as follows:

$$(UA'_{vl})_i = 1/(R'_{th\_inside,\,i} + R'_{th\_wall-outside,\,i})$$
$$R'_{th\_inside,\,i} = \frac{1}{\pi D_{vl} h_i^{1\phi}};\; R'_{th\_wall-outside,\,i} = \frac{1}{\left(UA'_{vl,\,wall\text{-}outside}\right)_i} \tag{2.37}$$

In this equation, $R'_{th\_inside,\,i}$ and $R'_{th\_wall-outside,\,i}$ are, respectively, the *per unit length* thermal resistance for the internal, single-phase, convection in the vapor-transport line segment *i*; and the external thermal resistance (sum of the thermal resistances associated with the pipe wall, insulating material, and the external heat transfer). Again, it is assumed here

that the rate of axial heat conduction through the pipe wall and the insulation are negligible compared to that in the radial direction, the convective heat transfer inside the pipe is fully developed.

Next, the calculation of the single-phase heat transfer coefficient, $h_i^{1\phi}$, for segment *i* is done following the usual practice in heat transfer calculations [Incropera and DeWitt (2002)]. For Re_{vl} <2300, the flow is considered to be laminar, and, for fully-developed conditions, available analytical and numerical solutions [Kays and Crawford (1993); Sparrow and Patankar (1977)] show that the Nusselt number, $\left(Nu_{vl} = h_{vl}^{1\phi} D_{vl} / k_v\right)$, is in the range $3.65 \leq Nu_{vl} \leq 4.36$: A value in the middle of this range, $Nu_{vl} = 4.0$, is used for this case.

For Re_{vl} >2300, a correlation proposed by Gnielinski (1976) is used to estimate the value of Nu_{vl}: For $0.5 < Pr < 2000$ and $2300 < \mathrm{Re_{vl}} < 5\times10^6$:

$$Nu_{vl} = \frac{\left(f/8\right)\left(\mathrm{Re}_{vl} - 1000\right)\mathrm{Pr}}{1 + 12.7\left(f/8\right)^{1/2}\left(\mathrm{Pr}^{2/3} - 1\right)} \tag{2.38}$$

Here, f is the Darcy friction factor, and *Pr* is the Prandtl number of the vapor.

The temperature at the entrance of the first segment (i = 1) of the vapor-transport line is T_{sat}, which is the saturation temperature at the exit of the evaporator. The average temperature in segment i, $\overline{T}_{vl,\,i}$, is initially assumed to be its inlet temperature, $\left(T_{vl,\,in}\right)_i$, and all vapor properties are based on this cell temperature. Once the temperature at the exit of segment *i*, $\left(T_{vl,\,out}\right)_i$, is determined using Eq. (2.36), the average temperature in segment *i* is re-computed based on the arithmetic mean of the inlet and exit temperatures: $\overline{T}_{vl,\,i} = \left[\left(T_{vl,\,in}\right)_i + \left(T_{vl,\,out}\right)_i\right]/2$. Following that, all cell thermofluid properties are based on this newly calculated value of $\overline{T}_{vl,\,i}$, and another iteration of the aforementioned pressure drops and heat transfer calculations is conducted for segment *i*. This process is repeated for segment *i* until subsequent changes in $\overline{T}_{vl,\,i}$ are within a user-specified tolerance (all absolute relative differences < 10^{-4} was used in this work). Then, a similar iterative process is conducted on each of the subsequent segments for

corresponding pressure drops and heat transfer calculations in the vapor-transport line (until $i = M_{vl}$ is reached).

The total rate of heat gain in the vapor-transport line is then obtained by adding together the rates of heat gain in all of the segments:

$$q_{vl-gain,\,\mathrm{tot}} = \sum_{i=1}^{M_{vl}} q_{vl-gain,\,i} = \dot{m}_{tot} \sum_{i=1}^{M_{vl}} \left(c_{p,v}\right)_i \left(T_{vl,\,out} - T_{vl,\,in}\right)_i \tag{2.39}$$

2.2.6 Condenser Unit

The condenser unit connects the exit of the vapor-transport line to the entrance of the liquid-transport line, as is shown in Figure 2.1. In the LHP considered here, the condenser unit essentially consists of a horizontal tube that experiences a heat loss to an external environment maintained at a fixed sink temperature, T_{sink}. Depending on the particular condenser design and operating conditions, the fluid exiting the condenser line either could be 1) a saturated-liquid, 2) a two-phase mixture, or 3) a subcooled-liquid. Figure 2.8 depicts a situation in which the fluid exits the condenser in a subcooled state.

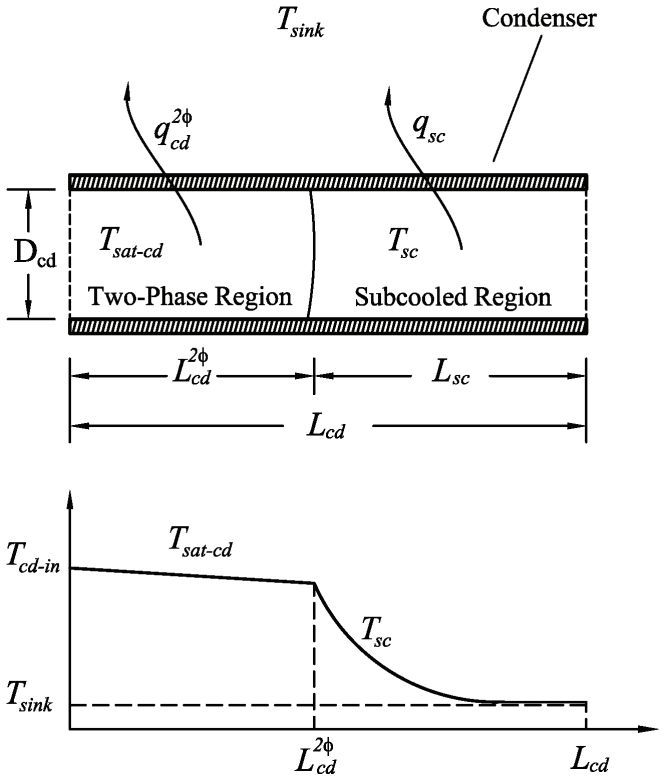

Figure 2.8: Schematic of the fluid flow through the condenser when $L_{cd}^{2\varphi} < L_{cd}$.

Here, the position where the zero-quality (x = 0, full condensation of the vapor) is first attained is located within the condenser pipe ($L_{cd}^{2\phi} < L_{cd}$). As shown in this figure, the vapor entering at temperature T_{cd-in} is condensed over the length $L_{cd}^{2\phi}$, and its temperature drops slightly over this length due to the drop in pressure. Over the remaining length of the condenser, L_{sc}, the condensed liquid is further cooled and exits in a subcooled state. If the condenser tube were long enough, the subcooled liquid temperature at the exit of the condenser would asymptotically approach the sink temperature in this instance.

A segmented quasi-one-dimensional model is used to simulate the thermofluid phenomena in the condenser line for the distinctive two-phase and subcooled flow regions schematically illustrated in Figure 2.8.

2.2.6 .1 Segmented Thermofluid Calculations in the Two-Phase Region

As presented in Figure 2.8, the saturated vapor enters the condenser pipe at $T_{cd,\,in}$ and fully condenses in the two-phase region of length $L_{cd}^{2\phi}$. As was mentioned earlier, the thermodynamic process in this region involves a pressure drop, and associated slight lowering of the saturation temperature, and the fluid reaches the saturated liquid state at the start of the subcooled region. However, $L_{cd}^{2\phi}$ is not known *a priori*, and the pressure drop and rate of heat loss and the pressure drop in the condenser depend on this length. The condenser sizing procedure presented in Rohsenow (1985) is adapted here to evaluate $L_{cd}^{2\phi}$.

The two-phase region of the condenser line is first discretized (segmented) into $M_{cd-2\phi}$ control-volumes or cells of *equal quality* change ($\Delta x = x_{cd,\,in} / M_{cd-2\phi} = \text{const.}$), where $x_{cd,\,in}$ is the quality of the vapor flow at the inlet of the condenser. Moreover, the mean quality in segment i is calculated from the arithmetic mean of the corresponding inlet and exit qualities: $\overline{x}_i = \left(x_{cd,\,in}\right)_i - \Delta x / 2$. The number of cells ($M_{cd-2\phi}$) suitable for simulation is determined heuristically: It is increased until the differences in the results obtained are negligibly small. In this equal-quality segmented approach, the corresponding lengths of the pipe segments, Δz_i, are not necessarily equal, and are

determined by applying the following steady-state energy balance in a segment-by-segment manner:

$$q_{cd-loss,\,i}^{2\phi} = \dot{m}_{tot}\, i_{fg}\Big|_{\overline{T}_{sat-cd,\,i}} \Delta x = (UA'_{cd-2\phi})_i \left(\overline{T}_{sat-cd,\,i} - T_{sink}\right)\Delta z_i$$

$$\Delta z_i = \frac{\dot{m}_{tot}\, i_{fg}\Big|_{\overline{T}_{sat-cd,\,i}} \Delta x}{(UA'_{cd-2\phi})_i \left(\overline{T}_{sat-cd,\,i} - T_{sink}\right)} \tag{2.40}$$

In this expression, $q_{cd-loss,\,i}^{2\phi}$ is the heat loss from segment *i* in the two-phase region of the condenser; $\overline{T}_{sat-cd,\,i}$ is the average saturation temperature in segment *i* of the condenser (equal to the arithmetic mean of the corresponding segment inlet and exit temperatures); $i_{fg}\Big|_{\overline{T}_{sat-cd,\,i}}$ is the latent heat of evaporation in the segment *i*; and $(UA'_{cd-2\phi})_i$ is the cell overall thermal conductance *per unit length*, and takes into account the convective *two-phase* heat transfer inside the condenser pipe, the radial heat conduction in the pipe wall and sleeve (if present), and the external heat transfer methods (free convection, forced convection, radiation, or a combination of them). The definition of the overall cell conductance, $(UA'_{cd-2\phi})_i$, is similar to that presented earlier for the two-phase region of the vapor-transport line:

$$(UA'_{cd-2\phi})_i = 1/(R'_{th\_inside,\,i} + R'_{th\_wall-outside,\,i})$$

$$R'_{th\_inside,\,i} = \frac{1}{\pi D_{cd} h_i^{2\phi}};\; R'_{th\_wall-outside,\,i} = \frac{1}{\left(UA'_{cd-2\phi,\,wall\text{-}outside}\right)_i} \tag{2.41}$$

In the above expression, $h_i^{2\phi}$ is the internal two-phase heat transfer coefficient in the i^{th} cell of the condenser pipe based on its inside surface area; $\left(UA'_{cd-2\phi,\,wall\text{-}outside}\right)_i$ is the overall conductance *per unit length* between the inside surface area of the condenser segment *i* and the outside external environment; and D_{cd} is the internal diameter of the condenser pipe. The internal heat transfer coefficient $h_i^{2\phi}$ for the condensing vapor inside segment i of the condenser depends on the related flow regimes that occur in the two-phase region inside the condenser. Therefore, following the procedure presented earlier for the two-phase region of the vapor-transport line, the correlation of Dobson and Chato (1998) is used to predict $h_i^{2\phi}$: See Eqs. (2.21) - (2.29) and related discussions in the last

subsection. Once $h_i^{2\phi}$ is calculated , then $(UA'_{cd-2\phi})_i$ and Δz_i are determined using Eqs. (2.41) and (2.40), respectively. Following that, the two-phase pressure drop across the calculated pipe length, Δz_i, is determined using the procedure presented earlier for the two-phase region of the vapor-transport line:

$$\left(\Delta P_{cd}^{2\phi}\right)_i = \left[\Delta P_f^{2\phi} + \Delta P_{mom} + \Delta P_{grav}\right]_i \tag{2.42}$$

It should be noted that all fluid properties in these calculations are obtained based on the average saturation temperature, $\overline{T}_{sat,\,i}$, of the condenser segment.

Next, the saturation temperature at the exit of condenser segment *i,* $\left(T_{sat-cd,\,out}\right)_i$, (which is the same as the temperature at the inlet of segment *i*+1) is obtained from the saturation temperature at the inlet of corresponding segment *i,* $\left(T_{sat-cd,\,in}\right)_i$, using the slope of the liquid-vapor saturation curve (P-T diagram) of the working fluid and the associated pressure drop $\left(\Delta P_{cd}^{2\phi}\right)_i$ in segment *i* computed from an equation akin to Eq. (2.42):

$$\left(T_{sat-cd,\,out}\right)_i = \left(T_{sat-cd,\,in}\right)_i - \left(\Delta P_{cd}^{2\phi}\right)_i \Big/ \left(\frac{dP_{sat}}{dT_{sat}}\right)_{\overline{T}_{sat-cd,\,i}} \tag{2.43}$$

At the entrance of the first segment in the condenser pipe, i = 1, the temperature corresponds to that at the exit of the vapor-transport line: $\left(T_{sat-cd,\,out}\right)_{i=M_{cs-2\phi}}$. The average temperature in segment i , $\overline{T}_{sat-vl,\,i}$, is initially assumed to be its inlet temperature, $\left(T_{sat-cd,\,in}\right)_i$. All vapor and liquid properties are then based on this temperature. Once the temperature at the exit of segment *i,* $\left(T_{sat-vl,\,out}\right)_i$, is calculated from Eq. (2.43), the average temperature in segment *i* is re-computed based on the arithmetic mean of the inlet and exit temperatures: $\overline{T}_{sat-cd,\,i} = \left[\left(T_{sat-cd,\,in}\right)_i + \left(T_{sat-cd,\,out}\right)_i\right] / 2$. Following that, another iteration of the aforementioned pressure drop and heat transfer calculations are conducted for segment *i* using the newly calculated value of $\overline{T}_{sat-cd,\,i}$. This process is repeated for segment *i* until subsequent changes in $\overline{T}_{sat-cd,\,i}$ are within a user-specified tolerance (10^{-4} was used in this work). A similar iterative process is then conducted on

the next i+1 segment (and so, until $i = M_{cd-2\phi}$ is reached) for corresponding pressure drops and heat transfer calculations in the two-phase part of the condenser line.

At this stage, the total length of the two-phase region of the condenser is calculated:

$$L_{cd}^{2\phi} = \sum_{i=1}^{M_{cd-2\phi}} \Delta z_i \tag{2.44}$$

Once $L_{cd}^{2\phi}$ is determined, it is compared to the total length of the condenser pipe, L_{cd}. As was mentioned previously, three possible cases could exist:

1) $L_{cd}^{2\phi} = L_{cd}$: The fluid exits the condenser as a saturated liquid state in this case, at the saturation temperature $T_{cd-exit}^{2\phi}$. The quality at the exit is $x_{cd-exit} = 0$, and the total rate of heat rejection in the condenser is:

$$q_{cd-loss,\,tot} = q_{cd-loss,\,tot}^{2\phi} = \sum_{i=1}^{M_{cd-2\phi}} (UA'_{cd-2\phi})_i \Delta z_i \left(\overline{T}_{sat-cd,\,i} - T_{sink}\right) = \dot{m}_{tot} \Delta x \sum_{i=1}^{M_{cd-2\phi}} i_{fg}\Big|_{\overline{T}_{sat-cd,i}} \tag{2.45}$$

2) $L_{cd}^{2\phi} > L_{cd}$: This situation occurs when the rate of heat rejection in the condenser is not enough to condense the vapor completely, and a two-phase (vapor-liquid) flow exits the condenser at the saturation temperature $T_{sat-cd,j}$. Here, j ($j < M_{cd-2\phi}$) denotes the segment at the end of which, collectively, the total length of the segments $0 \le i \le j$ is equal to the total length of the condenser pipe. In this case, the quality of the fluid at the exit would be $0 < x_{vqual,cdexit} < 1$, and the total rate of heat rejection in the condenser is:

$$\begin{aligned} q_{cd-loss,\,tot} &= \sum_{i=1}^{j} (UA'_{cd-2\phi})_i \Delta z_i \left(\overline{T}_{sat-cd,\,i} - T_{sink}\right) = \dot{m}_{tot} \Delta x \sum_{i=1}^{j} i_{fg}\Big|_{\overline{T}_{sat-cd,\,i}} \\ q_{cd-loss,\,tot} &= \dot{m}_{tot}\left(i_{cd-in} - i_{cd-exit}\right) \end{aligned} \tag{2.46}$$

In this equation, $i_{cd-exit}$ is the fluid specific enthalpy at the exit of the condenser, and i_{cd-in} is the fluid specific enthalpy at the inlet of the condenser. Both $q_{cd-loss,\,tot}$ and $i_{cd-exit}$ are determined using Eq. (2.46). Once $i_{cd-exit}$ is calculated, the quality at the exit of the condenser, $x_{cd-exit}$, can be determined as follows:

$$i_{cd-exit} = i_g\Big|_{\overline{T}_{sat-cd,\,j}} x_{cd-exit} + (1 - x_{cd-exit})\, i_f\Big|_{\overline{T}_{sat-cd,\,j}} \tag{2.47}$$

Here, i_f and i_g are the enthalpies of the saturated liquid and saturated vapor, respectively.

For this case, the vapor exiting the condenser would have to condense in the compensation chamber, relying on the heat loss to the ambient there. If this condition cannot be met, then T_{sat} in the evaporator would go up until one of the following situations prevails with respect to the vapor generated in the evaporator: 1) fully condenses with $L_{cd}^{2\phi} < L_{cd}$, if the compensation chamber is adiabatic or gains heat from the ambient; or 2) fully condenses in the condenser with $L_{cd}^{2\phi} = L_{cd}$, if the heat loss in the compensation chamber exactly balances the heat leak.

3) $L_{cd}^{2\phi} < L_{cd}$: In this situation, the ability of the condenser to reject heat is more than that required for completing condensation of the vapor, and the position where this happens ($x = 0$ if first reached) is located within the condenser pipe. As the rate of heat rejection to the sink continues over the rest of the condenser pipe, the fluid exits in a subcooled state. The total rate of heat rejection in the condenser is calculated as follows:

$$q_{cd-loss,\,tot} = q_{cd-loss,\,tot}^{2\phi} + q_{sc} \tag{2.48}$$

In this equation, $q_{cd-loss,\,tot}^{2\phi}$ is the rate of heat transfer required to fully condense the vapor in the condenser, see Eq. (2.45); and q_{sc} is the rate of heat rejection (total) from the condensed liquid, causing it to exit the condenser in a subcooled state. A segmented procedure for the calculation of q_{sc} is presented in the next subsection.

As was mentioned earlier, the two-phase pressure drop in the condenser is determined using the same procedures as those employed for this task in the vapor-transport line. The total pressure drop in the two-phase region of the condenser given by

$$\left(\Delta P_{cd}^{2\phi}\right)_{tot} = \sum_{i=1}^{M_{cd}^{2\phi}} \left(\Delta P_{cd}^{2\phi}\right)_i = \sum_{i=1}^{M_{cd}^{2\phi}} \left[\Delta P_f^{2\phi} + \Delta P_{mom} + \Delta P_{grav}\right]_i \tag{2.49}$$

2.2.6.2 Segmented Thermofluid Calculations in the Subcooled Region

The subcooled (or single-phase liquid) region exists in the condenser only if $L_{cd}^{sc} = \left(L_{cd} - L_{cd}^{2\phi}\right) > 0$. If such a subcooled region exists, then, it is discretized into control-volumes or cells of equal length ($\Delta z = L_{cd}^{sc} / M_{cd-sc} = \text{const.}$). Again, the appropriate value

of M_{cd-sc} is determined heuristically: It is increased until the differences in the results obtained are negligibly small.

The calculation procedure for the single-phase pressure drop and heat transfer in the subcooled region of the condenser is identical to that presented earlier for the single-phase region of the vapor-transport line, and thus the adapted equations are presented succinctly in this section.

The single-phase static pressure drop is calculated in each segment *i* in the subcooled region of the condenser as follows:

$$\Delta P_{cd-sc,\,i} = \frac{\dot{m}_{tot}}{2}\left[f\,\mathrm{Re}_{sc}\,\frac{\mu_l}{\rho_l A_{cd} D_{cd}^2}\right]_i \Delta z \tag{2.50}$$

The Reynolds number is defined as follows:

$$\mathrm{Re}_{sc} = \left[\frac{\dot{m}_{tot} D_{cd}}{\mu_l A_{cd}}\right] \tag{2.51}$$

For Re_{sc} <2300, the flow is considered to be laminar and fully-developed, and the Darcy friction factor, *f*, is calculated using the analytical solution [Kays and Crawford (1993)] $f\,\mathrm{Re}_{sc} = 64.0$.

For Re_{sc} >2300, the flow is considered to be turbulent and fully developed, and the Colebrook-White correlation [Colebrook (1939); White (1991)] is used to estimate the Darcy friction factor:

$$\frac{1}{\sqrt{f}} = -2.0\log_{10}\left[\frac{e/D_{cd}}{3.7} + \frac{2.51}{\mathrm{Re}_{sc}\sqrt{f}}\right] \tag{2.52}$$

In addition, the gravity pressure drop across segment *i* in the subcooled region of the condenser pipe is given by

$$\left(\Delta P_{grav}\right)_i = \left[\rho_l g\left(\sin\beta\right)\right]_i \Delta z_i \tag{2.53}$$

In this equation, β denotes the angle between the axis of the segment *i* and the horizontal, and g is the gravitational acceleration. In this work, only a horizontal or slightly inclined (< 5°) condenser pipe is considered.

Note that the Re_{sc}, f, $\Delta P_{sc,i}$, $\Delta P_{grav,\,i}$, and the related fluid properties are computed in a segment-by-segment manner based on the average fluid temperature in each segment of the subcooled region of the condenser pipe.

The total pressure drop in the subcooled region of the condenser line is then obtained as follows:

$$\left(\Delta P_{cd-sc}\right)_{tot} = \sum_{i=1}^{M_{cd-sc}} \left[\left(\Delta P_{cd-sc}\right)_i + \left(\Delta P_{grav}\right)_i\right] \tag{2.54}$$

Next, a steady-state energy balance over segment *i* in the subcooled region yields the following relation for the corresponding heat loss $q_{cd-sc-loss,\,i}$:

$$\begin{aligned} &q_{cd-sc-loss,\,i} = \dot{m}_{tot}\left(c_{p,l}\right)_i\left(T_{cd-sc,\,in} - T_{cd-sc,\,out}\right)_i \text{ , where} \\ &\left(T_{cd-sc,\,out}\right)_i = T_{sink} + \left[\left(T_{cd-sc,\,in}\right)_i - T_{sink}\right]\exp\left[-\left(\frac{UA'_{cd-sc}}{c_{p,l}}\right)_i \frac{\Delta z}{\dot{m}_{tot}}\right] \end{aligned} \tag{2.55}$$

In the above expressions, $\left(UA'_{cd-sc}\right)_i$, is the cell overall thermal conductance *per unit length* akin to the one introduced earlier, and takes into account the convective *single-phase* heat transfer inside the subcooled region of the condenser pipe, radial heat conduction in the pipe wall and sleeve (if present), and external heat transfer (free convection, forced convection, radiation, or a combination of them); $\left(T_{cd-sc,\,in}\right)_i$ and $\left(T_{cd-sc,\,\mathrm{out}}\right)_i$ are, respectively, the bulk fluid temperature at the inlet and exit of segment *i*; and $\left(c_{p,l}\right)_i$ is the specific heat at constant pressure of the liquid in the i^{th} cell.

As was discussed earlier, $(UA'_{cd-sc})_i$ can be expressed in terms of a *per unit length* thermal resistance for the internal, single-phase, convection in segment *i*; and an equivalent external thermal resistance (sum of the thermal resistances associated with the pipe wall, sleeve/saddle material, and the external heat transfer):

$$\begin{aligned} &(UA'_{cd-sc})_i = 1/(R'_{th\_inside,\,i} + R'_{th\_wall-outside,\,i}) \\ &R'_{th\_inside,\,i} = \frac{1}{\pi D_{cd} h_i^{1\phi}};\; R'_{th\_wall-outside,\,i} = \frac{1}{\left(UA'_{cd-sc,\,wall\text{-}outside}\right)_i} \end{aligned} \tag{2.56}$$

The calculation of the single-phase heat transfer coefficient, $h_i^{1\phi}$, for segment *i* is accomplished following the usual practice in heat transfer calculations [Incropera and

DeWitt (2002)]. For Re_{sc} <2300, the flow is considered to be laminar, and, for fully-developed conditions, available analytical and numerical solutions [Kays and Crawford (1993); Sparrow and Patankar (1977)] show that the Nusselt number, $\left(Nu_{cd-sc} = h^{1\phi}_{cd-sc} D_{cd} / k_l\right)$, is in the range 3.65 ≤ Nu_{cd-sc} ≤ 4.36: Again, a value in the middle of this range, Nu_{cd-sc} = 4.0, is used for this case.

For Re_{sc} >2300, a correlation proposed by Gnielinski (1976) is used to estimate the value of Nu_{cd-sc}: For 0.5 < *Pr* < 2000 and 2300 < Re_{sc} < 5×10^6:

$$Nu_{cd-sc} = \frac{\left(f/8\right)\left(\mathrm{Re}_{sc}-1000\right)\mathrm{Pr}}{1+12.7\left(f/8\right)^{1/2}\left(\mathrm{Pr}^{2/3}-1\right)} \tag{2.57}$$

Here, f is the Darcy friction factor, and *Pr* is the Prandtl number of the vapor.

Furthermore, the temperature at the entrance of the first segment (*i* = 1) in the subcooled region of the condenser line is $T^{2\phi}_{cd-exit}$, which is the temperature at the exit of the two-phase region of the condenser. The average temperature in segment *i* , $\overline{T}_{cd-sc,\,i}$, is initially assumed to be its inlet temperature, $\left(T_{cd-sc,\,in}\right)_i$, and all liquid properties are based on this cell temperature. Once the temperature at the exit of segment *i* , $\left(T_{cd-sc,\,out}\right)_i$, is determined from Eq. (2.55), the average temperature in segment *i* is re-calculated based on the arithmetic mean of the inlet and exit temperatures: $\overline{T}_{cd-sc,\,i} = \left[\left(T_{cd-sc,\,in}\right)_i + \left(T_{cd-sc,\,out}\right)_i\right] / 2$. Following that, all cell thermofluid properties are based on this newly calculated value of $\overline{T}_{cd-sc,\,i}$, and a reiteration of the pressure drops and heat transfer calculations is conducted for segment *i*. This process is repeated for segment *i* until subsequent changes in $\overline{T}_{cd-sc,\,i}$ are within a user-specified tolerance (all absolute relative differences < 10^{-4} was used in this work). Then, a similar iterative process is conducted on the next *i*+1 segment for corresponding pressure drops and heat transfer calculations in the subcooled (single-phase) region of the condenser pipe (and so on, until $i = M_{sc}$ is attained).

The total rate of heat loss in the subcooled portion of the condenser is then obtained by summing together the rates of heat loss in all of the associated segments:

$$q_{cd-sc-loss,\,\mathrm{tot}} = \sum_{i=1}^{M_{cd-sc}} \dot{m}_{tot} \left(c_{p,l}\right)_i \left(T_{cd-sc,\,in} - T_{cd-sc,\,out}\right)_i \tag{2.58}$$

2.2.7 Liquid-Transport Line

The liquid-transport line serves to convey the subcooled liquid exiting the condenser to the compensation chamber of LHPs. In well-designed LHPs, the vapor flow is fully condensed in an initial portion of the condenser, and a subcooled liquid exits the condenser to then enter into the liquid-transport line. The liquid-transport line is generally well insulated and typically assumed to be adiabatic [Kaya and Hoang (1999); Maydanik (2005)]. However, in practice there could be some heat exchange between the liquid-transport line and the external environment. In the proposed segmented thermofluid model, the liquid-transport line is discretized into control-volumes or cells of equal length ($\Delta z = L_{liquid-transport\ line} / M_{ll} = \text{const.}$) akin to the subcooled region of the condenser pipe. The segmented single-phase pressure drop and heat transfer calculations for each segment *i* of the liquid-transport line are done following the procedure outlined in section 2.2.6.2 for the subcooled region of the condenser line, so it is not repeated here.

2.2.8 Compensation Chamber

It is assumed that during the steady-state operation of the LHP, over the full range of the rate of heat input, the compensation chamber is always filled with a two-phase (liquid-vapor) mixture. Thus, for the desirable condition of $L_{cd}^{2\phi} < L_{cd}$, the following equation applies:

$$\begin{aligned} q_{cc-amb} &= q_{hl} + \dot{m}_{tot}\left(i_l\Big|_{T_{cc,\,in}} - i_l\Big|_{T_{sat,\,cc}}\right) \\ q_{cc-amb} &= U_{cc-amb} A_{cc}\left(T_{sat,\,cc} - T_{amb}\right) \end{aligned} \tag{2.59}$$

In this equation, q_{cc-amb} is the rate of heat loss from the fluid in the compensation chamber to the ambient environment; $T_{cc,\,in}$ is the bulk temperature of the subcooled fluid entering the compensation chamber; $T_{sat,\,cc}$ (= T_8) is the saturation temperature of the two-phase mixture inside the compensation chamber; $i_l\Big|_{T_{cc,\,in}}$ and $i_l\Big|_{T_{sat,\,cc}}$ are the specific enthalpies of the liquid at $T_{cc,\,in}$ and $T_{sat,\,cc}$, respectively; U_{cc-amb} is an overall heat transfer

coefficient and A_{cc} is the corresponding heat transfer surface area of the compensation chamber; and T_{amb} is the ambient temperature. The value of q_{cc-amb} could be negative or positive depending on the operating conditions of the LHP.

2.2.9 Total Pressure Drop in the Loop Heat Pipe

In the context of the discussions presented in Section 2.2.1 – 2.2.7, the total pressure *drop* in the entire LHP should not be higher than the maximum capillary pressure that is developed at the liquid-vapor interface in the wick structure. The total loop pressure drop, in its general form, is calculated as follows:

$$\Delta P_{tot} = \left(P_1 - P_9\right) = \Delta P_{l,wick} + \Delta P_{vg} + \Delta P_{vl} + \Delta P_{cd}^{2\phi} + \Delta P_{cd-sc} + \Delta P_{ll} \tag{2.60}$$

Here, $\Delta P_{l,wick}$ denotes the liquid pressure drop during its passage through the porous wick; ΔP_{vg} is the vapor pressure drop through the evaporator grooved channel; ΔP_{vl} is the vapor pressure drop through the vapor-transport line; $\Delta P_{cd}^{2\varphi}$ is the liquid-vapor mixture pressure drop in the two-phase part of the condenser; ΔP_{cd-sc} denotes the liquid pressure drop in the subcooled region of the condenser (single-phase part); and ΔP_{ll} indicates the liquid pressure drop through the liquid-transport line.

The maximum capillary head available in the wick is given by

$$\Delta P_{cap,\,max} = \frac{2\sigma\cos\theta_c}{r_p} \tag{2.61}$$

In this equation, θ_c is the contact angle at the static equilibrium condition (it depends on the wick material and the working fluid), σ is the liquid-vapor surface tension, and r_p is the maximum effective capillary pore radius.

For the successful operation of LHPs under steady-state conditions, the total pressure drop should be less than the maximum capillary head:

$$\Delta P_{tot} < \Delta P_{cap,\,max} \tag{2.62}$$

2.3 Model Implementation

The proposed steady-state segmented network thermofluid model was incorporated in a computer program written in FORTRAN, and an iterative solution procedure was used

to solve this model. When this computer program is started, the following required inputs are read in first: the geometrical parameters of the loop; curve fits to all required thermophysical property data of the working fluid; the sink temperature, T_{sink}; and the ambient temperature, T_{amb}. Next, the rate of heat transfer applied to the evaporator (q_{app}) and a corresponding guess value of the saturation temperature at the liquid-vapor interface in the wick, T_{sat}, are prescribed. The following overall iterative solution procedure is then used:

1. The total rate of evaporation, $\dot{m}_{tot}$, at the liquid-vapor interface in the wick is initially approximated from the rate of heat applied to the evaporator, q_{app}, alone (ignoring the contributions of q_{vsh} and q_{hl}): $\dot{m}_{tot} \approx q_{app} / i_{fg}\big|_{T_{sat}}$.

2. The vapor-transport line, the subcooled region of the condenser line (if it exists), and liquid-transport line are discretized (segmented) into control volumes or cells of *equal length*, Δz, while the two-phase region of the condenser line is divided into equal-quality segments, Δx. The flow regime map, quality, single- and two-phase pressure drop and heat transfer calculations are performed iteratively, as needed, in each contiguous cells or control-volumes corresponding to the vapor-transport-line, condenser line, and liquid-transport-line of the LHP.

3. The total pressure drop in the overall loop, ΔP_{tot}, is calculated from the sum of the pressure drop contributions (single- and two-phase frictional pressure drop, pressure drop required to sustain the momentum changes due to condensation, and pressure drop due to gravity) in various segmented elements of the LHP.

4. Next, the temperature of the liquid at the wick entrance, $T_{wick,\,ent} = T_8$, is determined based on the total pressure drop in the overall loop, ΔP_{tot}, the liquid pressure drop across the wick, $(\Delta P_{l,wick})_{drop}$, and slope of the liquid-vapor saturation curve (P-T diagram) of the working fluid:

$$T_{wick,\,ent} = T_{sat} - \left(\Delta P_{tot} - \Delta P_{l,wick}\right) \Big/ \left(\frac{dP_{sat}}{dT_{sat}}\right)_{T_{sat}} .$$

5. The effective thermal conductivity, k_{eff}, of the liquid-saturated wick is calculated using Eqs. (2.5) - (2.7). Following that, the rate of heat leak through the wick, q_{hl}, is obtained from Eq. (2.3) or Eq. (2.4) depending on the LHP evaporator design.

6. The calculated rate of heat leak through the wick, q_{hl}, is used in conjunction with Eq. (1) to compute a new (or corrected) total mass flow rate in the LHP: $\dot{m}_{tot,\,new} = (q_{app} - q_{hl}) / i_{fg}\big|_{T_{sat}}$.

7. The new and old values of the total mass flow rate in the loop are then compared with respect to a user specified tolerance:

   $\left|\dot{m}_{tot,\,new} - \dot{m}_{tot}\right| / \dot{m}_{tot,\,new} < TOL$ (10^{-4} was used).

8. If the absolute value of the difference between the two mass flow rates is not within the prescribed tolerance, then the total mass flow rate in the LHP is set equal to the new mass flow rate, $\dot{m}_{tot} = \dot{m}_{tot,\,new}$, and steps 2 - 7 are repeated until convergence is achieved in the value of the total mass flow rate in the LHP.

9. The rate of heat transfer in the evaporator, vapor-transport-line, condenser-line and liquid-transport-line are calculated based on the converged value of the total mass flow rate in the loop and suitable mean values of the temperature, thermofluid properties, quality, and heat transfer coefficient prevailing over each contiguous cells or control-volumes of the LHP. An overall energy balance is then applied on the compensation chamber of the LHP and the rate of heat loss from the fluid in the compensation chamber to the ambient environment, q_{cc-amb}, is obtained from Eq. (2.59): $q_{cc-amb} = q_{hl} + \dot{m}_{tot}\left(i_l\big|_{T_{cc,\,in}} - i_l\big|_{T_{sat,\,cc}}\right)$.

10. The rate of heat loss from the fluid in the compensation chamber to the ambient environment, q_{cc-amb}, is also computed based on the product of a prescribed overall heat transfer coefficient, U_{cc-amb}, a corresponding heat transfer surface area of the compensation chamber, A_{cc}, and the temperature difference between the saturation temperature of the two-phase mixture inside the compensation

chamber and the ambient temperature ($T_{sat,\,cc}$ - T_{amb}). In this stage of the iterations, this rate of heat loss is denoted as $\tilde{q}_{cc-amb}$, and calculated using the following equation: $\tilde{q}_{cc-amb} = U_{cc-amb} A_{cc} \left(T_{sat,\,cc} - T_{amb} \right)$.

11. The values of the rate of heat loss from the fluid in the compensation chamber to the ambient environment, q_{cc-amb} and $\tilde{q}_{cc-amb}$ calculated in steps 9 and 10, respectively, are compared with respect to a user specified tolerance: $\left| q_{cc-amb} - \tilde{q}_{cc-amb} \right| / \left| q_{cc-amb} \right| < TOL$ (TOL = 10^{-4} was used in this work). If the absolute value of the difference between the above-mentioned expression is not within the prescribed tolerance, then the initial guess value of the saturation temperature of the working fluid at the liquid-vapor interface in the wick, T_{sat}, is incorrect. The value of T_{sat} is therefore corrected, based on the Newton-Raphson or Secant method, for example, and steps 1-10 are repeated until convergence is achieved in the energy balance of the compensation chamber of the LHP.

12. Subsequently, steps 1 - 10 are repeated for a newly specified value of the rate of heat applied to the evaporator, q_{app}. Key elements of the iterative procedure used to solve the proposed segmented thermofluid network model of an LHP are presented in the flow chart shown in Figure 2.9.

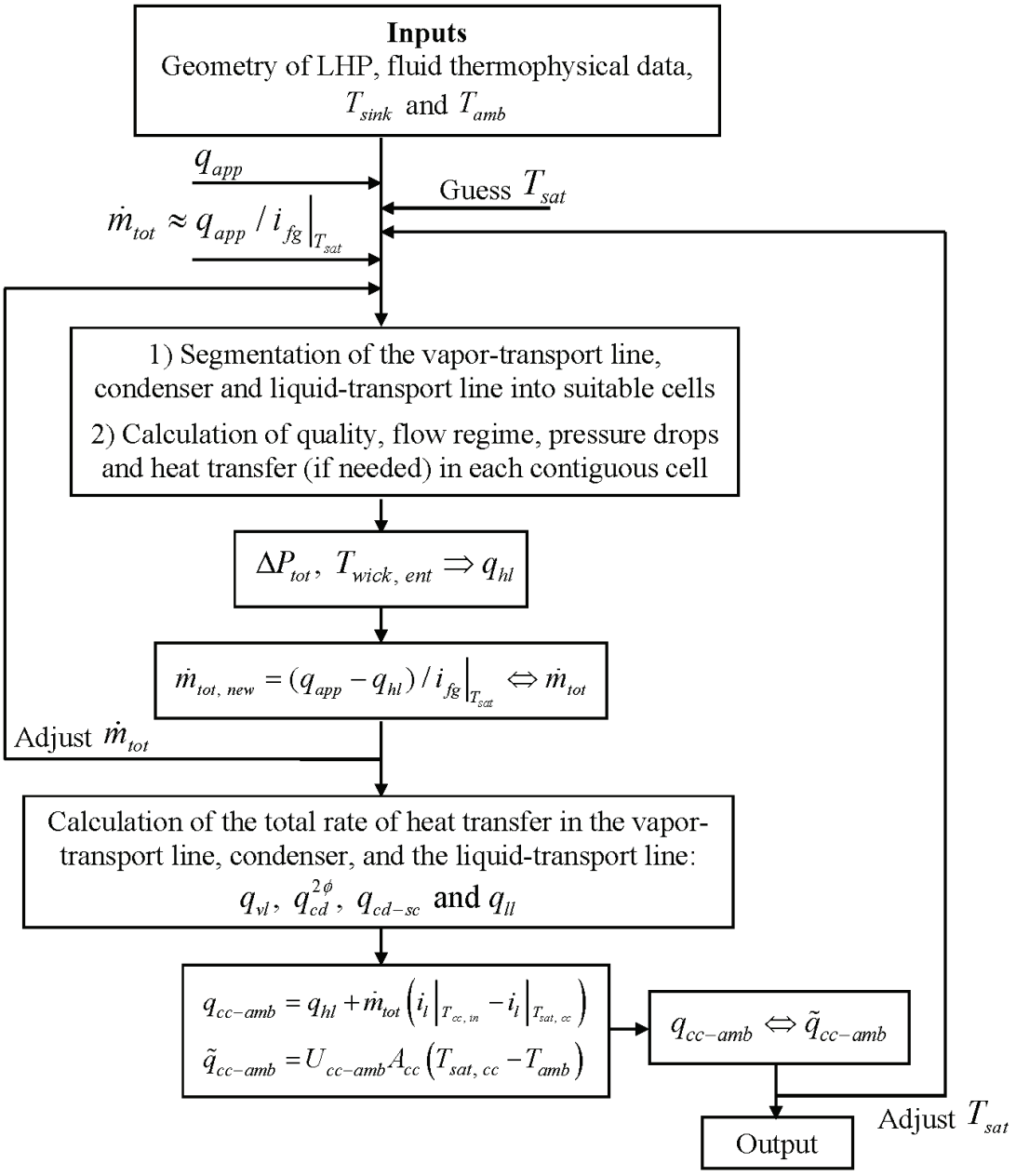

Figure 2.9: Flow chart illustrating key elements of the overall iterative procedure that was used to solve the segmented thermofluid network model.

2.4 Application to a Test Problem, Results and Discussions

The proposed segmented network thermofluid model was used to predict the steady-state operational characteristics of a conventional cylindrical-evaporator LHP with attributes akin to those depicted in Figures 2.1a and 2.3. Details of this LHP and the results obtained in this investigation are presented and discussed in this section.

2.4.1 Details of the LHP

The details of the LHP were similar to those of the GLAS LHP (LHP1) investigated by Kaya and Hoang (1999). However, not all required data were provided in this paper. Thus, the overall dimensions, porosity, and permeability of the wick, and the number and hydraulic diameter of the vapor grooves, were estimated using information available in related literature. Also, the overall heat transfer coefficient, U_{cc-amb}, from the inside surface to the compensation chamber to the ambient was fine-tuned to match the predicted results to the experimental data for a sink temperature of $T_{sink} = 283$ K.

The cylindrical evaporator had an external diameter of 25.4 mm, a length of 150 mm, and essentially rectangular vapor grooves. The total number of grooves in the evaporator was set equal to N = 16, each with an average cross-sectional area of $A_{c-s,\,groove} = 4$ mm², and a hydraulic diameter of $D_h = 2$ mm. A sintered powder-nickel wick with an effective pore radius of 1.2 μm was used. The wick porosity and permeability were set equal to $\varepsilon = 0.5$ and $K = 2.7\times10^{-14}$ m², and its inside and outside radii were assigned the values of $r_i = 6$ mm and $r_o = 10$ mm. The compensation chamber (CC) had an internal diameter of 46 mm and a length of 76 mm (volume = 126.3 ml; surface area $A_{cc} = 0.012645$ m^2 that exchanges heat with the ambient). The value of T_{amb} was fixed at 295 K. The CC was initially filled (at ambient temperature) with a two-phase mixture, of quality equal to 0.5. The charging strategy was the following: The liquid transport line, condenser pipe, evaporator liquid core, and the void volume of the wick structure were filled with saturated liquid ammonia; and the vapor transport line and the evaporator grooves were filled with saturated ammonia vapor at T_{amb}. The rate of heat transfer through the envelope of the CC to or from the ambient environment was estimated via an overall heat transfer coefficient, U_{cc-amb}, which was assigned a value of 20 W/m²-K, based on A_{cc}.

The vapor- and the liquid-transport lines of the LHP were identical smooth tubes made of stainless steel, each with an inner diameter of 4.52 mm and a length of 0.460 m. These vapor- and liquid-transport lines were very well insulated, and assumed to have adiabatic boundaries [Kaya and Hoang (1999)].

The condenser was a single-pass heat exchanger, with a tube of length 4.06 m and internal diameter of 4.52 mm. The overall thermal conductance *per unit length*, $UA'_{cd,\,wall\text{-}outside}$, from the inner surface of the condenser tube to the outer surface of the metallic sleeve (in which it is snugly fitted) was set equal to 4 W/m-K, and the outer surface temperature of this sleeve was set equal to the sink temperature T_{sink}. It was also assumed that this overall thermal conductance is constant over the entire length of the condenser pipe.

Ammonia was used as the working fluid in the LHP. The required thermophysical property data for this fluid were obtained from the NIST Standard Reference Database [Linstrom and Mallard (2005)], and appropriate curves were fitted to this data for use in the FORTRAN computer program. In this investigation, the range of the applied rate of heat input to the evaporator, q_{app}, was limited to ensure that the saturation temperature of the ammonia was in the range $200\ \text{K} < T_{sat} < 400\ \text{K}$, as the critical-point temperature of ammonia is 405.4 K [Avallone and Baumeister III (1987)].

The performance of the LHP was examined for q_{app} in the range 0 to 350 W, and two different values of the sink temperature: $T_{sink} = 273$ K and 283 K. The results obtained for these sink temperatures were qualitatively similar. Therefore, in this section, attention is limited to the results for $T_{sink} = 283$ K. In this work, the vapor-transport line, two-phase portion of the condenser, subcooled part of the condenser (if it exists), and the liquid-transport line were segmented into $M_{vl} = M_{cd-2\phi} = M_{sc} = M_{ll} = 100$ control-volumes: The differences in the results obtained with the assigned number of control volumes and the next augmented ($M_{vl} = M_{cd-2\phi} = M_{sc} = M_{ll} = 200$) number of such control volumes were negligible (all absolute differences < less than 10^{-4}).

2.4.2 Variations of T_{sat} and $T_{cd-exit}$ with q_{app}

The variations in the saturation temperature of ammonia at the liquid-vapor interface in the wick structure, T_{sat}, and the fluid temperature at the exit of the condenser, $T_{cd-exit}$, with the power input to the evaporator, q_{app}, are presented in Figure 2.10 for $T_{sink} = 273$ K and $T_{amb} = 295$ K.

For low power inputs (q_{app} < 78 W), the saturation temperature first decreases with q_{app} and then reaches a minimum value. For higher values of power input, T_{sat} increases with q_{app}, almost linearly. For low power inputs, $T_{cd-exit}$ remains almost constant and very close to the sink temperature, and when this temperature starts to rise with q_{app}, so does T_{sat}.

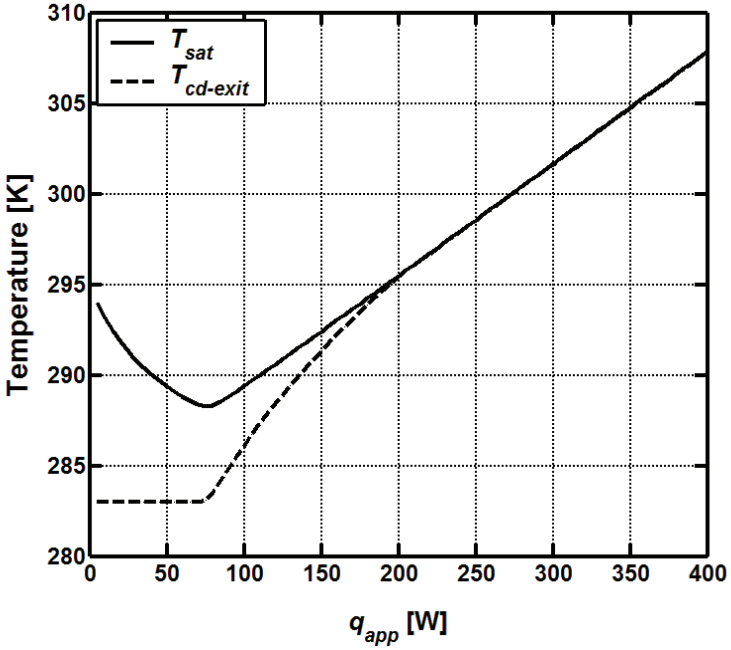

Figure 2.10: Variation of T_{sat} and $T_{cd-exit}$ with q_{app} for T_{sink} = 283 K and T_{amb} = 295 K.

Bienert and Wolf (1995) and Kaya and Hoang (1999) have also reported very similar results. In both studies, the authors concluded that at low power inputs, the fluid exits the condenser as a subcooled liquid and the LHP operates in variable conductance mode; and beyond the minimum point of the T_{sat} vs. q_{app} curve, the condenser becomes fully "open" (in that its entire length is filled with a two-phase fluid), and LHP operates in a fixed conductance mode, where T_{sat} increases almost linearly with q_{app}. This explanation is essentially correct, but not precise as was demonstrated in Atabaki (2006) and Atabaki, Jesuthasan and Baliga (2007): This is made known by the results presented in the next subsection.

2.4.3 Length of the Two-Phase Flow Region inside the Condenser

The variation of dimensionless length of the two-phase flow region in the condenser with q_{app} (for T_{sink} = 283 K and T_{amb} = 295 K) is shown in Figure 2.11. The results indicate that when $q_{app} < 78\ W$, roughly 88% of the condenser length is occupied by the two-phase flow region.

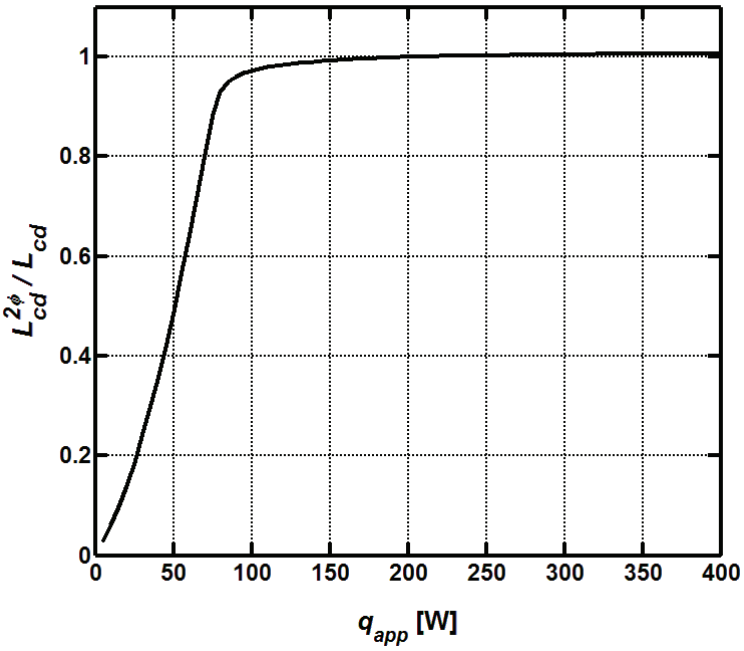

Figure 2.11: Non-dimensional length of the two-phase flow region in the condenser as a function of q_{app}, for T_{sink} = 283 K and T_{amb} = 295 K.

Thus, the location of the minimum point in Figure 2.10 does not coincide with the condenser becoming fully open, as proposed by Bienert and Wolf (1995) and Kaya and Hoang (1999). Indeed, at the location of the minimum point in the loop operating temperature, T_{sat}, the rate of growth of the two-phase region inside the condenser is decreased, and an inflection point is evident in Figure 2.11, close to q_{app} =75 W.

2.4.4 Comparison of Model Predictions with Experimental Data

As was mentioned previously in this section, the value of U_{cc-amb} was adjusted to closely match the predicted results (T_{sat} *vs.* q_{app}) with the corresponding experimental

data, for T_{sink} = 283 K. The numerical predictions obtained in this work are compared with the experimental results of Kaya and Hoang (1999) in Figure 2.12 for two values of the sink temperature: T_{sink} = 273 K and 283 K. As the fine-tuning of U_{cc-amb} was done with respect to T_{sink} = 283 K, the predicted and experimental results for this sink temperature show excellent agreement. Even for T_{sink} = 273 K, considering that several parameters of the LHP had to be estimated (see the related discussions in Section 2.4.1), the comparisons of the predicted and experimental results shown in Figure 2.12 can be regarded as being quite encouraging.

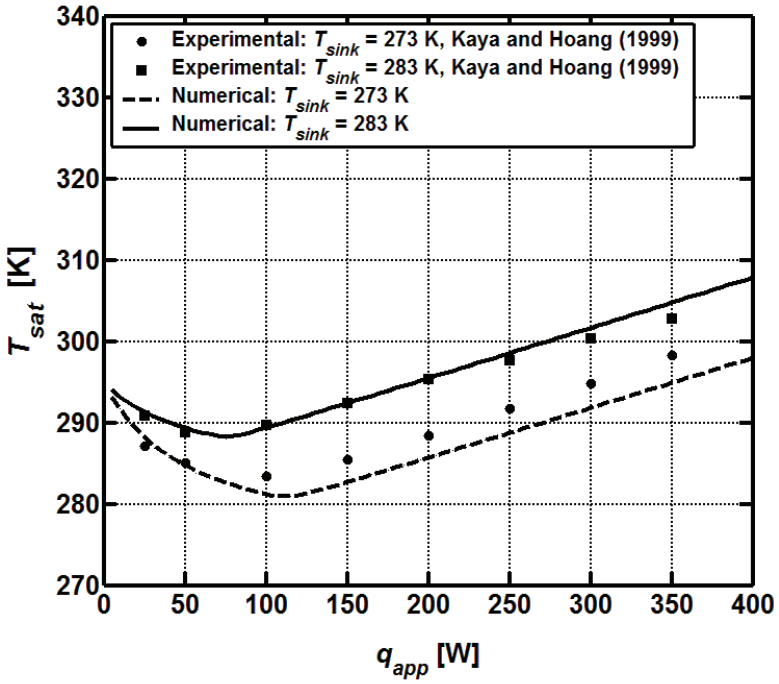

Figure 2.12: Comparisons of the experimental data of Kaya and Hoang (1999) with the numerical predictions obtained with the proposed segmented network thermofluid model, for T_{amb} = 295 K .

2.5 CONCLUDING REMARKS

A segmented network thermofluid model for the simulation of loop heat pipes (LHPs) operating under steady-state conditions was presented and discussed in the earlier sections of this chapter. Attention was focused on LHPs with one evaporator (cylindrical or flat), a vapor-transport line, one condenser, a liquid-transport line, and a compensation

chamber. Variations of thermophysical properties of the working fluid with temperature are taken into account, along with change in quality, pressure drop, and heat transfer in the two-phase regions, giving the proposed model enhanced capabilities compared to those of earlier thermofluid network models of LHPs, such as those of Bienert and Wolf (1995), Kaya and Hoang (1999), Maydanik (2005), Singh et al. (2007). In these earlier models, balances of mass, momentum, and energy are imposed on the full elements (rather than segmented portions) of the LHP, and the variations of quality and pressure drops in the liquid-vapor two-phase regions are overlooked.

The model proposed in this work was formulated by borrowing and extending key ideas from the works of Atabaki (2006) and Atabaki et al. (2007). These extensions, which have been reported in Jesuthasan et al. (2008) and Jesuthasan and Baliga (2009a), are the following: 1) in the models of Atabaki (2006) and Atabaki et al. (2007), calculations of pressure drop and heat transfer in the two-phase region of the LHP were done using correlations that could only handle the stratified-smooth regime, where as correlations that can handle the stratified-smooth, stratified-wavy, and annular-flow regimes have been implemented in the model proposed in this chapter, making it suitable for a wider range of applications; 2) the balances of mass, momentum, and energy over the segments (cells or control volumes) of the vapor-transport line, condenser pipe, and the liquid-transport line are done with fluid properties based on the mean bulk temperature within the cells (and in the case of two-phase flow, also the mean quality within the cell), and imposed using an inner-iterative procedure, whereas upstream properties (and quality) and a non-iterative procedure were used in Atabaki (2006) and Atabaki et al. (2007); and 3) the updating of the T_{sat} values in the overall iterations is done using a secant method, where as a trial-and-error procedure was used for these updates in Atabaki (2006) and Atabaki et al. (2007).

The proposed segmented network thermofluid model was used to simulate an LHP similar to the one investigated experimentally by Kaya and Hoang (1999). Results pertaining to the performance of this LHP over a range of operating conditions were presented, and their implications were discussed. These results indicated that the proposed model produces results that compare quite well (at least qualitatively) with the corresponding experimental results of Kaya and Hoang (1999).

In the proposed model and also in earlier quasi-one-dimensional models [Kaya and Hoang (1999); Ghajar and Darabi (2005); Maydanik (2005); Atabaki (2006); Atabaki et al. (2007); Launay et al. (2007); Jesuthasan et al. (2008); Jesuthasan and Baliga (2009a); Singh et al. (2009)], the total static pressure *drop* in the vapor grooves of the evaporator, ΔP_{vg}, is computed using correlations for a Darcy friction factor that strictly applies only in the fully-developed region of flows in straight ducts of circular and non-circular cross-sections with impermeable walls. This approach is inapplicable or ad hoc, at best, when the pressure drop in the vapor grooves is a significant contributor to the overall pressure drop in the LHP. To enhance the capabilities of current quasi one-dimensional models of LHPs, more accurate correlations for the calculation of the above-mentioned vapor-channel pressure drop are needed. A computational method is formulated in Chapter 3 and applied in Chapter 4 to develop accurate and cost-effective correlations for the prediction of the pressure drop in the vapor-removal channels of LHPs. The development and incorporation of these novel correlations, and their incorporation into the proposed segmented network thermofluid model of LHPs, are important contributions of this thesis. The capabilities of the resulting enhanced model are demonstrated in Chapter 6.

Chapter 3:

A Numerical Method for Three-Dimensional Parabolic Flow and Heat Transfer in Straight Ducts of Irregular Cross-Section

In this chapter, the emphasis is primarily on the formulation, implementation, and testing of a novel co-located equal-order control-volume-based finite element method (CVFEM) for the prediction of three-dimensional parabolic fluid flow and heat transfer in straight ducts of uniform regular- and irregular-shaped cross-section, akin to those shown schematically in Figure 3.1 [Jesuthasan and Baliga (2009b)].

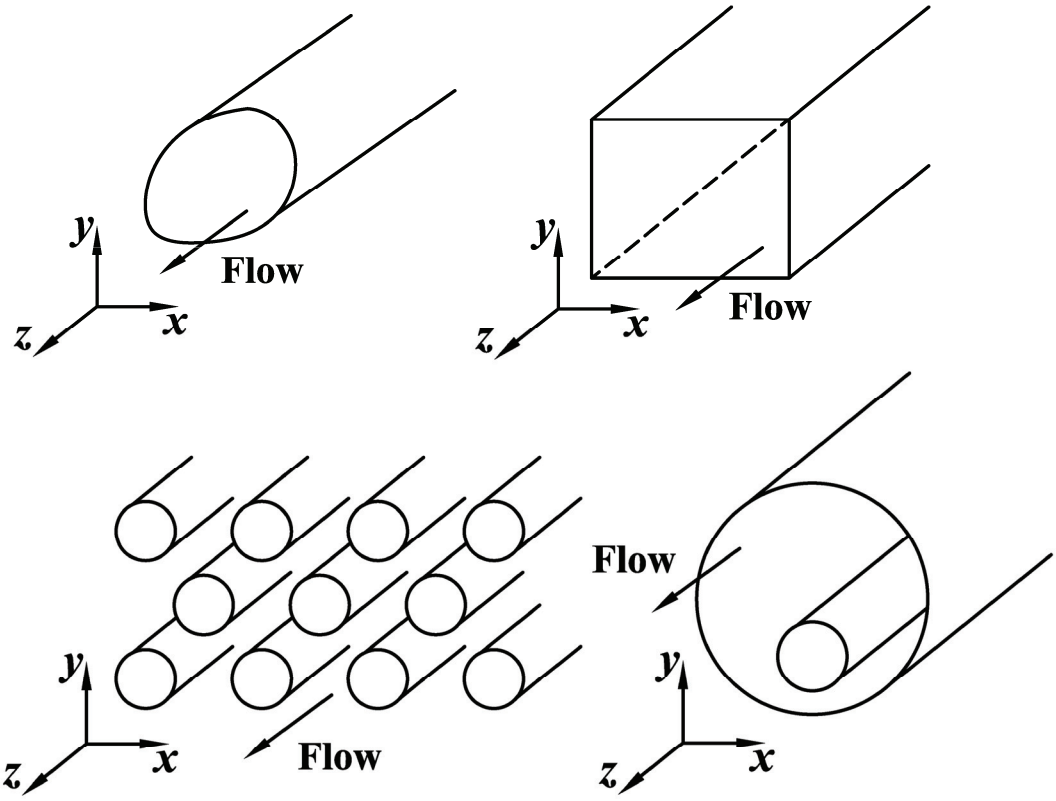

Figure 3.1: Examples of three-dimensional parabolic flows in straight ducts of uniform cross-section.

The formulation of the proposed novel CVFEM is based on extensions and amalgamation of ideas put forward in two earlier numerical methods for fluid flow and heat transfer: a seminal finite-volume method based on staggered Cartesian grids for the solution

of three-dimensional parabolic problems [Patankar an Spalding (1972)]; and a co-located equal-order control-volume-based finite element method for the solution of planar two-dimensional elliptic problems [Baliga and Atabaki (2006)]. An automatic axial step-size selection procedure for problems in which the dependent variables vary monotonically in the axial direction is also proposed. The validity of the proposed method is established by applying it to developing laminar fluid flow and forced convection in a straight duct of square cross-section, and comparing the results to those available in the literature.

Following the presentation of the above-mentioned CVFEM, the methodology put forward in it is adapted to formulate a simpler finite volume method (FVM) that is well suited for cost-effective predictions of three-dimensional parabolic fluid flow and heat transfer in straight ducts of *rectangular* cross-section. This FVM is used in Chapter 4 of this thesis to investigate fluid flow and heat transfer phenomena in straight rectangular vapor-removal grooves of LHP evaporators.

3.1 Background Information and Motivation

Fluid flow and heat transfer in regular- and irregular-shaped ducts or duct-like geometries are encountered in nature and in numerous engineering devices, equipment, and systems. Today, powerful general-purpose computational fluid dynamics (CFD) methods and codes, many of them direct offshoots or extensions of the pioneering work of Patankar and Spalding (1972), allow reliable predictions and investigations of such fluid flow and heat transfer phenomena, and facilitate the design and optimization of the related engineering devices, equipment, and systems. However, there are still opportunities for formulating focused CFD methods that are specialized or tailored for efficient predictions of specific classes or subsets of these duct flow and heat transfer phenomena. It is in this context that the work presented in this chapter was undertaken.

Attention here is limited to incompressible, steady, laminar, Newtonian fluid flow and heat transfer. However, the proposed CVFEM is formulated by borrowing and extending ideas from the three-dimensional parabolic and elliptic finite-volume methods of Patankar and Spalding (1972), Pratap and Spalding (1976), and Patankar (1980): these methods and/or their extensions have been used extensively for predictions of turbulent, single-phase and multiphase, steady and unsteady fluid flow and heat transfer phenomena in straight

regular-shaped ducts, using available mathematical models such as those discussed in Wilcox (1993), Launder and Sandham (2002), Brennen (2005), and Crowe (2006). Thus, it may be argued that the CVFEM proposed here could be readily adapted for the prediction of these phenomena in straight ducts of uniform regular- and irregular cross-section. However, explicit demonstrations of such adaptations are not within the scope of this thesis.

It should also be noted that the proposed CVFEM would be useful in investigations of many practical liquid or low-Mach number gas flows and heat transfer in ducts, such as the following: developing laminar forced convection in straight internally-finned ducts, similar to those discussed in Kays and London (1984) and Webb and Kim (2005); and developing laminar mixed convection in ducts, as discussed, for example, by Patankar et al. (1978), Choudhury and Patankar (1988), and Nesreddine et al. (1997). It could also be used for simulations of fluid flow and heat transfer in the entrance region of micro-scale channels and tubes, akin to those discussed in Peng and Petersen (1996), Adams et al. (1999), Ng and Tan (2004), Morini (2004), Thompson et al. (2005), and Liu et al. (2007). In addition, the proposed numerical method could be used in investigations of heat transfer in tubes conveying nanofluids, using mathematical models akin to those discussed by Daungthongsuk and Wongwise (2007) and Akbari and Behzadmehr (2007), for example.

Incompressible, laminar, parabolic flow and heat transfer in ducts are governed by equations that are intrinsically nonlinear and coupled to each other, as will be shown in the next section of this chapter. If major simplifications are introduced in these equations, such as linearizing the inertia terms in the momentum equations and neglecting cross-stream pressure gradients, then analytical solutions are possible, as shown, for example, in Fleming and Sparrow (1969). However, for the solution of problems in which the aforementioned major simplifications are invalid, numerical methods are needed. The seminal numerical methods for the solution of three-dimensional parabolic flows in ducts of rectangular cross-section are the finite-volume methods proposed by Caretto et al. (1972) and Patankar and Spalding (1972). In subsequent papers, variants of the method of Patankar and Spalding (1972) have been proposed by Carlson and Hornbeck (1973) and Briley (1974). These methods are best suited for solution of problems with regular-shaped domains, the boundaries of which lie along the axes of commonly used orthogonal coordinate systems. Ducts with irregular-shaped cross-section can be handled using finite volume or finite

difference methods that are designed to work with curvilinear orthogonal or non-orthogonal boundary-fitted grids, as is done in the work of Roberts and Forester (1979). However, such methods are not well suited for the solution of problems with highly irregular and/or multiply connected domains.

Several finite-element methods have been put forward for the solution of three-dimensional parabolic flow and heat transfer in straight ducts of regular- or irregular-shaped cross-section. An example of such a method is that proposed by Del Giudice et al. (1981). These finite-element methods typically use a non-iterative marching technique, achieved by using the upstream values of the dependent variables at each axial step to calculate the coefficients in the discretized equations, in a manner akin to that proposed in the work of Patankar and Spalding (1972). This non-iterative technique often necessitates the use of overly small axial step sizes in order to obtain results that are essentially independent of the sequence in which the dependent variables are solved.

The method proposed in this chapter contains several novel features that allow it to overcome the aforementioned limitations and difficulties. It is formulated by extending and amalgamating ideas put forward in two earlier methods: a seminal staggered-Cartesian-grid finite-volume method proposed by Patankar and Spalding (1972) for the prediction of three-dimensional parabolic fluid flow and heat transfer in straight ducts of rectangular cross-section; and a co-located equal-order control-volume-based finite element method (CVFEM) discussed by Baliga and Atabaki (2006) for planar two-dimensional elliptic fluid flow and heat transfer in irregular-shaped domains. This feature of the proposed CVFEM enables its application to straight ducts of uniform regular- and irregular-shaped cross-section. In each axial step of a marching solution procedure, a fully-implicit scheme is used to discretize the governing equations in the axial direction, and the non-linear coupled discretized equations are solved using an adaptation of a sequential iterative variable adjustment (SIVA) scheme proposed earlier by Saabas and Baliga (1994): thus, for any axial step size, the proposed method is able to generate results that are independent of the sequence in which the dependent variables are solved. Another novel feature of the proposed method is an automatic axial step-size selection procedure for problems in which the dependent variables vary monotonically in the axial direction.

3.2 MATHEMATICAL MODEL

Parabolic duct flows have the following characteristics: there exists a predominant flow along the duct (the main-stream direction), and no flow reversal is encountered in that direction; diffusion transport in the mainstream direction is negligible compared to the corresponding advection transport and the cross-stream diffusion transport; and the downstream pressure field has negligible influence on the upstream flow conditions. Following the discussions in the seminal work of Patankar and Spalding (1972), and with reference to the ducts and the Cartesian coordinate system shown in Figure 3.1, the equations that govern steady, parabolic, incompressible Newtonian fluid flow and heat transfer phenomena can be cast in the following forms:

Continuity:

$$\frac{\partial}{\partial x}(\rho u)+\frac{\partial}{\partial y}(\rho v)+\frac{\partial}{\partial z}(\rho w)=0 \tag{3.1}$$

x-momentum:

$$\frac{\partial}{\partial x}(\rho uu)+\frac{\partial}{\partial y}(\rho vu)+\frac{\partial}{\partial z}(\rho wu)=-\frac{\partial p}{\partial x}+\frac{\partial}{\partial x}(\mu\frac{\partial u}{\partial x})+\frac{\partial}{\partial y}(\mu\frac{\partial u}{\partial y})+S_u \tag{3.2}$$

y-momentum:

$$\frac{\partial}{\partial x}(\rho uv)+\frac{\partial}{\partial y}(\rho vv)+\frac{\partial}{\partial z}(\rho wv)=-\frac{\partial p}{\partial y}+\frac{\partial}{\partial x}(\mu\frac{\partial v}{\partial x})+\frac{\partial}{\partial y}(\mu\frac{\partial v}{\partial y})+S_v \tag{3.3}$$

z-momentum:

$$\frac{\partial}{\partial x}(\rho uw)+\frac{\partial}{\partial y}(\rho vw)+\frac{\partial}{\partial z}(\rho ww)=-\frac{d\bar{P}}{dz}+\frac{\partial}{\partial x}(\mu\frac{\partial w}{\partial x})+\frac{\partial}{\partial y}(\mu\frac{\partial w}{\partial y})+S_w \tag{3.4}$$

Energy:

$$\frac{\partial}{\partial x}(\rho uT)+\frac{\partial}{\partial y}(\rho vT)+\frac{\partial}{\partial z}(\rho wT)=\frac{\partial}{\partial x}(\frac{k}{c_p}\frac{\partial T}{\partial x})+\frac{\partial}{\partial y}(\frac{k}{c_p}\frac{\partial T}{\partial y})+S_T \tag{3.5}$$

In these equations, u, v, and w, are components of the velocity vector in the x, y, and z directions, respectively; T is the temperature; S_u, S_v, S_w, and S_T are volumetric source terms (which can also be used to account for extra terms, such as those due to non-constant dynamic viscosity) in the x-, y-, and z-momentum and energy equations, respectively; and ρ, μ, c_p, and k are the mass density, dynamic viscosity, specific heat

at constant pressure, and thermal conductivity of the fluid, respectively. The variables p and $\overline{P}$ in Eqs. (3.2) to (3.4) are a perturbation pressure and a cross-sectional average pressure, respectively, defined as follows:

$$P(x,y,z) = \overline{P}(z) + p(x,y,z)$$
$$\overline{P}(z) = \frac{1}{A_{c-s}} \int_{A_{c-s}} P(x,y,z)\,dxdy \tag{3.6}$$

In this equation, A_{c-s} is the cross-sectional area of the duct. Again following Patankar and Spalding (1972), it has been assumed in Eq. (3.4) that $(\partial p/\partial z) << d\overline{P}/dz$, and the following approximation and substitutions have been applied:

$$\partial P/\partial z = d\overline{P}/dz \;\; ; \;\; \partial P/\partial x = \partial p/\partial x \;\; ; \;\; \partial P/\partial y = \partial p/\partial y \tag{3.7}$$

In addition to the above-mentioned equations, a constraint on the overall or total mass flow rate through the duct must be respected. For steady flow in a duct with impermeable boundaries (except for the inlet and outlet planes), this constraint leads to the following equation:

$$\dot{m} = \int_{A_{c-s}} \rho w\,dA_{c-s} = \text{constant} \tag{3.8}$$

The six equations, (3.1) to (3.5) and (3.8), form a parabolic system in the main-stream or one-way (Patankar, 1980) coordinate direction, z, with six unknowns, u, v, w, p, T, and $(-d\overline{P}/dz)$. To specify the problem completely, the calculation domain geometry, fluid properties, and problem-specific conditions at the inlet-plane and boundaries of the duct must be specified. The proposed CVFEM can handle any commonly encountered conditions at the inlet-plane and boundaries of the duct.

3.3 Formulation of the Numerical Method

The various building blocks of the proposed numerical method are described concisely in this section.

3.3.1 Domain Discretization

The calculation domain is a straight uniform duct of regular- or irregular-shaped cross-section, akin to the samples shown in Figure 3.1. It is first divided into a series of

contiguous slabs perpendicular to the z axis (main-stream coordinate): each slab is made up of the region between two adjacent parallel cross-sectional planes, one upstream and the other downstream. These slabs need not have the same thickness (axial step-size, Δz). Indeed, the ability to work with a non-uniform Δz, adjusted suitably with reference to the axial gradients of the dependent variables in the developing duct flow and heat transfer problems of interest, is crucial to the formulation of a computationally-efficient method.

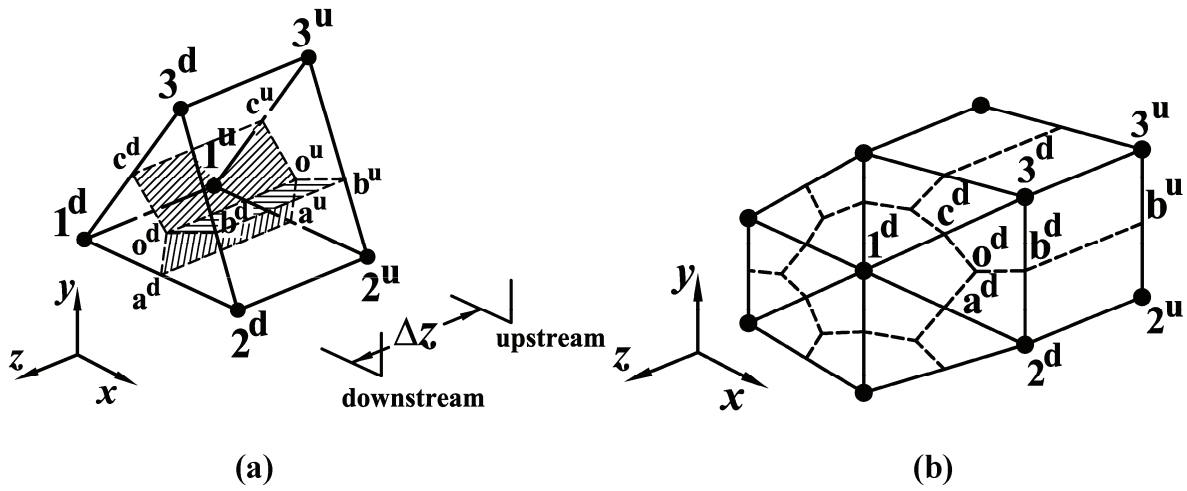

Figure 3.2: (a) Prism-shaped element of triangular cross-section, its discretization into portions of control volumes associated with each of the nodes, and associated notation; (b) prism-shaped control volume of polygonal cross-section associated with an internal node 1 and associated notation.

Following the discretization of the calculation into slabs, the *cross-section* of each slab is further discretized using a two-stage procedure: first, it is divided into three-node triangular elements; following that, the centroid of each three-node triangular element is joined to the mid-points of its three sides, to collectively associate each node with a control volume of polygonal cross-section. This cross-sectional discretization is swept through each slab in the axial (main-stream) direction to generate three-dimensional prism-shaped elements and control volumes of triangular and polygonal cross-sections, respectively, as shown schematically in Figure 3.2 along with the associated notation (the superscripts ‘u’ and ‘d’ indicate upstream and downstream locations, respectively). The rationale for using three-node triangular elements and the aforementioned polygonal

control volumes in each cross-section has been discussed by Baliga and Patankar (1980), Baliga (1997), and Baliga and Atabaki (2006), thus it is not repeated here. All slabs are discretized in the same manner. In each cross-section, all dependent variables are stored at the same three nodes of each element, leading eventually to a co-located equal-order numerical method.

3.3.2 Control-Volume Conservation Equations

The differential equations that govern the three-dimensional parabolic flow and heat transfer problems considered in the work, Eqs. (3.1) – (3.5), are integrated over control volumes such as the one shown in Figure 3.2 (b), and cast in the following general form with respect to a specific (per unit mass) scalar dependent variable ϕ:

$$\left[\begin{array}{l}\displaystyle\int_u^d \left\{\int_a^o \left(J_x\vec{i}+J_y\vec{j}\right).\vec{n}ds+\int_o^c \left(J_x\vec{i}+J_y\vec{j}\right).\vec{n}ds\right\}dz \\ \displaystyle+\iint_{1aoc}\left\{(\rho w\phi)^d-(\rho w\phi)^u\right\}dxdy-\int_u^d\left\{\iint_{1aoc} S_\phi dxdy\right\}dz\end{array}\right]$$
$$+\left[\text{Similar contributions from other elements associated with nodes } 1^u \text{ and } 1^d\right] \qquad (3.9)$$
$$+\left[\text{Boundary contributions, if applicable}\right]=0$$

In this equation, S_ϕ is a volumetric source term associated with ϕ; and J_x and J_y are the (advection + diffusion) fluxes of ϕ in the *x* and *y* directions, respectively:

$$J_x=J_{Advec,x}+J_{Diff,x}=\rho u\phi-\Gamma_\phi\frac{\partial\phi}{\partial x} \text{ and } J_y=J_{Advec,y}+J_{Diff,y}=\rho v\phi-\Gamma_\phi\frac{\partial\phi}{\partial y} \qquad (3.10)$$

In Eq. (3.10), Γ_ϕ is the diffusion coefficient associated with ϕ.

3.3.3 Interpolation Functions

In order to obtain algebraic approximations to the various terms in Eqs. (3.9) and (3.10), element-based interpolation functions in the cross-sectional plane ($x-y$) and in the mainstream direction (z) are prescribed for the fluid properties (ρ and Γ_ϕ), the volumetric source term (S_ϕ), and the dependent variable (ϕ). These interpolation functions are described in this subsection.

3.3.3.1 Fluid Properties and Volumetric Source Terms in the Cross-Sectional Plane (x-y)

In each cross-sectional plane of the duct of interest, with reference to Figure 3.2 (a), the values of ρ and Γ_ϕ at the centroid, *o*, are computed (if required), stored, and assumed to be uniform (prevail) over the element *123*. The source term, S_ϕ, is linearized, if required, and expressed in the following general form, following the recommendations of Patankar (1980):

$$S_\phi = G^{S_\phi} + E^{S_\phi}\phi \tag{3.11}$$

In *each* element, with reference to the element *123* in Figure 3.2 (a), the values of G^{S_ϕ} and E^{S_ϕ} at the nodes *1*, *2*, and *3* are computed (if required), stored, and assumed to prevail over the volumes *1aoc*, *2boa*, and *3cob*, respectively.

3.3.3.2 Velocity Components in the Mass Flux Terms in the Cross-Sectional Plane (x-y)

In the calculation of the mass fluxes across the control volume faces in the cross-sectional plane, the velocity components in the *x* and *y* directions are denoted by u^m and v^m, respectively. These velocity components (u^m and v^m), are interpolated using a special treatment borrowed from the works of Rhie and Chow (1983) and Prakash and Patankar (1985), in order to prevent the occurrence of spurious pressure oscillations in solutions yielded by the proposed co-located numerical method. The development of these special interpolation functions requires inputs from the discretized momentum conservation equations. Therefore, they will be presented later in this chapter.

3.3.3.3 Scalar Dependent Variable in the Diffusion Terms in the Cross-Sectional Plane (x-y)

In the derivations of algebraic approximations of the diffusion terms in the cross-sectional plane, the nodal values of the specific scalar dependent variable, ϕ, are interpolated linearly in each three-node triangular element.

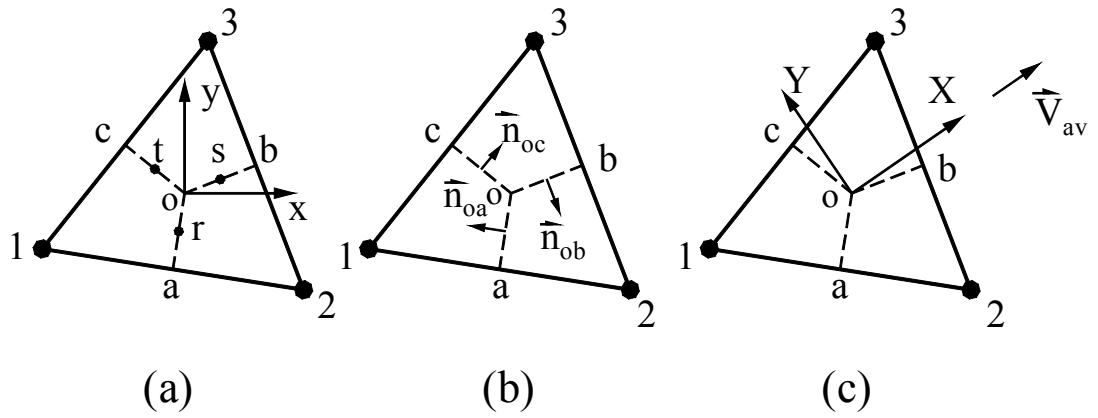

Figure 3.3: A typical three-node triangular element in a cross-sectional plane and related nomenclature: (a) local *x*,*y* coordinate system; (b) unit vectors normal to control volume faces; (c) local flow-oriented *X*,*Y* coordinate system.

Thus, with respect to the triangular element *123* shown in Figure 3.3 (a), the following linear interpolation function applies:

$$\begin{aligned}
&\phi = \phi = A_\Delta^D x + B_\Delta^D y + C_\Delta^D \ ; \ DET = (x_1 y_2 + x_2 y_3 + x_3 y_1 - y_1 x_2 - y_2 x_3 - y_3 x_1) \\
&A_\Delta^D = [(y_2 - y_3)\phi_1 + (y_3 - y_1)\phi_2 + (y_1 - y_2)\phi_3] / DET \\
&B_\Delta^D = [(x_3 - x_2)\phi_1 + (x_1 - x_3)\phi_2 + (x_2 - x_1)\phi_3] / DET \\
&C_\Delta^D = [(x_2 y_3 - x_3 y_2)\phi_1 + (x_3 y_1 - x_1 y_3)\phi_2 + (x_1 y_2 - x_2 y_1)\phi_3] / DET
\end{aligned} \tag{3.12}$$

3.3.3.4 Scalar Dependent Variable in the Advection Terms in the Cross-Sectional Plane (x-y)

In the derivations of algebraic approximations of the advection terms in the cross-sectional plane, the nodal values of the specific scalar dependent variable, ϕ, are interpolated using the flow-oriented upwind (FLO) scheme proposed by Baliga and Patankar (1980), which was formulated by borrowing and extending ideas from the works of Spalding (1972) and Raithby (1976). In this scheme, first, with reference to Figure 3.3 (a), the average mass-conserving velocity vector, $\vec{V}_{av}$, in the cross-sectional plane and its magnitude, U_{av}, in the element *123* are defined as follows:

$$\begin{aligned}
&u_{av}^m = (u_1^m + u_2^m + u_3^m)/3 \ ; \ v_{av}^m = (v_1^m + v_2^m + v_3^m)/3 \\
&\vec{V}_{av} = u_{av}^m \vec{i} + v_{av}^m \vec{j} \ ; \ U_{av} = |\vec{V}_{av}| = \{(u_{av}^m)^2 + (v_{av}^m)^2\}^{0.5}
\end{aligned} \tag{3.13}$$

Then the value of an element Peclet number, Pe_Δ, is computed as follows:

$$x_{max} = \max(x_1, x_2, x_3)\ ;\ x_{min} = \min(x_1, x_2, x_3)$$
$$y_{max} = \max(y_1, y_2, y_3)\ ;\ y_{min} = \min(y_1, y_2, y_3) \qquad (3.14)$$
$$L_\Delta = [(x_{max} - x_{min})^2 + (y_{max} - y_{min})^2]^{0.5}\ ;\ Pe_\Delta = (\rho)_o U_{av} L_\Delta / (\Gamma_\phi)_o$$

Here, the subscript '*o*' indicates centroidal values. At this stage, a new element-based Cartesian coordinate system (*X*,*Y*) and a variable, ξ, are introduced. If $Pe_\Delta \le 10^{-6}$, then (*X*,*Y*) is *identical* to the Cartesian coordinate system (*x*,*y*) shown in Figure 3 (a), and $\xi = X = x$ and $Y = y$. On the other hand, if $Pe_\Delta > 10^{-6}$, then a *local flow-oriented Cartesian coordinate system* (*X*,*Y*) shown in Figure 3.3 (c) is defined: the origin of this coordinate system is located at the centroid of the element *123*, and the *X*-axis is oriented along the element-average mass-conserving velocity vector, $\vec{V}_{av}$. In this case, the following equations relate the (*X*,*Y*) and the (*x*,*y*) coordinates:

$$X = (x - x_o)(u_{av}^m / U_{av}) + (y - y_o)(v_{av}^m / U_{av})\ ;\ Y = (x - x_o)(-v_{av}^m / U_{av}) + (y - y_o)(u_{av}^m / U_{av}) \qquad (3.15)$$

Furthermore, for $Pe_\Delta > 10^{-6}$, the variable ξ and the element-based interpolation function for ϕ are defined as follows:

$$X_{max} = \max(X_1, X_2, X_3)\ ;\ X_{min} = \min(X_1, X_2, X_3)$$
$$\xi = \frac{(\Gamma_\phi)_o}{(\rho)_o U_{av}} \left\{ \exp\left[\frac{(\rho)_o U_{av} (X - X_{max})}{(\Gamma_\phi)_o} \right] - 1 \right\}\ ;\ \phi = A_\Delta^C \xi + B_\Delta^C Y + C_\Delta^C \qquad (3.16)$$

The constants A_Δ^C, B_Δ^C, and C_Δ^C in this equation can be determined in a manner akin to that used to determine the constants in Eq. (3.12). It should also be noted that when $Pe_\Delta \to 0$, the FLO scheme reduces to the linear interpolation scheme given in Eq. (3.12).

In problems that involve acute-angle triangular elements and relatively modest values of Pe_Δ, the FLO scheme performs very well. However, in problems with large values of Pe_Δ, the FLO scheme can lead to negative contributions of the advection transport terms to the coefficients in the discretized equations, especially when large gradients of the cross-sectional velocity field occur within an element or when obtuse-angle triangular elements are used. If negative coefficients in the discretized equations are not admissible, as would be the case, for example, when always-positive variables such as the kinetic energy of turbulence are computed, or when the magnitudes of the negative coefficients lead to

divergence of iterative solution methods, then a suitable lower-order upwind scheme that guarantees positive advection contributions to the coefficients in the discretized equations is recommended: one such scheme is the mass-weighted (MAW) scheme described in the works of Schneider and Raw (1986) and Masson et al. (1994). Full details of the MAW scheme are also available in the work of Baliga and Atabaki (2006). Thus, they are not repeated here.

3.3.3.5 Perturbation Pressure in the Cross-Sectional Plane (x-y)

In the cross-sectional plane, the perturbation pressure, p, is interpolated linearly within each element:

$$p = A_{\Delta}^{p} x + B_{\Delta}^{p} y + C_{\Delta}^{p} \tag{3.17}$$

With reference to element *123* in Figure 3.3(a), A_{Δ}^{p}, B_{Δ}^{p}, and C_{Δ}^{p} are given by expressions akin to those for A_{Δ}^{D}, B_{Δ}^{D}, and C_{Δ}^{D} in Eq. (3.12), with ϕ_1, ϕ_2, and ϕ_3 replaced by p_1, p_2, and p_3, respectively.

3.3.3.6 Scalar Dependent Variable, Fluid Properties, and Volumetric Source Terms in the Mainstream (z) Direction

In the mainstream (z) direction, the fully-implicit scheme is used to interpolate the scalar dependent variable (ϕ), the fluid properties (ρ and Γ_{ϕ}), and the volumetric source term (S_{ϕ}) between the upstream and downstream locations: thus, in each slab of the duct, the downstream nodal values of ϕ, ρ, Γ_{ϕ}, and S_{ϕ} are assumed to prevail over the axial step size Δz. As discussed by Patankar (1980), the fully-implicit scheme provides good accuracy in the parabolic duct flow and heat transfer problems of interest, is unconditionally stable, and ensures positive contributions to the coefficients in the discretized equations. However, the fully-implicit scheme is only first-order accurate, and if more accurate discretization is considered necessary, then the Crank-Nicolson scheme or other higher-order schemes should be used with appropriate restrictions on the size of Δz to ensure positive contributions to the coefficients in the discretized equations. Additional information on such schemes is available in the works of Patankar and Baliga (1978), Patankar (1980), and Jothiprasad et al. (2003), among others.

3.3.4 Discretized Equations for ϕ

The discretized equations are obtained by first deriving algebraic approximations to the element contributions and the boundary contributions, if applicable, in Eq. (3.9), and then assembling these contributions appropriately. Each element contribution consists of the cross-sectional diffusion terms, the cross-sectional and mainstream advection terms, and the source terms. The interpolations functions discussed in the last subsection are used in the derivations of the algebraic approximations to these terms in the element contributions.

3.3.4.1 Contributions of the Diffusion Terms in the Cross-Section

In element *123*, the centroidal value of the diffusion coefficient, $(\Gamma_\phi)_o$, and the linear interpolation function given by the expressions in Eq. (3.12) are used to approximate the cross-sectional diffusion transport contributions of element of *123* to Eq. (3.9) as follows:

$$\int_u^d \left\{ \int_a^o \vec{J}_{Diff}.\vec{n}ds + \int_o^c \vec{J}_{Diff}.\vec{n}ds \right\} dz = \left\{ (\Gamma_\phi)_o [A_\Delta^D y_a - B_\Delta^D x_a] - (\Gamma_\phi)_o [A_\Delta^D y_c - B_\Delta^D x_c] \right\}_\int^d \Delta z \tag{3.18}$$

In this equation, the unit normal vectors ($\vec{n}$) point *outward* with respect to the control volume associated with node *1*, and the superscript '*d*' denotes downstream values, as shown in Figure 3.2 (a).

3.3.4.2 Contributions of the Advection Terms in the Cross-Section

In the element *123* shown in Figure 3.3 (a), the advection flux in the cross-sectional plane (*x*-y) is expressed as follows:

$$\vec{J}_{Advec}^{x-y} = J_{Advec,x}\vec{i} + J_{Advec,y}\vec{j} = (\rho_o u^m \phi)\vec{i} + (\rho_o v^m \phi)\vec{j} \tag{3.19}$$

where ϕ is given by Eqs. (3.15) and (3.16) when the FLO scheme is used, and ρ_o is the centroidal value of the mass density of the fluid. In the FLO scheme, algebraic approximations to the cross-sectional advection contributions of element *123* to Eq. (3.9) are evaluated numerically using the third-order accurate Simpson's rule:

$$\int_u^d \left\{ \int_a^o \vec{J}_{Advec}^{x-y} . \vec{n} ds + \int_o^c \vec{J}_{Advec}^{x-y} . \vec{n} ds \right\} dz =$$

$$\left\{ \begin{array}{l} -\frac{y_a}{6}[(J_{Advec,x})_o + 4(J_{Advec,x})_r + (J_{Advec,x})_a] \\ +\frac{x_a}{6}[(J_{Advec,y})_o + 4(J_{Advec,y})_r + (J_{Advec,y})_a] \\ +\frac{y_c}{6}[(J_{Advec,x})_o + 4(J_{Advec,x})_t + (J_{Advec,x})_c] \\ -\frac{x_c}{6}[(J_{Advec,y})_o + 4(J_{Advec,y})_t + (J_{Advec,y})_c] \end{array} \right\}^d \Delta z \qquad (3.20)$$

In this equation, *r* and *t* are the *midpoints* of the control-volume faces o-a and o-c, respectively, as shown in Figure 3.3 (a), the unit normal vectors ($\vec{n}$) point *outwards* with respect to the control volume associated with node *1*, and the superscript '*d*' denotes downstream values, as shown in Figure 3.2 (a).

3.3.4.3 Contributions of the Advection Terms in the Mainstream Direction

The contribution of the advection term in the mainstream direction to Eq. (3.9) is approximated as follows:

$$\iint_{1aoc} \left\{ (\rho w \phi)^d - (\rho w \phi)^u \right\} dxdy = \left\{ (\rho w \phi)^d - (\rho w \phi)^u \right\}_1 A_{1aoc} \qquad (3.21)$$

In this equation, A_{1aoc} is the area associated with node 1 in the element *123*, as shown in Figure 3.3 (a), and it is given by the following equation: $A_{1aoc} = |DET|/6$, with *DET* given in Eq. (3.12).

3.3.4.4 Source Term Contribution

The contribution of the source term to Eq. (3.9) is approximated as follows:

$$\int_u^d \left\{ \iint_{1aoc} S_\phi dxdy \right\} dz = \left\{ \left(G^{S_\phi} \right)_1 A_{1aoc} + \left(E^{S_\phi} \right)_1 \phi_1 A_{1aoc} \right\}^d \Delta z \qquad (3.22)$$

Here, $(G^{S_\phi})_1$ and $(E^{S_\phi})_1$ are the values of G^{S_ϕ} and E^{S_ϕ} associated with the node *1* in the element *123*, and the superscript '*d*' denotes downstream values.

3.3.4.5 Combined Element Contribution

Adding up the diffusion, advection, and source contributions, the total contribution of element *123* to Eq. (3.9) is obtained. The algebraic approximation to this combined element contribution can be expressed compactly as follows:

$$\int_u^d \left\{ \int_a^o \left(J_x \vec{i} + J_y \vec{j} \right).\vec{n} ds + \int_o^c \left(J_x \vec{i} + J_y \vec{j} \right).\vec{n} ds \right\} dz$$
$$+ \iint_{1aoc} \left\{ (\rho u \phi)^d - (\rho u \phi)^u \right\} dxdy - \int_u^d \left\{ \iint_{1aoc} S_\phi dxdy \right\} dz \qquad (3.23)$$
$$= C_1^{\phi,1} \phi_1^d + C_1^{\phi,2} \phi_2^d + C_1^{\phi,3} \phi_3^d + D_1^\phi$$

In this equation, the superscript '*d*' denotes downstream values, and the coefficient D_1^ϕ includes contributions of the related source terms and also the upstream value of the dependent variable, ϕ_1^u.

3.3.4.6 Assembled Discretized Equation

The coefficients in Eq. (3.25) are computed and appropriately assembled element-by-element to obtain the discretized equations for internal nodes. For boundary nodes, appropriate boundary contributions are also approximated algebraically, if needed, and then added to the element contributions to obtain the complete discretized equation. With reference to a node *i*, this discretized equation can be cast in the following general form:

$$a_{i,\phi} \phi_i^d = \sum_{nb} a_{nb,\phi} \phi_{nb}^d + b_{i,\phi} \qquad (3.24)$$

Again, the superscript '*d*' denotes downstream values, the subscript '*nb*' indicates neighbors of node *i*, and the coefficient $b_{i,\phi}$ includes contributions from $(S_\phi)^d$ and ϕ_i^u.

3.3.5 Discretized *x*- and *y*-Momentum Equations

Except for the presence of integrals of the perturbation pressure gradients and the particular source terms, the integral *x*- and *y*-momentum conservation equations are identical in form to the integral conservation equation for ϕ. With reference to node *1* in Figure 3.2 (a), the contribution of element *123* to integrals of these terms in the *x*- and *y*-momentum equations are approximated as follows:

$$\int_u^d \left\{ \iint_{1aoc} \{-(\partial p/\partial x) + S_u\} dxdy \right\} dz = \left\{ -(\partial p/\partial x)_\Delta^d A_{1aoc} + (G_1^{S_u})^d A_{1aoc} + (E_1^{S_u})^d u_1^d A_{1aoc} \right\} \Delta z$$
$$\int_u^d \left\{ \iint_{1aoc} \{-(\partial p/\partial y) + S_v\} dxdy \right\} dz = \left\{ -(\partial p/\partial y)_\Delta^d A_{1aoc} + (G_1^{S_v})^d A_{1aoc} + (E_1^{S_v})^d v_1^d A_{1aoc} \right\} \Delta z \quad (3.25)$$

The perturbation pressure gradients inside element *123* are computed using the linear interpolation function given in Eq. (3.17): $(\partial p/\partial x)_\Delta^d = A_\Delta^p$; $(\partial p/\partial y)_\Delta^d = B_\Delta^p$. Then, with reference to a node *i*, when all of the associated element and applicable boundary contributions are assembled, the discretized *x*- and *y*-momentum equations are obtained, and they can be cast in the following forms:

$$a_{i,u} u_i^d = \sum_{nb} a_{nb,u} u_{nb}^d + b_{i,u} + (-(\overline{\partial p/\partial x})_{\mathrm{V}_i}^d)\mathrm{V}_i$$
$$a_{i,v} v_i^d = \sum_{nb} a_{nb,v} v_{nb}^d + b_{i,v} + (-(\overline{\partial p/\partial y})_{\mathrm{V}_i}^d)\mathrm{V}_i \quad (3.26)$$

In this equation, the terms $(\overline{\partial p/\partial x})_{\mathrm{V}_i}^d$ and $(\overline{\partial p/\partial y})_{\mathrm{V}_i}^d$ are volume-averaged values of the perturbation pressure gradients in the various elements associated with node *i* in the downstream plane, and V_i is the volume of the control volume surrounding this node.

3.3.6 Discretized *z*-Momentum Equations

Except for the presence of integrals of the cross-sectional average pressure gradient and the particular source term, the integral *z*-momentum conservation equation is identical in form to the integral conservation equation for ϕ. With reference to node *1* in Figure 3.2 (a), the contribution of element *123* to integrals of the cross-sectional average pressure gradient and source term in the *z*-momentum equation are approximated as follows:

$$\int_u^d \left\{ \iint_{1aoc} \{-(d\bar{P}/dz) + S_w\} dxdy \right\} dz$$
$$= \left\{ -(d\bar{P}/dz) A_{1aoc} + (G_1^{S_w})^d A_{1aoc} + (E_1^{S_w})^d w_1^d A_{1aoc} \right\} \Delta z \quad (3.27)$$

With reference to a node *i*, when all of the associated element and applicable boundary contributions are assembled appropriately, the resulting discretized *z*-momentum equation is obtained, and it can be cast in the following form:

$$a_{i,w} w_i^d = \sum_{nb} a_{nb,w} w_{nb}^d + b_{i,w} + (-d\bar{P}/dz)\mathrm{V}_i \quad (3.28)$$

3.3.7 Mass-Conserving Velocity Components in the Cross-Sectional Plane (x-y)

The discretized *x*- and *y*-momentum equations are first cast in the following forms:

$$\hat{u}_i^d = \{\sum_{nb} a_{nb,u} u_{nb}^d + b_{i,u}\} / a_{i,u} \; ; \; \hat{v}_i^d = \{\sum_{nb} a_{nb,v} v_{nb}^d + b_{i,v}\} / a_{i,v}$$
$$d_{i,u} = \mathrm{V}_i / a_{i,u} \; ; \; d_{i,v} = \mathrm{V}_i / a_{i,v} \tag{3.29}$$
$$u_i^d = \hat{u}_i^d + d_{i,u}\{-\overline{(\partial p / \partial x)}_{\mathrm{V}_i}^d\} \; ; \; v_i^d = \hat{v}_i^d + d_{i,v}\{-\overline{(\partial p / \partial y)}_{\mathrm{V}_i}^d\}$$

For the evaluation of cross-sectional mass fluxes within the element *123* in Figure 3.2 (a), u^m and v^m in the downstream plane are interpolated using the following equations:

$$(u^m)^d = \hat{u}_{lin.\ int.}^d + (d_u)_o\{-(\partial p / \partial x)_\Delta^d\} \; ; \; (v^m)^d = \hat{v}_{lin.\ int.}^d + (d_v)_o\{-(\partial p / \partial y)_\Delta^d\}$$
$$(d_u)_o = (d_{1,u} + d_{2,u} + d_{3,u})/3 \; ; \; (d_v)_o = (d_{1,v} + d_{2,v} + d_{3,v})/3$$
$$\hat{u}_{lin.\ int.}^d = \{\text{linear interpolation of nodal values to the point of interest within element}\} \tag{3.30}$$
$$\hat{v}_{lin.\ int.}^d = \{\text{linear interpolation of nodal values to the point of interest within element}\}$$

The element-based pressure gradient terms in this equation are related to the nodal values of the perturbation pressure using the linear interpolation function given in Eq. (3.17).

3.3.8 Discretized Equations for Perturbation Pressure

First, the integral mass conservation equation applied to the control volume surrounding nodes 1^u and 1^d in Figure 3.2 (b) is cast in the following form:

$$\left[\int_u^d \left\{\int_a^o \left(\rho u^m \vec{i} + \rho v^m \vec{j}\right).\vec{n} ds + \int_o^c \left(\rho u^m \vec{i} + \rho v^m \vec{j}\right).\vec{n} ds\right\} dz + \iint_{1aoc} \left\{(\rho w)^d - (\rho w)^u\right\} dxdy\right]$$
$$+\left[\text{Similar contributions from other elements associated with nodes } 1^u \text{ and } 1^d\right] \tag{3.31}$$
$$+\left[\text{Boundary contributions, if applicable}\right] = 0$$

The contribution of the element *123* in Figure 3.2 (a) to this equation is approximated as follows:

$$\left[\int_u^d \left\{\int_a^o \left(\rho u^m \vec{i} + \rho v^m \vec{j}\right).\vec{n} ds + \int_o^c \left(\rho u^m \vec{i} + \rho v^m \vec{j}\right).\vec{n} ds\right\} dz + \iint_{1aoc} \left\{(\rho w)^d - (\rho w)^u\right\} dxdy\right]$$
$$= \left\{-\rho_o \left(u_r^m (y_a - y_o) - v_r^m (x_a - x_o)\right) + \rho_o \left(u_t^m (y_c - y_o) - v_t^m (x_c - x_o)\right)\right\}^d \Delta z \tag{3.32}$$
$$+ \left\{(\rho_o w)_1^d - (\rho_o w)_1^u\right\} A_{1aoc}$$

Here, *r* and *t* are *midway* points on the control volume faces o-a and o-c in the element *123*, as shown in Figure 3.3 (a). Using the interpolation functions given in Eq. (3.30), this

element contribution is evaluated in terms of the nodal values of the perturbation pressure and cast in the following form:

$$\left[\int_u^d\left\{\int_a^o\left(\rho u^m\vec{i}+\rho v^m\vec{j}\right).\vec{n}ds+\int_o^c\left(\rho u^m\vec{i}+\rho v^m\vec{j}\right).\vec{n}ds\right\}dz+\iint_{1aoc}\left\{(\rho w)^d-(\rho w)^u\right\}dxdy\right] \quad (3.33)$$
$$=C_1^{p,1}p_1^d+C_1^{p,2}p_2^d+C_1^{p,3}p_3^d+D_1^p+\left\{(\rho_o w)_1^d-(\rho_o w)_1^u\right\}A_{1aoc}$$

With reference to a node *i*, expressions analogous to that presented in this equation are derived for each element and appropriately assembled, along with any applicable boundary contributions, in accordance with Eq. (3.31). The result is then suitably rearranged to obtain the following form of the complete discretized equation for the perturbation pressure p_i^d:

$$a_{i,p}p_i^d=\sum_{nb}a_{nb,p}p_{nb}^d+b_{i,p} \quad (3.34)$$

3.3.9 Discretized Equation for the Axial Gradient of the Cross-Sectional Average Pressure

First, the z-momentum equation is cast in the following form:

$$\hat{w}_i^d=\{\sum_{nb}a_{nb,w}w_{nb}^d+b_{i,w}\}/a_{i,w}\quad;\quad d_{i,w}=\mathrm{V}_i/a_{i,w}\quad;\quad w_i^d=\hat{w}_i^d+d_{i,w}\{-d\overline{P}/dz\} \quad (3.35)$$

Then, in each slab of the duct of interest, with reference to the element *123* in Figure 3.2 (a), the overall mass conservation equation, Eq. (3.8), is approximated as follows:

$$\dot{m}_{specified}=\int_{A_{c-s}}\rho w dA_{c-s}=\text{constant}$$
$$=\sum_{\substack{All\ elements\\ in\ c-s}}\rho_o^d\left\{\frac{\hat{w}_1+\hat{w}_2+\hat{w}_3}{3}\right\}^d A_{123} \quad (3.36)$$
$$+(-\frac{d\overline{P}}{dz})\left[\sum_{\substack{All\ elements\\ in\ c-s}}\rho_o^d\left\{\frac{d_1^w+d_2^w+d_3^w}{3}\right\}^d A_{123}\right]$$

Using this equation, for a specified mass flow rate, the value of the axial gradient of the cross-sectional average pressure at each axial step can be expressed as follows:

$$\frac{d\overline{P}}{dz} = -\left[\frac{\dot{m}_{specified} - \sum_{\substack{All\ elements \\ in\ c-s}} \rho_o^d \left\{ \frac{\hat{w}_1 + \hat{w}_2 + \hat{w}_3}{3} \right\}^d A_{123}}{\sum_{\substack{All\ elements \\ in\ c-s}} \rho_o^d \left\{ \frac{d_1^w + d_2^w + d_3^w}{3} \right\}^d A_{123}} \right] \tag{3.37}$$

Finally, the value of $\overline{P}^d$ is given by the following equation:

$$\overline{P}^d = \overline{P}^u + (d\overline{P}/dz)\Delta z \tag{3.38}$$

3.3.10 Solution of the Discretized Equations

At each axial step, a sequential iterative variable adjustment procedure (SIVA), patterned after the one proposed by Saabas and Baliga (1994), is used to solve the nonlinear coupled sets of discretized equations for u, v, w, p, $d\overline{P}/dz$, and ϕ. This procedure is summarized below:

1. Set the values of u, v, w, p, and ϕ at the downstream location to the corresponding upstream values: $u^d = u^u$, $v^d = v^u$, $w^d = w^u$, $p^d = p^u$, and $\phi = \phi^u$. Set $d_u = 0$, $d_v = 0$, $\hat{u}^d = u^u$, $\hat{v}^d = v^u$, $(u^m)^d = u^u$, and $(v^m)^d = v^u$ at *all* nodes.

2. Calculate property values at the downstream nodes: ρ^d, μ^d, and Γ_ϕ^d.

3. Calculate coefficients in the discretized *z*-momentum equations; do not add the contributions of the axial gradient of the cross-sectional average pressure to the b_w terms, and do not under-relax these equations at this stage.

4. Calculate $\hat{w}^d$ using the latest available values of w^d; calculate and store values of d_w; and use these values along with the specified overall mass flow rate to calculate $(-d\overline{P}/dz)$.

5. Add the contributions of $(-d\overline{P}/dz)$ to the b_w terms in the discretized *z*-momentum equations; under-relax; and solve for $(w^d)_{calc}$.

6. Calculate the correction term $(d\overline{P}/dz)'$, using the right-hand side of Eq. (3.43) with $\hat{w}^d$ replaced by $(w^d)_{calc}$; and then calculate $w^d = (w^d)_{calc} + d_w(-d\overline{P}/dz)'$: this

ensures that the w^d distribution satisfies the overall mass conservation requirement in each step of this overall iterative procedure.

7. Calculate coefficients in the discretized *x*-momentum equations; do not add perturbation pressure gradient contributions to the b_u terms, and do not under-relax these equations at this stage; store the center-point coefficients ($a_{i,u}$) and the constant terms ($b_{i,u}$).

8. Add the perturbation pressure gradient contributions to the b_u terms in the discretized *x*-momentum equations; under-relax; solve for u^d.

9. Calculate $\hat{u}^d$ and d_u, using the non-under-relaxed center-point coefficients and the constant terms stored in Step 6, and the latest available values of u^d.

10. Calculate coefficients in the discretized *y*-momentum equations; do not add perturbation pressure gradient contributions to the b_v terms, and do not under-relax these equations at this stage; store the center-point coefficients ($a_{i,v}$) and the constant terms ($b_{i,v}$).

11. Add the perturbation pressure gradient contributions to the b_v terms in the discretized *y*-momentum equations; under-relax; solve for v^d.

12. Calculate $\hat{v}^d$ and d_v, using the non-under-relaxed center-point coefficients and the constant terms stored in Step 9, and the latest available values of v^d.

13. Calculate coefficients in the discretized equations for the perturbation pressure; do not under-relax; solve these equations; and then store and use the *newly calculated* perturbation pressure values, $(p_{nc})^d$, in computations of the mass-conserving velocity components, $(u^m)^d$ and $(v^m)^d$.

14. Update the perturbation pressure field using under-relaxation as follows: $p^d = \alpha_p (p_{nc})^d + (1-\alpha_p)(p_{old})^d$.

15. Calculate coefficients, suitably under-relax, and sequentially solve the discretized equations for all other dependent variables (ϕ).

16. With the latest available values of u^d, v^d, w^d, p^d, and ϕ^d as the new guess values, return to Step 2, and repeat Steps 2-16 until suitable convergence criteria (which are specified by the user) are satisfied.

An implicit scheme proposed by Patankar (1980) is used to under-relax the discretized equations. Thus, for example, Eq. (3.26) is under-relaxed as follows:

$$\left(\frac{a_{i,\phi}}{\alpha_\phi}\right)\phi_i^d = \sum_{nb} a_{nb,\phi}\phi_{nb}^d + b_{i,\phi} + \left(\frac{1-\alpha_\phi}{\alpha_\phi}\right)a_{i,\phi}\phi_i^* \tag{3.39}$$

In this equation, α_ϕ is an under-relaxation parameter and ϕ_i^* is the latest available value of ϕ. Suitable values of this parameter for the various dependent variables should be established for each problem of interest by doing some exploratory preliminary computations. As a rough guide, the combination $\alpha_u = 0.7$, $\alpha_v = 0.7$, $\alpha_w = 0.7$, $\alpha_p = 0.9$, and $\alpha_\phi = 1.0$ has worked quite well.

In each of the overall iterations of the SIVA solution procedure, it is necessary to solve sets of linearized and decoupled discretized equations. If a line-by-line structured grid is used, these equations are solved using an iterative line-Gauss-Seidel method, akin to that discussed in Patankar (1980). If an unstructured grid is used, an iterative point-Gauss-Seidel method is used to solve these equations. Implementation of techniques to accelerate the convergence of these iterative linear equation solvers is highly recommended, especially for the solution of the discretized perturbation pressure equations. In particular, an additive-correction multigrid method with adaptive volume agglomeration, akin to that proposed by Elias et al. (1997), has been found to be very useful by Venditti and Baliga (1998).

At each axial step, the above-mentioned SIVA procedure was terminated when the following convergence criterion was satisfied: suitably normalized maximum residuals of the discretized equations for the dependent variable of interest are all less than or equal to 10^{-6}.

3.3.11 Automatic Selection of Axial Step-Size

In three-dimensional parabolic fluid flow and heat transfer problems, the dependent variables could change significantly and nonlinearly with the axial coordinate, *z*,

especially in the vicinity of the entrance region of the straight ducts, and they become progressively invariant or change linearly with z as the fully-developed region is approached. Typical variations with z of the maximum value of the axial velocity component, w_{max}, and a peripherally-averaged Nusselt number, Nu, are shown in Figures 3.4 (a) and (b), respectively. Thus, for computational efficiency, it is desirable to start with a very small value of the axial step-size, Δz, and adjust it appropriately in response to the relative changes of the dependent variables as the solution is advanced downstream. A procedure to automatically adjust Δz in this manner is described in this section.

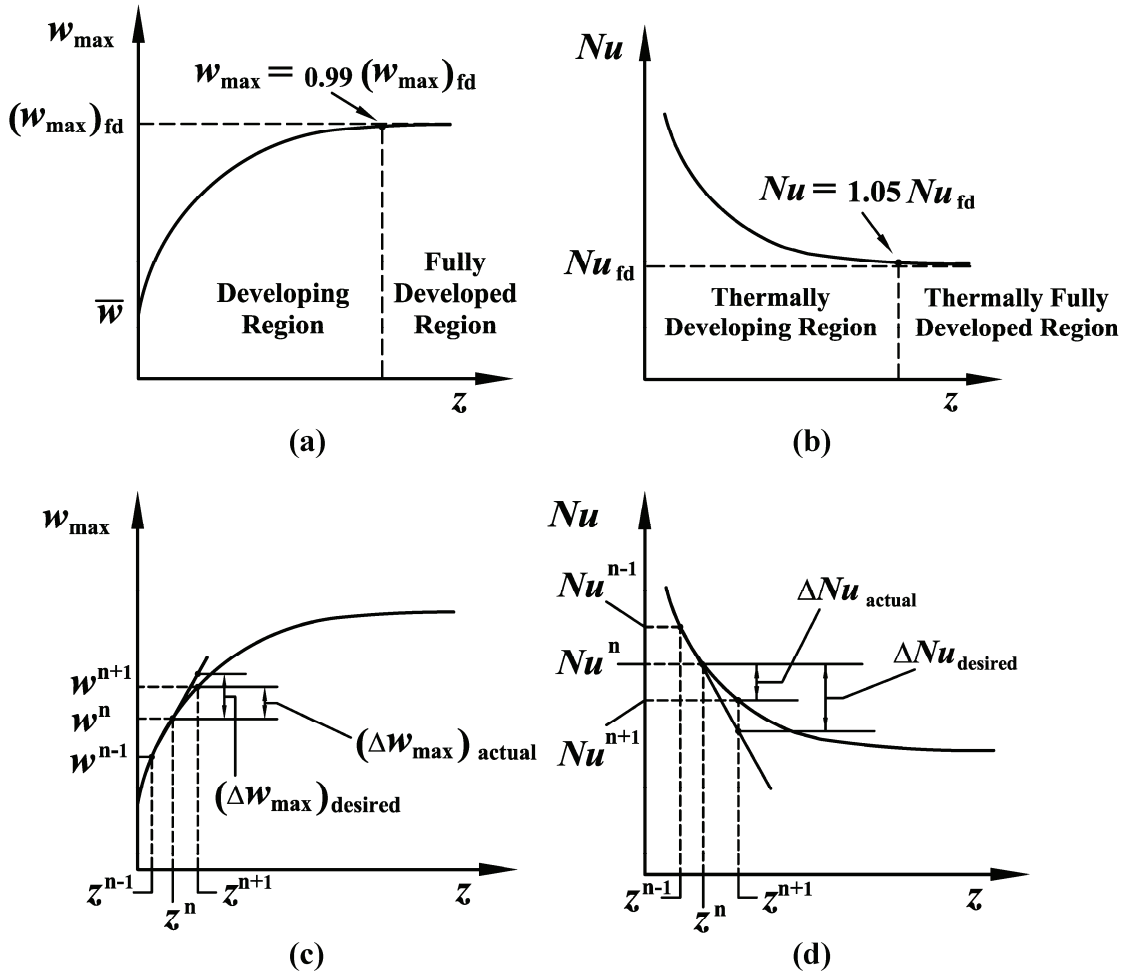

Figure 3.4: (a) Typical variation of w_{max} with z; (b) typical variation of peripherally-averaged Nusselt number, Nu, with z; (c) schematic illustration of the variables used in the automatic axial step-size selection procedure based on the axial variation of w_{max}; and (d) schematic illustration of the variables used in the automatic axial step-size selection procedure based on the axial variation of Nu.

Referring to Figures 4 (a) and (b), the desired changes in $w_{\max}$ and Nu are specified in terms of an ideal number of axial steps, *IDEAL*, as follows:

$$\left[\Delta w_{\max}\right]_{desired} = \frac{[w_{\max}]_{fd} - \overline{w}}{IDEAL} \quad ; \quad \left[\Delta Nu\right]_{desired} = \frac{Nu^{n=2} - [Nu]_{fd}}{IDEAL} \tag{3.40}$$

Here, it should be noted that $w_{\max}$ increases and Nu decreases with z, as shown in Figures 3.4 (a) and (b), respectively, and the subscript 'fd' indicates fully-developed values. The absolute values of the slopes ($dw_{\max}/dz$) and (dNu/dz) at the axial station z^n (n = 1 is the first axial station and it is coincident with the inlet plane) are approximated as follows, using the notation shown schematically in Figures 3.4 (c) and (d):

$$\left|\frac{dw_{\max}}{dz}\right| \simeq \frac{w_{\max}^n - w_{\max}^{n-1}}{z^n - z^{n-1}} \quad ; \quad \left|\frac{dNu}{dz}\right| \simeq \frac{Nu^{n-1} - Nu^n}{z^n - z^{n-1}} \tag{3.41}$$

Using linear extrapolation and the slopes given in Eq. (3.41), the axial step sizes required to produce the desired changes in $w_{\max}$ and Nu are calculated as follows:

$$\begin{aligned} [(\Delta z)^{w_{\max}}]^n &= (z^{n+1} - z^n)^{w_{\max}} = \left[\Delta w_{\max}\right]_{desired} \Big/ \left(\frac{w_{\max}^n - w_{\max}^{n-1}}{z^n - z^{n-1}} \right) \\ [(\Delta z)^{Nu}]^n &= (z^{n+1} - z^n)^{Nu} = \left[\Delta Nu\right]_{desired} \Big/ \left(\frac{Nu^{n-1} - Nu^n}{z^n - z^{n-1}} \right) \end{aligned} \tag{3.42}$$

As is illustrated in Figures 3.4 (c) and (d), for the problems considered here, the actual changes in $w_{\max}$ and Nu produced by the axial step sizes yielded by the expressions in Eq. (3.42) would be less than those desired: thus, these step sizes are conservative ones. However, as the fully-developed region is approached, Eq. (3.42) could give rise to undesirably large values of Δz, as the corresponding spatial rates of change of $w_{\max}$ and Nu with z are very small. This difficulty was avoided by adjusting $\left[\Delta w_{\max}\right]_{desired}$, $\left[\Delta Nu\right]_{desired}$, and Δz for $n > 3$ as follows:

$$\begin{aligned} [\Delta w_{\max}]_{desired}^n &= \min\left[[\Delta w_{\max}]_{desired}^{n-1}, \left\{ (w_{\max})_{fd} - w_{\max}^{n-1} \right\} \right] \\ [\Delta Nu]_{desired}^n &= \min\left[[\Delta Nu]_{desired}^{n-1}, \left\{ Nu^{n-1} - Nu_{fd} \right\} \right] \\ [\Delta z]^n &= \min\left[\left\{ [\Delta z]^n \text{ yielded by the expressions in equation (3.42)} \right\}, (\Delta z)_{\max} \right] \end{aligned} \tag{3.43}$$

In Eq. (3.43), $(\Delta z)_{\max}$ is a user-prescribed maximum axial step-size.

In the developing fluid flow and heat transfer problems of interest, the computations were stopped when the following conditions were satisfied:

$$w_{\max}^{n} \geq 0.99(w_{\max})_{fd} \quad ; \quad Nu^{n} \leq 1.05 Nu_{fd} \tag{3.44}$$

In the solution of the problems of interest, the computations were started by prescribing a very small value of Δz for the first axial step, and then initiating the above-mentioned automatic step-size selection procedure.

3.4 Application to a Test Problem and Results

3.4.1 Problem Statement

Steady, developing, laminar fluid flow and forced convection in a straight duct of square cross-section are considered in this test problem. The fluid is Newtonian, and its properties are assumed to be constant. The fluid flow is governed by Eqs. (3.1) to (3.4), (3.6) and (3.8); and the heat transfer is governed by Eq. (3.5). At the inlet plane, the following conditions apply: $w = w_{av}$; $u = v = 0$; and $T = T_i$. On the walls of the duct, $w = u = v = 0$. Two thermal boundary conditions on the walls are considered: (i) constant wall temperature (T); and (ii) uniform wall heat flux (H). The value of the Prandtl number was fixed at Pr = 0.72. This problem is relatively simple yet effective for validating the proposed method, especially because well-established analytical, experimental, and numerical results are available for it in the published literature.

3.4.2 Computational Details

The geometry of the duct is shown schematically in Figure 3.5(a). Taking advantage of the symmetry surfaces in the problem, the calculation domain was limited to one-quarter of the duct cross-section, shown by the hatched region in Figure 3.5(a). The cross-section of the calculation domain was discretized using a non-uniform line-by-line grid consisting of L1xM1 nodes, as shown in Figure 3.5 (b). The lines parallel to the *y* and *x* axes are indicated by the integers I and J, respectively. The positions of these lines was established by using the following equations for I = 1, 2, …, L1 and J = 1, 2, …, M1:

$$x(I,J) = [(I-1)/(L1-1)]^{Power} * (L/2) \quad ; \quad y(I,J) = [(J-1)/(M1-1)]^{Power} * (L/2) \tag{3.45}$$

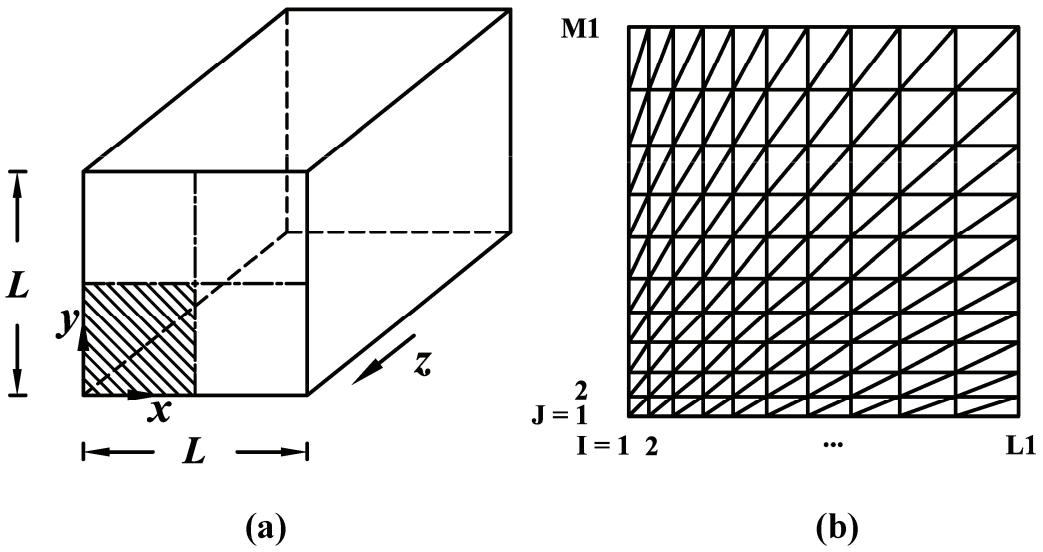

Figure 3.5: (a) Schematic representation of a straight duct of square cross-section, the calculation domain (the hatched region of the cross-section), and related notation; and (b) line-by-line discretization of the cross-section of the calculation domain into elements, and related notation.

3.4.3 Grid Checks

The effect of changing the number of grid lines in the cross-section (L1 and M1) and the value of *Power*, which determines their distribution, was assessed by calculating the product of the Darcy friction factor, f, the Reynolds number, Re_{D_h}, and the peripherally averaged Nusselt numbers, $Nu_{(T)}$ and $Nu_{(H)}$, all based on the hydraulic diameter, D_h:

$$f = \frac{(-d\bar{P}/dz)D_h}{0.5\rho w_{av}^2} \;\; ; \;\; Re_{D_h} = \frac{\rho w_{av} D_h}{\mu} \;\; ; \;\; D_h = \frac{4A_{c-s}}{Peri_{wetted}}$$

$$Nu_{(T)} = \frac{\bar{q}_w'' D_h}{(T_w - T_b)k} \;\; ; \;\; Nu_{(H)} = \frac{q_w'' D_h}{(\bar{T}_w - T_b)k} \;\; ; \;\; T_b = \frac{\int_{A_{c-s}} \rho w c_p T dA_{c-s}}{\int_{A_{c-s}} \rho w c_p dA_{c-s}} \qquad (3.46)$$

Here, w_{av} is the average axial velocity in the duct; $\bar{q}_w''$ is the peripherally-averaged wall heat flux in the (T) problems; $\bar{T}_w$ is the peripherally-averaged wall temperature in the (H) problems; T_b is the bulk temperature of the fluid; and k is the thermal conductivity of the fluid.

Table 3.1: Laminar Fluid Flow in a Straight Duct of Square Cross-Section - Grid Checks based on ($f \cdot Re_{D_h}$)fd.

L1 x M1	*Power*	$(f.Re_{D_h})_{\text{fd, computed}}$	$(f.Re_{D_h})_{\text{fd, analytical}}$	% Error
		Proposed Method	**Shah and London (1978)**	
11 x 11	1	57.146	56.908	0.42
11 x 11	1.2	57.093		0.33
11 x 11	1.4	57.092		0.32
11 x 11	1.6	57.107		0.35
11 x 11	1.8	57.133		0.40
11 x 11	2	57.160		0.44
15 x 15	1	56.991		0.15
15 x 15	1.2	56.969		0.11
15 x 15	1.4	56.976		0.12
15 x 15	1.6	56.991		0.15
15 x 15	1.8	57.003		0.17
15 x 15	2	57.023		0.20
19 x 19	1	56.890		0.01
19 x 19	1.2	56.901		0.01
19 x 19	1.4	56.912		0.01
19 x 19	1.6	56.923		0.03
19 x 19	1.8	56.941		0.06
19 x 19	2	56.952		0.08

For the duct of square cross-section shown in Figure 3.5 (a), $D_h = L$. For *fully-developed*, laminar, Newtonian fluid flow in a straight duct of square cross-section, it can be shown analytically that the product $f \cdot Re_{D_h}$ = 56.908 = constant, as discussed, for example, in Shah and London (1978). The fully-developed value of $f \cdot Re_{D_h}$ yielded by the proposed method for several different values of L1, M1, and *Power* are presented in Table 3.1: These results show that successive refinements of the grid systematically decrease the percentage error; for a grid of 19x19 nodes and *Power* = 1.4, the error in the computed value of $f \cdot Re_{D_h}$ is as low as 0.01%; for a fixed number of nodes, there is an optimum value of *Power* for which the percentage error is a minimum. The grid checks

for the corresponding thermal problems with the (T) and (H) wall boundary conditions are given in Table 3.2.

On the basis of the grid checks presented in Table 3.1 and Table 3.2, a cross-sectional grid of 11x11 nodes with *Power* = 1.4 was chosen for the final computations. The automatic axial step-size selector was used with an initial axial step-size of $\{[\Delta z]^{n=1} / (D_h Re_{D_h})\} = 10^{-7}$ and *IDEAL* = 25.

Table 3.2: Laminar Forced Convection in a Straight Duct of Square Cross-Section - Grid Checks base on $(Nu_{(T)})_{\text{fd.}}$

L1 x M1	*Power*	$(Nu_{(T)})_{\text{fd, computed}}$	$(Nu_{(T)})_{\text{fd, analytical}}$	% Error, $(Nu_{(T)})_{\text{fd}}$
		Proposed Method	**Shah and London (1978)**	
11 x 11	1.4	2.939	2.976	1.26
15 x 15	1.4	2.958		0.61
19 x 19	1.4	2.965		0.37

Table 3.3: Laminar Forced Convection in a Straight Duct of Square Cross-Section - Grid Checks base on $(Nu_{(H)})_{\text{fd.}}$

L1 x M1	*Power*	$(Nu_{(H)})_{\text{fd, computed}}$	$(Nu_{(H)})_{\text{fd, analytical}}$	% Error, $(Nu_{(H)})_{\text{fd}}$
		Proposed Method	**Shah and London (1978)**	
11 x 11	1.4	3.048	3.091	1.41
15 x 15	1.4	3.067		0.78
19 x 19	1.4	3.074		0.54

3.4.4 Variations of Cross-Sectional Average Pressure and Centerline Axial Velocity with Axial Distance

The variations with axial distance of dimensionless cross-sectional average pressure and dimensionless centerline axial velocity are shown graphically in Figures 3.6(a) and 3.6(b), respectively, along with the corresponding experimental results of Beavers et al. (1970) and Goldstein and Kreid (1967). In both these figures, the computed results yielded by the proposed method are in excellent agreement with the aforementioned experimental results.

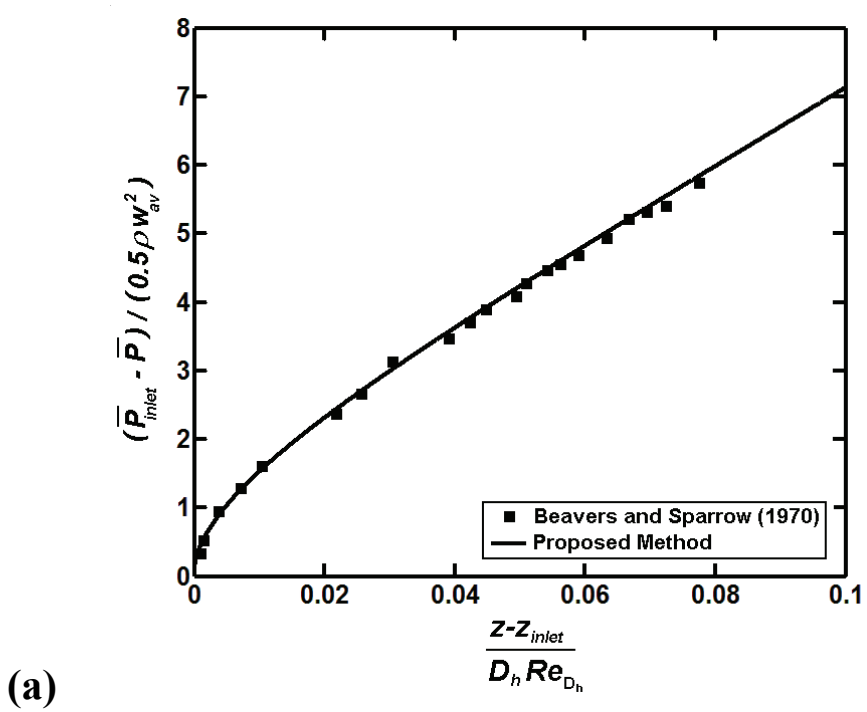

(a)

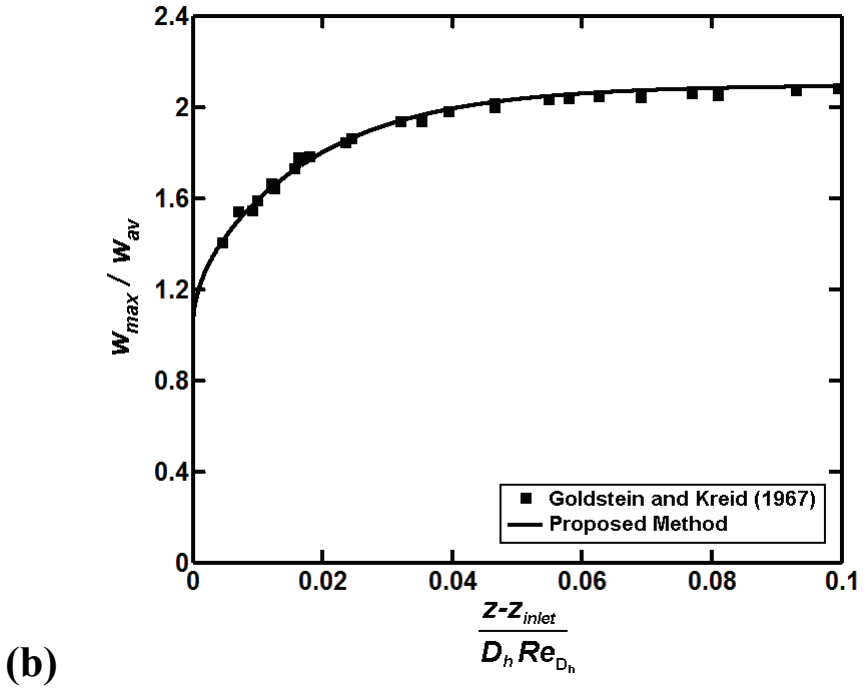

(b)

Figure 3.6: Developing laminar flow in a straight duct of square cross-section: variation with axial distance of (a) dimensionless cross-sectional average pressure; and (b) dimensionless centerline axial velocity.

3.4.5 Variations of Peripherally-Averaged and Mean Nusselt Numbers with Axial Distance for the (T) Thermal Boundary Condition

The peripherally-averaged Nusselt number, $Nu_{(T)}$, is defined in Eq. (3.46). The mean Nusselt number from the inlet plane to the axial location z for the (T) thermal boundary condition, $(Nu_{(T)})_m$, is defined below:

$$(Nu_{(T)})_m = \frac{1}{(z - z_{inlet})} \int_{z_{inlet}}^{z} Nu_{(T)} dz \tag{3.47}$$

The variations with axial distance of the peripherally-averaged and the mean Nusselt numbers, $Nu_{(T)}$ and $(Nu_{(T)})_m$, respectively, are presented in Figure 3.7. The computed results of Chandrupatla and Sastri (1978) for $(Nu_{(T)})_m$ are also shown in this figure. There is excellent agreement between the $(Nu_{(T)})_m$ results yielded by the proposed method and those of Chandrupatla and Sastri (1978) is excellent.

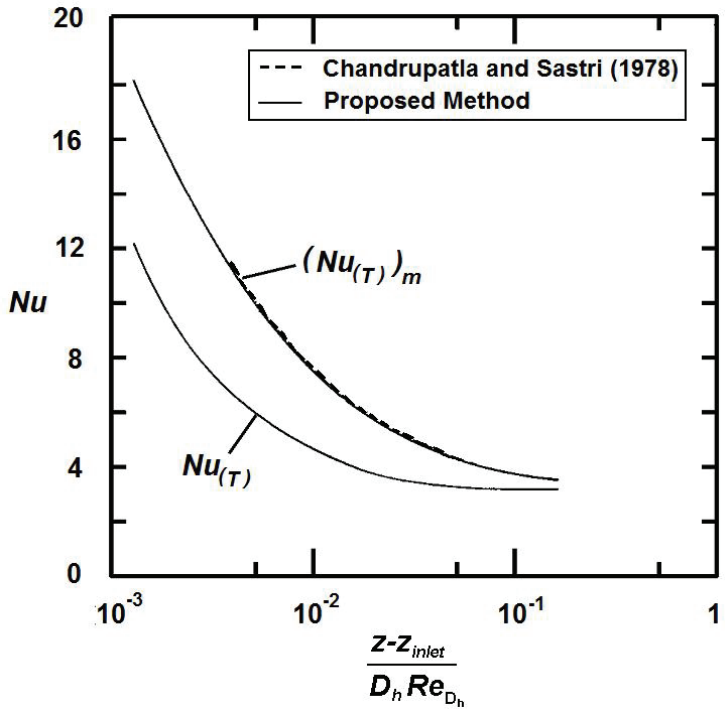

Figure 3.7: Developing laminar forced convection in a straight duct with square cross-section: variation with axial distance of $Nu_{(T)}$ and $(Nu_{(T)})_m$ for Pr = 0.72.

3.5. A FINITE VOLUME METHOD FOR THREE-DIMENSIONAL PARABOLIC FLOW AND HEAT TRANSFER IN STRAIGHT DUCTS OF RECTANGULAR CROSS-SECTION

A CVFEM for the prediction of three-dimensional parabolic fluid flow and heat transfer in straight ducts of uniform *regular- and irregular*-shaped cross-section was formulated and tested in earlier portions of this chapter. A simpler finite volume method (FVM) based on the methodology put forward in the aforementioned CVFEM is presented in this section. This FVM is specially adapted (and thus very cost-effective) for the solution of three-dimensional parabolic fluid flow and heat transfer in straight ducts of *rectangular* cross-section. As the full details of the CVFEM have already been presented in earlier sections of this chapter, only a succinct overview of the main features of the three-dimensional FVM is presented this section.

3.5.1 Rectangular Domain Discretization

The calculation domains considered in this section consist of straight uniform ducts of rectangular cross-section. Following a discretization process similar to the previously formulated CVFEM, the calculation domain is first segmented into a series of contiguous slabs perpendicular to the z-axis: each slab encompasses the region between two adjacent parallel cross-sectional planes, one upstream and the other downstream. These slabs need not have the same thickness (axial step-size, Δz).

Next, each cross-sectional (x-y) plane of the duct is first discretized into contiguous rectangular control volumes that fill the domain exactly. Then, nodes or grid points are located at the geometric centers of the control volumes. These grid points or nodes lie on lines that are parallel to the coordinate axes, and these grid lines could be non-uniformly spaced. This discretization of the rectangular duct cross-section and the associated nomenclature are illustrated in Figures 3.8 and 3.9, respectively.

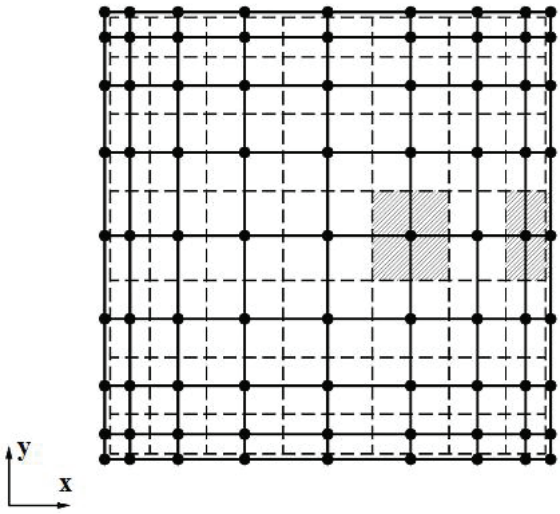

Figure 3.8: Discretization of a rectangular cross-section of the duct at each axial (z) location: dashed lines indicate control volume faces; solid dots indicate nodes or grid points; solid lines denote grid lines; and the hatched regions show two control volumes, one in the domain interior and the other adjacent to its boundary.

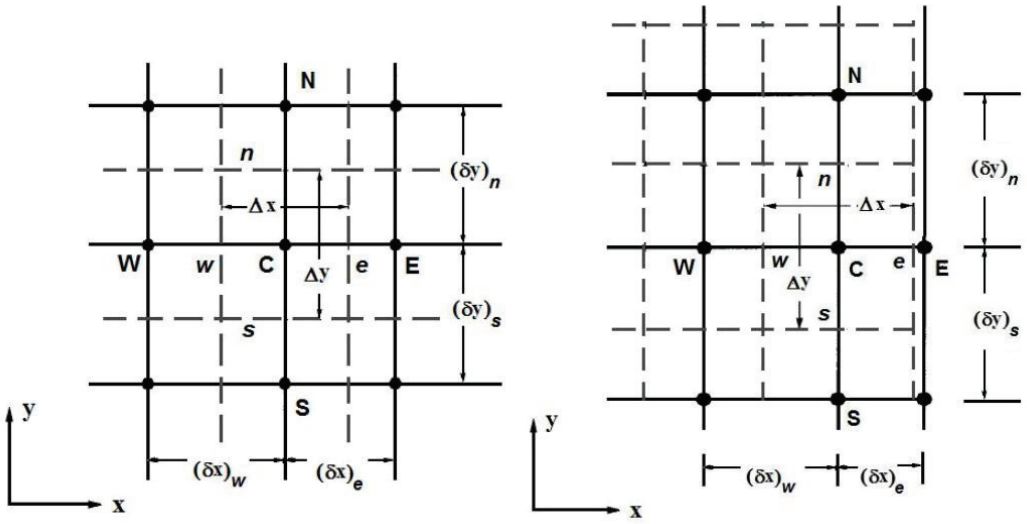

Figure 3.9: Cross-sectional grid and related nomenclature for (a) a node C located in the domain interior; and (b) a node C located adjacent to a boundary.

The boundaries of the cross-sectional control volumes associated with corresponding pairs of upstream and downstream nodes are joined to form rectangular parallelepiped control volumes of extents Δx, Δy, and Δz in the x, y, and z coordinate directions, respectively as shown in Figure 3.10. All dependent variables and the fluid thermophysical

properties are stored at the same set of nodes (co-located formulation) in the upstream (z) and downstream (z + Δz) cross-sections.

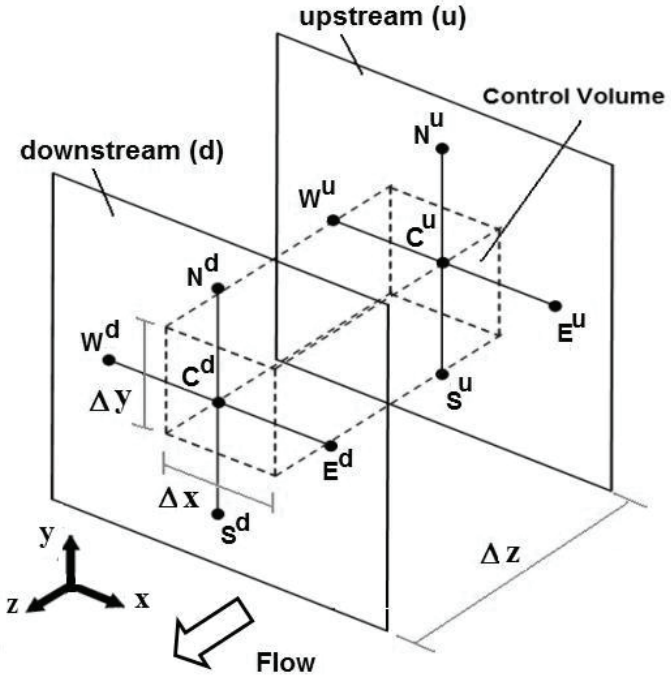

Figure 3.10: Formation of a rectangular parallelepiped control volume with corresponding pairs of upstream and downstream nodes, and related notation.

3.5.2 Discretization of the Conservation Equations

The governing differential equations, Eqs. (3.1) - (3.5), are first integrated over the control volumes, such as the one shown in Figure 3.10, and then cast in the following form with respect to a specific (per unit mass) scalar dependent variable ϕ:

$$\int_u^d \left\{ \int_s^n \left[\left(J_x\right)_e - \left(J_x\right)_w \right] dy + \int_w^e \left[\left(J_y\right)_n - \left(J_y\right)_s \right] dx \right\} dz + \int_s^n \int_w^e \left[\left(\rho w \phi\right)_d - \left(\rho w \phi\right)_u \right] dx dy - \int_u^d \int_s^n \int_w^e S_\phi dx dy dz = 0 \tag{3.48}$$

In this equation, S_ϕ is a volumetric source term associated with ϕ; indices w, e, s, n, u, and d correspondingly refer to the west-, east-, south-, north-, upstream- and downstream-faces of the rectangular parallelepiped control volume based on the nomenclature

presented in Figures 3.9 and 3.10; and J_x and J_y are the (advection + diffusion) fluxes of ϕ in the *x* and *y* directions, respectively:

$$J_x = J_{Advec,x} + J_{Diff,x} = \rho u\phi - \Gamma_\phi \frac{\partial \phi}{\partial x} \text{ and } J_y = J_{Advec,y} + J_{Diff,y} = \rho v\phi - \Gamma_\phi \frac{\partial \phi}{\partial y} \qquad (3.49)$$

In Eq. (3.49), Γ_ϕ is the diffusion coefficient associated with ϕ.

In the derivation of these discretized equations, the x- and *y*-direction advection and diffusion transport terms are discretized using the hybrid scheme [Patankar (1980)]. This scheme is second-order accurate at low velocities (strictly, at grid Peclet number values less than 2) and uniform grids; a second-order quadratic interpolation is used at the cross-sectional boundaries, and appropriately adjusted to incorporate the specified boundary conditions [Baliga and Atabaki (2006)].

The reduced perturbation pressure, p, in the cross-sectional (x-y) plane is interpolated using piecewise-linear functions between the nodes. In the mass flow rate terms, the *u* and *v* velocity components are interpolated using the so-called momentum interpolation scheme [Rhie and Chow (1983)], to avoid undesirable checkerboard-type pressure and velocity distributions that would otherwise afflict this equal-order co-located FVM [Patankar (1980)]. In this work, the fluid properties ρ, μ, c_p, and k are assumed to be essentially constant for each case of interest. In the main-stream (z) direction, a fully-implicit discretization scheme is used [Patankar (1980)] at each axial step, Δz.

Following the recommendations of Patankar (1980), the source term is linearized, if required, as follows: $S_\phi = (S_C)_\phi + (S_P)_\phi \phi$.

The algebraic approximations to the integral conservation equations are derived using the above-mentioned interpolation functions for the dependent variable (ϕ) the corresponding fluid properties (ρ and Γ_ϕ) and the source term (S_ϕ).

The final algebraic approximation is rearranged to obtain the following form of the discretized equation for ϕ_C:

$$
\begin{aligned}
&a_C^\phi \phi_C = a_E^\phi \phi_E + a_W^\phi \phi_W + a_N^\phi \phi_N + a_S^\phi \phi_S + b^\phi \\
&a_E^\phi = D_e^\phi \, A\left(\left|Pe_e^\phi\right|\right) + Max\left(-F_e, 0\right) \;\; ; \;\; a_W^\phi = D_w^\phi A\left(\left|Pe_w^\phi\right|\right) + Max\left(F_w, 0\right) \\
&a_N^\phi = D_n^\phi \, A\left(\left|Pe_n^\phi\right|\right) + Max\left(-F_n, 0\right) \;\; ; \;\; a_S^\phi = D_s A\left(\left|Pe_s^\phi\right|\right) + Max\left(F_s, 0\right) \\
&b^\phi = (S_c)_\phi \Delta x \Delta y \Delta z + \left(\rho w \phi_C\right)_u \Delta x \Delta y \\
&a_C^\phi = a_E^\phi + a_W^\phi + a_N^\phi + a_S^\phi - \left(S_P\right)_\phi \Delta x \Delta y \Delta z + \left(\rho w\right)_d \Delta x \Delta y + \left(F_e - F_w + F_n - F_s\right) \\
&\Rightarrow a_C^\phi = a_E^\phi + a_W^\phi + a_N^\phi + a_S^\phi + \left(\rho w\right)_u \Delta x \Delta y - \left(S_P\right)_\phi \Delta x \Delta y \Delta z \\
&\qquad + \left(F_e - F_w + F_n - F_s\right) + \left[\left(\rho w\right)_d - \left(\rho w\right)_u\right] \Delta x \Delta y
\end{aligned}
\tag{3.50}
$$

In the above equation, the grid-related diffusion conductances, D, the mass flow rates, F, and the Peclet numbers, Pe, are given by the following expressions, with respect to the notation in Figures 3.9 and 3.10:

$$
\begin{aligned}
&D_e^\phi = \Gamma_{\phi,e} \Delta y \Delta z / (\delta x)_e \;\; ; \;\; D_w^\phi = \Gamma_{\phi,w} \Delta y \Delta z / (\delta x)_w \\
&D_n^\phi = \Gamma_{\phi,n} \Delta x \Delta z / (\delta y)_n \;\; ; \;\; D_s^\phi = \Gamma_{\phi,s} \Delta x \Delta z / (\delta y)_s \\
&F_e = (\rho u)_e \Delta y \Delta z \qquad ; \;\; F_w = (\rho u)_w \Delta y \Delta z \\
&F_n = (\rho v)_e \Delta x \Delta z \qquad ; \;\; F_s = (\rho v)_s \Delta x \Delta z \\
&Pe_e^\phi = F_e / D_e^\phi \qquad ; \;\; Pe_w^\phi = F_w / D_w^\phi \\
&Pe_n^\phi = F_n / D_n^\phi \qquad ; \;\; Pe_s^\phi = F_s / D_s^\phi
\end{aligned}
\tag{3.51}
$$

In the hybrid scheme, the function $A\left(\left|Pe_\beta^\phi\right|\right)$ is given by the following equation [Patankar (1980)]:

$$
A\left(\left|Pe_\beta^\phi\right|\right) = Max\left[0, 1 - 0.5\left|Pe_\beta^\phi\right|\right] \tag{3.52}
$$

It should also be noted that when the solution is fully converged, continuity requirements are satisfied for each control volume and $(F_e - F_w + F_n - F_s) + \left[\left(\rho w\right)_d - \left(\rho w\right)_u\right] \Delta x \Delta y = 0$.

3.5.3 Solution of the Discretization Transport Equations

To advance the solution from an upstream cross-section at z to the next downstream cross-section at $z + \Delta z$, an overall sequential iterative solution procedure was used to solve the nonlinear coupled discretized equations. This procedure incorporates elements of the sequential iterative variable adjustment (SIVA) procedure proposed by Saabas and Baliga (1994) and the semi-implicit method for pressure-linked equations revised (SIMPLER) of Patankar (1980). In each overall iteration of this procedure, decoupled and

linearized sets of the discretized equations for u, v, w, p, and φ were solved iteratively using a line-Gauss-Seidel method [Sebben and Baliga (1995)], and $(-d\bar{P}/dz)$ was calculated using the overall mass flow rate balance requirement given in Eq. (3.8). Full details of this iterative solution method are summarized in section 3.3.10 of this chapter and also provided in the work of Jesuthasan and Baliga (2009b). The discretized equations for u, v, p, and φ were under-relaxed using an implicit scheme proposed by Patankar (1980), with the following under-relaxation factors: $\alpha_u = \alpha_v = 0.8$, $\alpha_p = 0.9$, and $\alpha_\varphi = 1.0$; no under-relaxation was used or necessary in the solution of the discretized equations for w and $(-d\bar{P}/dz)$. At each axial step, convergence of the aforementioned overall sequential iterative solution procedure was assumed to be achieved when suitably normalized absolute residues of the discretized equations for the dependent variables were all less than 10^{-6}.

3.6. SUMMARY

A control volume finite element method (CVFEM) for the prediction of three-dimensional parabolic fluid flow and heat transfer in straight ducts of *uniform regular*- and *irregular*-shaped cross-sections was first presented and discussed in this chapter. The method has the following novel features: a formulation based on *extensions* and amalgamation of ideas put forward in a seminal staggered-Cartesian-grid three-dimensional parabolic finite-volume method proposed by Patankar and Spalding (1972) and a co-located equal-order planar two-dimensional elliptic control-volume finite element method discussed by Baliga and Atabaki (2006); a step-by-step marching solution procedure in which the non-linear coupled discretized equations are solved at each axial step using an adaptation of a sequential iterative variable adjustment scheme (SIVA) proposed earlier by Saabas and Baliga (1994); and a computationally efficient automatic axial step-size selection procedure. The proposed method was applied to a relatively simple but effective test problem that involved developing laminar fluid flow and forced convection in a straight duct of square cross-section. The results obtained were checked against some well-established analytical, experimental, and numerical results available in the published literature [Shah and London

(1978); Goldstein and Kreid (1967); Beavers and Sparrow (1970); and Chandrupatla and Sastri (1978)]: the agreement between the various results was uniformly excellent, indicating the validity of the formulation and the successful implementation of the proposed numerical method.

Following that, the methodology put forward in the proposed CVFEM was adapted to formulate a simpler finite volume method (FVM), particularly well suited for predictions of three-dimensional parabolic fluid flow and heat transfer in straight ducts of *rectangular* cross-section. This FVM is used in the next chapter to study fluid flow and heat transfer phenomena in the rectangular vapor grooves of LHP evaporators. Based on this study, novel correlations for reliable and cost-effective calculations of the overall pressure drop and bulk temperature of the vapor in these grooves are proposed.

Chapter 4:

Modeling Laminar Flow and Heat Transfer in Rectangular Vapor Grooves of Evaporators used in Loop Heat Pipes

The modeling of steady laminar flow and heat transfer in straight rectangular vapor grooves machined into the metallic walls of flat evaporators used in LHPs, akin to that shown in Figure 2.1(b) and illustrated once more (for convenience) in Figure 4.1, is the main focus of this chapter. The problems of interest involve a straight rectangular duct with one end blocked, and inflow of vapor from the bottom lateral surface with an injection velocity, v_{inj}, and temperature, T_{inj} , as shown schematically in Figure 4.2.

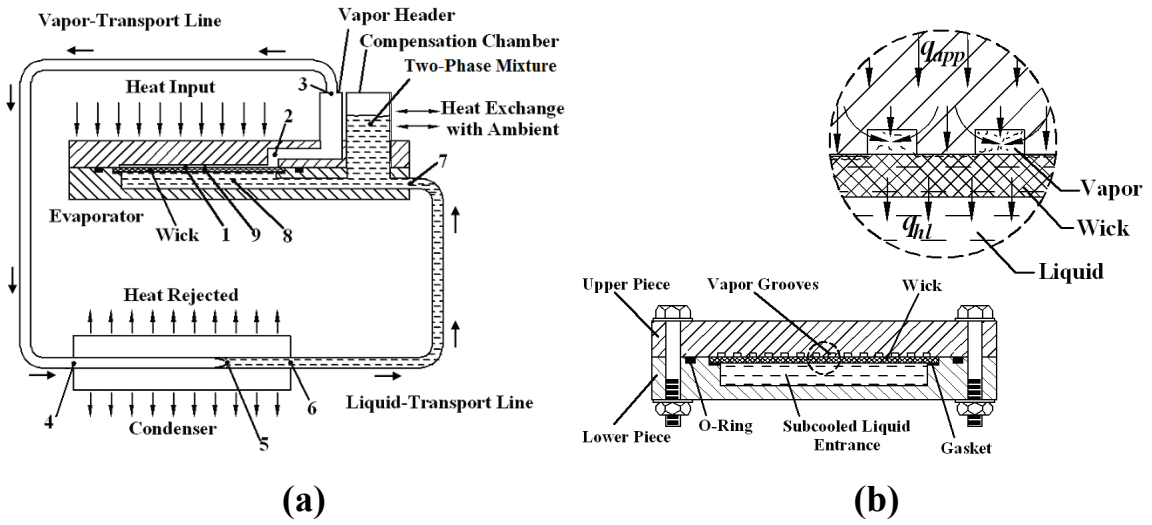

Figure 4.1: (a) schematic representation (not to scale) of a loop heat pipe with a flat evaporator; and (b) details of a cross-section of the flat evaporator.

As was mentioned earlier in Chapter 2, in available quasi-one-dimensional models of LHPs, for example, in the works of Kaya and Hoang (1999), Ghajar and Darabi (2005), Maydanik (2005), Atabaki (2006), Atabaki et al. (2007), Bai et al. (2009b), and Singh et al. (2009), and also in a recent quasi three-dimensional model of heat transfer in an LHP evaporator with a fully-saturated wick [Li and Peterson (2011)], the pressure drops for vapor flowing through grooves in the metallic walls of the evaporator are computed using a friction-factor correlation that applies strictly only in the fully-developed region of fluid

flows in straight rectangular ducts with impermeable walls. This approach is inapplicable or ad hoc, at best, and the resulting errors can become serious if the pressure drop in the vapor grooves is a significant contributor to the overall pressure drop in the LHP. Thus, more accurate correlations for predicting the pressure drop in the vapor grooves are needed. There is also a need for correlations for calculating the bulk temperature of the vapor as it leaves the vapor grooves and enters the vapor header of the evaporator. The work reported in this chapter addresses these needs.

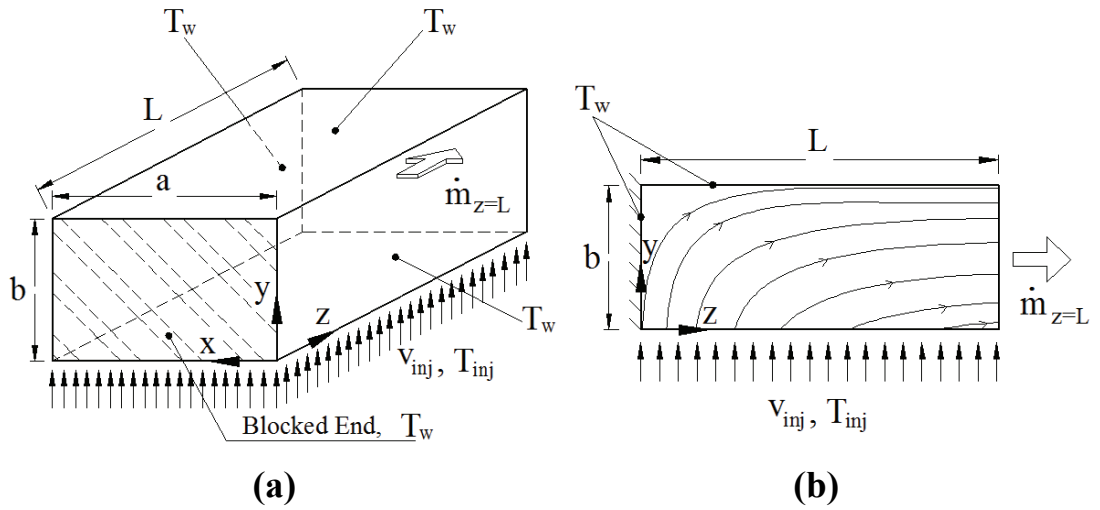

Figure 4.2: (a) schematic representation of vapor flow in rectangular grooves of a flat evaporator of an LHP; (b) cross-sectional (y-z plane) view of this flow.

In the published literature, there are many papers related to steady laminar flow and heat transfer in straight ducts with an inlet velocity imposed at one end, blowing or suction along one or more lateral surfaces, a variety of thermal boundary conditions, and an outflow condition at the other end: examples include the works of Berman (1953), Taylor (1956), Yuan and Finkelstein (1958), Kinney (1968), Bundy and Weissberg (1970), Pederson and Kinney (1971), Raithby (1971), Raithby and Knudsen (1974), Rhee and Edwards (1981), Ku and Leidenfrost (1981), Hwang et al. (1993), Cheng et al. (1994), and Beale (2005). The fluid flows investigated in these papers are different from the vapor flows of interest in which, as shown schematically in Figure 4.2, one end of the rectangular duct is blocked (there is no inlet velocity at this end). Nevertheless, beyond a sufficient distance downstream of the inlet plane in the fluid flow problems investigated

by Hwang et al. (1993) and Cheng et al. (1994), and the blocked end in the problems of interest ($z = 0$ in Figure 4.2), the flows become fully developed (for the case of uniform injection on the bottom wall) and essentially similar (details of this fully-developed region will be elaborated later in this chapter). However, Hwang et al. (1993) and Cheng et al. (1994) reported values and correlations for only cross-sectional average skin-friction coefficient (akin to the Fanning friction factor, based on the cross-sectional average wall shear stress), and those results cannot be used for computing the overall pressure drops in the vapor grooves of interest in this work. The thermal boundary conditions considered by Hwang et al. (1993) and Cheng et al. (1994), namely, constant heat flux at the bottom wall, adiabatic conditions at the other walls, and a uniform fluid temperature at the inlet plane of the duct, are also different from those that are relevant to the problems investigated in this work. Yuan et al. (2001) have investigated fully-developed laminar flow and heat transfer in fuel cell ducts with different rectangular and trapezoidal cross-sections. However, they seem to have ignored cross-stream velocities in the fully-developed region, considered only relatively low values of an injection (or suction) Reynolds number (magnitude of 2.5 and lower, which may be adequate for fuel cells, but not for LHP applications), reported only fanning friction factor values (based on the average shear stress on the walls), and used thermal boundary conditions different from those considered here. Thus, their results too are not directly applicable for the vapor flows and heat transfer phenomena investigated in this work.

There are also many published papers on vapor flows in heat pipes: examples include the works of Busse (1973), Tien and Rohani (1974), Chen and Faghri (1990), and Leong et al. (1996). However, in heat pipes, both ends of the core vapor-flow passage are blocked, with blowing (inflow) and suction (outflow) along portions of the lateral surface of this passage, and these boundary conditions are not the same as those in the vapor grooves of LHP evaporators.

Detailed studies aimed at elucidating the fluid flow, heat transfer, and liquid-vapor phase-change phenomena in the wick, forced convection in the vapor grooves, and conjugate heat conduction in the body of LHP evaporators have been presented in Cao and Faghri (1994), Figus et al. (1999), Kaya and Goldak (2006), Ren et al. (2007), Chernysheva and Maydanik (2008), Li and Peterson (2011), and Ren (2011). While these

studies have enhanced the understanding of the physics of the aforementioned transport phenomena, they do not provide information or correlations that can been directly used to enhance available cost-effective quasi one-dimensional models of LHPs.

In this work, the three-dimensional parabolic finite volume method (FVM) put forward in Chapter 3 is used to simulate laminar, steady, Newtonian fluid flow and heat transfer in straight rectangular passages akin to that shown schematically in Figure 4.2, for parameter ranges representative of LHP operating conditions. The goal is not only to enhance the understanding of the fundamental aspects of such transport phenomena, but also to provide correlations that can be used to improve current quasi one-dimensional models of LHPs. The corresponding mathematical models, numerical solution method, results, and correlations for dimensionless pressure drop and bulk temperature of the vapor are presented and discussed in the following sections of this chapter.

4.1 MATHEMATICAL MODELS

Mathematical models of the steady vapor flow and heat transfer phenomena schematically depicted in Figures 4.1 and 4.2 are presented in this section. The assumptions invoked in these models are presented first. Next, three-dimensional elliptic and parabolic approaches to the formulation of such models, their applicability to the flows of interest, and related issues are discussed concisely. Finally, the three-dimensional parabolic forms of the governing equations and boundary conditions are presented in suitable dimensionless forms, along with related comments.

4.1.1 Assumptions

The vapor is assumed to be a Newtonian fluid. Its density, dynamic viscosity, specific heat at constant pressure, and thermal conductivity for each case (or combination of parameters) of interest are evaluated at average values of the absolute pressure and the bulk temperature, and assumed to prevail (remain constant) over the whole flow passage (see Figure 4.2) for that case.

For the range of operating conditions of the LHPs considered in this work, the maximum value of Reynolds number, based on the hydraulic diameter of the grooves in the evaporator and the maximum value of the mean vapor velocity (which occurs at the

exit plane of the flow passage), is 2000 or lower. So it is assumed that the vapor flows of interest remain laminar throughout their passage through the grooves.

With respect to the thermal problem, the upper-half of the metallic body of the flat evaporator, in which the rectangular vapor grooves are cut (see Figure 4.1), has relatively high thermal conductance: thus, for each value of the specified rate of heat input (q_{app}), the corresponding steady-state value of the temperature of the impermeable walls of the vapor groove (indicated by T_w in Figure 4.2) is essentially constant. For detailed discussions of the liquid-vapor phase-change processes in the wick, the readers are referred to the works of Cao and Faghri (1994), Figus et al. (1999), Kaya and Goldak (2006), Li and Peterson (2011), and Ren (2011). Here, it should be noted that the total pressure *drop* in the vapor grooves is typically a small fraction of the average *absolute* pressure in these grooves. Thus, for each case of interest, the corresponding values of the saturation temperature, T_{sat}, at the liquid-vapor interface and the temperature difference ($T_w - T_{sat}$) that drives the liquid-vapor phase-change process in the wick are assumed to be essentially constant. It is also assumed that the viscous dissipation and compression work terms in the energy equation can be ignored (because values of the Eckert number are all much smaller than one), and compressibility effects are negligible (because values of the Mach number are all less than 0.1).

In the context of the above-mentioned assumptions, and keeping in mind that one of the key objectives of this work is to generate relatively simple and effective correlations that are suitable as inputs to practical quasi-one-dimensional models of LHPs (similar to the one put forward in Chapter 2), the injection velocity and temperature of the vapor entering the groove through its bottom surface (see Figure 4.2), v_{inj} and $T_{inj} \simeq T_{sat}$, respectively, are considered to be essentially uniform for each case of interest.

4.1.2 Overview of Elliptic and Parabolic Approaches, their Applicability, and Related Issues

In the region adjacent to the blocked end of the rectangular vapor groove (the x-y surface or plate at $z = 0$ in Figure 4.2), though the overall fluid flow is in the positive z direction and the cross-sectional-average value of the z-direction velocity component, w_{av}, increases with the axial coordinate, z, a zone of recirculating fluid flow can be

established next to the upper surface (y = b). In this region of the vapor groove, the velocity, pressure, and temperature fields are governed by the continuity equation, and the full three-dimensional, elliptic, forms of the Navier-Stokes and energy equations [White (1991)]. For the problems of interest, however, results of preliminary computer simulations based on these full forms of the governing equations for large values of the aspect ratio (AR = a/b $\to \infty$, so the fluid flow and heat transfer are essential two-dimensional, with negligible variations in the x direction) showed that the maximum z-extent of the aforementioned zone of recirculating flow is less than $0.1D_h$, where D_h = 4ab/{2(a+b)} is the hydraulic diameter of the rectangular vapor groove. The results of these preliminary computations also showed that for $z \geq 4D_h$, that is, sufficiently downstream of the aforementioned recirculating flow zone, the following conditions prevail: there exists a predominant fluid flow along the lengthwise (positive z) direction of the vapor groove, and no flow reversal is encountered in this direction; the rates of viscous and conduction transport in this mainstream (z) direction are negligible compared to the corresponding rates of advection transport and the rates of cross-stream viscous and conduction transport; and the influence of the downstream pressure field on the upstream flow conditions is negligible. Thus, for $z \geq 4D_h$, the steady vapor flow and heat transfer phenomena considered in this work can be characterized as three-dimensional parabolic, with corresponding significant simplifications of the governing equations, as discussed in the seminal work of Patankar and Spalding (1972) and also detailed in Chapter 3 of this thesis.

For large values of the aspect ratio, $AR = \text{a/b} \to \infty$, simulations of the essentially two-dimensional fluid flow and heat transfer phenomena of interest were undertaken using both elliptic and parabolic forms of the governing equations. The differences between the corresponding results of these two sets of simulations (some of which will be presented in subsequent sections), including those between cumulative results such as overall drop of cross-sectional-average reduced pressure ($\overline{P}_{z=0} - \overline{P}_z$) and increase in bulk temperature ($T_{b,z} - T_{b,z=0}$) of the vapor, became essentially imperceptible (negligibly small) for $z \geq 4D_h$. For finite (and with respect to LHP designs, practical) values of the aspect ratio, the extent of the above-mentioned zone of recirculating flow in the region

adjacent to the blocked end plate (at $z = 0$) would be comparable to that for $AR \to \infty$, considering the confining effects of the two vertical side walls (at $x = 0$ and $x = a$ in Figure 4.2): thus, the corresponding results produced by elliptic and parabolic models would become similar for $z \geq 4D_h$. In practice and also in several recent publications on LHPs [Chu et al. (2004); Ghajar et al. (2005); Bai et al. (2009a); Vasiliev et al. (2009); Lin et al. (2010)], values of the length-to-hydraulic-diameter ratio (L/D_h) of the vapor grooves lie in the range of about 6 to 190. Thus, even though the parabolic model cannot predict the relatively small zone of the recirculating flow (z-extent less than $0.1D_h$) in the region adjacent to the blocked end ($z = 0$) of the vapor groove, and it is not applicable to the flow and heat transfer in this recirculating zone, from a practical point of view, it can be used for satisfactory and computationally cost-effective predictions of the overall pressure drop and increase in bulk temperature over the full length of the vapor groove (L) in problems of interest. This approach was adopted in the investigation presented in this chapter. The governing equations of the parabolic model are reviewed in the next subsection.

4.1.3 Dimensionless Forms of Three-Dimensional Parabolic Governing Equations and Boundary Conditions

With reference to the Cartesian coordinate system and notation shown in Figure 4.2, the components of the velocity vector in the x, y, and z directions are denoted by u, v, and w, respectively. The temperature of the fluid is denoted by T. In the context of the assumptions discussed earlier, the mass density, ρ, the dynamic viscosity, μ, the specific heat at constant pressure, c_p, the thermal conductivity, k, the wall temperature, T_w, the injection velocity, v_{inj}, and the injection temperature, $T_{inj} = T_{sat}$, are uniform and constant for each case of interest.

The reduced pressure (static pressure minus the hydrostatic pressure) is denoted by P, and following the parabolic model proposed by Patankar and Spalding (1972), it is expressed in terms of its cross-sectional average value, $\overline{P}$, and a perturbation component about this average, p, as follows:

$$P(x,y,z) = \overline{P}(z) + p(x,y,z);\ \overline{P}(z) = \frac{1}{A_{c-s}} \int_{A_{c-s}} P(x,y,z)dxdy \tag{4.1}$$

In this equation, A_{c-s} is the cross-sectional area of the duct. Again following Patankar and Spalding (1972), it is assumed that $(\partial p/\partial z) << d\overline{P}/dz$, and the following approximation and expressions apply:

$$\partial P/\partial z \cong d\overline{P}/dz;\ \partial P/\partial x = \partial p/\partial x;\ \partial P/\partial y = \partial p/\partial y \tag{4.2}$$

At this stage, with reference to the Cartesian coordinate system and notation shown in Figure 4.2, the following dimensionless variables and parameters are introduced:

$$\begin{aligned}
&X = x/\mathrm{b};\ Y = y/\mathrm{b};\ Z = z/\mathrm{b};\ AR = a/\mathrm{b}\\
&U = u/v_{inj};\ V = v/v_{inj};\ W = w/v_{inj}\\
&p^* = p/(0.5\rho v_{inj}^2);\ \overline{P}^* = \overline{P}/(0.5\rho v_{inj}^2)\\
&\theta = (T - T_{inj})/(T_w - T_{inj})\\
&\mathrm{Re}_{inj} = \rho v_{inj}\mathrm{b}/\mu;\ \mathrm{Pr} = \mu c_p/k
\end{aligned} \tag{4.3}$$

Here, Re_{inj} is the injection Reynolds number based on the height of the vapor groove, b, and the injection velocity, v_{inj} (see Figure 4.2).

In the context of the above-mentioned assumptions and in terms of the dimensionless variables and parameters given in Eq. (4.3), the differential equations in the three-dimensional parabolic model of the laminar flow and heat transfer phenomena of interest can be cast in the following forms (note that the dimensional forms of these equations were presented earlier in Section 3.2, so they are not presented here):

Continuity:

$$\frac{\partial U}{\partial X} + \frac{\partial V}{\partial Y} + \frac{\partial W}{\partial Z} = 0 \tag{4.4}$$

x-momentum:

$$\frac{\partial}{\partial X}(UU) + \frac{\partial}{\partial Y}(VU) + \frac{\partial}{\partial Z}(WU) = -\frac{\partial p^*}{\partial X} + \frac{1}{\mathrm{Re}_{inj}}\left(\frac{\partial^2 U}{\partial X^2} + \frac{\partial^2 U}{\partial Y^2}\right) \tag{4.5}$$

y-momentum:

$$\frac{\partial}{\partial X}(UV) + \frac{\partial}{\partial Y}(VV) + \frac{\partial}{\partial Z}(WV) = -\frac{\partial p^*}{\partial Y} + \frac{1}{\mathrm{Re}_{inj}}\left(\frac{\partial^2 V}{\partial X^2} + \frac{\partial^2 V}{\partial Y^2}\right) \tag{4.6}$$

z-momentum:

$$\frac{\partial}{\partial X}(UW) + \frac{\partial}{\partial Y}(VW) + \frac{\partial}{\partial Z}(WW) = -\frac{d\overline{P}^*}{dZ} + \frac{1}{\mathrm{Re}_{inj}}\left(\frac{\partial^2 W}{\partial X^2} + \frac{\partial^2 W}{\partial Y^2}\right) \tag{4.7}$$

Energy:

$$\frac{\partial}{\partial X}(U\theta)+\frac{\partial}{\partial Y}(V\theta)+\frac{\partial}{\partial Z}(W\theta)=\frac{1}{\mathrm{Re}_{inj}\,\mathrm{Pr}}\left(\frac{\partial^2\theta}{\partial X^2}+\frac{\partial^2\theta}{\partial Y^2}\right) \tag{4.8}$$

In addition to Eqs. (4.4) to (4.8), an equation for the overall or total mass flow rate through the duct at each value of the main-stream coordinate (z) is needed and must be respected. With reference to the notation given in Figure 4.2, and with the assumption of uniform injection velocity, v_{inj}, this equation can be expressed in the following form:

$$\begin{aligned}&\dot{m}=\int_{A_{c-s}}\rho w dA_{c-s}=\rho(\mathrm{a}z)v_{inj}=\rho(\mathrm{ab})w_{av},\ \text{or}\\&W_{av}=w_{av}/v_{inj}=(z/\mathrm{b})=Z\end{aligned} \tag{4.9}$$

Equations (4.4) to (4.9) form a parabolic system in the main-stream coordinate direction, Z, with six unknowns, U, V, W, p^*, θ, and $(-d\bar{P}^*/dZ)$. To complete the mathematical description of the problem, the boundary conditions and the dimensionless parameters (AR, Re_{inj}, and Pr) must be specified. Once the problem description is completed, the parabolic model allows a marching solution procedure in the Z direction, so the solution can be advanced step-by-step along the duct, from $Z = 0$ to $Z = L/\mathrm{b}$, as was described earlier in Chapter 3 [Patankar and Spalding (1972); Jesuthasan and Baliga (2009b)].

In this work, with respect to the problem schematic given in Figure 4.2, and the dimensionless variables and parameters given in Eq. (4.3), the following boundary conditions apply:

$$\begin{aligned}&\text{At } X=0 \text{ and } X=AR,\ U=V=W=0,\ \theta=1\\&\text{At } Y=0,\ U=W=0,\ V=1,\ \theta=0\\&\text{At } Y=1,\ U=V=W=0,\ \theta=1\\&\text{At } Z=0,\ U=V=W=0,\ \theta=1,\ \bar{P}^*=\bar{P}^*_{ref}\\&\text{In each c-s, at } X=0.5AR \text{ and } Y=0.5,\ p^*=p^*_{ref}\end{aligned} \tag{4.10}$$

In the parabolic mathematical model, in the main-stream direction, boundary conditions are needed only at $Z = 0$. With respect to the boundary conditions on $\bar{P}^*$ and p^*, as the fluid density (ρ) is assumed to be essentially constant, the absolute value of the fluid pressure is immaterial, and only the drops in the fluid pressure (that drive the fluid flow) matter [Patankar (1980)]. In the proposed parabolic model, as is indicated in Eq. (4.10), the value

of $\overline{P}^*$ is assigned a suitable reference value ($\overline{P}^*_{ref}$) at $Z = 0$; and in each cross-section, p^* is assigned a suitable reference value (p^*_{ref}) at $X = 0.5AR$ and $Y = 0.5$. Considering that sintered porous metals of relatively low porosity (typically, 0.30 – 0.50) and small pore diameter (2.0 to 70 μm) are the materials of choice for the wick in LHPs, the following conditions were assumed to apply at the interface between the wick and the bottom surface of the vapor groove, $y = 0$, as shown in Figure 4.2: the velocity components tangential to this interface are zero; the normal component of the velocity is equal to the injection velocity (thus, $V = v/v_{inj} = 1$); and the temperature of the fluid is equal to the injection temperature (thus, $\theta = 0$). Thus, the dimensionless velocity components and temperature, defined in Eq. (4.3), respect the following conditions at $Y = 0$: $U = W = 0$, $V = 1$, and $\theta = 0$. In this context, it should also be noted that the so-called interfacial stress-jump and flux-jump conditions, which are often used to account for implied excess viscous and inertial stresses and heat fluxes that are caused if the porosity of the wick is assumed to be uniform right up to its interface with the open domain [Beavers and Joseph (1967); Ochoa-Tapia and Whitaker (1995); Nield and Bejan (2006)], are considered to have negligible effects in the problems of interest in this work.

4.2 NUMERICAL SOLUTION METHOD

4.2.1 Background

The co-located finite volume method (FVM) presented earlier in Chapter 3 was used to solve the three-dimensional parabolic mathematical model described in the previous section. Its formulation is closely related to that of the three-dimensional parabolic, co-located, control-volume finite element method (CVFEM) of Jesuthasan and Baliga (2009b). The full details of these numerical methods have already been presented in Chapter 3. So they are not presented again in this section. Rather, some notes on the verification of this FVM are presented in the next subsection.

4.2.2 Notes on Verification of the FVM

Before using the proposed three-dimensional parabolic FVM to investigate the fluid flow and heat transfer phenomena of interest, the computer program incorporating this FVM was verified by using it to solve several test problems and comparing the results to corresponding analytical, numerical, and experimental results available in the literature. Three most relevant of these test problems are presented and discussed in this section.

The proposed three-dimensional parabolic FVM was used to solve a problem studied earlier by Berman (1953). This problem involves laminar flow in a parallel-plate channel as shown schematically in Figure 4.3 (a): a parabolic velocity distribution (characteristic of Poiseuille flow in a parallel-plate channel) with an average value of $w_{av,\,inlet}$, is prescribed at its inlet plane; and uniform injection velocity, v_{inj}, is imposed on its top and bottom permeable walls. The following dimensionless parameters were investigated: $\mathrm{Re}_{inlet} = (\rho w_{av,inlet} H/\mu) = 1000$, and $\mathrm{Re}_{inj,\,H} = (\rho v_{inj} H/\mu) = 2$. With reference to the notation given in Figure 4.3 (a), the proposed three-dimensional FVM was used to solve this problem with the following uniform grids: $\Delta(x/H) = 1/(\mathrm{NX}-2)$, with NX = 5 and slip and impermeability conditions imposed at (x/H) = 0 and 1; $\Delta(y/H) = 1/(\mathrm{NY}-2)$, with NY = 22, 42, and 82; and $\Delta(z/H) = 0.050$, 0.025, and 0.0125. At each value of (z/H), the dimensionless cross-sectional reduced pressure drop, $(\overline{P}^{*}_{z=0} - \overline{P}^{*}) = \{(\overline{P}_{z=0} - \overline{P})/(0.5\rho v_{inj}^2)\}$, and dimensionless maximum z-direction velocity component, $(w/w_{av})_{max}$, computed using the proposed FVM, were compared to the corresponding results yielded by the perturbation solution proposed by Berman (1953). The agreement between these results was uniformly excellent. For example, the absolute differences between the essentially grid-independent values of $(\overline{P}^{*}_{z=0} - \overline{P}^{*})$ and $(w/w_{av})_{max}$ at (z/H) = 100 (obtained using the extrapolation technique proposed by Richardson (1910) and the computed results yielded by the proposed FVM with the two finest grids in the y and z directions) and the corresponding results of Berman (1953) were 0.37% and 0.33%, respectively.

In the next test, the proposed three-dimensional parabolic FVM was used to solve a problem studied earlier by Raithby (1971). This problem, which is an extension of the Berman (1953) problem discussed in the previous paragraph, involves laminar flow and heat transfer in a parallel-plate channel shown schematically in Figure 4.3 (b): uniform fluid

velocity and temperature, w_{inlet} and T_{inlet}, respectively, are prescribed at its inlet plane; uniform injection velocity, v_{inj}, is imposed on its top and bottom permeable walls; over an initial unheated length, $(L_{unheated}/H) = 50$, that is long enough to ensure full-developed fluid flow prevails at $z = 0$ (for $z \geq 0$, $w_{F.D.} / w_{av}$ is invariant with z, where w_{av} is the local cross-sectional average velocity component in the axial direction; additional details of this fully-developed flow are provided in Section 4.3), the injected fluid temperature is T_{inlet}; over the remainder of the permeable top and bottom walls ($z > 0$), the injected fluid temperature is $T_{inj} > T_{inlet}$. The following dimensionless parameters were investigated: $\mathrm{Re}_{inlet} = (\rho w_{inlet} H / \mu) = 1000$, $\mathrm{Re}_{inj,H} = (\rho v_{inj} H / \mu) = 10$, and $\mathrm{Pr} = 4.0$.

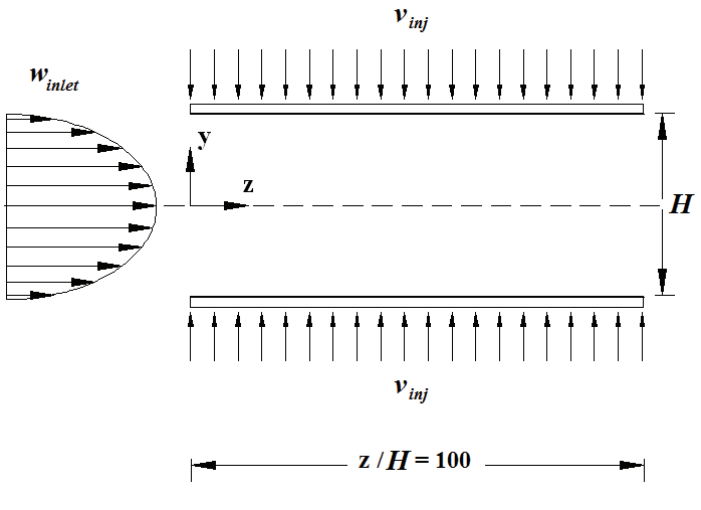

(a)

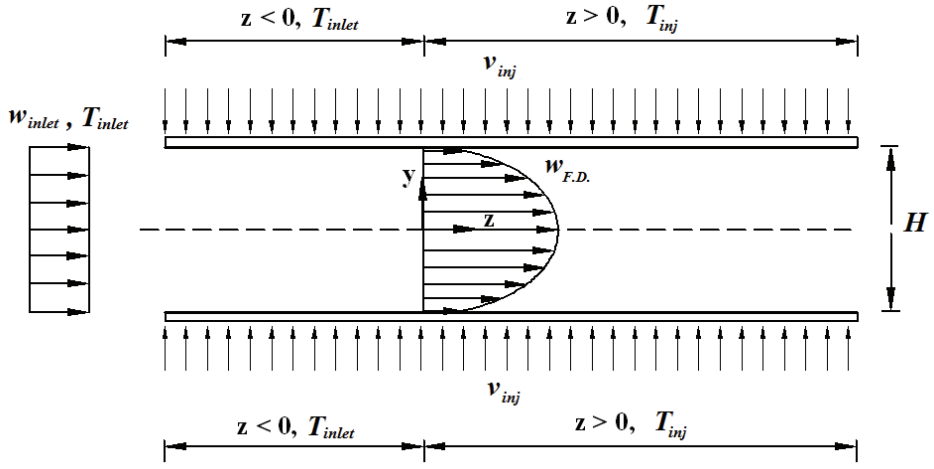

(b)

Figure 4.3: Schematic illustrations of two of the test problems that were used for verification of the proposed FVM: (a) problem investigated and solved by Berman (1953); and (b) problem investigated and solved by Raithby (1971).

With reference to the notation given in Figure 4.3 (b), the proposed three-dimensional FVM was used to solve this problem with the following uniform grids: $\Delta(x/H)$ = 1/(NX – 2), with NX = 5 and slip and impermeability conditions imposed at (x/H) = 0 and 1; $\Delta(y/H)$ = 1/(NY – 2), with NY = 22, 42, 82, 102, and 122; and $\Delta(z/H)$ = 0.0125. In this problem, for $(z/H) > 20$, a fully-developed regime is established in which both (w/w_{av}) and $\theta = (T - T_{inj})/(T_{y=0} - T_{inj})$ are independent of (z/H). For (z/H) values in this fully-developed region, the values of θ, computed using the proposed FVM, were compared to the corresponding results yielded by the asymptotic-expansions solution proposed by Raithby (1971). The agreement between these results was uniformly very good. For example, the absolute differences between the essentially grid-independent values of θ at (y/H) = 0.1 and 0.2 (obtained using the extrapolation technique proposed by Richardson (1910) and the computed results yielded by the proposed FVM with the two finest grids in the y direction) and the corresponding results of Raithby (1971) were less than 1.16% and 1.10 % (of the centerline value of θ = 1), respectively.

In a final test, the proposed three-dimensional parabolic FVM was used to solve the fluid flow portion of a problem studied numerically by Hwang et al. (1993). This problem involves laminar flow in a straight duct of square cross-section, with uniform fluid flow specified at the inlet plane, and uniform injection on the lower surface: the schematic illustration given in Figure 4.3 applies to this problem, but with the blocked end at z = 0 replaced with uniform flow specified at the inlet plane, and with AR = a/b = 1. Beyond a sufficient distance downstream from z = 0, the fluid flow in this test problem becomes fully developed. In this fully-developed region, the following conditions are achieved [Hwang et al. (1993)]: w/w_{av} is invariant with z (where w_{av} is the local cross-sectional-average axial velocity at z); and $f_{Fanning}\,\mathrm{Re}_{D_h} = \{\tau_{w,\,z,\,c-s\,av}/(0.5\rho w_{av}^2)\}(\rho w_{av} D_h/\mu)$ = constant, where $\tau_{w,\,z,\,c-s\,av}$ is the cross-sectional-average wall shear stress in the axial direction, and $D_h = b$ when AR = 1. The proposed FVM was used to compute the values of $(w/w_{av})_{max,\,F.D.}$ and $(f_{Fanning}\,\mathrm{Re}_{D_h})_{F.D.}$ for $\mathrm{Re}_{inj} = (\rho v_{inj} b/\mu)$ = 5, 10, and 20, with uniform cross-sectional grids of 41 x 41 nodes (Grid 1), 61 x 61 nodes (Grid 2), and 81 x 81 nodes (Grid 3). Essentially grid-independent values were then obtained using the extrapolation technique of

Richardson (1910) with the values obtained with Grids 2 and 3, and the extrapolated results were compared to the corresponding numerical results of Hwang et al. (1993), which were obtained with a uniform cross-sectional grid of 41 x 41 nodes. These results and comparisons are summarized in Table 1. The values yielded by the proposed FVM with the successively finer grids converge monotonically to the corresponding extrapolated results. The extrapolated results compare very well with the corresponding numerical results of Hwang et al. (1993), with |% Diff| values less than 0.255 and 1.736 for $(w/w_{av})_{max,\,F.D.}$ and $(f_{Fanning}\,\mathrm{Re}_{D_h})_{F.D.}$, respectively.

Table 4.1: Computed values of $(w/w_{av})_{max,\,F.D.}$ and $(f_{Fanning}\,\mathrm{Re}_{D_h})_{F.D.}$ for AR = 1, and comparisons with the results of Hwang et al. (1993).

Re_{inj}	Results	Grid 1 41 x 41	Grid 2 61 x 61	Grid 3 81 x 81	Richardson extrapolation / Grids 2 & 3	Hwang et al. (1993)	|% Diff|
5	$(w/w_{av})_{max,\,F.D.}$	2.018	2.020	2.021	2.022	2.020	0.099
	$(f_{Fanning}\,\mathrm{Re}_{D_h})_{F.D.}$	15.931	15.882	15.857	15.837	15.73	0.676
10	$(w/w_{av})_{max,\,F.D.}$	1.988	1.975	1.968	1.963	1.968	0.255
	$(f_{Fanning}\,\mathrm{Re}_{D_h})_{F.D.}$	17.240	17.552	17.691	17.799	17.49	1.736
20	$(w/w_{av})_{max,\,F.D.}$	1.891	1.895	1.896	1.897	1.893	0.211
	$(f_{Fanning}\,\mathrm{Re}_{D_h})_{F.D.}$	21.235	21.062	20.985	20.926	20.65	1.319

4.3 RESULTS AND DISCUSSIONS

4.3.1 Overview: Dimensionless Parameter Ranges Considered and Definitions of Dimensionless Forms of Results

The results and discussions presented in this section pertain to computer simulations of steady laminar flow and heat transfer in straight rectangular vapor grooves machined into the metallic walls of evaporators used in LHPs, similar to those shown in Figures 4.1 and 4.2. Keeping in mind practical applications [Chi (1976); Faghri (1995); Silverstein

(1992); Chu et al. (2004); Maydanik (2005); Launay et al. (2007); Wang et al. (2008); Bai et al. (2009); Vasiliev et al. (2009)], and with respect to the notation shown in Figure 4.2 and the dimensionless parameters defined in Eq. (4.3), the following values of the aspect ratio, AR, injection Reynolds number, Re_{inj}, and fluid Prandtl number, Pr, were considered in this work:

$$
\begin{aligned}
&AR = (a/b) = 1,\ 2,\ 5,\ \infty \\
&\mathrm{Re}_{inj} = (\rho v_{inj} b/\mu) = 0,\ 0.1,\ 1,\ 10,\ 50, \text{ and } 100 \\
&\mathrm{Pr} = (\mu c_p/k) = 1,\ 2, \text{ and } 3
\end{aligned}
\tag{4.11}
$$

The groove with infinitely large aspect ratio (AR → ∞) was not selected for any particular practical relevance. Rather, it was chosen because it provides a computationally convenient setting for testing of the proposed FVM (see test problems described Section 4.2) and also for simulations using both elliptic and parabolic forms of the governing equations (and a comparative evaluation of the results, as described in the next subsection). It should also be noted that Re_{inj} = 0, which corresponds to no injection (or no rate of heat input to the LHP and thus no liquid-vapor phase-change process in the evaporator), was chosen mainly to allow checks of the FVM predictions against analytical solutions to the equations that govern fully-developed fluid flow in straight rectangular ducts with impermeable walls.

The chosen values of the Prandtl number bracket those of saturated vapors of ammonia, distilled water, ethanol, and isopropanol in the temperature range 300 K $\le T_{sat} \le$ 400 K.

The results are presented in this section using the following dimensionless forms, in addition to the dimensionless variables and parameters already defined in Eq. (4.3):

$$
\begin{aligned}
&z/D_h = z/\{4ab/(2a+2b)\}\ ;\ \text{hydraulic diameter } D_h = \{4ab/(2a+2b)\} \\
&w/w_{av} = w/\{(az)v_{inj}/(ba)\}\ ;\ \text{local average axial vlocity } w_{av} = \{(az)v_{inj}/(ab)\} \\
&\theta_b = (T_b - T_{inj})/(T_w - T_b)\ ;\ \text{local bulk temperature } T_b = \{\iint_{A_{c-s}} \rho w c_p T dxdy\}/\{\iint_{A_{c-s}} \rho w c_p dxdy\} \\
&\mathrm{Re}_{D_h} = \rho w_{av} D_h/\mu\ ;\ \mathrm{Re}_{inj} = \rho v_{inj} b/\mu\ ;\ \mathrm{Pr} = \mu c_p/k\ ;\ \mathrm{Pe}_{inj} = \mathrm{Re}_{inj}\,\mathrm{Pr} \\
&f = f_{Darcy} = (-d\bar{P}/dz)D_h/(0.5\rho w_{av}^2)\ ;\ f_{Fanning} = \tau_{w,z,c-s\,av}/(0.5\rho w_{av}^2) \\
&f_{app} = \{(\bar{P}_{z=0} - \bar{P}_z)/z\}D_h/(0.5\rho w_{av}^2)
\end{aligned}
\tag{4.12}
$$

In this equation, $\tau_{w,z,\,c-s\,av}$ is the cross-sectional-average wall shear stress in the axial direction.

4.3.2 Computational Grids used in the Final Simulations for AR = 1, 2, and 5

Based on the results of grid-independence checks done for the test problems described in Section 4.2, the axial step size in the final three-dimensional parabolic FVM simulations of the problems of interest was chosen to be $\Delta(z/D_h)$ = 0.02, for all the values of the parameters specified in Eq. (4.11). For the values of Re_{inj} = 100 and Pr = 3, which produce the steepest gradients of the dependent variables in the calculation domain for the cases considered, computations were done with uniform cross-sectional grids of 41 x 41 nodes (Grid 1), 61 x 61 nodes (Grid 2), and 81 x 81 nodes (Grid 3) for each value of AR (1, 2, and 5). In each of these checks, beyond a sufficient distance downstream from z = 0, the fluid flow and heat transfer become fully developed, and the following conditions prevail (elaborated further in Sections 4.3.4 – 4.3.5): w/w_{av} is invariant with z; $f\,\mathrm{Re}_{D_h}$ = constant; θ_b is invariant with z. The absolute differences in the computed values of $(f\,\mathrm{Re}_{D_h})_{F.D.}$ and $(\theta_b)_{F.D.}$ obtained with Grid 3 (81 x 81 nodes) and their essentially grid-independent values (obtained by applying the extrapolation technique of Richardson (1910) to the values obtained with Grids 2 and 3) were less than 0.31% and 0.30%, respectively. Based on these grid checks, all final simulations of the problems of interest, for AR = 1, 2, and 5, were done with a uniform cross-sectional grid of 81 x 81 nodes, and $\Delta(z/D_h)$ = 0.02. Details of the grid used in the computations for AR → ∞ are presented in the next subsection, along with other related results and discussions.

4.3.3 Comparative Evaluation of Results Yielded by Elliptic and Parabolic Models for AR → ∞

In the rectangular groove with AR → ∞, which corresponds to a parallel-plate channel, the steady laminar fluid flow and heat transfer phenomena of interest (see schematic in Figure 4.2) are essentially two-dimensional. This problem was solved using an elliptic, two-dimensional, co-located, equal-order FVM [Baliga and Atabaki (2006)] and also the proposed three-dimensional parabolic FVM (described in Section 4.2 and

detailed in Chapter 3). The following dimensionless parameters were investigated: $\mathrm{Re}_{inj} = (\rho v_{inj} b/\mu) = 0.1$, 1, 10, 50, and 100; $\mathrm{Pr} = 3$; and $(L/D_h) = 8$, where the hydraulic diameter is $D_h = 2b$ when AR $\rightarrow \infty$. The boundary conditions specified in Eq. (4.10) apply here to both the elliptic and parabolic models. In the elliptic model, additional conditions are needed at the outlet plane located at $(z/D_h) = (L/D_h) = 8$: the so-called outflow conditions (namely, negligible viscous and conduction transport in the z direction, compared to the advection transport in this direction) were imposed at the outlet plane [Patankar (1980)]. Using guidance from the results of test problems described in Section 4.2, the following essentially comparable grids were used: with the two-dimensional elliptic FVM, a uniform grid of 81 nodes in the y direction and 402 nodes in the z direction; and with the three-dimensional parabolic FVM, $\Delta(z/D_h) = 0.02$ = constant, a uniform grid of 81 nodes in the y direction, and $\Delta(x/b) = 1/(\mathrm{NX} - 2)$, with NX = 5 and slip and impermeability conditions imposed at (x/H) = 0 and 1.

Streamline patterns obtained with the two-dimensional elliptic FVM for $\mathrm{Re}_{inj} = 0.1$ and 100 are presented in Figure 4.4 (a) and 4.4 (b), respectively.

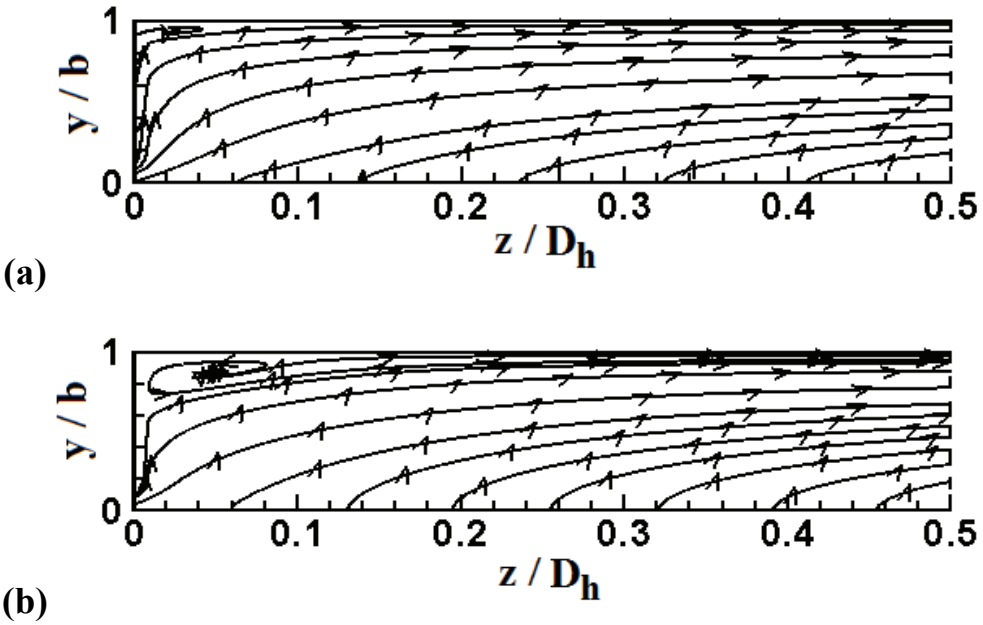

Figure 4.4: Streamline patterns obtained with the two-dimensional elliptic FVM for AR $\rightarrow \infty$ and (a) $\mathrm{Re}_{inj} = 0.1$ and (b) $\mathrm{Re}_{inj} = 100$.

There is a recirculating-flow region in the top left-hand corner in both cases: the length of this recirculating-flow region in the z direction is less than $0.05\,D_h$ and $0.1\,D_h$ for $\mathrm{Re}_{inj} = 0.1$ and 100, respectively. These lengths of the recirculating flow zone are quite small, considering that the vapor grooves in the evaporators of LHPs reported in the published literature have lengths that lie in the range $6 \le (L/D_h) \le 190$.

The plots of the variations of $f\,\mathrm{Re}_{D_h}$, $f_{app}\,\mathrm{Re}_{D_h}$, and θ_b with (z/D_h) presented in Figures 4.5 (a), 4.5 (b), and 4.5 (c), respectively, show that for all practical purposes, fully-developed conditions (namely, invariance of all these results with z) prevail for $(z/D_h) \ge 4$. The plots in Figure 4.5 (a) show that the values of $f\,\mathrm{Re}_{D_h}$ initially drop steeply with (z/D_h), then exhibit a mild increase, and finally asymptote to fully-developed (constant) values. The mild increase in the values of $f\,\mathrm{Re}_{D_h}$, which is especially evident in the results for Re_{inj} = 50 and 100, is due to the recovery of the cross-sectional-average static pressure as the fluid flows past the recirculating zones in the top left-hand corner of the groove (see Figure 4.4). This mild recovery of the cross-sectional-average static pressure is also evident in the plots of $f_{app}\,\mathrm{Re}_{D_h}$ vs. (z/D_h) in Figure 4.5 (b), but not to the same extent as it is in Figure 4.5 (a), as the cumulative pressure drop per unit length, $(\overline{P}_{z=0} - \overline{P}_z)/z$, is used in the definition of f_{app} whereas the local axial gradient of this pressure, $-d\overline{P}/dz$, is used in f.

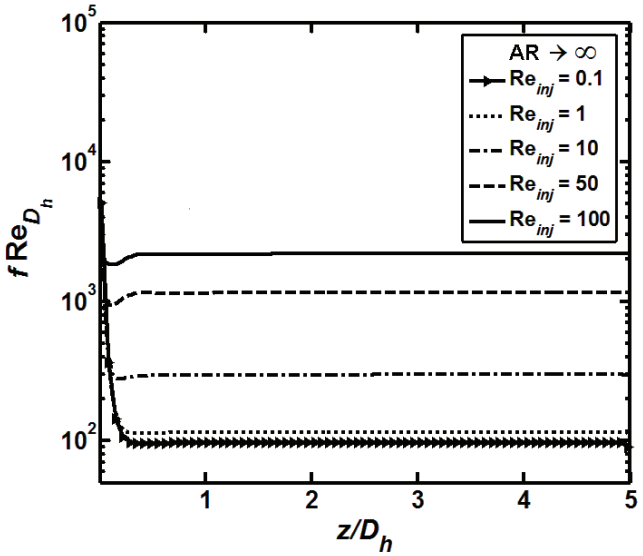

(a)

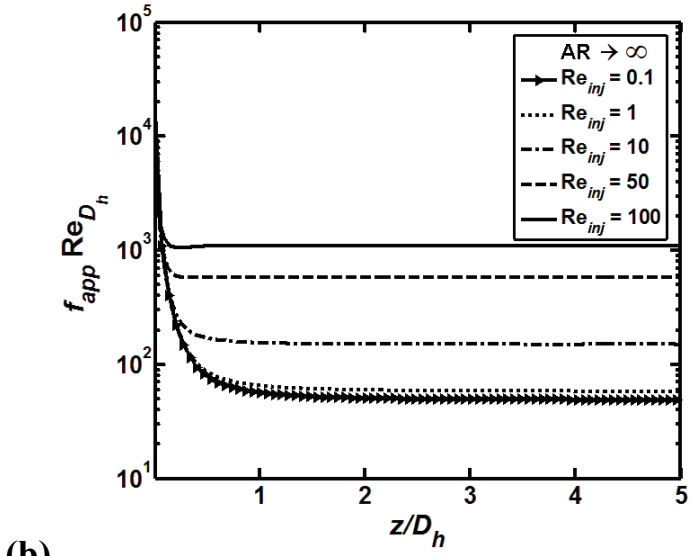

(b)

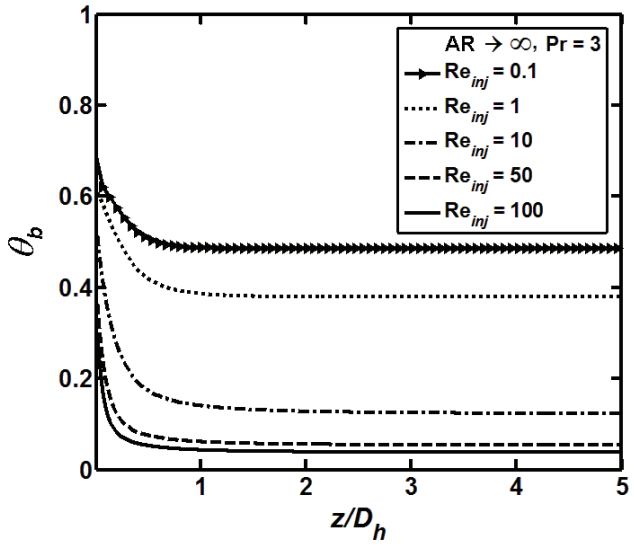

(c)

Figure 4.5: Results obtained using the two-dimensional elliptic FVM for AR → ∞: variations with (z/D_h) of (a) $f\,\mathrm{Re}_{D_h}$, (b) $f_{app}\,\mathrm{Re}_{D_h}$, and (c) θ_b.

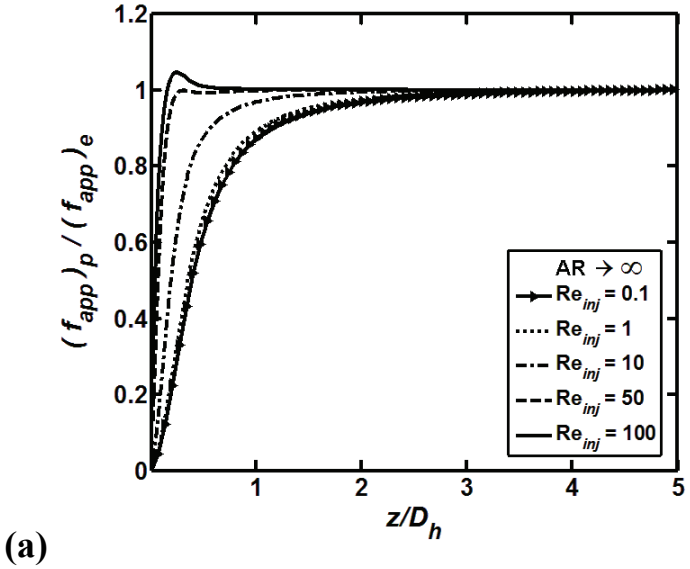

(a)

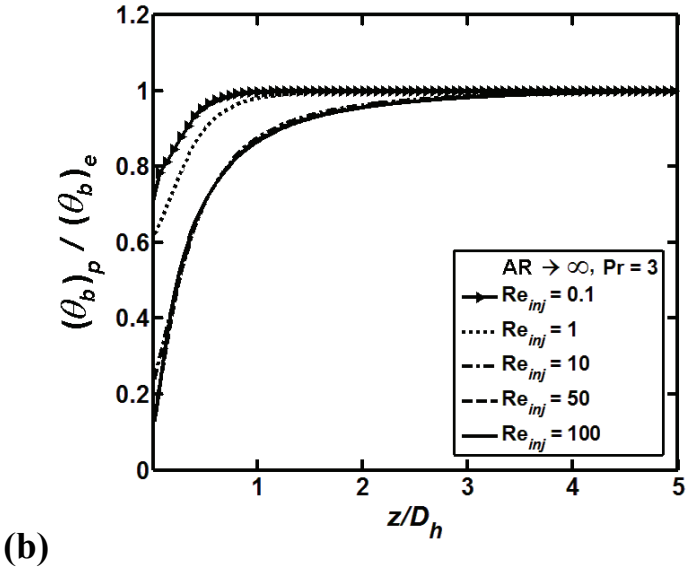

(b)

Figure 4.6: Comparisons of results obtained using the two-dimensional elliptic and three-dimensional parabolic FVMs for AR → ∞: variations with (z/D_h) of (a) $(f_{app})_p/(f_{app})_e$ and (b) $(\theta_b)_p/(\theta_b)_e$.

Plots of the variations of $(f_{app})_p/(f_{app})_e$ and $(\theta_b)_p/(\theta_b)_e$ with (z/D_h), where the subscripts p and e indicate results obtained with the parabolic and elliptic FVMs, respectively, are given in Figures 4.6 (a) and 4.6(b), respectively. For $(z/D_h) \geq 4$, these

plots show that the cumulative results yielded by the parabolic and elliptic FVM are essentially the same, for all practical purposes. The distributions of (w/w_{av}) and θ at $(z/D_h) = 4$ obtained with the elliptic and parabolic FVMs are compared in Figures 4.7 (a) and 4.7 (b), respectively, and they too show that the differences between these results are negligible for all practical purposes.

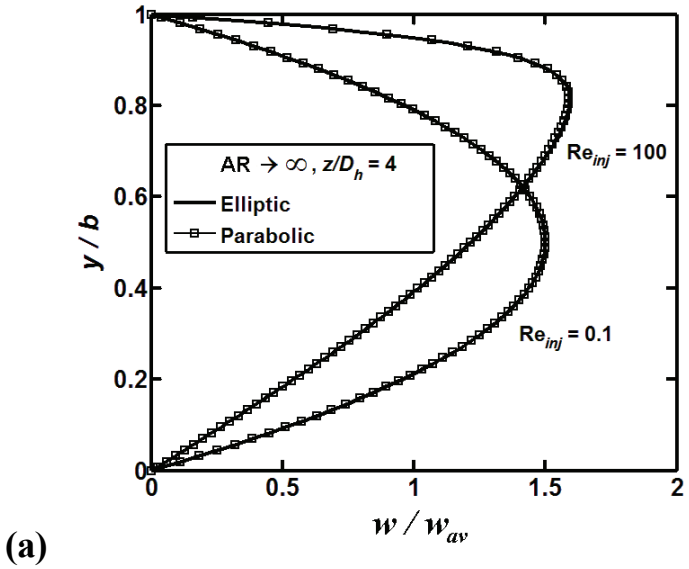

(a)

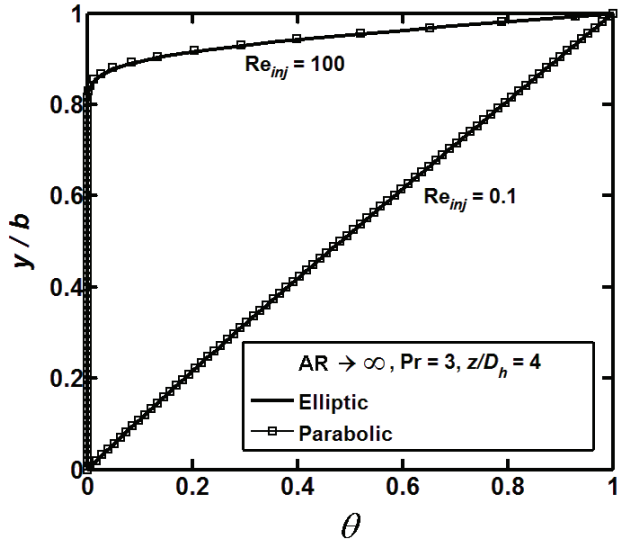

(b)

Figure 4.7: Comparisons of results obtained using the two-dimensional ellptic and three-dimensional parabolic FVMs for AR $\rightarrow \infty$ at $(z/D_h) = 4$: distributions of (a) w/w_{av} and (b) θ.

For AR = 1, 2, and 5, taking into consideration the confining effects of the impermeable walls at $(x/b) = 0$ and AR, similar favourable comparisons between the results obtained with the elliptic and parabolic FVMs as those demonstrated in Figures 4.6 and 4.7 are expected for $(z/D_h) \geq 4$. As was mentioned earlier, the vapor grooves in the evaporators of LHPs reported in the published literature have lengths that lie in the range $6 \leq (L/D_h) \leq 190$. Thus, it was concluded that the three-dimensional parabolic FVM (which is computationally much less expensive than the elliptic FVM, especially for AR = 1, 2, and 5) is satisfactory for obtaining values of (w/w_{av}), θ, f, f_{app}, and θ_b in the region $4 \leq (z/D_h) \leq (L/D_h)$ of the vapor grooves in the problems of interest, and it was used for all of the final simulations.

4.3.4 Distributions of $(w/w_{av})_{F.D.}$ and $\theta_{F.D.}$

As was mentioned earlier, at a sufficient distance downstream of the blocked end (z = 0) of the vapor groove, $(z/D_h) \geq 4$ in the problems of interest, the distributions of (w/w_{av}) and θ become essentially invariant with (z/D_h). Here, these fully-developed distributions are denoted by $(w/w_{av})_{F.D.}$ and $\theta_{F.D.}$. Plots of $(w/w_{av})_{F.D.}$ vs. (y/b) in the longitudinal symmetry plane at $(x/b) = 0.5AR$ are shown in Figure 4.8 (a) for AR = 1: at Re_{inj} = 0.1, the rate of injection of vapor at the bottom surface of the groove is relative low, and the $(w/w_{av})_{F.D.}$ profile is almost symmetrical about the geometrical centerline at $(y/b) = 0.5$ and close to the profile for laminar full-developed flow in a straight duct with impermeable walls (no injection); and as Re_{inj} is increased, this dimensionless velocity profile get skewed and the location of $(w/w_{av})_{F.D.,\max}$ shifts progressively upwards towards $(y/b) = 1$. Plots of $(\theta)_{F.D.}$ vs. (y/b) in the longitudinal symmetry plane at $(x/b) = 0.5AR$ are shown in Figure 4.8 (b) for AR = 1 and Pr = 3.0: at the lowest injection rate, Re_{inj} = 0.1, the $\theta_{F.D.}$ profile is concave, with a value close to one ($T = T_w$) over a large portion of the duct cross-section; and as Re_{inj} is increased, the $\theta_{F.D.}$ distribution gets progressively more convex, with the injected fluid temperature prevailing (yielding $\theta = 0$) over an increasing portion of

the duct cross-section. The distributions of $(w/w_{av})_{F.D.}$ for AR = 1 given in Figure 4.8 (a) were qualitatively similar to those obtained for AR = 2, 5, and ∞; and the distributions of $\theta_{F.D.}$ given in Figure 4.8 (b) for AR = 1 and Pr = 3 were qualitatively similar to those calculated for AR = 2, 5, and ∞ and Pr = 1 and 2; therefore, they are not presented here.

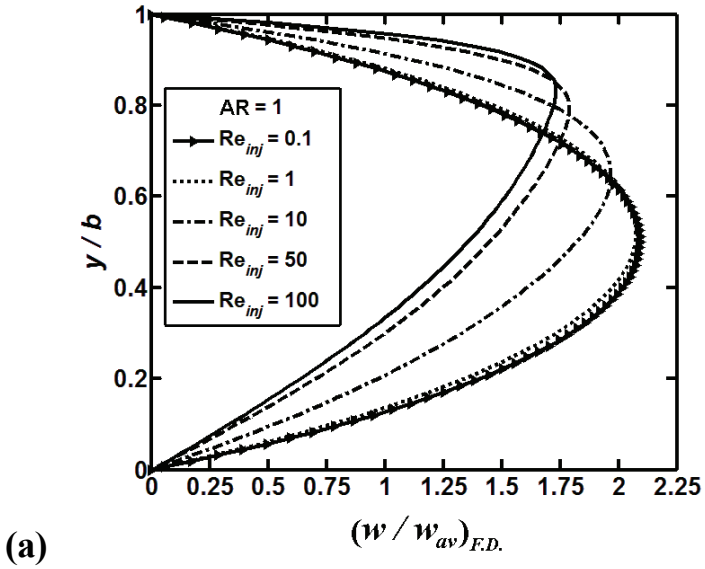

(a)

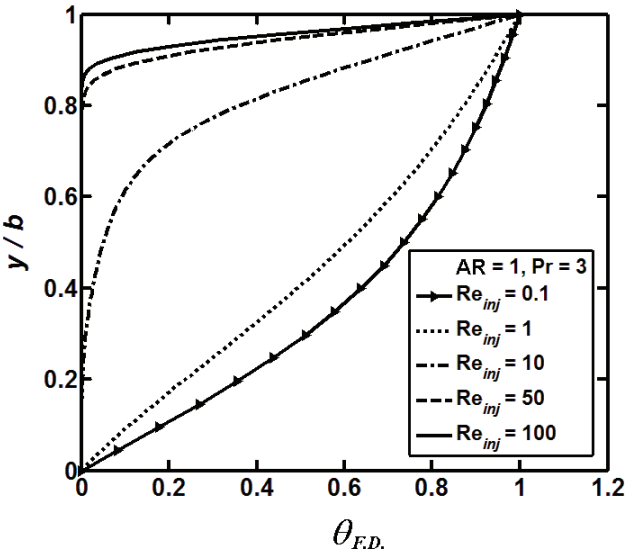

(b)

Figure 4.8: Distributions of fully-devloped dimensionless velocity and temperature profiles on the longitudial symmetry plane located at $(x/b) = 0.5AR$: (a) $(w/w_{av})_{F.D.}$ for AR = 1; and (b) $\theta_{F.D.}$ for AR = 1 and Pr = 3.

4.3.5 Axial Variations of $(f_{app}\,\mathrm{Re}_{D_h})/(f\,\mathrm{Re}_{D_h})_{F.D.}$ and θ_b

The axial variation of the product of the apparent friction factor and Reynolds number, $(f_{app}\,\mathrm{Re}_{D_h})$ normalized by the value of the product of Darcy friction factor and Reynolds number in the fully developed region $(f\,\mathrm{Re}_{D_h})_{F.D.}$ is plotted in Figure 4.9 (a) for AR = 1. These results show that for all cases considered, $(f_{app}\,\mathrm{Re}_{D_h})/(f\,\mathrm{Re}_{D_h})_{F.D.}$ almost equals its asymptotic value of 0.5 for $z \geq 4$. The rationale for the asymptotic value of 0.5 for this ratio is stated in the next paragraph.

In the problems of interest, $(w/w_{av})_{F.D.}$ is invariant with axial distance z, as was discussed in the previous subsection. Thus, $w_{F.D.} = fnc(x,y)w_{av}$, where $fnc(x,y)$ is a function of the cross-section coordinates x and y, and with uniform injection on the bottom surface of the vapor groove, w_{av} varies linearly with z, as was shown in Eq. (4.12). With this condition in the fully-developed region, the corresponding cross-sectional-average wall shear stress in the axial direction varies linearly with z; the associated axial gradient of total rate of transport of z-moment in the fully-developed region varies linearly with z; and the axial gradient of the cross-sectional-average reduced pressure needed to sustain the flow in the fully developed region also varies linearly with z. Thus, if the z = 0 were located in the fully developed region, and $(-d\overline{P}/dz)_{F.D.} = \Im z$ (which applies if z is large enough to make the value of $(-d\overline{P}/dz)_{F.D.}$ at z = 0 negligibly small), then $(\overline{P}_z - \overline{P}_{z=0}) = \Im z^2/2$, and the ratio $\{(\overline{P}_z - \overline{P}_{z=0})/z\}/(-d\overline{P}/dz)_{F.D.} = 0.5$. Therefore, in the actual problems of interest, at sufficiently large values of the axial distance z, $(f_{app}\,\mathrm{Re}_{D_h})/(f\,\mathrm{Re}_{D_h})_{F.D.}$ asymptotes to the value of 0.5, regardless of the value of the aspect ratio or the shape of the cross-section of the vapor groove (as long as it is straight and axially uniform). The results given in Figure 4.9 (a) for AR = 1 show this behavior. Qualitatively similar results and the asymptotic value of 0.5 for $(f_{app}\,\mathrm{Re}_{D_h})/(f\,\mathrm{Re}_{D_h})_{F.D.}$ were also obtained for AR = 2, 5, and ∞.

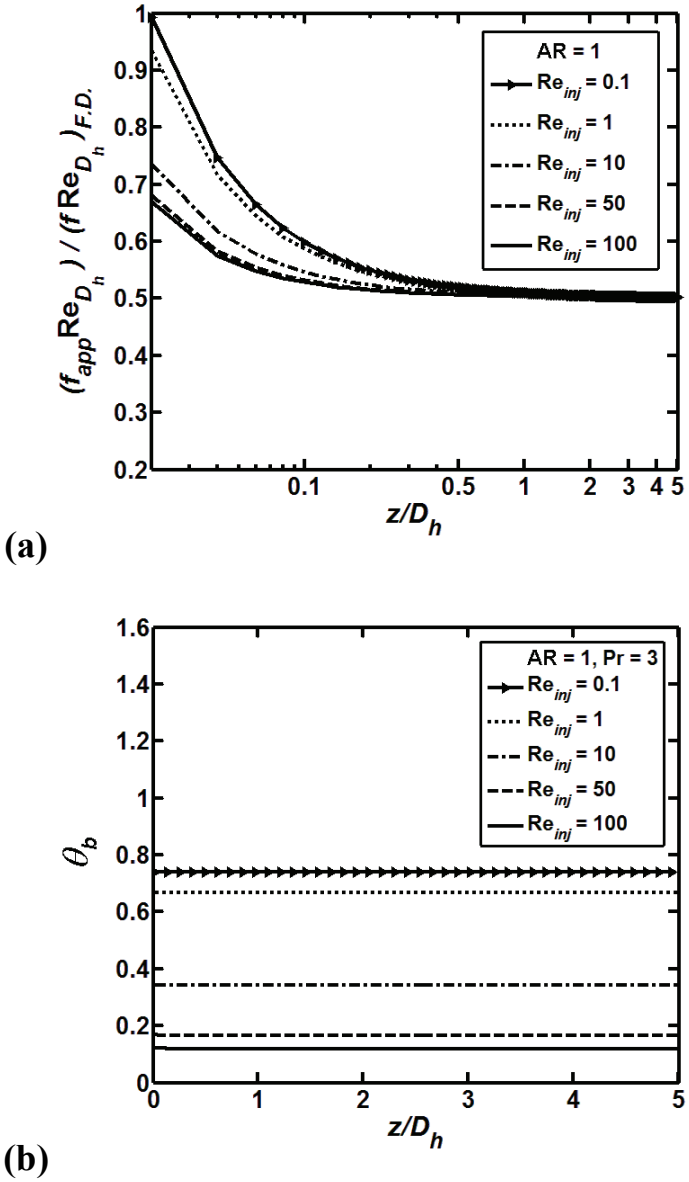

Figure 4.9: Axial variations of (a) $(f_{app}\,\mathrm{Re}_{D_h})/(f\,\mathrm{Re}_{D_h})_{F.D.}$ for AR = 1, and (b) θ_b for AR = 1 and Pr = 3.

The axial variation of the dimensionless bulk temperature, θ_b, is presented in Figure 4.9 (b) for AR = 1 and Pr = 3. The results in this figure show that θ_b becomes invariant with z in the thermally fully-developed region. Qualitatively similar results were also obtained for AR = 2, 5, and ∞, and Pr = 1 and 2. Predictions obtained with the three-dimensional parabolic FVM indicates that this thermally fully-developed regime is established at very small values of (z/D_h), but the elliptic FVM simulations done for AR

= ∞ show that almost thermally fully-developed conditions prevail for $(z/D_h) \geq 4$, and the values of $(\theta_b)_{F.D.}$ obtained with the elliptic and parabolic FVMs are the same for all practical purposes.

4.3.6 Variations of $(f\,\mathrm{Re}_{D_h})_{F.D.}$ and $(f_{Fanning}\,\mathrm{Re}_{D_h})_{F.D.}$ with AR and Re_{inj}, and Correlations

The computed values of the $(f\,\mathrm{Re}_{D_h})_{F.D.}$ and $(f_{Fanning}\,\mathrm{Re}_{D_h})_{F.D.}$ are presented in Figures 4.10 (a) and 4.10 (b), respectively, and also in Table 4.2.

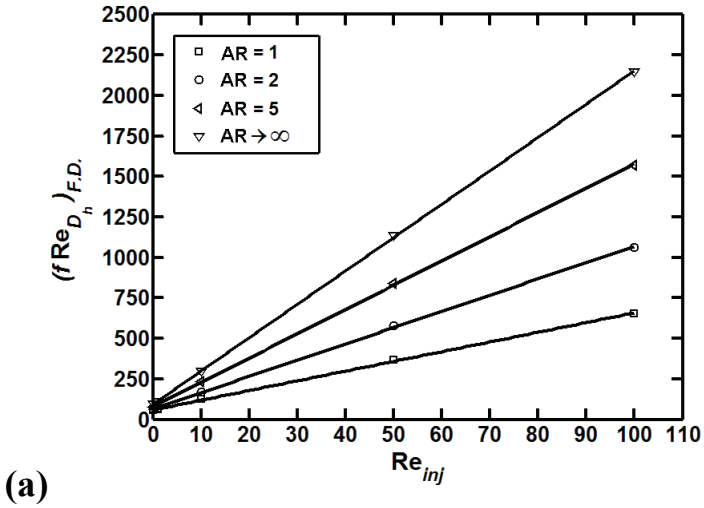

(a)

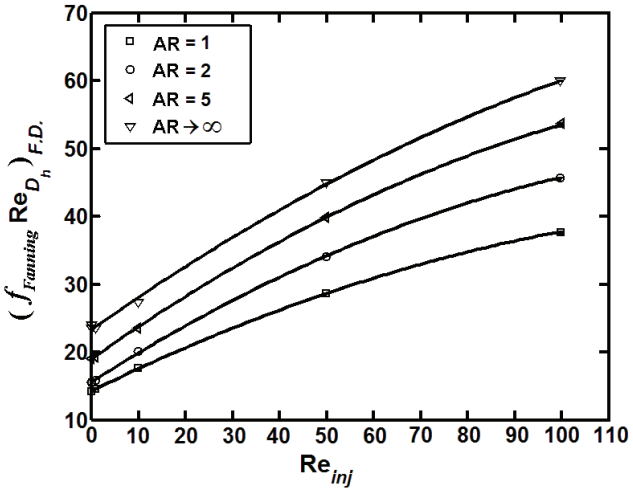

(b)

Figure 4.10: Variations of (a) $(f\,\mathrm{Re}_{D_h})_{F.D.}$ and (b) $(f_{Fanning}\,\mathrm{Re}_{D_h})_{F.D.}$ with Re_{inj} for AR = 1, 2, 5, and ∞.

Table 4.2: Computed values of $(f\,\mathrm{Re}_{D_h})_{F.D.}$ and $(f_{Fanning}\,\mathrm{Re}_{D_h})_{F.D.}$

Re_{inj}	Results	AR			
		1	2	5	∞
0	$(f\,\mathrm{Re}_{D_h})_{F.D.}$	5.691E+01	6.219E+01	7.628E+01	9.600E+01
	$(f_{Fanning}\,\mathrm{Re}_{D_h})_{F.D.}$	1.423E+01	1.555E+01	1.907E+01	2.400E+01
0.1	$(f\,\mathrm{Re}_{D_h})_{F.D.}$	5.755E+01	6.327E+01	7.774E+01	9.591E+01
	$(f_{Fanning}\,\mathrm{Re}_{D_h})_{F.D.}$	1.425E+01	1.558E+01	1.909E+01	2.352E+01
1	$(f\,\mathrm{Re}_{D_h})_{F.D.}$	6.341E+01	7.305E+01	9.111E+01	1.126E+02
	$(f_{Fanning}\,\mathrm{Re}_{D_h})_{F.D.}$	1.450E+01	1.593E+01	1.932E+01	2.352E+01
10	$(f\,\mathrm{Re}_{D_h})_{F.D.}$	1.235E+02	1.714E+02	2.318E+02	2.982E+02
	$(f_{Fanning}\,\mathrm{Re}_{D_h})_{F.D.}$	1.769E+01	2.014E+01	2.363E+01	2.733E+01
50	$(f\,\mathrm{Re}_{D_h})_{F.D.}$	3.690E+02	5.800E+02	8.422E+02	1.135E+03
	$(f_{Fanning}\,\mathrm{Re}_{D_h})_{F.D.}$	2.862E+01	3.410E+01	3.994E+01	4.500E+01
100	$(f\,\mathrm{Re}_{D_h})_{F.D.}$	6.530E+02	1.062E+03	1.571E+03	2.148E+03
	$(f_{Fanning}\,\mathrm{Re}_{D_h})_{F.D.}$	3.785E+01	4.584E+01	5.354E+01	6.003E+01

The values of $(f\,\mathrm{Re}_{D_h})_{F.D.}$, Re_{inj}, and AR presented in Figure 4.10 (a) and Table 4.2 were used to obtain the following correlation ($R^2 = 0.99$):

$$(f\,\mathrm{Re}_{D_h})_{F.D.} = a_o + a_1\,\mathrm{Re}_{inj}$$

$$a_0 = -57.76\left(AR^{-3}\right) + 143.7\left(AR^{-2}\right) - 125.0\left(AR^{-1}\right) + 96 \qquad (4.13)$$

$$a_1 = -11.99\left(AR^{-3}\right) + 30.85\left(AR^{-2}\right) - 33.41\left(AR^{-1}\right) + 20.57$$

With uniform injection on the bottom surface of the vapor groove, w_{av} increases linearly with z, and in the fully-developed region, the axial gradient of the rate of transport of z-momentum also increases linearly with z. Thus, in the fully-developed region, the axial gradient of the cross-sectional-average reduced pressure has to not only overcome the wall-shear force, but it must also provide the force necessary to maintain the rate of

increase of z-moment in the duct. The values of $(f\,\mathrm{Re}_{D_h})_{F.D.}$, $(f_{Fanning}\,\mathrm{Re}_{D_h})_{F.D.}$, AR, and Re_{inj} given in Table 4.2 were used to obtain the following correlation (maximum absolute error < 4.8%):

$$\left(f\,\mathrm{Re}_{D_h}\right)_{F.D.} = 4\left(f_{fanning}\,\mathrm{Re}_{D_h}\right)_{F.D.} + \beta\,\mathrm{Re}_{inj}$$
$$\beta = -8.776\left(AR^{-3}\right) + 24.08\left(AR^{-2}\right) - 28.59\left(AR^{-1}\right) + 18.62 \qquad (4.14)$$

It should be noted that when $\mathrm{Re}_{inj} = 0$, $\left(f\,\mathrm{Re}_{D_h}\right)_{F.D.} = 4\left(f_{fanning}\,\mathrm{Re}_{D_h}\right)_{F.D.}$, which is the correct relationship for fully-developed flows in straight in ducts with impermeable walls.

4.3.7 Variations of $(\theta_b)_{F.D.}$ with AR, Re_{inj}, and Pr, and Correlations

The computed values of the $(\theta_b)_{F.D.}$ are presented in Figures 4.11 and also in Table 4.3.

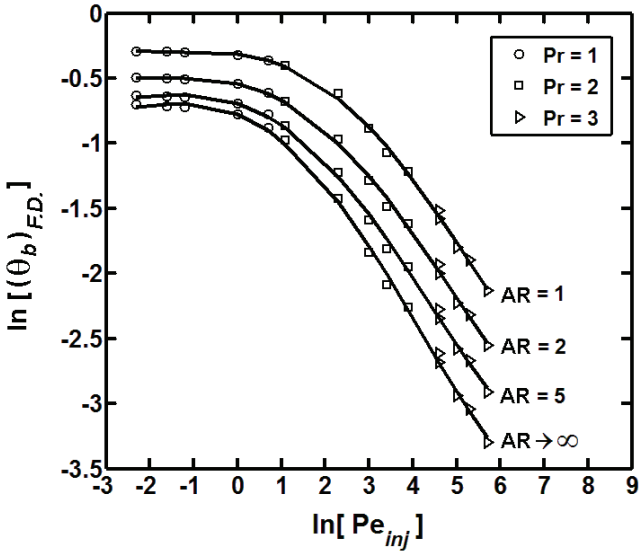

Figure 4.11: Variation of $(\theta_b)_{F.D.}$ with Pe_{inj} for AR = 1, 2, 5, and ∞, and Pr = 1, 2, and 3.

Table 4.3: Computed values of $(\theta_b)_{F.D.}$

Re_{inj}	Pr	Pe_{inj}	$(\theta_b)_{F.D.}$			
			AR = 1	AR = 2	AR = 5	AR = ∞
0.1	1	0.1	7.477E-01	6.086E-01	5.326E-01	4.958E-01
1		1	7.261E-01	5.799E-01	5.000E-01	4.593E-01
10		10	5.376E-01	3.794E-01	2.930E-01	2.399E-01
50		50	2.963E-01	1.980E-01	1.420E-01	1.045E-01
100		100	2.191E-01	1.453E-01	1.030E-01	7.323E-02
0.1	2	0.2	7.446E-01	6.045E-01	5.280E-01	4.909E-01
1		2	6.962E-01	5.419E-01	4.587E-01	4.153E-01
10		20	4.110E-01	2.768E-01	2.042E-01	1.587E-01
50		100	2.068E-01	1.360E-01	9.589E-02	6.823E-02
100		200	1.502E-01	9.885E-02	6.919E-02	4.780E-02
0.1	3	0.3	7.416E-01	6.004E-01	5.234E-01	4.860E-01
1		3	6.671E-01	5.071E-01	4.219E-01	3.765E-01
10		30	3.412E-01	2.257E-01	1.632E-01	1.235E-01
50		150	1.655E-01	1.080E-01	7.569E-02	5.296E-02
100		300	1.191E-01	7.821E-02	5.462E-02	3.709E-02

The values of $(\theta_b)_{F.D.}$, $\mathrm{Pe}_{inj} = \mathrm{Re}_{inj}\,\mathrm{Pr}$, and AR presented in Table 4.3 were used to obtain the following correlation ($R^2 = 0.998$):

$$
\begin{aligned}
&\ln\left[(\theta_b)_{F.D.}\right] = a_4\left[\ln(Pe_{inj})\right]^4 + a_3\left[\ln(Pe_{inj})\right]^3 + a_2\left[\ln(Pe_{inj})\right]^2 + a_1\left[\ln(Pe_{inj})\right] + a_0 \\
&a_4 = -7.313\text{x}10^{-4}\left(AR^{-3}\right) + 1.730\text{x}10^{-3}\left(AR^{-2}\right) - 1.277\text{x}10^{-3}\left(AR^{-1}\right) + 1.113\text{x}10^{-3} \\
&a_3 = 4.742\text{x}10^{-3}\left(AR^{-3}\right) - 9.133\text{x}10^{-3}\left(AR^{-2}\right) + 1.477\text{x}10^{-3}\left(AR^{-1}\right) - 4.217\text{x}10^{-3} \\
&a_2 = 2.887\text{x}10^{-2}\left(AR^{-3}\right) - 6.574\text{x}10^{-2}\left(AR^{-2}\right) + 6.669\text{x}10^{-2}\left(AR^{-1}\right) - 6.462\text{x}10^{-2} \\
&a_1 = 3.232\text{x}10^{-2}\left(AR^{-3}\right) - 8.243\text{x}10^{-2}\left(AR^{-2}\right) + 1.452\text{x}10^{-1}\left(AR^{-1}\right) - 1.369\text{x}10^{-1} \\
&a_0 = -2.139\text{x}10^{-1}\left(AR^{-3}\right) + 3.151\text{x}10^{-1}\left(AR^{-2}\right) + 3.625\text{x}10^{-1}\left(AR^{-1}\right) - 7.756\text{x}10^{-1}
\end{aligned}
\tag{4.15}
$$

4.4 SUMMARY

In this chapter, steady laminar flow and heat transfer phenomena in straight rectangular vapor grooves machined into the metallic walls of flat evaporators used in LHPs were investigated numerically using a three-dimensional parabolic FVM presented earlier in Chapter 3 . The straight rectangular grooves have one end blocked, and inflow of vapor along the bottom lateral surface with an injection velocity, v_{inj}, and temperature, T_{inj} . The following values of the dimensionless parameters that govern the problems of interest were analyzed: AR = 1, 2, 5, and ∞; Re_{inj} = 0.1, 1, 10, 50, and 100; Pr = 1, 2, and 3; and (L/D_h) = 8. For AR = ∞, simulations were conducted with a two-dimensional elliptic FVM [Baliga and Atabaki (2006)] and the proposed three-dimensional parabolic FVM: the differences between results yielded by these two methods become essentially imperceptible for $(z/D_h) \geq$ 4. Thus, all of the final simulations were done using the proposed cost-effective three-dimensional parabolic FVM.

In each of the cases considered, for $(z/D_h) \geq$ 4, a special fully-developed regime is established with the following characteristics: (w/w_{av}) and $\theta = (T - T_{inj})/(T_w - T_{inj})$ become invariant with axial distance z; $(f\,\mathrm{Re}_{D_h})$, $(f_{Fanning}\,\mathrm{Re}_{inj})$, and θ_b achieve constant values. The values of $(f\,\mathrm{Re}_{D_h})_{F.D.}$, $(f_{Fanning}\,\mathrm{Re}_{inj})_{F.D.}$, and $(\theta_b)_{F.D.}$ were computed for the above-mentioned range of the governing parameters. These values were used to propose a correlation that relates $(f\,\mathrm{Re}_{D_h})_{F.D.}$ to AR and Re_{inj}, and a correlation that relates

$(\theta_b)_{F.D.}$ to AR, Re_{inj}, and Pr. Another correlation that relates $(f\,\mathrm{Re}_{D_h})_{F.D.}$ to $(f_{Fanning}\,\mathrm{Re}_{D_h})_{F.D.}$, AR, and Re_{inj} was also proposed. It was also shown that the ratio $(f_{app}\,\mathrm{Re}_{D_h})/(f\,\mathrm{Re}_{D_h})_{F.D.}$ achieves an asymptotic value of 0.5 regardless of the value of the aspect ratio or the shape of the cross-section of the vapor groove (as long as it is straight and axially uniform). The computed results also showed that for all practical purposes, $(f_{app}\,\mathrm{Re}_{D_h})/(f\,\mathrm{Re}_{D_h})_{F.D.}$ can be considered equal to its asymptotic value of 0.5 for $(z/D_h) \geq 4$. These results and correlations are intended to enhance the capabilities of available quasi-one-dimensional thermofluid models of LHPs, akin to that proposed in Chapter 2. The relevance of these model enhancements are demonstrated and discussed later in Chapter 6 of this thesis.

Chapter 5:

Properties of Liquid-Saturated Sintered Powder-Metal Wicks

Porous materials of excellent rigidity and low effective pore size can be easily manufactured by sintering metal powders. These key attributes of porous sintered-powder-metal plates and tubes make them the materials of choice for the construction of wicks used in heat pipes (HPs), capillary pumped loops (CPLs), and loop heat pipes (LHPs) [Dunn and Reay (1986); Silverstein (1992); Faghri (1995); Leong et al. (1997); Maydanik (2005); Vasiliev et al. (2009); Li and Peterson (2011)]. As was seen in the discussion given in Chapter 2, the required inputs to mathematical models of LHPs include the porosity, maximum effective pore size, effective permeability, and effective thermal conductivity of the liquid-saturated porous material of the wick. Primarily borrowing ideas and discussions from the work of Atabaki (2006), and also deriving guidance from the works of Alexander (1972), Stepanov et al. (1977), Hadley (1986), Silverstein (1992), Kaviany (1999), Nield and Bejan (2006), Clark (2009), and Civan (2011), the determination of the aforementioned properties by means of simple and effective experiments, procedures, and correlations is demonstrated in this chapter, using a sample porous sintered-powder-metal plate made of stainless steel 316, saturated with high-purity (99.9%) isopropanol.

5.1 Sample Porous Sintered-Powder-Metal Plate

A porous sintered-powder-metal plate made of stainless steel 316 was used as the sample in this work. This plate was purchased from a manufacturer of specialized filters (Mott Corporation, Connecticut, U.S.A) in the form of a disk with nominal dimensions of 185.4 mm (7.3") diameter and 3.18 mm (1/8") thickness. Laser machining was used to cut a few smaller disk-shaped samples from this porous plate. This machining process also ensured that the peripheral surfaces (cut edges) of these disk-shaped samples were sealed (impermeable to the working fluid).

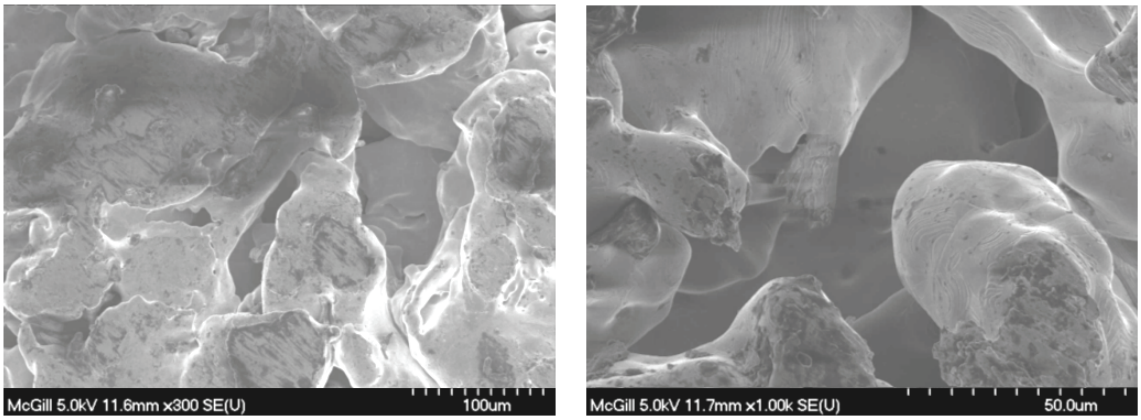

(a) (b)

Figure 5.1: Scanning electron microscopy images of a stainless steel 316, sintered powder-metal, plate at magnifications of (a) 300X and (b) 1000X.

Photomicrographs of the porous sintered-powder-metal sample of stainless steel 316, obtained using a Hitachi S-4700 scanning electron microscope, are shown below in Figure 5.1. These images clearly indicate that the particles of the metal powder used in the fabrication of the sample sintered porous plate are not spherical in shape, but have quite random shapes and are not uniformly sized. In addition, these images show that the sintering process produces excellent connections (solid-to-solid contact zones) between these particles. Thus, it is clear that available analytical, semi-analytical, and numerical correlations for effective properties of porous materials made of uniformly sized, regularly spaced, and packed (unconsolidated or consolidated) spherical particles [Kunii and Smith (1960); Chen and Tien (1973); Ogniewicz and Yovanovich (1978); Hadley (1986); Kaviany (1999); Hsu (2000); Bahrami et al. (2004); Nield and Bejan (2006); Montillet (2007)] are not applicable to the porous sintered-powder-metal plate considered in this work. Therefore, specialized experiments, procedures, and correlations for the determination of the above-mentioned effective properties of liquid-saturate porous sintered-powder-metal plates are needed, and some of these are presented and discussed in this chapter.

5.2 POROSITY

The porosity of a porous material is defined as the ratio of the volume occupied by the voids (or empty space) within it to its total volume, and accounts for all pores

(through pores, blind pores, and closed pores). The *effective* porosity is similarly defined, but accounts for only the volume of the interconnected pores within the porous material. Extensive examination of photomicrographs of sintered metal fibers and screens lead Kunz et al. (1967) to conclude that the pores in these types of porous materials are essentially interconnected. However, the authors also observed the occurrence of isolated voids during the compaction of powders to form sintered materials. Nevertheless, they argued that by adequately packing the powder prior to the compacting and sintering process, the probability of isolated void formation could be minimized. Based on these observations, it is assumed in this work that for well-fabricated porous materials constructed of both sintered fibers and powders, the porosity and the effective porosity are essentially equal. In this context, following the arguments of Kunz et al. (1967), the porosity of porous sintered-powder-metals is estimated as follows:

$$\varepsilon = \frac{V_{void}}{V_{total}} = 1 - \frac{m_{dry\_porous\_matl}}{\rho_s V_{total}} \tag{5.1}$$

where V_{void} is the total volume of the voids inside the porous material; V_{total} is the total volume of the porous material; $m_{dry\_porous\_matl}$ is the total mass of the dry porous material; and ρ_s is the mass density of the solid. In this equation, the mass of the air filling the voids is overlooked in comparison to the mass of the solid part of the porous material.

Techniques for measuring the porosity of porous metal plates are discussed in Dullien (1992). A simple procedure, the so-called density (or Archimedes') method [Dullien (1992)], was used in this work to determine the porosity of the sample porous material. The procedure is outlined below:

1. Measure the geometrical dimensions of the sample several times, and average the measurements to obtain their corresponding mean values. Use these mean values to calculate the total volume of the porous sample.
2. Measure the ambient temperature, and then obtain the value of the mass density (ρ_s) of the solid component of the porous sample at this temperature.
3. Dry the porous sample and then weigh it (in this work, an electronic balance with an accuracy of ±0.1g was used).
4. Use Eq. (5.1) to estimate the porosity of the sample.

In the experiments, the mass of the sample porous stainless steel 316 disk, having a diameter of 22.30 mm and a thickness of 3.11 mm, was measured to be 6.08 g. The ambient temperature during these experiments was about 22^{o}C throughout. At this temperature, the mass density of solid stainless steel 316 is 8238 kg/m^3 [Incropera and DeWitt (2002)]. Using this data and Eq. (5.1), the porosity of the sample porous sintered-powder-metal plate made of stainless-steel 316 was determined to be the following:

$$\varepsilon = 0.393\ (\pm\ 0.011)$$

The uncertainty in the porosity was calculated using the method described in ASHRAE Standard 41.5-75 (1976).

5.3 MAXIMUM EFFECTIVE PORE SIZE

The maximum effective pore size is a property that is required for the determination of the maximum capillary pressure that can be sustained at the liquid-vapor interface in the wick, which, in turn, dictates the so-called capillary-limit on the maximum rate of heat transfer possible in HPs, CPLs, and LHPs. In this section, an experimental apparatus that was originally designed and constructed by Atabaki (2006), and later modified by the author, for the determination of the maximum effective pore size of the wick is presented. The related experiments were conducted with a disk-shaped sample cut (using laser machining) from the above-mentioned porous sintered-powder-metal plate made of stainless steel 316. The results of these experiments are also described and discussed in this section.

5.3.1 Theoretical Aspects

A schematic representation of a liquid-vapor interface that is concave with respect to the vapor-phase is presented in Figure 5.2. The two principal radii of curvature, R_1 and R_2, characterize an arbitrarily-curved interface. Under static conditions with no mass transfer across the interface, the normal components of the surface tension forces are exactly in balance with the force generated due to the pressure jump from the liquid-phase to the vapor-phase. This statement is strictly valid only for regions of the curved liquid-vapor interface that are away from the solid walls. However, de Gennes (1985) and

Vissersa et al. (2000) argued that in many applications, the influence of the near-wall region that is affected by the Van der Waals force of the solid is less than 100 Å.

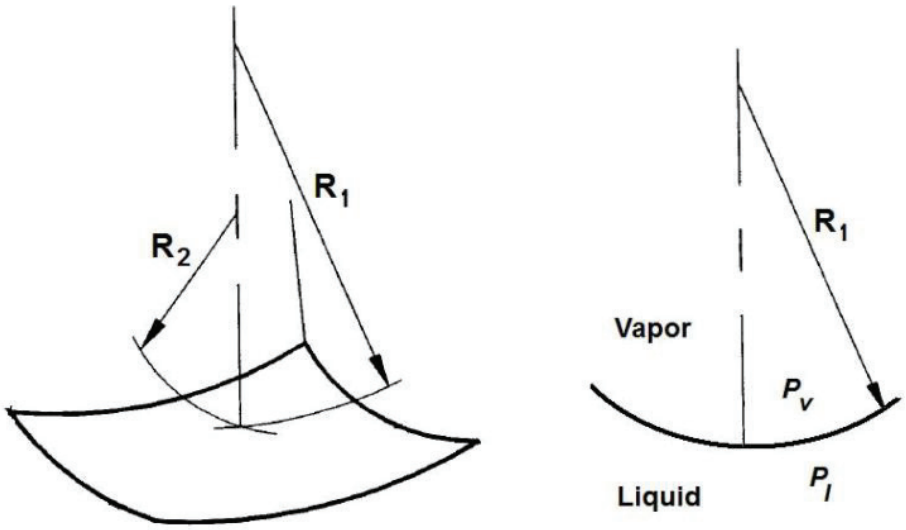

Figure 5.2: An arbitrarily-curved liquid-vapor interface and related notation.

The pressure difference across the curved liquid-vapor interface (shown in Figure 5.2) is given by the Young-Laplace equation [Silvertein (1992)]:

$$\Delta P_{cap} = (P_v - P_l) = 2\sigma_{lv} / r_c \quad ; \quad \frac{1}{r_c} = \left(\frac{1}{R_1} + \frac{1}{R_2} \right) / 2 \tag{5.2}$$

In this equation, P_v and P_l denote, respectively, the thermodynamic pressure in the vapor and the liquid phases adjacent to the interface; σ_{lv} represents the surface tension at the liquid-vapor interface; and r_c is the mean radius of curvature. As is common practice [Alexander (1972); Stepanov et al. (1977); Silverstein (1992)], it is assumed here that the liquid-vapor surface tension is essentially equal to that of the liquid-air interface, and both are referred to as the liquid surface tension, σ. Furthermore, it is mandatory in HPs, LHPs, and CPLs to obtain a positive value of the pressure jump ($P_v - P_l$) to balance the overall pressure drop in the rest of the working-fluid circuit. Therefore, a working fluid that wets the solid in the porous wick is required.

In the simple experimental setup schematically illustrated in Figure 5.3, the capillary force ensures that the liquid inside the vertical pipe (of relatively small diameter) to rise

to an equilibrium height of h_{cap}. Ignoring the weight of the air column with respect to that of the liquid column, the following equation is obtained:

$$(P_a - P_l) = (2\sigma / r_c) = \rho_l g h_{cap} \quad ; \quad r_c = r_p / \cos(\theta_c) \tag{5.3}$$

In Eq. (5.3), ρ_l is the mass density of the liquid; σ is the surface tension at the liquid-air interface; g is the gravitational acceleration; r_p is the inner radius of the pipe; and θ_c is the contact angle at static equilibrium [Stepanov et al. (1977)].

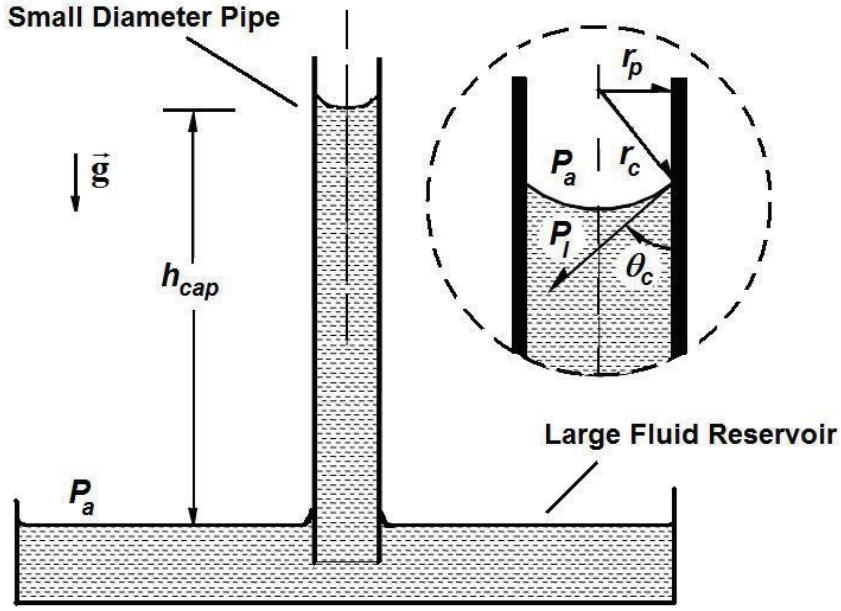

Figure 5.3: Schematic representation of capillary action inside a small diameter pipe.

The experiment depicted in Figure 5.3 could also be repeated if the pipe were replaced by a cylinder made of a porous material. The equilibrium height of the liquid column that would rise up in the porous cylinder could then be used in Eq. (5.3) to calculate a value of r_p, which would represent the effective pore radius of the interstices of the porous material under "rising" conditions.

Another experiment with a cylindrical piece of porous material inserted in a sample holder with a pipe attached to its *bottom* could be conducted as follows: Immerse the entire assembly in a pool of liquid contained in a vertical tube of larger diameter; after the porous disk (or cylinder) is fully saturated with the liquid and the tube at the bottom of the sample holder is completely filled, slowly withdraw the liquid in the larger tube until

the liquid column inside the bottom tube breaks away from the porous sample. The height of this liquid column just prior to its collapse is then used in Eq. (5.3) to compute a corresponding value of r_p, which would represent the effective pore radius under "falling" conditions [Alexander (1972); Stepanov et al. (1977)].

In earlier experimental studies [Alexander (1972); Stepanov et al. (1977)], values of the effective pore size ($d_p = 2r_p$) obtained under rising conditions have been found to be consistently less than those obtained under falling conditions, but no convincing explanation has been advanced for this observation. However, a careful examination of the data indicated that these rising and falling values are dictated by the minimum and maximum effective pore radii, respectively, of the interstices of the porous material [Atabaki (2006)].

Furthermore, in HPs, CPLs, and LHPs operating just beyond their capillary limit [Silverstein (1992)], the vapor pushes the liquid out of the wick material, and the corresponding capillary pressure is that obtained with the falling (or maximum) value of the effective pore size. The determination of this maximum effective pore size is the focus of the experimental work described next.

5.3.2 Experimental Apparatus and Procedure

The apparatus that was designed, constructed, and used in this work was adopted directly from the work of Atabaki (2006), and is depicted in Figure 5.4. It is an improved version of an apparatus designed by Alexander (1972).

This apparatus was designed to accommodate cylindrical (disk-shaped) test samples of 22.23 mm diameter and 3.18 mm thickness (nominal). As was mentioned previously, in this study, disk-shaped (cylindrical) samples cut from a 3.18 mm thick (nominal) porous sintered-powder-metal plate of stainless steel (SS) 316 were tested. It is important to note again that these disk-shaped samples were cut out of the porous plates using laser machining, which ensured that their curved surface (cut edge) was sealed (impermeable to the working fluid).

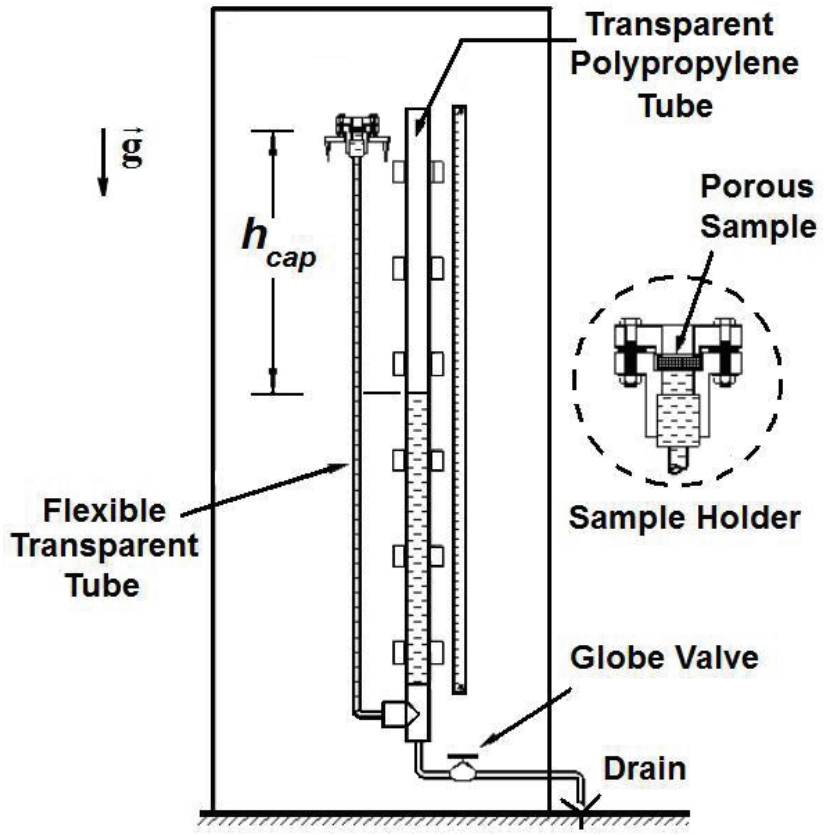

Figure 5.4: Schematic representation of the experimental apparatus used for measurements of the maximum effective pore size.

In the apparatus illustrated in Figure 5.4, the straight Polypropylene tube has an outer diameter of 50.8 mm and a total length of 2 m. The porous metal sample was sandwiched between two specially designed flanges, along with ring-shaped gaskets (see inset in Figure 5.4). In this work, isopropanol (99.9% purity) was used as the working fluid. At the start of each experimental run, the porous sample was thoroughly cleaned using high-pressure nitrogen to sequentially push high-purity (99.9%) isopropanol several times through the porous sample. Next, the test cell was located in its fixed position (as shown in Figure 5.4), the globe valve fully closed, and the entire system completely filled with high-purity (99.9%) isopropanol. Following this, the globe valve was opened slightly to allow the isopropanol to very slowly drain out of the system. In the early stages of this draining process, the isopropanol levels both in the Polypropylene tube and on top of the porous sample decreased. However, once the liquid-air interface entered the porous sample, a capillary pressure jump was created, and isopropanol drained only from the

Polypropylene tube. In each run, the isopropanol in the Polypropylene tube was allowed to continue draining until the column of isopropanol in the flexible transparent tube (supported by capillary forces in the porous material) broke away from the sample: The height of this isopropanol column in the flexible transparent tube, h_{cap}, was recorded and used in Eq. (5.3) to compute the maximum (falling) effective pore size ($d_p = 2r_p$) of the sample.

5.3.3 Results and Discussions

Table 5.1: Results of the maximum effective pore size experiment.

Test No.	h_{cap} [m]	ΔP [kPa]	θ_c [deg]	d_p [mm]
1	0.375	2.877	20	27.44
2	0.375	2.877	20	27.44
3	0.380	2.915	20	27.08
4	0.378	2.896	20	27.26
5	0.375	2.877	20	27.44
6	0.375	2.877	20	27.44
7	0.378	2.896	20	27.26
8	0.378	2.896	20	27.26
9	0.378	2.896	20	27.26
10	0.378	2.896	20	27.26

The final results obtained from ten runs with the stainless steel 316 cylindrical porous sample considered in this work are reported in Table 5.1. The contact angle was obtained from Stepanov et al. (1977). The average isopropanol temperature in the experiments was 25.1°C. For the porous sample tested, the values of the maximum effective pore size, $d_p = 2r_p$, were repeatable to within ± 0.9 % of the mean value.

The overall relative uncertainty in the maximum effective pore size was calculated using the method described in ASHRAE Standard 41.5-75 (1976).

The mean value of the maximum effective pore size, d_p, for the stainless steel 316 sample is the following:

$$d_p = 27.31\ \mu\text{m}\ (\pm\ 5.79\%).$$

5.4 EFFECTIVE PERMEABILITY

The effective permeability is needed for calculating the pressure drop associated with the flow of liquid through the wick, as was described in Chapter 2. A combined experimental-numerical method proposed by Atabaki (2006) was adapted and used to determine the permeability of the porous sintered-powder-metal disk made of stainless steel 316, and having a diameter of 22.23 mm and a nominal thickness of 3.18 mm. Some theoretical considerations, the aforementioned experiment-numerical method, and the usefulness of determining the effective permeability of the wick material with reference to the particular working fluid used in the LHP are discussed in this section.

5.4.1 Theoretical Considerations

In 1856, the French engineer Henry Philibert Gaspard Darcy conducted an experiment in Dijon, France, which is now regarded as a classical experiment on laminar flow through a homogenous porous medium. A schematic illustration of Darcy's experimental setup is provided in Figure 5.5. It consists of a homogenous porous material of height h packed inside a pipe of cross-sectional area $A_{c\text{-}s}$. An incompressible liquid is circulated through this porous material, and its volumetric flow rate, Q, is measured. A manometer is used to calculate the pressure drop across the top and bottom boundaries of the porous medium. Darcy conducted numerous experiments with this setup and observed a linear relationship between the volumetric flow rate of the liquid and the reduced pressure gradient across the porous medium.

Assuming that the mass density of the liquid, ρ_l, and the gravitational acceleration vector, g, are constant, Darcy's observation can be mathematically formulated as follows:

$$U = \frac{K}{\mu}\frac{(P_1 - P_2 + \rho_l g h)}{h} = \frac{K}{\mu}\frac{(\Delta \mathrm{P})_{fric}}{h} \tag{5.4}$$

In the above equation, U is the area-averaged velocity of the fluid ($U = Q/A_{c\text{-}s}$), μ is the dynamic viscosity of the fluid, K is the effective permeability of the porous medium, and $(\Delta P)_{fric}$ is the so-called friction pressure drop associated with the flow through the porous medium. This expression, originally proposed by Darcy as an empirical relation, has been derived by volume-averaging the Stokes equation by many researchers [Hubbert

(1956); Whitaker (1969); Slattery (1969); Lehner (1979)]. Furthermore, Beavers and Sparrow (1969) showed that departures of experimental results from Darcy's law, as expressed in Eq. (5.4), occur at values of Reynolds number (based on the square-root of the permeability of the porous material as the characteristic length) of the order of one or greater. As the porous sintered-powder-metal plates or tubes used in LHPs have fine pores, they also tend to have very low effective permeabilities. In addition, the flow rate in LHP wicks is usually very small. Thus, in this work, it is assumed that Darcy's law governs the liquid flow through the wick in LHPs.

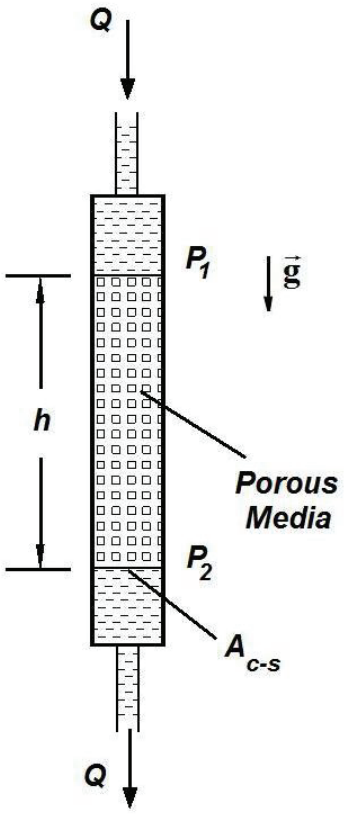

Figure 5.5: Schematic representation of Henry Philibert Gaspard Darcy's experimental setup in Dijon (France) for measurements of effective permeability.

The effective permeability is a geometrical property of porous materials. For porous media with simple and regular structures, such as homogeneous packed beds of spheres, analytical relations are available for determining the effective permeability: Some of these relations are presented in the works of Scheidegger (1974), Chi (1976), Dunn and Reay (1982), Faghri (1995), and Ochterbeck and Peterson (1997). However, as can be

seen from the photomicrographs presented in Figure 5.1, the geometry of the porous sintered-powder-metal plate used in this work is quite complex and highly irregular: Thus, the aforementioned analytical relations cannot be used to determine its effective permeability, and this task is best accomplished using an experimental method.

Experimental setups similar to Darcy's (see Figure 5.5) are commonly used to determine the effective permeability of porous materials by first assuming a macroscopic one-dimensional flow through the test section, and then using an equation akin to Eq. (5.4). However, for this approach to be strictly valid, the porous material must be fitted in the flow passage in such a manner that at its boundary with the walls of the test section, the effective permeability is unaltered. Welding, soldering, or press-fitting the sintered power-metal porous media into the test section is a viable approach to achieving good accuracy of the aforementioned one-dimensional formulation. Moreover, assuming that these operations would change the porosity and permeability of the porous media in a region immediately adjacent to the confining walls, possibly over a cross-sectional area $A_{c-s,peripheral}$, it is important to ensure that $A_{c-s,peripheral} / A_{c-s} << 1$. However, this approach may not always be convenient, practical, or cost-effective.

Another approach is to use laser machining to cut the sample of the sintered powder-metal porous medium (which seals its cut edge) and then place flat gaskets over peripheral regions of its upper and lower surfaces to seal it into the test section. Even with this procedure, in order to ensure the validity of the one-dimensional approach, it is necessary to ensure $(A_{c-s} - A_{open,c-s}) / A_{c-s} << 1$, where $A_{open,c-s}$ is the cross-sectional area on the upper and lower surfaces of the sample that is open to the flow (not blocked by the gaskets). In cases where it is not practical to make $(A_{c-s} - A_{open,c-s}) / A_{c-s} << 1$, it is necessary to use a multidimensional formulation of Darcy's law to model the flow in the porous media in between the gaskets, and use a numerical solution of the governing equations, with inputs of experimental data, to obtain the effective permeability. Such an experimental/numerical approach was presented in Atabaki (2006), and its application for the determination of the effective permeability of the porous sintered-powder-metal (stainless steel 316) plate considered in this work is described in this section. The

experimental setup is explained in the next subsection, followed by subsections describing the experimental data, the experimental/numerical procedure, and the results.

5.4.2 Description of the Experimental Setup and Procedure

A schematic representation of the experimental setup that was designed, constructed, and used to measure the effective permeability of samples of the sintered powder-metal plate is given in Figure 5.6. High-purity (99.9%) isopropanol was used as the working fluid in the experiments.

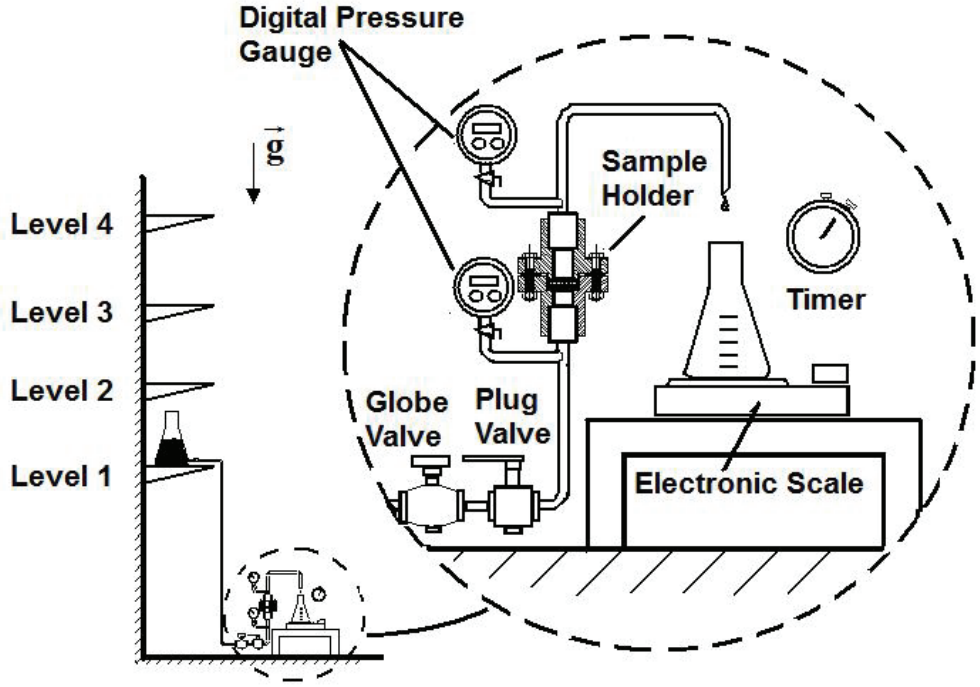

Figure 5.6: Schematic representation of the experimental setup used for measurements of effective permeability.

As shown above in Figure 5.6, the isopropanol was gravity fed from a reservoir (a glass flask), which could be located at four different levels above the floor of the laboratory. A flexible tube was used to connect this reservoir to the test cell (labeled as sample holder in Figure 5.6) in which the porous material was held. A plug valve was used to turn the flow on and off, and a globe valve was used to control the flow rate. Two digital pressure gauges (Omega DPG1000B, 0-15 psig) were used for measuring the static pressure immediately before and directly after the test cell. The mass flow rate of the isopropanol was obtained by collecting it in a small glass flask (250 ml Erlenmeyer flask) until it was

nearly full, recording the related time, weighing the flask plus the isopropanal (using an electronic balance accurate to ±0.01 g), subtracting out the mass of the empty (dry) flask, and dividing the mass of the isopropanol by the recorded time. A cylindrical (disk-shaped) test sample having a diameter of 22.23 mm and a nominal thickness of 3.18 mm (cut using laser machining) was used in this experiment.

As was mentioned previously, flat gaskets were used for sealing the stainless steel 316 porous sample in the test cell. The areas sealed by gaskets on the upper and lower surfaces of the cylindrical sample are schematically presented in Figures 5.7. The peripheral surfaces of the porous sample were also sealed (impermeable), given that they were cut using laser machining.

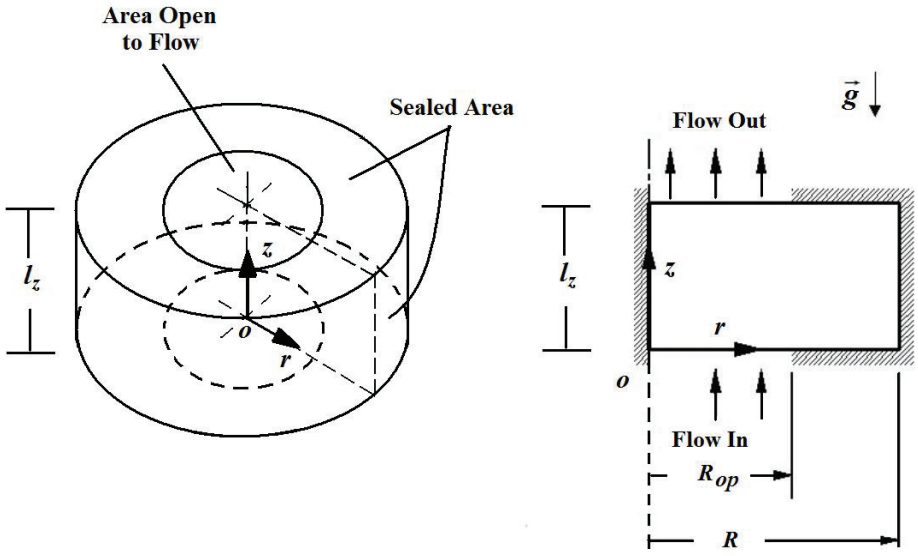

(a) (b)

Figure 5.7: Geometrical description of the cylindrical (disk-shaped) porous sample: (a) isometric view of the sample; and (b) the *rz* plan view of the sample.

The dimensions of the cylindrical (stainless steel 316) porous sample as per the notation given in Figure 5.7 are the following:

$$R = 1.11\text{x}10^{-2}[\text{m}],\ R_{op} = 5.74\text{x}10^{-3}[\text{m}],\ \text{and}\ l_z = 3.18\text{x}10^{-3}[\text{m}]$$

In terms of the notation shown in Figure 5.7, the open (unblocked) area for flow through the bottom and top surfaces of the cylindrical porous sample is $A_{o,cyl} = \pi R_{op}^2$.

Before starting the experiments, the test samples were cleaned using the same procedure as that used in the experiments to measure the maximum effective pore size

(see Subsection 5.3.2). Then, the desired test-sample and test-cell combination were installed in the setup, and the entire flow circuit shown in Figure 5.6 was filled with high purity (99.9%) isopropanol. The reservoir was located at level 4 (highest point), and all valves were fully opened, allowing the isopropanol to flow through the porous sample. About six liters of isopropanol were circulated through the porous sample in order to purge any residual air or nitrogen inside it. Then the plug valve was closed, the empty 250 ml Erlenmeyer flask was weighed, and the isopropanol temperature was measured. The two electronic pressure gauges were turned on, and their readings were recorded: The difference between these readings in the no-flow condition represents the hydrostatic pressure drop across the porous sample. To obtain the friction pressure drop, the hydrostatic pressure drop was subtracted from the difference in the readings of these pressure gauges with the isopropanol flowing through the porous sample assuming that the minor losses in the fittings at the low flow rates used in these experiments were negligible compared to the friction pressure drop through the porous material.

After the above-mentioned preparations and preliminary measurements, the experimental setup was considered ready for the final measurements. For each of the reservoir position, it was important to first record the arithmetic means of at least five sets of measurements of the mass flow rate of the isopropanol and the associated frictional pressure drop across the porous sample with both the plug valve and the globe valve fully open, after which several additional sets of these measurements were obtained at lower flow rates (using the globe valve for flow control).

5.4.3 Experimental Determination of the Effective Permeability

The experimental data obtained for the cylindrical (disk-shaped) porous sample made of stainless steel 316 is shown in Figure 5.8. The symbols in this figure correspond to the experimental data, and the straight line is a least-square fit to the data which is forced to pass through the origin (0,0): The equation that represents this line is given in title of this figure. As is indicated by the results presented in Figure 5.8, the frictional pressure drop across the porous sample, $(\Delta P)_{fric}$, varies linearly with the mass flow rate, $\dot{m}$, indicating that the flow is in the Darcy regime for all cases considered here.

The absolute uncertainties in the pressure-drop measurements were all less than ±365.5 Pa. The vertical error bars in Figure 5.8 represent these absolute uncertainties in the measurements of the friction pressure drop across the porous samples. The maximum relative uncertainty in the pressure-drop measurements for the disk-shaped stainless steel 316 sample is ±6.51%. The uncertainty in the mass flow rate data was found to be less than ±1.0%.

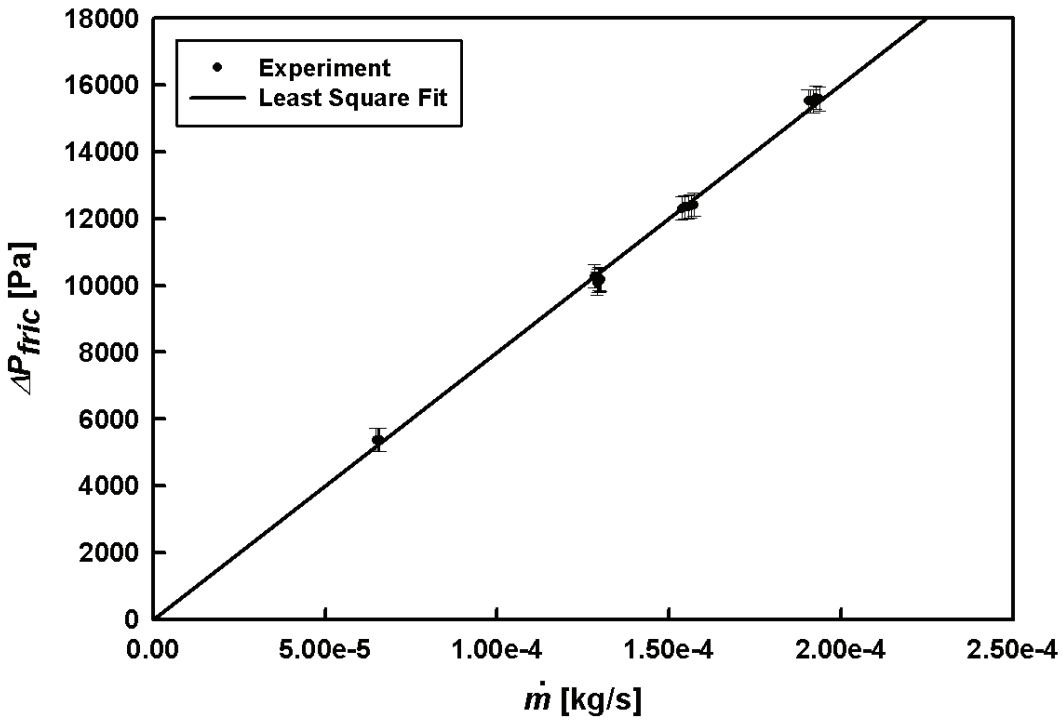

Figure 5.8: Data from the permeability experiments on a cylindrical sample of stainless steel 316. Least-squares straight line: $(\Delta P)_{fric}\ [\mathrm{Pa}] = 8.031\mathrm{x}10^{7}\,\dot{m}\ [\mathrm{kg/s}]$.

If one-dimensional flow through the considered sample porous media is assumed, the area-averaged liquid velocity can be obtained using the following expression:

$$U = \dot{m} / (\rho A_{o,cyl}) = \dot{m} / (\rho \pi R_{op}^2) \qquad (5.5)$$

In this equation, R_{op} is the radial dimension of the open (unblocked) flow areas on the top and bottom surfaces of the cylindrical porous sample (see Figures 5.7). The area-averaged velocity, *U*, given by Eq. (5.5), is used in the one-dimensional formulation of Darcy's law, Eq. (5.4), to calculate the permeability *K*.

The experiments were performed at a temperature of 21.1 ^{o}C. At this temperature, the values of mass density and dynamic viscosity of isopropanol are the following [Incropera and DeWitt (2002)]: ρ_l = 784.71 kg/m³ and μ = 2.21×10^{-03} kg/m-s. Based on these properties of isopropanol, the experimental data presented in Figure 5.8, and the U value computed using Eq. (5.5), the experimental value of the effective permeability of the porous sintered-powder-metal sample made of stainless steel 316 was determined (based on the one-dimensional Darcy flow assumption):

$$K_{1D} = 8.875\text{x}10^{-13}\ \text{m}^2\ (\pm\ 3.1\%)$$

5.4.4 Validity of the One-Dimensional Darcy Flow Assumption

In the previous section, the determination of the effective permeability of a sample sintered powder-metal porous material using a relatively simple experimental approach was demonstrated. However, this exercise was conducted without strictly verifying the validity of the underlying assumption that the flow through the porous media is essentially one-dimensional. As was mentioned earlier, in order to ensure the validity of the one-dimensional approach, it is necessary to maintain $(A_{c-s} - A_{open,c-s}) / A_{c-s} << 1$. Based on the reported values of $R = 1.11\text{x}10^{-2}$ [m] and $R_{op} = 5.74\text{x}10^{-3}$ [m], the ratio $(A_{c-s} - A_{open,c-s}) / A_{c-s} = 0.73$ was calculated, which is clearly non-negligible. Therefore, in this case, the cross-sectional area of the gasket used to properly seal the top and bottom surfaces of the sample porous material in the test cell (see Figure 5.7) becomes comparable to the cross-section area of the porous sample, and invalidates the underlying one-dimensional flow assumption strictly required for the proposed experiment.

Possible remedies for this difficulty would be to (1) reduce the size of the gasket used to seal the porous material in the test cell, and/or (2) to increase the diameter of the porous sample utilised in the experiment. However, reducing the size of the gasket could result in poor sealing of the porous media in the test cell and lead to leakage in the test cell: This approach is impractical. On the other hand, increasing the size of the porous test specimen may not be always convenient, practical or cost-effective.

An alternative method would be to solve a multidimensional formulation of Darcy's law, with the above-mentioned experimental data as inputs, and check the corresponding values of the effective permeability. This multidimensional experimental/numerical approach to the calculation of the effective permeability and the results are presented in the following subsection based on the work of Atabaki (2006).

5.4.5 A Multidimensional Technique for the Evaluation of Effective Permeability

For an axisymmetric, constant-property fluid flow through a porous material with constant permeability, K, Darcy's law in the cylindrical coordinate (r, z) can be written as follows [Kaviany (1999); Nield and Bejan (2006)]:

$$u_r = -\left(\frac{K}{\mu}\right)\frac{\partial \mathrm{P}}{\partial r}; \quad u_z = -\left(\frac{K}{\mu}\right)\frac{\partial \mathrm{P}}{\partial z} \tag{5.6}$$

In this equation, u_r and u_z are the velocity components in r and z directions, respectively, and P is the reduced pressure: $\mathrm{P} = P + \rho_l g z$, where P is the static pressure, g is the gravitational acceleration, and the term $\rho_l g z$ represents the hydrostatic pressure. It is assumed here that the gravitational acceleration vector is directed along the negative z direction.

Assuming steady-state, constant-property, incompressible fluid flow in the porous medium, the continuity equation is

$$\frac{1}{r}\frac{\partial\left(r u_r\right)}{\partial r} + \frac{\partial u_z}{\partial z} = 0 \tag{5.7}$$

Combining Eqs. (5.6) and (5.7), the following equation is obtained:

$$\frac{1}{r}\frac{\partial}{\partial r}\left(r\frac{\partial \mathrm{P}}{\partial r}\right) + \frac{\partial^2 \mathrm{P}}{\partial z^2} = 0 \tag{5.8}$$

Next, with reference to the schematic representations of the calculation domains and the notations given in Figure 5.7, the boundary conditions that apply to the cylindrical porous sample are as follows:

$$
\begin{aligned}
&r = 0;\ 0 \le z \le l_z \quad \frac{\partial \mathrm{P}}{\partial r} = 0 \\
&r = R;\ 0 \le z \le l_z \quad \frac{\partial \mathrm{P}}{\partial r} = 0 \\
&z = 0;\ 0 \le r \le R_{op} \quad \mathrm{P} = \mathrm{P}_1 \\
&z = l_z;\ 0 \le r \le R_{op} \quad \mathrm{P} = \mathrm{P}_2 \\
&z = 0;\ R_{op} \le r \le R \quad \frac{\partial \mathrm{P}}{\partial z} = 0 \\
&z = l_z;\ R_{op} \le r \le R \quad \frac{\partial \mathrm{P}}{\partial z} = 0
\end{aligned}
\tag{5.9}
$$

In these equations, P_1 and P_2 are the reduced pressures that prevail over the inlet and outlet flow areas of the cylindrical porous sample.

Equation (5.8) is akin to the equation that governs steady-state, constant-property, diffusion-type problems with a diffusion coefficient of one (unity) and no (zero) volumetric source term. A well-established finite volume method proposed by Patankar (1980) was used to discretize and solve Eq. (5.8) subject to the boundary conditions given by Eq. (5.9): In these numerical solutions, P_2 was set equal to zero (for convenience), and P_1 was set equal to a specified value, such that $(P_1 - P_2)$ covered the range of the friction pressure drops involved in the permeability experiments (see Figure 5.8). It should be noted here that as the working fluid (isopropanol) is assumed to be incompressible, the absolute level of pressure is unimportant and can be set to any convenient value [Patankar (1980)]: The pressure difference imposed across the porous sample is what drives the flow through it. In each case, once the pressure field was computed, the corresponding inlet (or outlet) mass flow rate was calculated with velocity components obtained using Eq. (5.6) for the cylindrical sample, along with prescribed values of the liquid mass density, ρ_l, and dynamic viscosity, μ: These calculated mass flow rates were in the form $\Im K$, where $\Im$ is a computed number and K is the (unknown) permeability of the porous medium. The experimental data were used to determine the permeability K as follows: For each prescribed value of $(P_1 - P_2)$, the computed mass flow rate, $\Im K$, was equated to the corresponding experimentally measured value, $\dot{m}$, and the permeability was calculated using $K = \dot{m} / \Im$.

To test for grid independence of the numerical results, the computations were conducted with $(K/\mu)=1$ on two different grids for each sample: For the cylindrical sample with grids of 101×401 and 126x501 nodes (in the *r* and *z* directions) the relative difference between the calculated values of permeability was less than ±0.05%. Based on these findings, in the final computations, a grid of 101x401 nodes was used for the cylindrical sample

The numerical results obtained for the cylindrical (disk-shaped) sintered powder-metal plate made of stainless steel subjected to an overall pressure difference ($P_1 - P_2$) of 1000 Pa are presented in Figure 5.9:

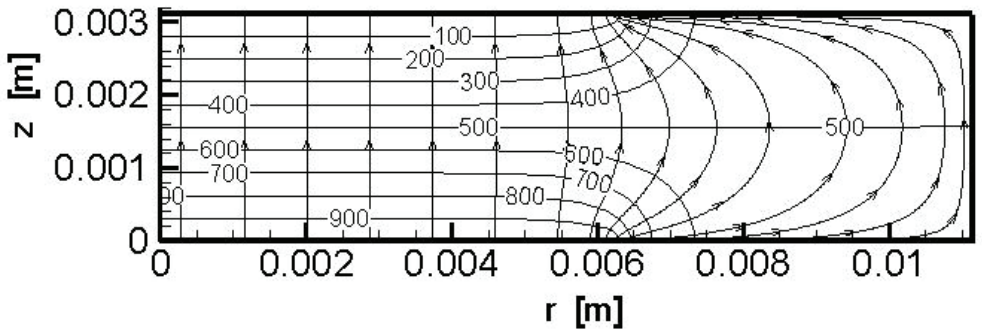

Figure 5.9: Numerically calculated isobars (reported in Pa) and streamlines (not to scale) in a diametrical cross section of the cylindrical, stainless steel 316, porous specimen: Pressures imposed at the inlet and outlet planes are P_1=1000 Pa and P_2=0 Pa, respectively.

The results for the cylindrical sample ($R=1.11\text{x}10^{-2}[\text{m}]$, $R_{op}=5.74\text{x}10^{-3}[\text{m}]$, and $l_z=3.18\text{x}10^{-3}[\text{m}]$) presented in Figure 5.9, indicate that the streamlines (lines with arrow heads) are significantly bent (indicating two-dimensional flow) in the outer regions, over almost half of the radius: This is because the sealing gaskets block significant portions of the top and bottom surfaces of this sample (see Figure 5.7): $(R-R_{op})/R=0.478$.

The permeability value computed using the proposed experimental/numerical method for the cylindrical, sintered power-metal, porous specimen made of stainless steel 316 is the following:

$$K_{Multi-D}=7.356\text{x}10^{-13}\ \text{m}^2\ (\pm\ 2.5\%)$$

In comparison with the corresponding results obtained using the simple one-dimensional method (see the previous subsection, $K_{1-D} = 8.875\text{x}10^{-13}\ \text{m}^2$), the permeability for the cylindrical sample is about 20.6 % lower, as the multidimensional effects are quite pronounced, and the effective flow area in the central region of the sample, in between the gaskets, is quite a bit larger than the open areas in the inlet and outlet planes.

5.4.6 Impact of Test Fluids Used in the Determination of Effective Permeability

The permeability of a porous medium is considered to be a geometrical property related to the inherent microstructure of the material [Vafai (2005); Nield and Bejan (2006)], and, as such, should not be dependent on the specific type of fluid used to determine this property. In most industrial settings, inert gases (instead of liquids) are used as the more convenient and preferred test fluids due to their ease of handling, transportation, and storage. In fact, many manufacturers of porous materials commonly only test and report the gas-permeability (permeability determined using a gas as the test fluid) of their products.

However, there are reports of discrepancies observed in the experimental determination of permeability depending on the phase (gas or liquid) of the test fluid used, and also the type of liquid (water, ethanol, isopropanol, etc.) considered; and these differences are more pronounced for small-pore-size materials (such as the wicks used in LHPs, for example) [Klinkenberg (1941); ISO 4022 (1987); Loosveldt et al. (2002)]. The gas-to-liquid permeability ratio, and the liquid-to-liquid permeability ratio can, at times, range between 2 - 140 [Loosveldt et al. (2002].

A possible explanation for the discrepancy observed between the gas- and liquid-permeability has been linked to the adsorptive reaction that some metals exhibit with certain liquids. In this case, the pore size of the porous material is effectively reduced due to the adhesion of atoms, ions, or molecules on the metal surfaces [ISO 4022 (1987)] leading to a decrease in the effective permeability.

It is clear that there is a need to accurately and reliably determine the effective permeability of wicks used in LHPs (and also HPs and CPLs), for the design, modeling, and optimization of these devices. Based on the observations and discussions presented

above, it is strongly advisable to select the same test fluid in the permeability experiments as the particular working fluid of the LHPs (and also HPs and CPLs). This approach would provide the most reliable estimate of the effective permeability of the wick material under actual operating conditions of the LHP.

5.5 EFFECTIVE THERMAL CONDUCTIVITY

In mathematical models of LHPs, the effective thermal conductivity of the wick structure is needed to calculate the so-called *heat-leak* from the wick to the compensation chamber, as was illustrated in Chapter 2. In this section, some available analytical and semi-analytical correlations for the effective thermal conductivity of porous media are reviewed. Following that, a correlation put forward by Atabaki and Baliga (2007) for the calculation of the effective thermal conductivity in liquid-saturated, porous sintered-powder-metal plates is presented and discussed.

In the published literature, there are several analytical and numerical correlations for the determination of the effective thermal conductivity of fluid-saturated porous materials as a function of the fluid and solid thermal conductivities and geometrical details of the porous structure. Some examples include the works of Maxwell (1954), Kunii and Smith (1960), Dul'nev (1965), Ofuchi and Kunii (1965), Hadley (1986), Prasad et al. (1989), Bauer (1993), Hsu et al. (1995), Calmidi and Mahajan (1999), Boomsma and Poulikakos (2001), Bahrami et al. (2004), Petrasch et al. (2008), and Yu et al. (2011). Furthermore, various experimental investigations, and corresponding correlations, of the effective thermal conductivity of porous materials made of sintered powders and fibers, with a liquid, gas, or vacuum in the interstices or voids are presented in the works of Alexander (1972), Singh et al. (1973), Hadley (1986), Peterson and Fletcher (1987), Mantle and Chang (1991), and Atabaki (2006).

5.5.1 Review of Some Available Correlations

The discussion in this section is largely borrowed from Atabaki (2006) and Atabaki and Baliga (2007). Some well-established analytical and semi-analytical correlations that relate the *effective* thermal conductivity of a porous media, k_{eff}, to its porosity, ε, and the

thermal conductivities of the fluid and solid phases, k_f and k_s, respectively, are briefly reviewed in this section.

The parallel and series arrangements of solid spherical particles with fluid in the interstices are the simplest geometrical structures considered in analytical models of the effective thermal conductivity of porous media; these arrangements yield upper and lower limits, respectively, of this property [Batchelor and Obrien (1977); Hadley (1986); Kaviany (1999)]. The parallel model provides the following result:

$$\frac{k_{eff}}{k_f} = \varepsilon + (1-\varepsilon)\frac{k_s}{k_f} \tag{5.10}$$

The following expression is obtained using the series model:

$$\frac{k_{eff}}{k_f} = \frac{(k_s / k_f)}{\varepsilon(k_s / k_f) + (1-\varepsilon)} \tag{5.11}$$

Maxwell (1954) performed analytical studies of two solid-fluid systems and proposed equations for the prediction of their effective specific electrical-resistance. His work can be adapted to obtain the corresponding effective thermal conductivity of solid-fluid systems similar to fluid-saturated porous media [Hadley (1986)]. The first such system consists of a dilute suspension of solid spherical particles in an infinite uniform fluid. Its effective thermal conductivity is given by the following equation:

$$\frac{k_{eff}}{k_f} = \frac{2\varepsilon + (k_s / k_f)(3-2\varepsilon)}{3-\varepsilon + (k_s / k_f)\varepsilon} \tag{5.12}$$

This equation has been referred to by Hadley (1986) as the "lower Maxwell formula". The second system analyzed by Maxwell consists of a solid body containing a dilute dispersion of fluid-filled voids. The effective thermal conductivity of this second system is given by the following equation, referred to by Hadley (1986) as the "upper Maxwell formula":

$$\frac{k_{eff}}{k_f} = \frac{2(k_s / k_f)^2 (1-\varepsilon) + (1+2\varepsilon)(k_s / k_f)}{(2+\varepsilon)(k_s / k_f) + 1 - \varepsilon} \tag{5.13}$$

Dul'nev (1965) modelled porous materials as a combination of cubic unit cells with interconnected pores. He applied a resistance analogy to obtain an effective thermal

conductivity of the unit cell, based on an assumption of unidirectional heat conduction. His analytical solution is presented below:

$$\frac{k_{eff}}{k_f} = \frac{k_s}{k_f} s^2 + (1-s)^2 + \frac{2s(1-s)}{1-s\left[(k_s/k_f - 1)/(k_s/k_f)\right]}$$
$$s = y/(0.5-y)/\left[1 + y/(0.5-y)\right] \qquad (5.14)$$
$$4y^3 - 3y^2 + (1-\varepsilon)/4 = 0$$

Alexander (1972) experimentally determined the effective thermal conductivities of some samples of porous materials saturated with water (wet) or air (dry). These samples were made of metal felts, sintered powders, layers of wire cloth, and unconsolidated bead beds. He used his experimental data to propose the following empirical correlation:

$$\frac{k_{eff}}{k_f} = \left(k_s/k_f\right)^{(1-\varepsilon)^\delta} \qquad (5.15)$$

The following values are recommended for the parameter δ in this equation [Alexander (1972)]: For metal felts, δ = 0.34; sintered powders, δ = 0.53; layers of wire cloth, δ = 0.59; and for unconsolidated beads, δ = 0.44.

Hadley (1986) has proposed a general approach to modeling the effective thermal conductivity of packed metal powders. The approach involves combining a theoretical expression appropriate for conduction through a contiguous solid (the upper Maxwell formula) and another such expression that is suitable for conduction through a suspension (not necessarily dilute) of solid particles. For a solid-fluid (two-phase) system, where the solid is connected (consolidated by cold pressing), Hadley (1986) proposed the following equation for the effective thermal conductivity:

$$\frac{k_{eff}}{k_f} = (1-\alpha_{con})\left[\frac{\varepsilon f_0 + (k_s/k_f)(1-\varepsilon f_0)}{1-\varepsilon(1-f_0)+(k_s/k_f)\varepsilon(1-f_0)}\right] + \alpha_{con}\left[\frac{2(k_s/k_f)^2(1-\varepsilon)+(1+2\varepsilon)(k_s/k_f)}{(2+\varepsilon)(k_s/k_f)+1-\varepsilon}\right] \qquad (5.16)$$

where the values of the parameters α_{con} and f_o are to be determined with reference to experimental data. The parameter α_{con} depends strongly on what Hadley (1986) refers to as the "degree of consolidation"; it will be referred to here as the consolidation

parameter. The value of the parameter f_o lies between the theoretical upper and lower limits provided by Maxwell's formulas: Thus,

$$f_{o,\min} = \frac{2}{3} \quad ; \quad f_{o,\max} = \frac{2(k_s / k_f)}{2(k_s / k_f) + 1} \quad ; \quad f_{o,\min} < f < f_{o.\max} \tag{5.17}$$

Here, $(k_s / k_f) \geq 1$. For Hadley's experimental data (1986), $0.8 \leq f_o \leq 0.9$. The values of the parameter α_{con} as a function of $(1-\varepsilon)$ for evacuated samples ($k_s / k_f \to \infty$) have been presented graphically by Hadley (1986): Nonlinear (semi-log) curve fits to Hadley's data for α_{con}, as proposed by Kaviany (1999), are given below:

$$\log(\alpha_{con}) = \begin{cases} -4.898\varepsilon & for\ 0 \leq \varepsilon \leq 0.0827 \\ \left(-0.405 - 3.154\left(\varepsilon - 0.0827\right)\right) & for\ 0.0827 < \varepsilon \leq 0.298 \\ \left(-1.084 - 6.778\left(\varepsilon - 0.298\right)\right) & for\ 0.298 < \varepsilon \leq 0.580 \end{cases} \tag{5.18}$$

Bauer (1993) has presented an analytical approach for the determination of the effective thermal conductivity of porous media. He started with the theoretical lower formula of Maxwell, Eq. (5.17), for dilute suspensions of spherical particles, and then extended it to suspensions of solid particles of random shapes and different concentrations. Bauer proposed the following implicit correlation for the calculation of the effective thermal conductivity of porous materials with a single type of randomly oriented pores:

$$\frac{k_{eff} - k_p}{k_o - k_p}\left(\frac{k_o}{k_{eff}}\right)^{1-2/(3\beta)} = 1 - \varepsilon \tag{5.19}$$

Here, k_o and k_p respectively denote the thermal conductivities of the continuous medium and the material inside the pores. The term, β, in this equation is a shape factor: Its value lies in the range $2/3 < \beta \leq 1$, with the upper limit of unity applicable to spherical pores. Its value for specific materials is determined using corresponding experimental data.

5.5.2 Correlation for the Effective Thermal Conductivity of Liquid-Saturated Sintered Powder-Metals

Based on an earlier experimental investigation [Atabaki (2006)], Atabaki and Baliga (2007) proposed a correlation for the effective thermal conductivity of liquid-saturated

sintered powder-metal porous media by borrowing and extending ideas from the works of Kunii and Smith (1960) and Hadley (1986). In this work, the authors focused on the thermal conductivity of liquid-saturated *sintered* powder-metal plates. These sintered porous metal plates are different from the *cold-pressed* packed metal-powder porous media used by Hadley (1986), in that the thermal conduction across the solid-to-solid contacts zones between the metal particles created by the sintering process is better than that across similar contact zones created by the cold-pressing process.

In the proposed correlation, the basic combined expression, Eq. (5.16), proposed by Hadley (1986) was retained. However, it was hypothesized that, in this combined expression, the parameters α_{con} and f_o are functions of not only the porosity, ε, as originally proposed by Hadley (1986), but also of the conductivity ratio k_s / k_f. The inspiration for this postulate was derived from the earlier work of Smith and Kunii (1960). The following function was then proposed for the consolidation parameter, α_{con}:

$$\ln(1-\alpha_{con}) = \frac{-\Lambda\left(\frac{1-\varepsilon}{\varepsilon}\right)^m}{\left[1-\left(\frac{k_s}{k_f}\right)^{-n}\right]} \quad \text{or} \quad \alpha_{con} = 1-\exp\left\{\frac{-\Lambda\left(\frac{1-\varepsilon}{\varepsilon}\right)^m}{\left[1-\left(\frac{k_s}{k_f}\right)^{-n}\right]}\right\} \tag{5.20}$$

This expression is applicable to systems for which $(k_s / k_f) \geq 1$: Note that when $(k_s / k_f) \to 1$ and $0 < \varepsilon < 1$, $\alpha_{con} \to 1$. The parameter f_o is assumed to be the following porosity-weighted average of the values corresponding to Maxwell's upper and lower limits:

$$f_{o,\min} = \frac{2}{3} \quad ; \quad f_{o,\max} = \frac{2(k_s / k_f)}{2(k_s / k_f)+1} \quad ; \quad f_o = f_{o,\min}\varepsilon + f_{o,\max}(1-\varepsilon) \tag{5.21}$$

Equations (5.20) and (5.21) guarantee that when the porosity approaches very small values ($\varepsilon \to 0$), $\alpha_{con} \to 1$ and $f_o \to f_{o,\max}$; and when the porosity approaches its highest value ($\varepsilon \to 1$), $\alpha_{con} \to 0$ and $f_o \to f_{o,\min}$.

Based on the application of curve fitting techniques with the experimentally determined values of the effective thermal conductivity detailed in Atabaki (2006), and

also on the experimental results reported by Peterson and Fletcher (1987), the constants in the Eq. (5.20) were determined [Atabaki (2006); Atabaki and Baliga (2007)]:

$$\Lambda = 0.148 \quad ; \quad m = 0.283 \quad ; \quad n = 0.04$$

The correlation proposed by Atabaki and Baliga (2007) predicted all of the values of the effective thermal conductivity experimentally determined by Atabaki (2006), and also those reported by Peterson and Fletcher (197) with a mean deviation of less than $\pm 5.67\%$ and a maximum deviation of $\pm 19.39\%$. Their correlation was selected for implementation in the segmented network thermofluid model of LHPs proposed in Chapter 2, and also in the enhanced version of this model that is demonstrated in Chapter 6.

Chapter 6:

Enhanced Segmented Network Thermofluid Simulations of a Loop Heat Pipe Operating with Four Different Working Fluids

A segmented network thermofluid model of loop heat pipes (LHPs) operating under steady-state conditions was proposed in Chapter 2. The methods and models put forward in Chapters 3 and 4 were used to proposed novel correlations for predicting the pressure drop and bulk temperature in the vapor-grooves of LHP evaporators. These novel correlations were then incorporated into the above-mentioned segmented network thermofluid model to obtain an enhanced version of this model.

In this chapter, the capabilities of this enhanced segmented network thermofluid model are demonstrated by using it to simulate a sample LHP running with four different working fluids (ammonia, distilled, ethanol, and isopropanol) for a range of operating conditions relevant to the thermal management of a state-of-the-art central processing unit (CPU) installed in a server that is part of a so-called cloud-computing system [Mell and Grance (2011)]. First, the influence of the operating conditions on the characteristics of the sample LHP running with ammonia as the working fluid are presented and discussed. Following that, results that illustrate differences in the predictions obtained with the aforementioned novel and the old correlations for the pressure drop in LHP vapor grooves are presented and discussed. Then, pressure drops in the various components of the sample LHP running with the four aforementioned working fluids for a baseline set of operating conditions are presented, along with comparative discussions. Finally, some of the features of the two-phase flow in the condenser of the sample LHP are presented with reference to a flow regime map proposed by Taitel and Dukler (1976).

6.1 Background Note on the Demonstration Problem

Thermal management of modern digital computers and electronics is becoming increasing important and challenging due to the relentless demand for more powerful, faster, and smaller devices. Currently, state-of-the-art central processing units (CPUs) and graphics processing units (GPUs), which will be referred to as chips in this chapter

(following standard terminology), dissipate between 100 W and 150 W, and the external heat transfer area of these chips has become less than 4 cm^2 [Singh. et al. (2007); Maynadik et al. (2010)]. The related thermal management problems are considerable, to say the least, and are further complicated by packaging-space limitations, and the requirement that the chip-case temperature be between 70 - 80 °C to ensure operation.

Heat pipes (HPs) have been successfully used to address some of the above-mentioned thermal-management challenges. However, as noted by Maydanik (2010), when the power dissipation requirements of these electronic devices exceeds 150 W, both the size and the heat transfer capacity of HPs pose a serious impediment to their usage. Loop heat pipes (LHPs) offer a viable alternative for meeting these ever-growing thermal-management requirements, but the manufacturing costs of LHPs are currently about one order of magnitude higher than those of conventional HPs. As a result, presently, there is great deal of interest in theoretical, experimental, and numerical investigations aimed at improving the designs of LHPs adapted for cooling of chips in personal computers, supercomputers, servers, and datacenters [Singh et al. (2007); Zimbeck et al (2008); Maydanik et al. (2010); Li et al. (2010); Li and Peterson (2011)].

With the above-mentioned observations in mind, it was decided to demonstrate the capabilities of the proposed enhanced segmented network thermofluid model by applying it to a sample LHP intended for thermal management of the chips in a cloud-computing server unit. The objective is to evaluate the performance of the proposed sample LHP in maintaining the casing temperature of the chip (akin to Intel Xeon Processor X5690) below a safe-operating limit of 70°C while dissipating a maximum of 260 W. Four different working fluids (ammonia, distilled water, ethanol, and isopropanol) are considered, for a representative range of operating conditions. Details of the sample LHP and the operating conditions considered are presented in the next section.

6.2 Details of the Sample LHP and the Operating Conditions Considered

The sample LHP has a flat evaporator and its other attributes are similar to those illustrated in Figure 2.1b. The wick fitted in the evaporator consists of a 80 mm x 80 mm x 3.175 mm sintered-powder-metal plate made of stainless steel 316, with properties matching those presented earlier in Chapter 5. Fourteen (14) rectangular vapor-removal

channels (each with length x width x height combination of 80 mm x 2 mm x 1 mm) are machined in the upper-part of the evaporator, as shown in Figure 2.4. The vapor- and liquid-transport lines, as well as the condenser unit, are made of a smooth stainless steel 316 tubing, with inner diameter of 5 mm, wall thickness of 1 mm, and an effective length of 300 mm. The vapor-transport line is assumed to be well insulated, with allowance for only partial condensation. The liquid-transport line is also well insulated, and is assumed to be essentially adiabatic. The condenser unit is attached with excellent thermal contact to a copper cold-plate maintained at a sink temperature, T_{sink}, following a design similar to one described in Maydanik et al. (2010). The overall *per unit length* thermal conductance of the condenser, $\left(UA'_{cd}\right)_{wall-outside}$, evaluated from the inside wall of the condenser pipe to the outside constant-temperature copper cold-plate, is set equal to 31.4 W/m-°C. The compensation chamber is assumed to be always filled with a two-phase mixture during the full range of operation of the considered LHP. An overall thermal conductance, $\left(UA\right)_{cc-amb}$, of 0.1 W/°C between the inner surface of the compensation chamber and the ambient condition is used. The elevation difference between the evaporator and the condenser is denoted by H_g. For the baseline operating conditions, $T_{amb} = 35$ °C, $T_{sink} = 20$ °C, and $H_g = 0$ are used, based on values used in the works of Singh et al. (2007), Zimbeck et al. (2008), and Maydanik et al. (2010). It is important to note that the more stringent US-military specification of the ambient temperature for such electronics-cooling applications of LHPs is 45 °C [Zimbeck et al. (2008)].

The geometric details of the various elements of the sample LHP, the selected materials, some characteristics of the sintered powder metal wick, and the operating conditions considered in this demonstration problem are summarized in Table 6.1. Using terminology introduced by Li et al. (2010), with the chosen inner diameters (5 mm) of the vapor-transport, liquid-transport, and condenser-pipe of the sample LHP, it would fall in the category of "compact LHPs," for which the diameters of the "connecting pipelines" fall in the 3 - 5 mm range.

In the remainder of this chapter, the term LHP (baseline) is used to indicate that the baseline operating conditions indicated in Table 6.1 apply.

Table 6.1: Characteristics of the sample LHP and the operating conditions considered.

EVAPORATOR		**CONDENSER**	
Wick		Pipe Material:	SS 316
Sintered Metal Powder:	SS 316	Inner Diameter:	5 mm
Dimensions (L x W x H) :	80 mm x 80 mm x 3.175 mm	Wall Thickness:	1 mm
Porosity:	39.3 %	Effective Length:	300 mm
Max. Effective Pore Size:	27.31 μm	$\left(UA'_{cd}\right)_{wall-outside}$:	23.6 W/m-°C, 31.4 W/m-°C (baseline), and 39.3 W/m-°C
Effective Permeability:	7.356×10^{-13} m^2	**COMPENSATION CHAMBER**	
Vapor Grooves		Pipe Material:	SS 316
Number of Grooves:	14	$\left(UA\right)_{cc-amb}$:	0 W/°C, 0.1 W/°C (baseline), and 0.2 W/°C
Dimensions (L x W x H):	80 mm x 2 mm x 1 mm		
VAPOR-AND LIQUID-TRANSPORT LINES		**OPERATING CONDITIONS**	
Pipe Material:	SS 316	T_{sink}:	10 °C, 20 °C (baseline), and 30 °C
Inner Diameter:	5 mm	T_{amb}:	25 °C , 35 °C (baseline), and 45 °C
Wall Thickness:	1 mm	Elevation between Evaporator and Condenser, H_g:	0.0 mm (baseline), 50.8 mm, and 101.6mm
Effective Length:	300 mm		

6.3 IMPACT OF OPERATING CONDITIONS ON PERFORMANCE OF THE SAMPLE LHP RUNNING WITH AMMONIA

In this section, the impact of operating conditions considered (Table 4.1) on the performance of the sample LHP running with ammonia is presented and discussed. Power inputs to the evaporator, q_{app} , in the range of 0 - 400 W are considered here.

6.3.1 Influence of the Sink Temperature

The variation of the saturated vapor temperature at the exit of the evaporator, denoted by T_{sat} , is shown in Figure 6.1 for three different sink temperatures: T_{sink} = 10, 20, and 30 °C. At low power inputs, T_{sat} first decreases with q_{app} , indicating that the LHP is

operating in a variable-conductance mode. For higher values of q_{app}, the LHP operates in an essentially constant-conductance mode, and T_{sat} increases almost linearly. As T_{sink} is increased, the transition between the variable- and constant-conductance mode begins at lower values of q_{app}. As T_{sink} is increased, the driving temperature difference for heat rejection in the condenser decreases. Therefore, the ability of the condenser to reject heat is reduced, and in order to evacuate the same amount of heat as before, the condenser becomes progressively more open (the location of the vapor-liquid interface in the condenser moves closer to its exit). As a result, when T_{sink} increases, the condenser becomes fully open at lower power inputs, and the LHP operates in a constant-conductance mode, as shown in Figure 6.1.

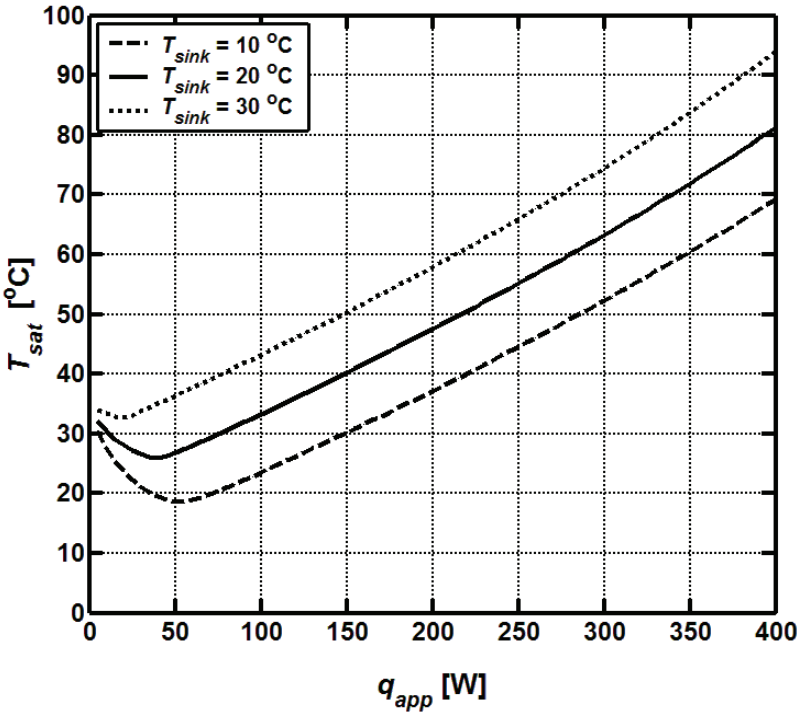

Figure 6.1: Variations of T_{sat} with q_{app} for the sample LHP operating with ammonia for T_{sink} = 10, 20, and 30 °C, T_{amb} = 35 °C, $\left(UA'_{cd}\right)_{wall-outside}$ = 31.4 W/m-°C, $\left(UA\right)_{cc-amb}$ = 0.1 W/°C, and H_g = 0.

Furthermore, in the constant conductance mode, a given increase in T_{sink}, with respect to a reference value, results in an increase in T_{sat} by an equal amount. This is also demonstrated in Figure 6.1.

6.3.2 Influence of the Ambient Temperature

Figure 6.2 shows the changes in T_{sat} with q_{app} for three different ambient temperatures, T_{amb} = 25, 35, and 45 °C. At low power inputs, the rate of evaporation in the LHP evaporator is reduced, leading to a small mass flow rate in the loop. As indicated by an energy balance on the compensation chamber (refer to Eq. 2.59), the saturation temperature of the compensation chamber, $T_{sat,\,cc}$, approaches T_{amb} .at low mass flow rates. It is important to note that, in these situations, $T_{sat,\,cc}$ and T_{sat} are very close, and thus T_{sat} also approaches T_{amb}. This behavior is evident in Figure 6.2.

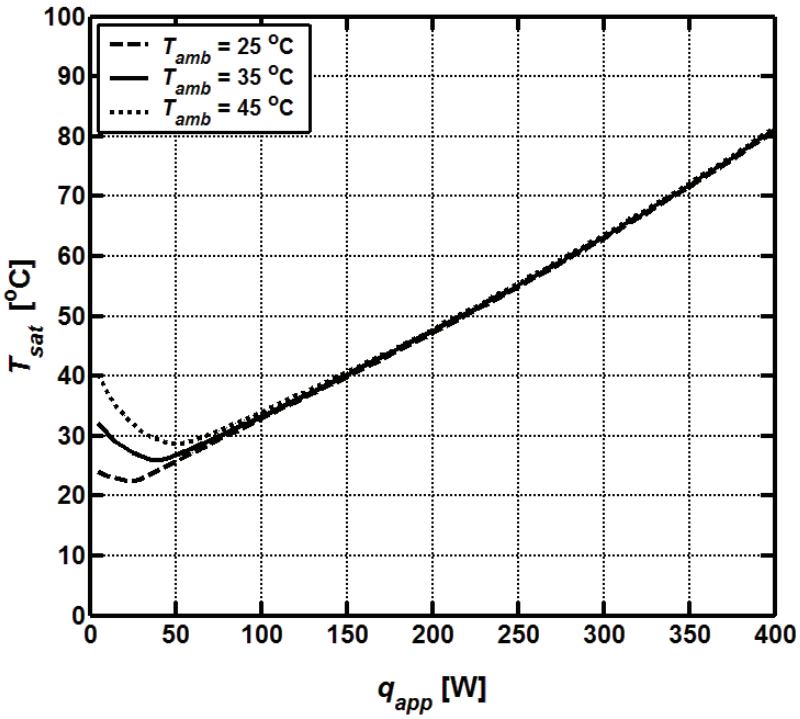

Figure 6.2: Variations of T_{sat} with q_{app} for the sample LHP operating with ammonia for T_{amb} = 25, 35, and 45 °C, T_{sink} = 20 °C, $\left(UA'_{cd}\right)_{wall-outside}$ = 31.4 W/m-°C, $\left(UA\right)_{cc-amb}$ = 0.1 W/°C, and H_g = 0.

In summation, an increase in T_{amb} yields a higher value of T_{sat} at low values of the power input. The higher value of T_{sat}, augments the heat rejection capability of the LHP condenser and delays the transition from variable- to constant-conductance mode of LHP operation, as can be seen from the results given in Figure 6.2.

6.3.3 Effect of the Conductance between Compensation Chamber and Ambient

The impact of $(UA)_{cc-amb}$ on the variations of T_{sat} with q_{app} is illustrated in Figure 6.3. In the case of the LHP considered, an increase in the conductance value implies a heat gain in the compensation chamber for q_{app} < 110 W, and consequently leads to an increase in $T_{sat,\,cc}$ and T_{sat}. An increase in the value of $(UA)_{cc-amb}$ for q_{app} > 110 W results in heat loss in the compensation chamber, which accounts for the slight decrease in T_{sat} observed in Figure 6.3 for high power inputs.

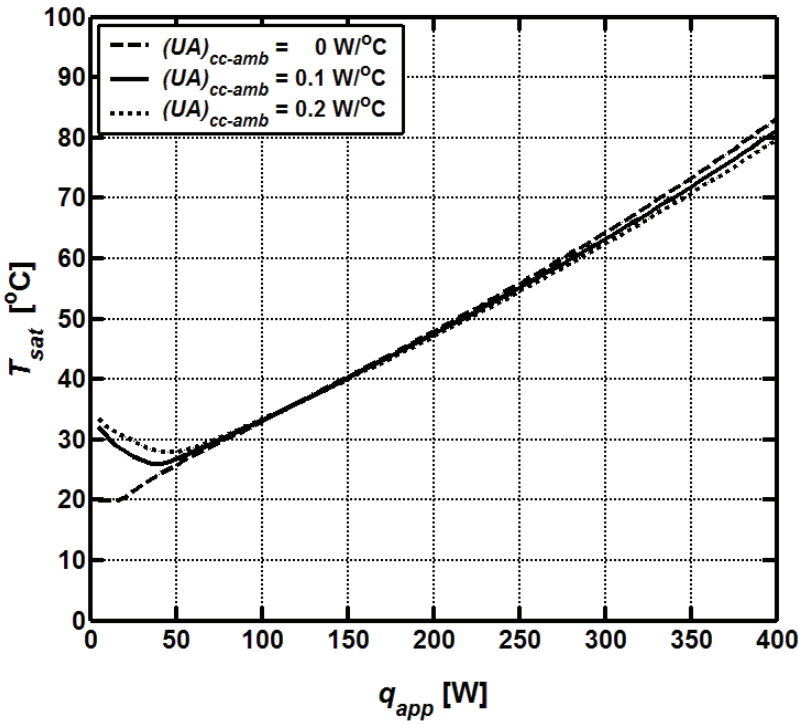

Figure 6.3: Variations of T_{sat} with q_{app} for the sample LHP operating with ammonia for $(UA)_{cc-amb}$ = 0, 0.1, and 0.2 W/°C, T_{amb} = 35 °C, T_{sink} = 20 °C, $(UA'_{cd})_{wall-outside}$ = 31.4 W/m-°C, and H_g = 0.

For a completely insulated compensation chamber, $(UA)_{cc-amb}$ = 0 W/°C, the heat leak to this chamber from the evaporator must be exactly balanced by the associated cooling caused by the subcooled liquid entering this chamber. Thus, at low power inputs, $T_{sat,\,cc}$ and T_{sat} are closely related to the temperature of the subcooled liquid, which equals the sink temperature at low values of q_{app}. This behavior is evident in Figure 6.3.

6.3.4 Effect of the Condenser Overall Wall-to-Outside Conductance

The variations of T_{sat} with q_{app} for three different values of the overall thermal conductance *per unit length* between the condenser inner wall to the outside sink environment, $(UA')_{cd,\,wall-outside}$ = 23.6, 31.4, and 39.3 W/m-°C, are shown in Figure 6.4.

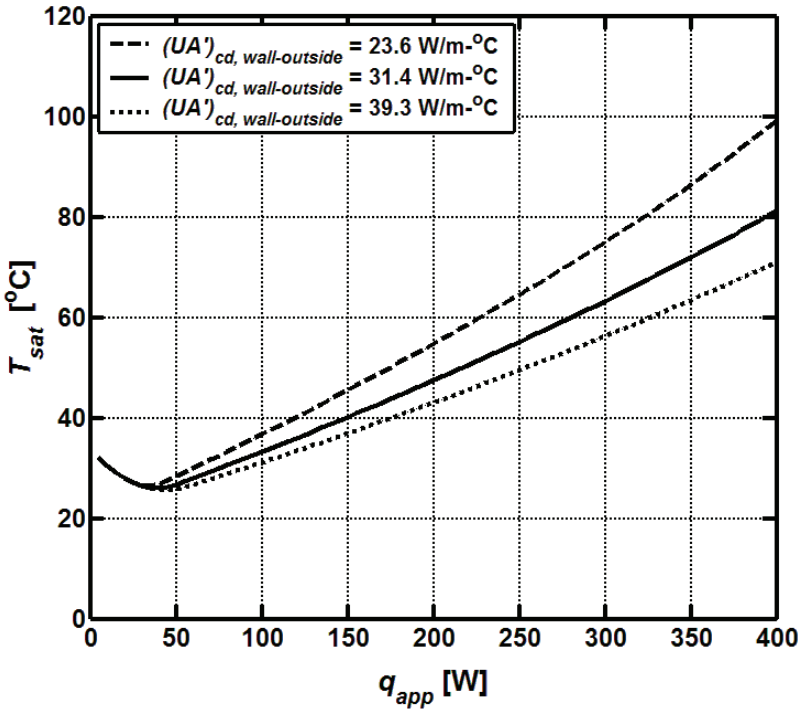

Figure 6.4: Variations of T_{sat} with q_{app} of the sample LHP operating with ammonia for $(UA')_{cd,\,wall-outside}$ = 23.6, 31.4, and 39.3 W/m-°C, T_{amb} = 35 °C, T_{sink} = 20 °C, $(UA)_{cc-amb}$ = 0.1 W/°C, and H_g = 0.

At low power inputs (q_{app} < 50 W) the LHP operates in the variable conductance mode, and T_{sat} is greatly influenced by T_{amb}, as mentioned earlier in section 6.3.2. Thus, all three curves are essentially the same in this operational regime. Conversely, there is a clear distinction in the variation of T_{sat} with q_{app} in the constant-conductance mode of operation (q_{app} > 50 W), and an increase in $(UA')_{cd,\,wall-outside}$ augments the heat rejection capability of the condenser. This consequently delays the transition between the variable- and constant-conductance modes of operation and reduces the operating temperature T_{sat} in the evaporator for the same q_{app}. Furthermore, the slopes of the nearly linear T_{sat} versus q_{app} curves in Figure 6.4 represent the effective thermal resistance (or inverse of the effective conductance) of the LHP evaluated between T_{sat} and T_{sink}.

6.3.5 Impact of Adverse Elevation between LHP Evaporator and Condenser

When the condenser of a LHP is positioned at a distance H_g *below* the evaporator/compensation chamber unit, an additional pressure head is required to overcome the associated gravitational pressure drop in the liquid-transport line. Here, this distance or height is referred to as an adverse elevation between the LHP evaporator and condenser. Figure 6.5 presents the operating characteristics of the LHP for three different adverse heights, H_g = 0, 50.8, and 101.6 mm.

As shown in Figure 6.5, the adverse elevation has a noticeable impact on the performance of the LHP at low power inputs (q_{app} < 50 W), which corresponds to variable-conductance mode of operation. With increase in H_g, the total pressure drop in the LHP is also increased, leading to an increase in (T_{sat} - $T_{sat,\,cc}$). This consequently augments the *heat leak* from the evaporator to the compensation chamber and raises $T_{sat,\,cc}$. Since $T_{sat,\,cc}$ and (T_{sat} - $T_{sat,\,cc}$) are increased, it follows that the operating temperature of the evaporator T_{sat} itself is also increased. An increase in T_{sat} augments the heat transfer capability in the condenser and defers the transition between the variable- and constant-conductance operating regimes of the LHP. This behavior is illustrated in Figure 6.5, but is not only restricted to adverse elevation effects in LHPs:

Any other changes to the LHP that lead to an increase in the total pressure drop (such as an increase in the length of the vapor-transport line or decreasing the permeability of the wick material) will have a similar impact on its performance.

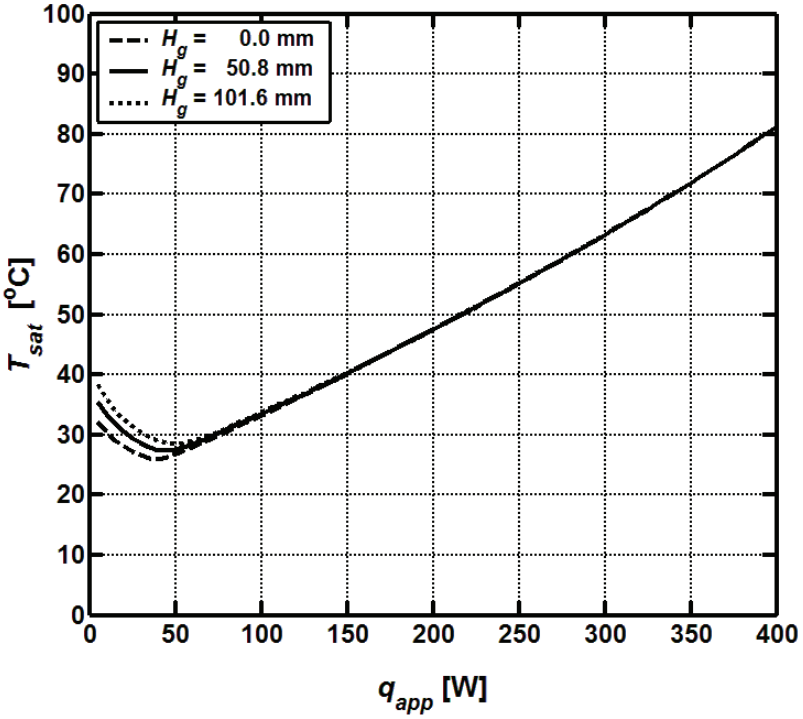

Figure 6.5: Variations of T_{sat} with q_{app} for the sample LHP operating with ammonia for H_g = 0, 50.8, and 101.6 mm, T_{amb} = 35 °C, T_{sink} = 20 °C, $\left(UA'_{cd}\right)_{wall-outside}$ = 31.4 W/m-°C, and $\left(UA\right)_{cc-amb}$ = 0.1 W/°C.

It is important to note that care should be taken when operating with adverse elevations to ensure that the total pressure drop in the LHP, ΔP_{tot}, never exceeds the maximum capillary pressure drop, $\Delta P_{cap,\,max}$, that can be sustained at the liquid-vapor interface in the wick. Figure 6.6 presents the variation of $\Delta P_{tot} / \Delta P_{cap,\,max}$ with q_{app} for H_g = 0, 50.8, and 101.6 mm. As shown in this figure, the LHP operating with ammonia reaches the capillary limit ($\Delta P_{tot} / \Delta P_{cap,\,max}$ = 1) at q_{app} = 375 W when the condenser is adversely positioned 101.6 mm below the evaporator.

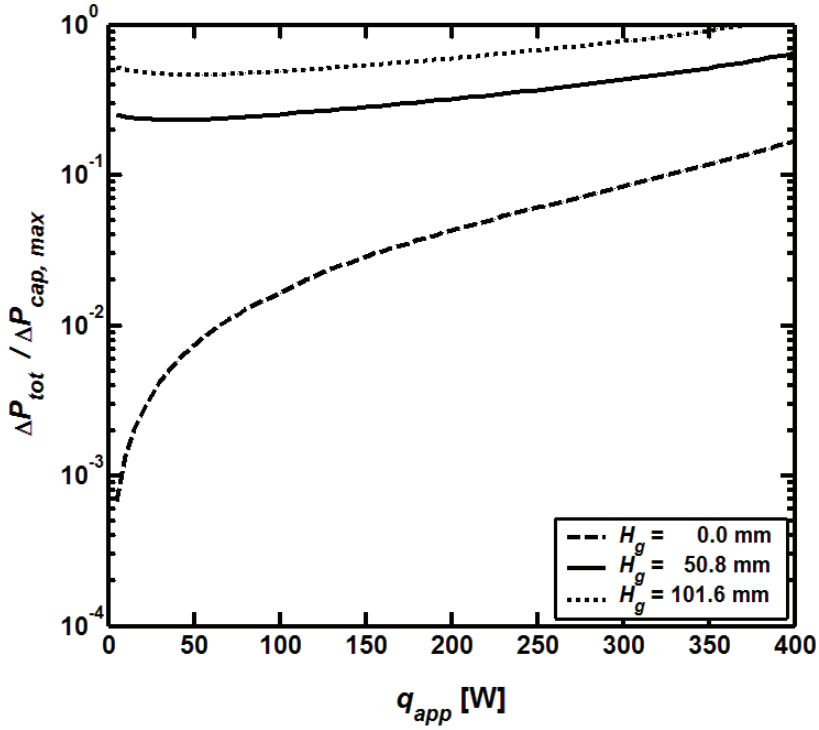

Figure 6.6: Variations of $\Delta P_{tot} / \Delta P_{cap,\,max}$ with q_{app} for the sample LHP operating with ammonia for H_g = 0, 50.8, and 101.6 mm, T_{amb} = 35 °C, T_{sink} = 20 °C, $\left(UA'_{cd}\right)_{wall-outside}$ = 31.4 W/m-°C, and $\left(UA\right)_{cc-amb}$ = 0.1 W/°C.

6.4 Simulations of the Sample LHP Operating with Four Different Working Fluids

As was stated earlier, the sample LHP (see characteristics in Table 6.1) is intended for the thermal management of a chip (Intel Xeon Processor X5690) used in a server unit for cloud-computing. The objective of this demonstration exercise is to evaluate the performance of this sample LHP in maintaining the chip-casing temperature below the 70°C limit (for safe operation) when the chip is dissipating a maximum of 260 W.

It should be noted that unless otherwise stated explicitly, the results in the rest of this chapter correspond to the baseline operating conditions of the sample LHP: T_{amb} = 35 °C, T_{sink} = 20 °C, $\left(UA'_{cd}\right)_{wall-outside}$ = 31.4 W/m-°C, $\left(UA\right)_{cc-amb}$ = 0.1 W/°C, and H_g = 0.

In this demonstration exercise, it is assumed that the metallic upper-part of the sample LHP evaporator (refer to Figure 2.4) is thin enough to render the thermal resistance of the related conductive wall minute. Consequently, the surface temperature of the evaporator

can be assumed to be equal to the saturated vapor temperature, T_{sat}, in the evaporator. It is further assumed that the thermal contact resistance at the interface between the chip-casing and evaporator is very small: so for all practical purposes, the surface temperature of the chip-casing is equal to T_{sat}. These thermal resistances are considered negligible in this section only for convenience in the presentation. However, if needed in practice, the actual chip-casing temperature, $T_{chip-case}$, can easily be approximated as follows:

$$T_{chip-case} = T_{sat} + q_{app} / \sum R_{th}$$

In this expression, $\sum R_{th}$ is the sum of the thermal resistances (resistance due to conduction in the evaporator casing and thermal contact resistance at the chip-evaporator interface) between $T_{chip-case}$ and T_{sat}.

The proposed enhanced segmented network thermofluid model is used for the simulation of the sample LHP operating under steady-state conditions with four different working fluids (ammonia, distilled water, ethanol and isopropanol) for power inputs to the evaporator, q_{app}, in the range of 0 - 400 W. The obtained results are presented and compared in the following subsections.

6.4.1 LHP Operating Temperatures and Impact of the New Correlation for Pressure Drop in the Vapor Grooves

The variation of T_{sat} with q_{app} of the sample LHP (see Table 6.1) operating at the baseline conditions with ammonia, distilled water, ethanol, and isopropanol are presented in Figures 6.7 - 6.10, respectively. The impact of the newly proposed correlation for predictions of the pressure drop in the rectangular vapor grooves of the sample LHP, $\Delta P_{vg,\,\mathrm{new-corr.}}$, on the variation of T_{sat} with q_{app} is also shown in these figures, with reference to the corresponding results obtained with the classical baseline correlation for fully-developed Darcy friction factor, referred to here as $\Delta P_{vg,\,baseline-corr.}$, used in many current thermofluid models of LHPs [Kaya and Hoang (1999); Ghajar and Darabi (2005); Maydanik (2005); Launay et al. (2007); Singh et al. (2009); Li and Peterson (2011)].

LHP Operated with Ammonia

Figure 6.7 indicates that the sample LHP operating with ammonia functions in the variable-conductance mode for q_{app} < 50 W, and in the constant-conductance mode for q_{app} > 50 W. This LHP is capable of transferring up to 335 W from the chip while maintaining its casing temperature ($T_{chip-case} = T_{sat}$) below 70 °C. At the rated maximum chip power dissipation of 260 W, the chip-casing temperature reaches a value close to 56.9 °C, which is well below the stated limit of 70 °C. As shown in Figure 6.7, the influence of $\Delta P_{vg,\,\text{new}-corr.}$ is not apparent when this LHP operates with ammonia under the established working conditions. As will be shown later (in Figure 6.12), this is because the pressure drop in the vapor grooves represents only a small portion of the overall pressure drop in the sample LHP when operating with ammonia as the working fluid.

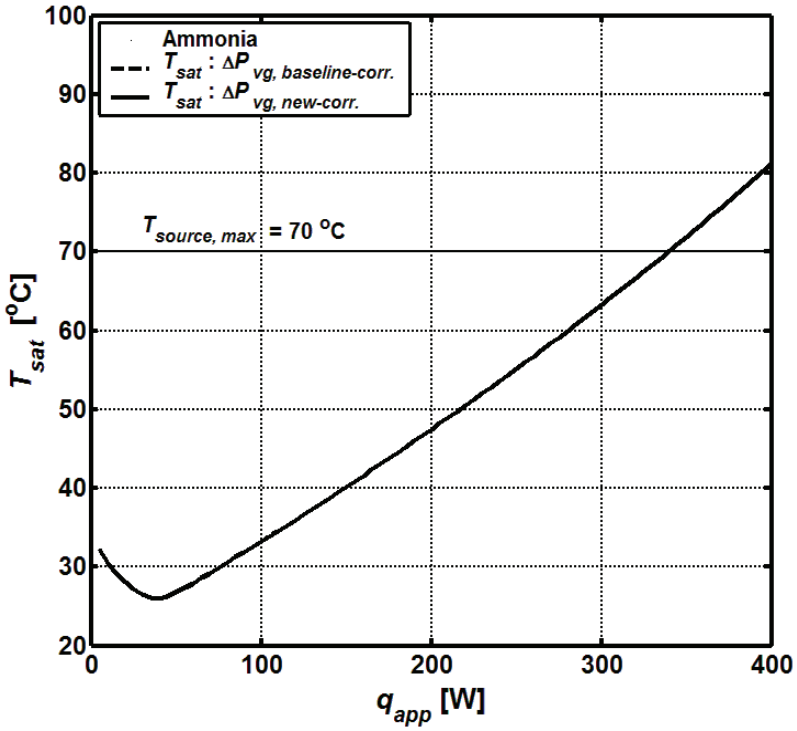

Figure 6.7: Variations of T_{sat} with q_{app} for sample LHP (baseline) operating with ammonia.

LHP Operated with Distilled Water

As is evident in Figure 6.8, when the LHP is operated with distilled water, there *is* an appreciable difference in the variation of T_{sat} with q_{app}, when the simulations are conducted with the baseline and new pressure-drop correlations (corresponding results indicated by $\Delta P_{vg,\,baseline-corr.}$ or $\Delta P_{vg,\,\text{new}-corr.}$). A maximum difference of 4.5 °C is observed in the predictions of T_{sat} at q_{app} = 35 W obtained with the two-pressure drop correlations. This occurs because, with distilled water as the working fluid, the pressure drop in the vapor grooves contributes significantly to the overall pressure drop in the LHP.

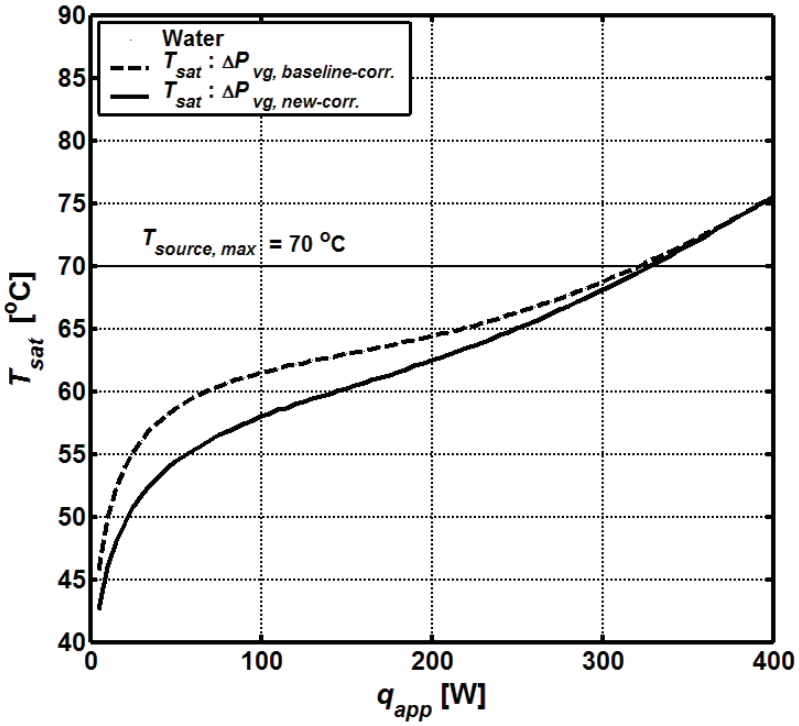

Figure 6.8: Variations of T_{sat} with q_{app} for the sample LHP operating with distilled water.

As is also illustrated by the results presented in Figure 6.8, the difference in T_{sat} obtained with the baseline and new correlations for the pressure drop in the vapor grooves decreases with increasing q_{app}. At higher power inputs, the pressure drop in other elements of the LHP has more of an impact, and therefore reduces the overall

impact of $\Delta P_{vg,\,baseline-corr.}$ or $\Delta P_{vg,\,\text{new}-corr.}$ on the total pressure drop in the loop. This is demonstrated later in Figure 6.12.

As an example, if the goal is to maintain the chip-casing temperature below 60 °C with distilled water as the working fluid in the sample LHP, then the differences in the predictions obtained using the two different pressure-drop correlations are critically important (as shown in Figure 6.8). The results obtained using the baseline Darcy friction factor correlation for the pressure drop in the vapor grooves indicates that the compact LHP is limited to a maximum rate of heat transfer of 65 W in order to keep the chip-casing temperature below the stated limit of 60 °C. However, the predictions obtained with the newly-proposed vapor-groove pressure-drop correlation reveal that the sample LHP operating with distilled water can handle a maximum heat transfer rate of 150 W at the maximum chip-casing temperature of 60 °C. Thus, the use of the baseline Darcy friction factor correlation can, under certain conditions, produce erroneous predictions of the LHP operating characteristics, leading to inaccurate decision-making in the design and optimization of LHPs. This example clearly demonstrates the importance of accurate predictions of the pressure drop in the vapor removal channels in the evaporators of LHPs.

Moreover, as illustrated by the non-linear variation of T_{sat} with q_{app} in Figure 6.8, the sample LHP essentially operates in the variable-conductance mode over most of the considered range of power inputs. This LHP approaches a constant-conductance mode of operation only very close to q_{app} = 400 W. In addition, this sample LHP operating with distilled water is capable of handling a maximum heat load of 325 W, while maintaining the chip-casing temperature below 70°C. This is comparable to the capability of the ammonia-operated LHP demonstrated earlier. At the rate maximum chip power dissipation of 260 W, the chip-casing temperature attains a value of 65.7 °C, which is 8.8 °C higher than that obtained when the sample LHP is operated with ammonia.

LHP Operated with Ethanol

The transition between the variable- and constant-conductance modes of operation occurs close to q_{app} = 270 W when ethanol is used as the working fluid in the sample

LHP, as illustrated in Figure 6.9. However, this sample LHP is only able to accommodate a heat transfer rate of 240 W from the chip, if its casing temperature is to be maintained below 70 °C. Thus, with ethanol as the working fluid, the sample LHP is incapable of handling the stated maximum power of 260 W. At this rated maximum power, the chip-casing temperature is 73.4 °C, exceeding the stated limit of 70 °C for safe and reliable operation of the chip. This sample LHP operating with ethanol is not suited for operations beyond q_{app} = 240 W for the considered application.

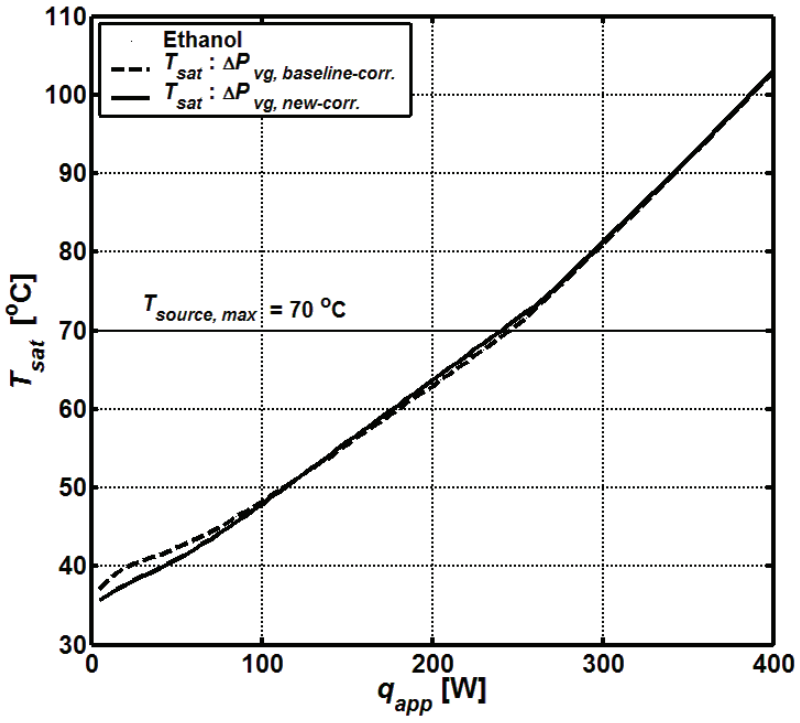

Figure 6.9: Variations of T_{sat} with q_{app} for the sample LHP operating with ethanol.

Figure 6.9 also shows the impact of the baseline and newly proposed correlations for the pressure drop, $\Delta P_{vg,\ baseline-corr.}$ and $\Delta P_{vg,\ \text{new}-corr.}$, in the vapor-removal channels of this LHP: A maximum temperature difference of 2.2 °C is obtained in the predictions of T_{sat} at q_{app} = 15 W with the two-pressure drop correlations. Thus, the importance of accurate predictions of the pressure drop in the vapor grooves of the evaporator at low power inputs is once again demonstrated.

LHP Operated with Isopropanol

The thermofluid properties of isopropanol (high-purity, 99.9%) are quite close to those of ethanol. Consequently, the performance of the sample LHP operating with these two fluids is qualitatively very similar. For the isopropanol-based LHP, the transition between the variable and constant-conductance regime of operation takes place near q_{app} = 290 W. In addition, as illustrated in Figure 6.10, this LHP can only handle a maximum heat transfer rate of 230 W from the chip, with the stated chip-casing temperature limit of 70 °C. At the higher chip-power rating of 260 W, T_{sat} (and also $T_{chip-case}$) reaches a temperature of 75 °C, exceeding the established safety limit by 5 °C. As a result, this LHP operating with isopropanol is not suited for operations beyond q_{app} = 230 W for the considered application.

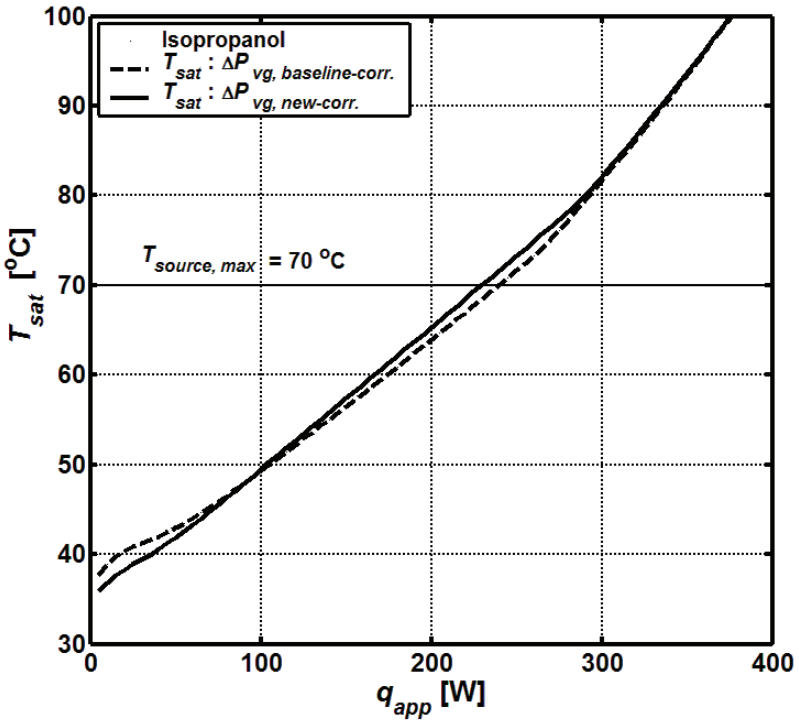

Figure 6.10: Variations of T_{sat} with q_{app} for the sample LHP operating with isopropanol.

Moreover, Figure 6.10 further illustrates the influence of the baseline and new correlations on the predicted variations of T_{sat} with q_{app}. A maximum temperature

difference of 2.1 °C in the predicted values of T_{sat} at q_{app} = 20 W is obtained with the two pressure-drop correlations. In addition, there is a difference of 1.6 °C in the predictions of T_{sat} at q_{app} = 230 W yielded by the two correlations: The baseline Darcy friction factor correlation under predicts T_{sat}, which could lead to detrimental consequences, such as overheating and failure of the electronic components the LHP is supposed to cool.

Importance of Accurate Correlations for the Pressure Drop in Vapor Grooves

The relative differences in ΔP_{vg} predictions obtained with the newly-proposed and baseline correlations for sample LHP are presented in Figure 6.11. These results show that the baseline Darcy friction factor correlation *over*-predicts the pressure drop in the vapor-removal channels of the sample LHP at low power inputs by nearly 50 % , while *under*-predicting this pressure drop at higher power inputs by up to 200 %.

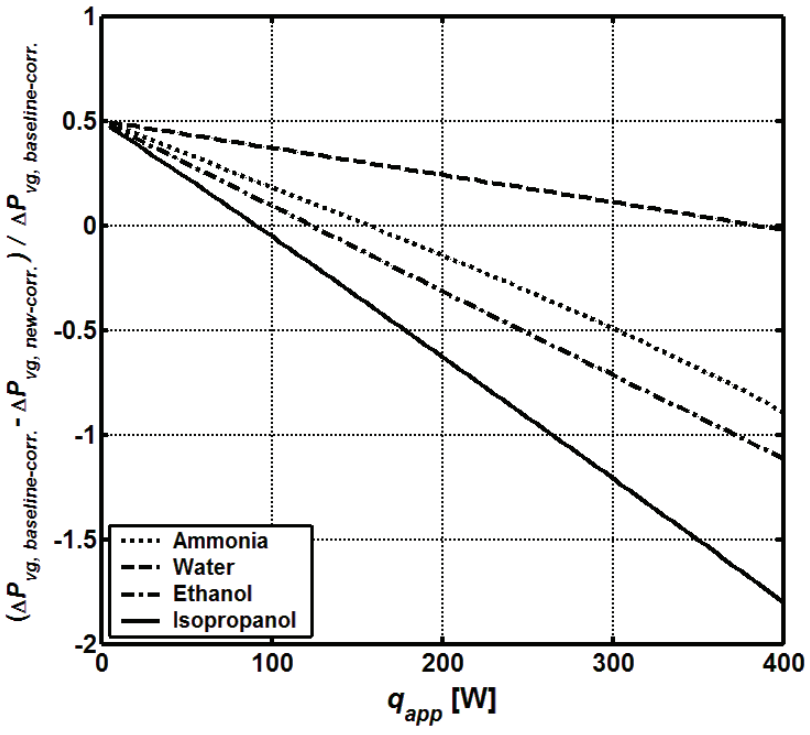

Figure 6.11: Comparison of $\Delta P_{vg,\ baseline-corr.}$ and $\Delta P_{vg,\ new-corr.}$ for the sample LHP.

Figure 6.12 illustrates the contribution of the pressure drop, for all four working fluids, sustained in the rectangular vapor grooves, ΔP_{vg}, of the sample LHP, to the total overall pressure drop, ΔP_{tot}. The $\Delta P_{vg} / \Delta P_{tot}$ ratio is the highest when the LHP is operated with distilled water (between 60 - 90%), followed by ethanol (about 33 - 50 %), isopropanol (close to 36 - 50 %), and ammonia (between 14 - 18 %).

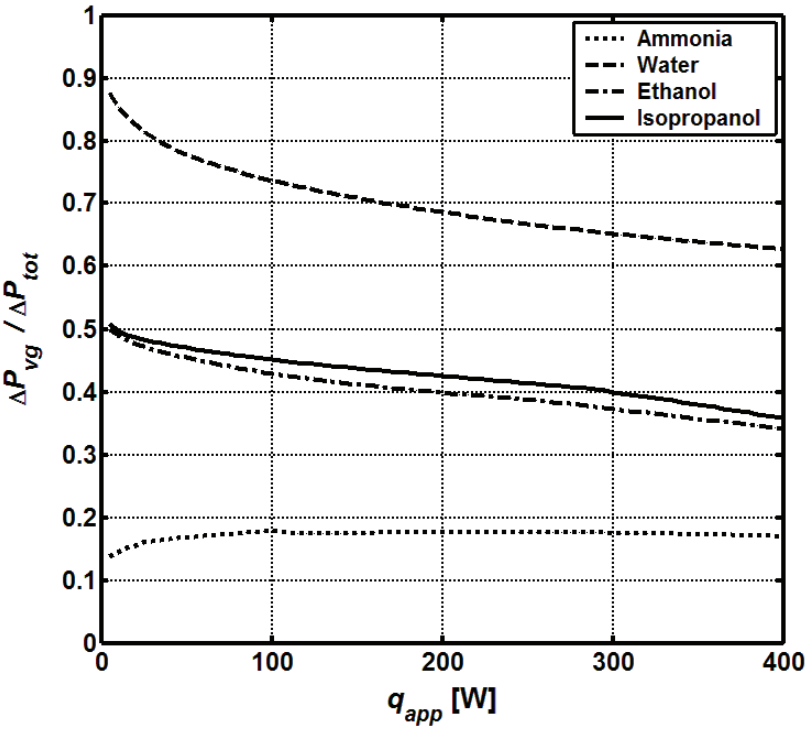

Figure 6.12: Variations of $\Delta P_{vg} / \Delta P_{tot}$ with q_{app} for the sample LHP operating with ammonia, distilled water, ethanol and isopropanol.

Finally, the predicted variations of T_{sat} with q_{app} obtained with the newly-proposed correlation for the calculation of the pressure drop in the rectangular vapor-removal channels, with the sample LHP operating with ammonia, distilled water, ethanol and isopropanol, are presented in Figure 6.13.

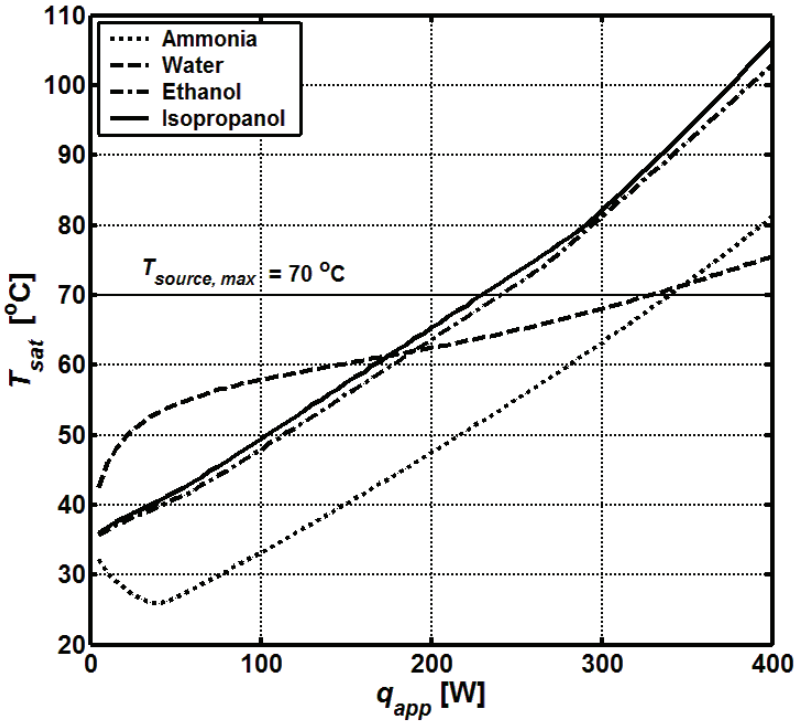

Figure 6.13: Variations of T_{sat} with q_{app} for the sample LHP operating with ammonia, distilled water, ethanol and isopropanol (prediction obtained with the new correlation for calculating ΔP_{vg}).

6.4.2 Pressure Drop Contributions from Other Elements of the LHP

The pressure drops in various other elements of the sample LHP operating with ammonia, distilled water, ethanol and isopropanol incorporating are presented in Figures 6.14 - 6.17. All of the results in these figures pertain to the baseline operating conditions of the sample LHP: T_{amb} = 35 °C, T_{sink} = 20 °C, $\left(UA'_{cd}\right)_{wall-outside}$ = 31.4 W/m-°C, $\left(UA\right)_{cc-amb}$ = 0.1 W/°C, and H_g = 0.

Pressure Drop in the Sintered-Powder-Metal Wick

As indicated in Figure 6.17, the pressure drop in the wick, ΔP_{wick}, represents between 53 - 72 % of the total pressure drop, ΔP_{tot}, of the ammonia-operated LHP, and is the most

significant contributor to the overall pressure drop in this LHP. The pressure drops sustained in the wick of the LHP operating with ethanol and isopropanol are nearly identical, ranging between 28 - 42 % of the overall pressure drop. When the sample LHP is operated with distilled water, $\Delta P_{wick} / \Delta P_{tot} < 10$ %.

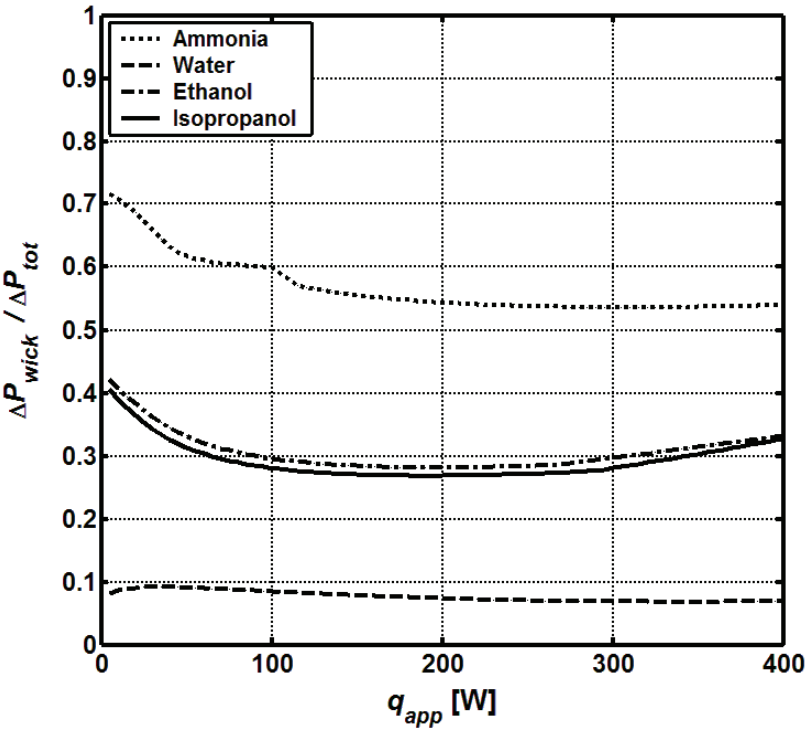

Figure 6.14: Variations of $\Delta P_{wick} / \Delta P_{tot}$ with q_{app} for the sample LHP operating with ammonia, distilled water, ethanol and isopropanol.

Pressure Drop in the Vapor-Transport Line

The variations of $\Delta P_{vl} / \Delta P_{tot}$ with q_{app} for the sample LHP are shown in Figure 6.15. When ammonia is used as the working fluid, $\Delta P_{vl} / \Delta P_{tot}$ initially decreases with an increasing q_{app}, but when approaching q_{app} = 100 W, there is a noticeable jump in ΔP_{vl}. This sudden increases in ΔP_{vl} is due to the laminar to turbulent transition of the vapor flow in the vapor-transport line. The value of $\Delta P_{vl} / \Delta P_{tot}$ for the ammonia-operated LHP ranges between 8 - 18 %. The values of $\Delta P_{vl} / \Delta P_{tot}$ for the ethanol- and isopropanol-operated LHP increase with q_{app} up to about 230 W, and then decrease as q_{app} increases.

In this case, $\Delta P_{vl} / \Delta P_{tot}$ is between 5 - 40 % for the considered range of q_{app}. The value of $\Delta P_{vl} / \Delta P_{tot}$ for the sample LHP operating with distilled water is observed to continuously increase, and it attains a maximum value of 50 % at q_{app} = 400 W.

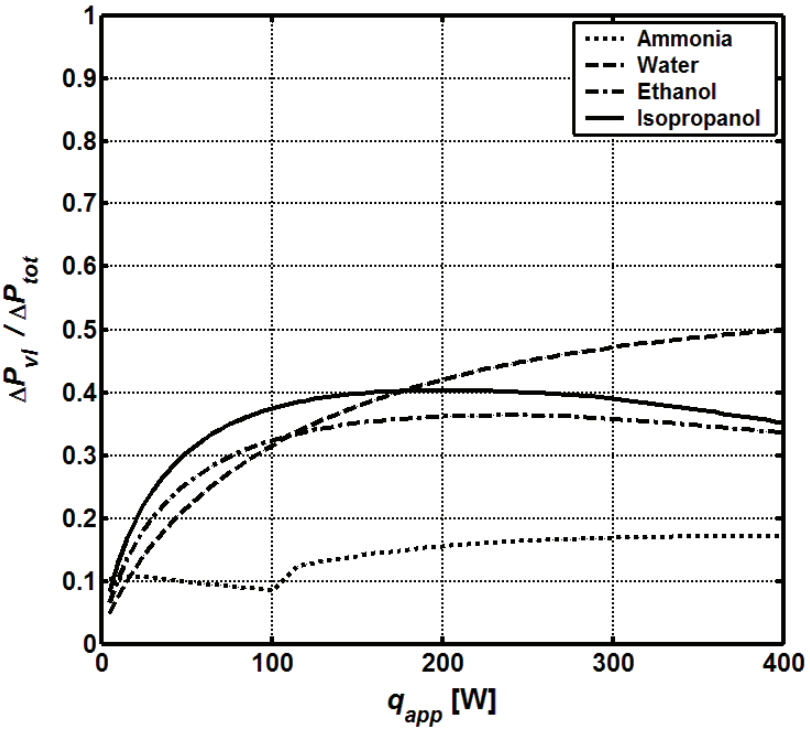

Figure 6.15: Variations of $\Delta P_{vl} / \Delta P_{tot}$ with q_{app} for the sample LHP operating with ammonia, distilled water, ethanol and isopropanol.

Pressure Drop in the Condenser Section

Figure 6.16 illustrates the variations of the total pressure drop (accounting for both two-phase and sub-cooled regions) in the condenser, $\Delta P_{cd,\,tot}$, with respect to the overall total pressure drop sustained in the sample LHP. For the ammonia-based LHP, $\Delta P_{cd,\,tot} / \Delta P_{tot}$ increases with q_{app} and reaches a maximum value of 12.6 % at q_{app} = 100 W; beyond the q_{app} = 100 W mark, $\Delta P_{cd,\,tot} / \Delta P_{tot}$ slightly decreases and asymptotes to a value of 10 %. For LHP operations with ethanol and isopropanol, $\Delta P_{cd,\,tot} / \Delta P_{tot}$ first decreases with q_{app} reaching a minimum value of 6 and 12 %, respectively, and then

increases with q_{app}. The observed decrease in $\Delta P_{cd,\,tot} / \Delta P_{tot}$ indicates that the pressure *recovery* due to changes in momentum caused by condensation of the vapor in the condenser exceeds the corresponding two-phase friction pressure *drop* in the condenser. As a result, there is a negative total pressure drop (or a pressure recovery) in the condenser. Similarly, a pressure recovery is observed for the LHP operating with distilled water, representing nearly 20 % of the total pressure drop in the LHP.

This exercise also demonstrates that the total pressure drop (single- and two-phase pressure drop) in the condenser of an LHP could represent an important portion of the overall pressure drop in the LHP (for certain combination of LHP geometry, working fluid, and operating conditions), and should not be ignored in thermofluid models of LHPs, contrary to what was suggested by Maydanik (2005).

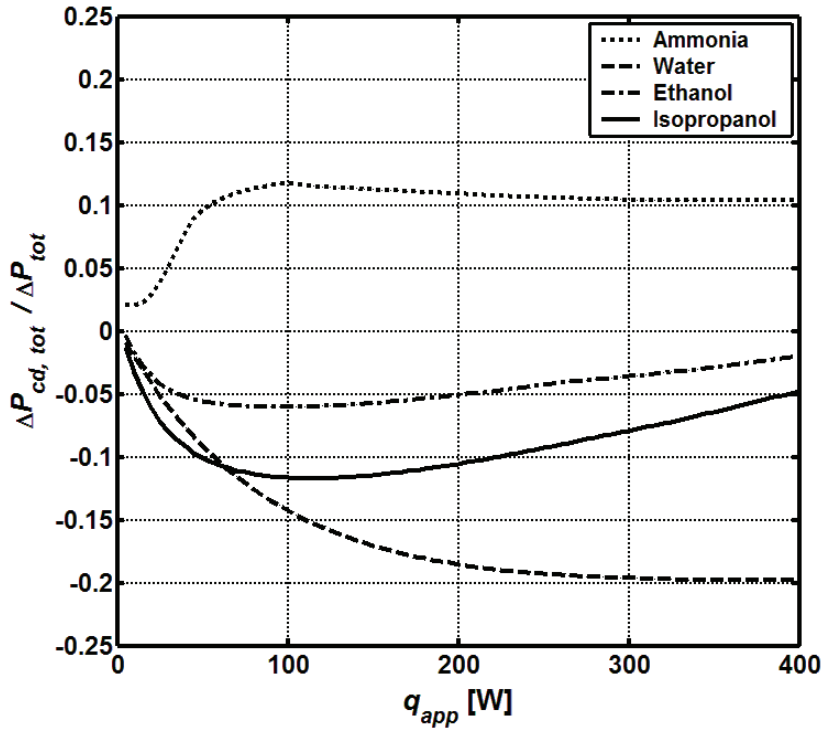

Figure 6.16: Variations of $\Delta P_{cd,\,tot} / \Delta P_{tot}$ with q_{app} for the sample LHP operating with ammonia, distilled water, ethanol and isopropanol.

Pressure Drop in the Liquid-Transport Line

Figure 6.17 shows the variations of $\Delta P_{ll} / \Delta P_{tot}$ with q_{app} for the sample LHP operating with ammonia, distilled water, ethanol and isopropanol. The liquid flow is slow and laminar in the liquid-transport line, and the associated pressure drop is also small: The values of $\Delta P_{ll} / \Delta P_{tot}$ are well under 2.5 %, 1.6 %, 1.5 %, and 0.5 % for the sample LHP operating with ammonia, ethanol, isopropanol, and distilled water, respectively.

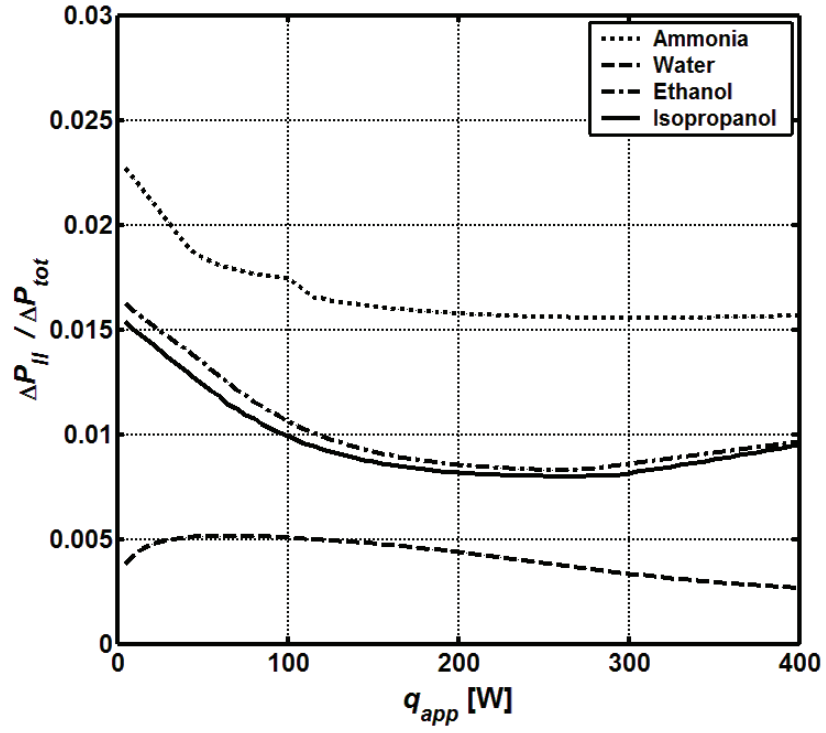

Figure 6.17: Variations of $\Delta P_{ll} / \Delta P_{tot}$ with q_{app} for the sample LHP operating with ammonia, distilled water, ethanol and isopropanol.

6.4.3 Variations of $\Delta P_{tot} / \Delta P_{cap,\,max}$ with q_{app}

The changes in $\Delta P_{tot} / \Delta P_{cap,\,max}$ with q_{app} are presented in Figure 6.18 for the sample LHP (baseline conditions) working with ammonia, distilled water, ethanol and isopropanol. For operations with ammonia and distilled water, $\Delta P_{tot} / \Delta P_{cap,\,max}$ reaches a maximum value of 16.9 % and 17.1 %, respectively. However, an inspection of the

slopes of the related $\Delta P_{tot} / \Delta P_{cap,\,max}$ versus q_{app} curves indicates that for ammonia, $\Delta P_{tot} / \Delta P_{cap,\,max}$ continues to rise rapidly beyond q_{app} = 400 W, whereas $\Delta P_{tot} / \Delta P_{cap,\,max}$ starts to plateau past q_{app} = 400 W for water. The variations of $\Delta P_{tot} / \Delta P_{cap,\,max}$ with q_{app} are very similar for the ethanol and isopropanol-operated LHP, and $\Delta P_{tot} / \Delta P_{cap,\,max}$ attains a value of 63 % and 66 % for ethanol and isopropanol, respectively.

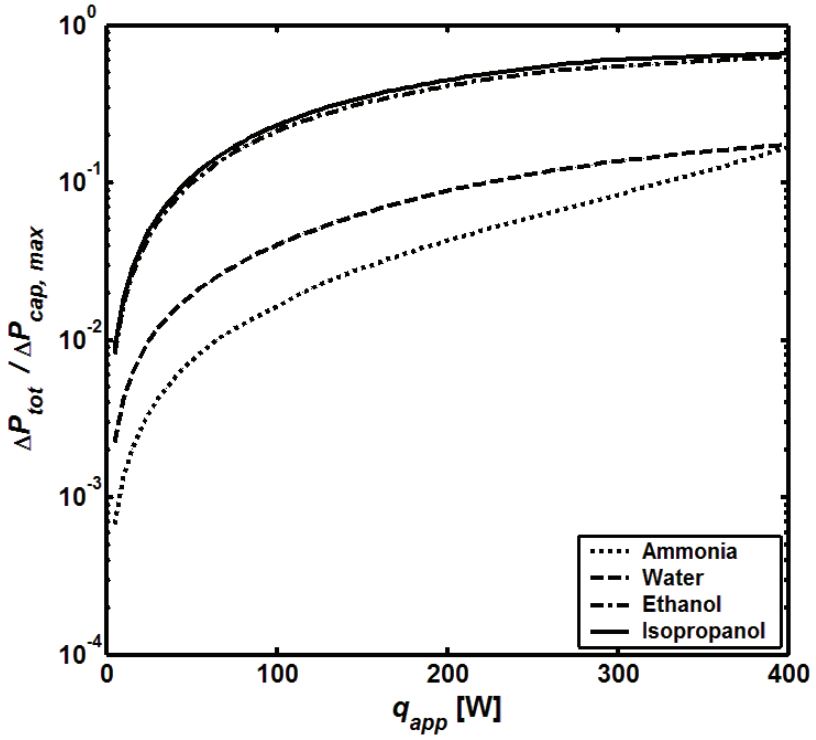

Figure 6.18 Variations of $\Delta P_{tot} / \Delta P_{cap,\,max}$ with q_{app} for the sample LHP operating with ammonia, distilled water, ethanol and isopropanol.

Based on these results, ammonia and distilled water would be the preferred working fluids for the sample LHP, as they would allow operation of the LHP well below the capillary limit, and could further accommodate additional pressure drops in the LHP such as those due to adverse elevations (as shown in 6.3.5).

6.4.4 Variations of P_{sat} / P_{atm} with q_{app}

The P_{sat} / P_{atm} results for the sample LHP (baseline conditions) operating with ammonia, distilled water, ethanol and isopropanol are presented in Figure 6.19. The values of P_{sat} / P_{atm} are relatively high for the ammonia-operated LHP, ranging from 10.2 - 42.0 atm. For distilled water, these values are the lowest of all the working fluids considered here, ranging between 0.08 - 0.39 atm. The values of P_{sat} / P_{atm} for ethanol and isopropanol are low to moderate, ranging from roughly 0.14 - 2.46 atm and 0.11 - 2.42 atm, respectively.

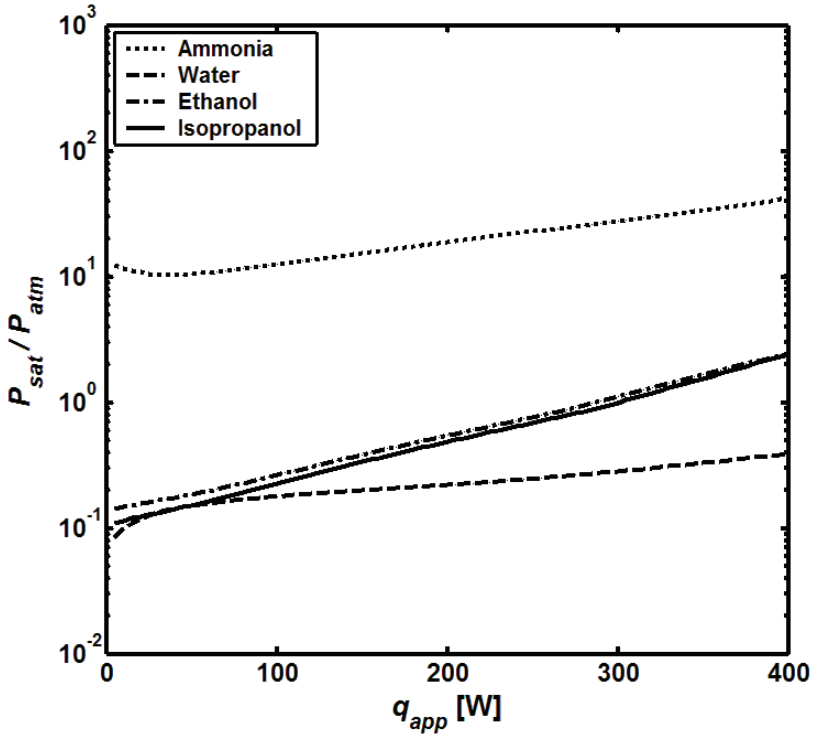

Figure 6.19 Variations of P_{sat} / P_{atm} with q_{app} for the sample LHP operating with ammonia, distilled water, ethanol and isopropanol.

Therefore, from a strictly operational-safety standpoint, for the sample LHP and the baseline operating conditions given in Table 6.1, distilled water would to be the most favorable, and ammonia the least suitable, of the four working fluids considered in this work.

6.4.5 Variations of $1/R_{th,\,\mathrm{LHP}}$ with q_{app}

Figure 6.20 shows the variations of the overall thermal conductance, $1/R_{th,\,\mathrm{LHP}} = q_{app}/(T_{sat} - T_{sink})$ with q_{app} for the sample LHP (baseline conditions) operating with ammonia, distilled water, ethanol, and isopropanol as the working fluids.

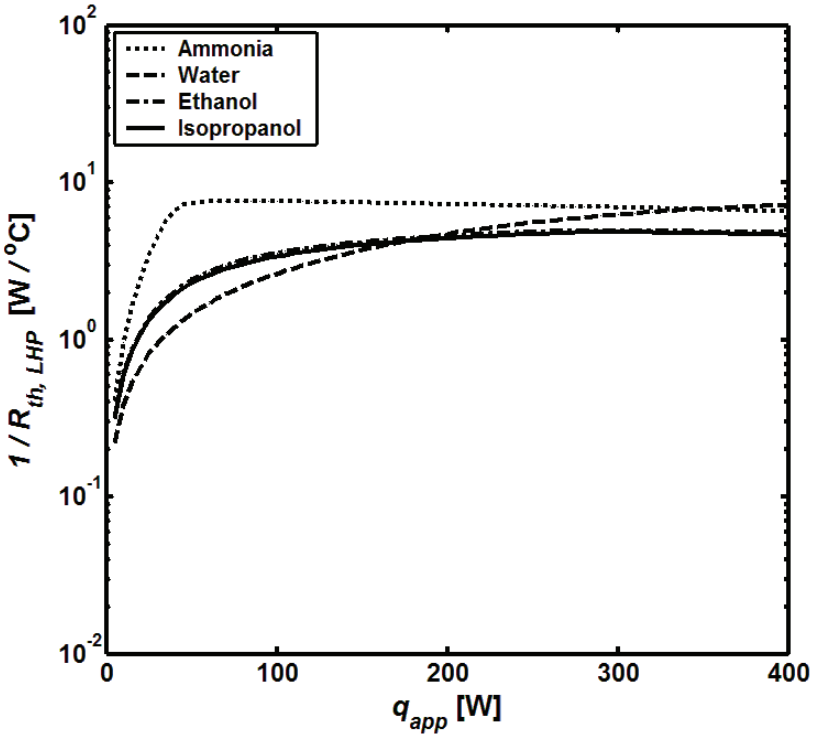

Figure 6.20 Variations of $1/R_{th,\,\mathrm{LHP}}$ with q_{app} for the ample LHP (baseline conditions) operating with ammonia, distilled water, ethanol and isopropanol.

For ammonia, $1/R_{th,\,\mathrm{LHP}}$ rapidly increases with q_{app} in the range $0 \le q_{app} \le 50$ W corresponding to the variable-conductance operation of the LHP, and reaches an essentially uniform conductance of 6.8 W/°C for higher power inputs, in the fixed-conductance-mode of operation of the LHP. The variation of $1/R_{th,\,\mathrm{LHP}}$ with q_{app} is much more gradual for distilled water, ethanol and isopropanol. At low power inputs, the LHP clearly operates in the variable-conductance mode, as shown in Figure 6.20. In the fixed-conductance mode of operation, the LHP attains an overall conductance of 4.8 W/°C for ethanol and 4.7 W/°C for isopropanol. The LHP operating with distilled water, however,

remains in the variable-conductance mode of operation for full range of the power input, $0 \leq q_{app} \leq$ 400 W, and attains a conductance of 7.1 W/°C at q_{app} = 400 W.

6.4.6 Condenser Two-Phase Flow Features

The two-phase flow features in the condenser of the compact LHP for low and high power inputs (q_{app} 50 and 400 W) are illustrated on the flow regime map of Taitel and Dukler (1976) in Figures 6.21 and 6.22, respectively. In these figures, the abscissa, X_{lt}, represents the laminar (liquid) - turbulent (gas) Lockhart-Martinelli parameter, whereas the ordinate, F_{TD}, corresponds to a modified Froude number proposed by Taitel and Dukler (1976). The modified Froude number , $F_{TD,}$ is used to distinguish between the *stratified* and *annular-dispersed liquid* flow regimes, which are accounted for in the proposed segmented network thermofluid model of LHPs (refer to Chapter 2). The symbols represent conditions in each of the cells into which the condenser pipe is segmented, with the entrance to the condenser corresponding to the left-extreme symbols and the end of the two-phase region to the right-extreme symbols.

As is shown by the results presented in Figures 6.21 and 6.22, the entire two-phase flow section of the condenser is in the stratified regime for all four working fluids for the power inputs considered. Moreover, as the power input is increased, the two-phase flow section of the condenser moves closer to the annular-dispersed liquid regime: The results presented in Figures 6.21 and 6.22 show that this effect is more apparent for ammonia and distilled water than it is for ethanol and isopropanol.

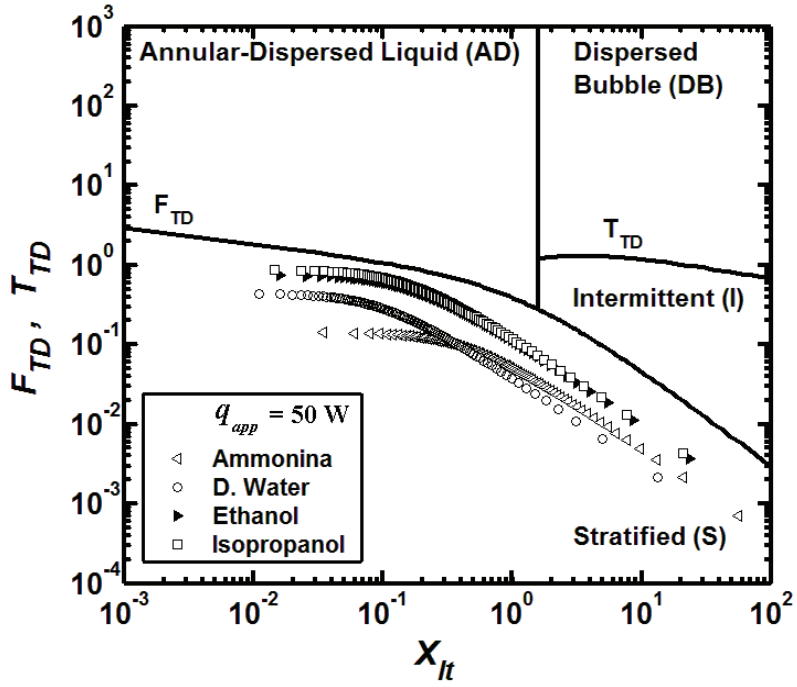

Figure 6.21 Two-phase flow conditions in the condenser plotted on the flow regime map of Taitel and Dukler (1976) for q_{app} = 50 W.

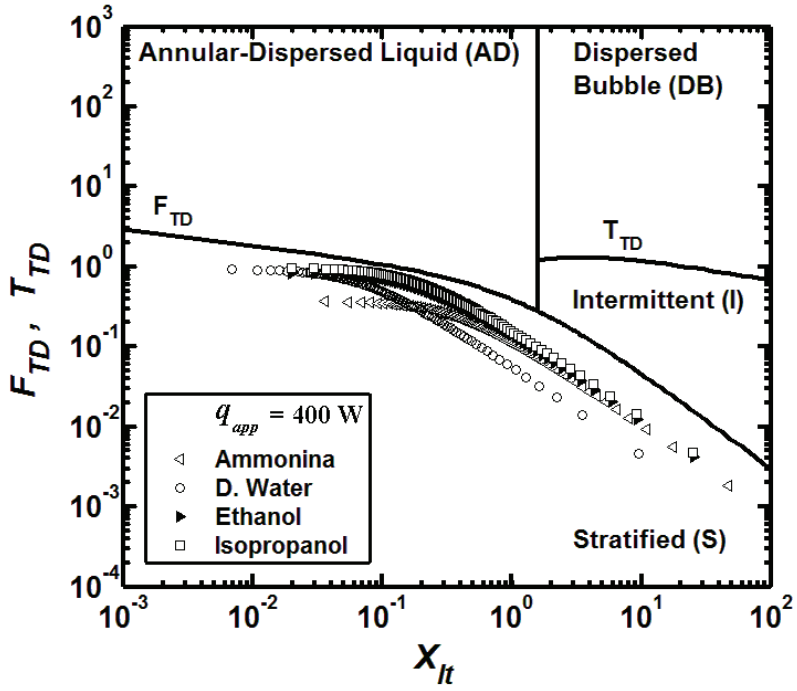

Figure 6.22 Two-phase flow conditions in the condenser plotted on the flow regime map of Taitel and Dukler (1976) for q_{app} = 400 W.

Chapter 7:
Conclusion

This final chapter is divided into the following two sections: (1) a review of the thesis and its main contributions; and (2) some recommendations for extensions of this work.

7.1 Review of the Thesis and its Main Contributions

In this section, a review of the work reported in this thesis and its main contributions are presented in six salient parts, which corresponds to the first six chapters.

1. In the first chapter, first, the motivation for this work, the overall goals of this thesis, and some background material on heat pipes (HPs), capillary pumped loops (CPLs), and loop heat pipes (LHPs) were presented. A review of the published literature relevant to this work was then presented, and some shortcomings in available quasi-one-dimensional thermofluid models of LHPs were identified. Finally, the specific objectives of this work were presented.

2. In the second chapter, a segmented network thermofluid model for the simulation of LHPs operating under steady-state conditions was presented and discussed. Attention was focused on LHPs with one evaporator (cylindrical or flat), a vapor-transport line, one condenser, a liquid-transport line, and a compensation chamber. The distinguishing features of the proposed model compared to those of earlier thermofluid network models of LHPs include the following:

- Variations of thermophysical properties of the working fluid with temperature are taken into account, along with change in quality, pressure drop, and heat transfer in the two-phase regions, giving the proposed model enhanced capabilities compared to those of earlier thermofluid network models of LHPs, such as those of Bienert and Wolf (1995), Kaya and Hoang (1999), Maydanik (2005), Singh et al. (2007). In these earlier models, balances of mass, momentum, and energy were imposed on the full elements (rather than segmented portions) of the LHP, and the

variations of quality and pressure drops in the liquid-vapor two-phase regions were overlooked.

- In the models of Atabaki (2006) and Atabaki et al. (2007), calculations of pressure drop and heat transfer in the two-phase region of the LHP were done using correlations that could only handle the stratified-smooth regime, whereas correlations that can handle the stratified-smooth, stratified-wavy, and annular-flow regimes are implemented in the proposed model, making it suitable for a wider range of applications.
- The balances of mass, momentum, and energy over the segments (cells or control volumes) of the vapor-transport line, condenser pipe, and the liquid-transport line are done with fluid properties based on the mean bulk temperature within the cells (and in the case of two-phase flow, also the mean quality within the cell), and imposed using an inner-iterative procedure, whereas upstream properties (and quality) and a non-iterative procedure were used in Atabaki (2006) and Atabaki et al. (2007);
- The updating of the T_{sat} values in the overall iterations is done using a secant method, where as a trial-and-error procedure was used for these updates in Atabaki (2006) and Atabaki et al. (2007).

The model proposed in this chapter, was also used to simulate an LHP experimentally investigated by Kaya and Hoang (1999): The predictions of the proposed model were in very good (qualitative) agreement with the experimental results.

3. It was noted (through an extensive literature survey) that in earlier quasi-one-dimensional models of LHPs, the pressure drop for vapor flow through the grooves in the evaporator is computed using a friction-factor correlation that applies strictly only in the fully-developed region of fluid flows in straight ducts with impermeable walls. This approach becomes unacceptable when this pressure drop is a significant contributor to the overall pressure drop in the LHP. Thus, a more accurate correlation for predicting this pressure drop was needed.

To fulfill this need, first, a novel co-located equal-order control-volume finite element method (CVFEM) for predicting three-dimensional parabolic fluid flow and heat transfer in straight ducts of uniform *regular*- and *irregular*-shaped cross-section was put forward in the third chapter of this thesis.

A marching procedure in the axial direction was used to construct the solution step-by-step from the inlet to the exit planes of the duct. In each step or slice, the following formulation was used: the slice was first discretized into six-node prism-shaped elements of triangular cross-section; then, prism-shaped control volumes of polygonal cross-section were constructed around each set of corresponding upstream and downstream nodes; algebraic approximations to integral mass, momentum, and energy conservation equations for each of the aforementioned control volumes were then derived using appropriate element-based interpolation functions for the dependent variables; and the resulting discretized equations were solved using an adaptation of a sequential iterative variable adjustment scheme.

Following that, this three-dimensional parabolic CVFEM was adapted to formulate a simpler finite volume method (FVM) designed for predicting developing fluid flow and heat transfer in straight ducts of *regular* rectangular cross-section, akin to the geometry of vapor grooves (or vapor-removal channels) used in the evaporators of LHPs considered in this work.

4. In the fourth chapter, the FVM formulated in Chapter 3 was used to investigate steady, laminar, Newtonian fluid flow and heat transfer in straight vapor grooves of rectangular cross-section. The straight rectangular grooves have one end blocked, and inflow of vapor from the bottom lateral surface with an injection velocity, v_{inj}, and temperature, T_{inj}. The following values of the dimensionless parameters that govern the problems of interest were analyzed: AR = 1, 2, 5, and ∞; Re_{inj} = 0.1, 1, 10, 50, and 100; Pr = 1, 2, and 3; and (L/D_h) = 8. The main points of note and the related novel findings are summarized below:

- For AR = ∞, simulations were conducted with a two-dimensional elliptic FVM [Baliga and Atabaki (2006)] and the proposed three-dimensional

parabolic FVM: it was shown that the differences between results yielded by these two methods become essentially imperceptible for $(z/D_h) \geq 4$. Consequently, all of the final simulations were done using the proposed cost-effective three-dimensional parabolic FVM.

- In each of the cases considered, for $(z/D_h) \geq 4$, a special fully-developed regime was established with the following characteristics: (w/w_{av}) and $\theta = (T - T_{inj})/(T_w - T_{inj})$ become invariant with axial distance z; $(f\,\mathrm{Re}_{D_h})$, $(f_{Fanning}\,\mathrm{Re}_{inj})$, and θ_b achieve constant values. The values of $(f\,\mathrm{Re}_{D_h})_{F.D.}$, $(f_{Fanning}\,\mathrm{Re}_{inj})_{F.D.}$, and $(\theta_b)_{F.D.}$ were computed for the above-mentioned range of the governing parameters. These values were used to propose a correlation that relates $(f\,\mathrm{Re}_{D_h})_{F.D.}$ to AR and Re_{inj}, and a correlation that relates $(\theta_b)_{F.D.}$ to AR, Re_{inj}, and Pr. Another correlation that relates $(f\,\mathrm{Re}_{D_h})_{F.D.}$ to $(f_{Fanning}\,\mathrm{Re}_{D_h})_{F.D.}$, AR, and Re_{inj} was also proposed.
- It was also shown that the ratio $(f_{app}\,\mathrm{Re}_{D_h})/(f\,\mathrm{Re}_{D_h})_{F.D.}$ achieves an asymptotic value of 0.5 regardless of the value of the aspect ratio or the shape of the cross-section of the vapor groove (as long as it is straight and axially uniform). The computed results also showed that for all practical purposes, $(f_{app}\,\mathrm{Re}_{D_h})/(f\,\mathrm{Re}_{D_h})_{F.D.}$ can be considered equal to its asymptotic value of 0.5 for $(z/D_h) \geq 4$.

These results and correlations are intended to enhance the capabilities of available quasi-one-dimensional thermofluid models of LHPs, akin to that put forward in Chapter 2 of this thesis.

5. In the fifth chapter, the use of simple and effective experiments, procedures, and correlations for the determination of the porosity, maximum effective pore size, effective permeability, and effective thermal conductivity of the liquid-saturated, sintered-powder-metal, wicks (required as inputs to mathematical models) in

LHPs was demonstrated. This demonstration exercise was conducted using a sample porous sintered-powder-metal plate made of stainless steel 316, and the corresponding results were presented and discussed.

6. In the sixth chapter, the capabilities of the proposed enhanced segmented network thermofluid model (comprised of the segmented network thermofluid model presented in Chapter 2, coupled with the correlations developed from the detailed numerical analysis of the flow and heat transfer in the vapor grooves, as outlined in Chapter 4) were illustrated through a demonstration problem. In this problem, a sample LHP running with four different working fluids (ammonia, distilled water, ethanol, an isopropanol), and operating under conditions relevant to the cooling of a state-of-the-art central processor unit (CPU) installed in a server of a cloud-computing set-up, was simulated using the proposed enhanced segmented network thermofluid model. The results obtained were presented and comparatively discussed.

7.2 RECOMMENDATIONS FOR EXTENSIONS OF THIS WORK

A few recommendations for extensions of this work are listed in this section.

The segmented network thermofluid model presented in this thesis was focused on the steady-state modeling of LHPs. It would be worthwhile to extend this model to allow simulations of LHPs operating in transient modes, such as startup, power-down, and power-up. Some guidance for such extensions could be obtained, for example, from the works of Ku (2003), Ku and Rodriguez (2003), Chen et al. (2006), Launay et al. (2007b), and Vlassov and Riehl (2008).

Attention in this thesis was limited to the modeling of LHPs with one evaporator (cylindrical or flat), a vapor-transport line, one condenser, a liquid-transport line, and a compensation chamber. It would be very interesting and useful to extend this model for the simulations of LHPs with multiple evaporators. A multi-evaporator LHP would allow the transfer of heat from multiple heat sources to a corresponding sink. The works of Yun et al. (1999), Nagano and Ku (2006), Ku et al. (2009), and Anderson et al. (2010) would be helpful in this regard.

In this work, a FVM, particularly well suited for predictions of three-dimensional parabolic fluid flow and heat transfer in straight ducts of *rectangular* cross-section, was used to investigate the fluid flow and heat transfer phenomena in the rectangular vapor-removal grooves of LHP evaporators. Based on this study, novel correlations for the reliable and cost-effective calculations of the overall pressure drop and bulk temperature of the vapor in these so-called vapor grooves were proposed. The development of similar correlations for vapor grooves of *irregular* cross-section, such as trapezoidal and triangular, using the CVFEM presented in Chapter 3 would represent a very useful and original endeavor. This could also be particularly useful for shape-optimization studies of the vapor grooves in LHP evaporators.

It would also be useful to design and build an LHP with a flat evaporator (akin to that explored in Chapter 6), and to use this LHP to obtain measurements that characterize its performance in *both* steady-state and transient modes of operation. The corresponding experimental measurements could be ultimately used to further check and refine the proposed enhanced segmented network thermofluid model.

The enhanced segmented network thermofluid model of LHPs proposed in this thesis, after incorporation of some of the extensions suggested above, could be used for achieving optimal designs of these devices for applications in advanced sustainable energy systems, state-of-the-art computers and electronics, process and materials industries, agriculture and food industries, transportation systems, biomedical systems, and spacecrafts, for example. The author hopes that the work presented in this thesis will have such a fitting evolution.

References

Adams, T.M., Dowling, M.F., Abdel-Khalik, S.I. and Jeter, S.M. (1999), Applicability of Traditional Turbulent Single-Phase Forced Convection Correlations to Non-Circular Microchannels, *Int. J. Heat Mass Transfer*, Vol. 42, pp. 4411-4415.

Akbari, M. and Behzadmehr, A. (2007), Developing Mixed Convection of a Nanofluid in a Horizontal Tube with Uniform Heat Flux, *Int. J. Num. Methods for Heat & Fluid Flow*, Vol. 17, pp. 566-586.

Alazmi, B. and Vafai, K. (2000), Analysis of Variants within the Porous Media Transport Models, *ASME Journal of Heat Transfer*, Vol. 122, pp. 303-326.

Alexander, E.J. Jr. (1972), *Structure-Property Relationships in Heat Pipe Wicking Materials,* Ph.D. Thesis, Dept. of Chem. Eng., North Carolina State University, U.S.A.

Anderson, W.G., Hartenstine, J., Ellis, M., Montgomery, J. and Peters, C. (2010), Electronics Cooling using High Temperature Loop Heat Pipes with Multiple Condensers, *SAE International*, Paper # 2010-01-1736, pp. 1-10.

Antwerpen, W., Toit, C. and Rousseau, P. (2010), A Review of Correlations to Model the Packing Structure and Effective Thermal Conductivity in Packed Beds of Mono-Sized Spherical Particles, *Nuclear Engineering and Design*, Vol. 240, pp. 1803-1818.

ASHRAE Standard 41.5-75 (1976), *Standard Measurement Guide: Engineering Analysis of Experimental*, American Society of Heating, Refrigerating, and Air-Conditioning Engineers, Inc.

Atabaki, N. (2006), *Experimental and Computational Studies of Loop Heat Pipes*, Ph.D. Thesis, Dept. of Mech. Eng., McGill Univ., Montreal, Quebec, Canada.

Atabaki, N. and Baliga, B.R. (2007), Effective Thermal Conductivity of Water-Saturated Sintered Powder-Metal Plates, *Heat and Mass Transfer*, Vol. 44, pp. 85-99.

Atabaki, N., Jesuthasan, N., and Baliga, B.R. (2007), Steady-State Network Thermofluid Models of Loop Heat Pipes, *Proc. ASME-JSME Thermal Engineering Summer Heat Transfer Conference*, Paper HT2007-32681, pp. 1-11, Vancouver, British Columbia, Canada, July 8-12.

Avallone, E.A. and Baumeister III, T. (1987), *Mark's Standard Handbook for Mechanical Engineers*, Chapter 4, pp. 38-39, McGraw-Hill, New York.

Bahrami, M., Yovanovich, M.M., and Culham, J.R. (2004), Compact Analytical Models for Effective Thermal Conductivity of Rough Spheroid Packed Beds, *Proc. ASME International Mechanical Engineering Congress*, Anaheim, CA, November 13-19.

Bahrami, M., Yovanovich, M.M., and Culham, J. (2006), Effective Thermal Conductivity of Rough Spherical Packed Beds, *Int. J. of Heat and Mass Transfer*, Vol. 49, pp. 3691-3701.

Bai, L., Lin, G., Wen, D. and Feng, J. (2009a), Experimental Investigation of Start-Up Behaviours of a Dual Compensation Chamber Loop Heat Pipe with Insufficient Fluid Inventory, *Applied Thermal Engineering*, Vol. 29, pp. 1447-1456.

Bai, L., Lin, G., Zhang, H. and Wen, D. (2009b), Mathematical Modeling of Steady-State Operation of a Loop Heat Pipe, *Applied Thermal Engineering*, Vol. 29, pp. 2643-2654.

Baker, O. (1954), Simultaneous Flow of Oil and Gas, *Oil and Gas Journal*, Vol. 53, pp. 185-195.

Baliga, B.R. (1997), Control-Volume Finite Element Methods for Fluid Flow and Heat Transfer, in *Advances in Numerical Heat Transfer*, W.J. Minkowycz, and E.M. Sparrow (Editors), Taylor & Francis, Washington, D.C., Vol. 1, Chapter 3, pp. 97-135.

Baliga, B.R. and Atabaki, N. (2006), Control-Volume-Based Finite Difference and Finite Element Methods, in *Handbook of Numerical Heat Transfer*, 2nd Ed., W.J. Minkowycz, E.M. Sparrow, and J.Y. Murthy (Editors), Chapter 6, John Wiley & Sons, New York.

Baliga, B.R. and Patankar, S.V. (1980), A New Finite-Element Formulation for Convection-Diffusion Problems, *Num. Heat Transfer*, Vol. 3, pp. 393-409.

Batchelor, G.K. (1967), *An Introduction to Fluid Dynamics*, Cambridge University Press, Cambridge, U.K.

Batchelor, G.K. (1974), Transport Properties of Two-Phase Materials with Random Structure, *Annual Review of Fluid Mechanics*, Vol. 6, pp. 227-255.

Batchelor, G.K. and O'Brien, R.W. (1977), Thermal or Electrical Conduction through a Granular Material, *Proceedings of the Royal Society of London*, Vol. A355, pp. 313-333.

Bauer, T.H. (1993), A General Analytical Approach Toward the Thermal Conductivity of Porous Media, *International Journal of Heat and Mass Transfer*, Vol. 36, pp. 4181-4191.

Beale S.B. (2005), Mass Transfer in Plane and Square Ducts, *Int. J. Heat Mass Transfer*, Vol. 48, pp. 3256-3260.

Beavers, G.S. and Joseph, D.D. (1967), Boundary Conditions of a Naturally Permeable Wall, *J. Fluid Mech.*, Vol. 30, pp. 197-207.

Beavers, G.S. and Sparrow E.M. (1969), Non-Darcy Flow Through Fibrous Porous Media, *Journal of Applied Mechanics,* pp. 711-714.

Beavers, G.S., Sparrow, E.M. and Magnuson, R.A. (1970), Experiments on Hydrodynamically Developing Flow in Rectangular Ducts of Arbitrary Aspect Ratio, *Int. J. Heat Mass Transfer*, Vol. 13, pp. 689-702.

Bejan, A. (1995), *Convection Heat Transfer*, 2nd Edition, John Wiley, New York.

Berman, A.S. (1953), Laminar Flow in Channels with Porous Walls, *J. Appl. Physics*, Vol. 24, pp. 1232-1235.

Bienert, W.B. and Wolf, D.A. (1995), Temperature Control with Loop Heat Pipe: Analytical Model and Test Results, *Proc. 9th International Heat Pipe Conference,* Los Alamos National Laboratory, Albuquerque, New Mexico.

Bird, R.B., Stewart, W.E. and Lightfoot, E.N. (2002), *Transport Phenomena*, 2nd Edition, John Wiley, New York.

Bloomfield, J.P. and Williams, A.T. (1995), Empirical Liquid Permeability-Gas Permeability Correlation for use in Aquifer Properties Studies, *Quarterly Journal of Engineering Geology*, Vol. 28, pp. S143–S150.

Bonnefoy, M., Ochterbeck, J.M., Drolen, B.L. and Nikitkin, M.N. (2004), Effective Thermal Conductivity of Saturated Sintered Nickel Loop Heat Pipe Wicks, *37th Thermophysics Conference*, AIAA Paper # 2004-2571, pp. 1-10, Portland, Oregon, June 28 – July 1.

Boomsma, K. and Poulikakos, D. (2001), On the Effective Thermal Conductivity of a Three Dimensionally Structured Fluid-Saturated Metal Foam, *International Journal of Heat and Mass Transfer*, Vol. 44, pp. 827-836.

Bouré, J.A. and Delhaye, J.M. (1982), General Equations and Two-Phase Flow Modeling, in *Handbook of Multiphase Systems, Section 1.2*, G. Hetsroni (Editor), McGraw-Hill, New York.

Brennen, C.E. (2005), *Fundamentals of Multiphase Flow*, Cambridge University Press, Cambridge, U.K.

Briley, W.R. (1974), Numerical Method for Predicting Three-Dimensional Steady Viscous Flow in Ducts, *J. Comp. Physics*, Vol. 14, pp. 8-28.

Bundy, R.D. and Weissberg, H.L. (1970), Experimental Study of Fully Developed Laminar Flow in a Porous Pipe with Wall Injection, *Phys. Fluids*, Vol. 13, pp. 2613-2615.

Busse, C.A. (1973), Theory of the Ultimate Heat Transfer Limit of Cylindrical Heat Pipes, *Int. J. Heat Mass Transfer*, Vol. 16, pp. 169-186.

Calmidi, V.V. and Mahajan, R.L. (1999), The Effective Thermal Conductivity of High Porosity Fibrous Metal Foams, *ASME Journal of Heat Transfer*, Vol. 121, pp. 466-471.

Cao, Y. and Faghri, A. (1994), Conjugate Analysis of a Flat-Plate Type Evaporator for Capillary Pumped Loops with Three-Dimensional Vapor Flow in the Groove, *Int. J. Heat Mass Transfer*, Vol. 37, pp. 401-409.

Caretto, L.S., Curr, R.M. and Spalding, D.B. (1972), Two Numerical Methods for Three-Dimensional Boundary Layers, *Comp. Meths Appl. Mech. Eng.*, Vol. 1, pp. 39-57.

Carey, V.P. (1992), *Liquid-Vapor Phase-Change Phenomena: An Introduction to the Thermophysics of Vaporization and Condensation Processes in Heat Transfer Equipment*, Taylor & Francis, New York.

Carlson, G.A. and Hornbeck, R.W. (1973), A Numerical Solution of Laminar Entrance Flow in a Square Duct, *J. Appl. Mechanics*, Vol. 40, pp. 25-30.

Chandrupatla, A.R. and Sastri, V.M.K. (1978), Constant wall Temperature Entry length Laminar Flow of and Heat Transfer to a Non-Newtonian Fluid in a Square Duct, in *Proc. 6th Int. Heat Transfer Conference*, Toronto, pp. 323-328.

Chang, S.W. (1990), Porosity and Effective Thermal Conductivity of Wire Screens, *ASME Journal of Heat Transfer*, Vol. 112, pp. 5-9.

Chato, J.C. (1962), Laminar Condensation Inside Horizontal and Inclined Tubes, *ASHRAE Journal*, Vol. 4, pp. 52-60.

Chen, C.K. and Tien, C.-L. (1973), Conductance of Packed Sphere in Vacuum, *ASME Journal of Heat Transfer*, Vol. 95, pp. 302-308.

Chen, M.M. and Faghri, A. (1990), An Analysis of the Vapor Flow and the Heat Conduction Through the Liquid-Wick and Pipe Wall in a Heat Pipe with Single and Multiple Heat Sources, *Int. J. Heat Mass Transfer*, Vol. 33, pp. 1945-1955.

Chen, Y., Groll, M., Mertz, R., Maydanik, Y. F. and Vershinin, S. V. (2006), Steady-State and Transient Performance of a Miniature Loop Heat Pipe, *International Journal of Thermal Sciences*, Vol. 45, pp. 1084–1090.

Cheng, L., and Mewes, D. (2006), Review of Two-Phase Flow and Flow Boiling of Mixtures in Small and Mini Channels, *Int. J. Multiphase Flow*, Vol. 32, pp. 183-207.

Cheng, L., Ribatski, G. and Thome, J.R. (2008), Two-Phase Flow Patterns and Flow Pattern Maps: Fundmentals and Applications, *ASME Appl. Mech. Reviews*, Vol. 31, pp. 1-28.

Cheng, Y.C., Hwang, G.J., and Ng, M.L. (1994), Developing Laminar Flow and Heat Transfer in a Rectangular Duct with One-Walled Injection and Suction, *Int. J. Heat Mass Transfer*, Vol. 37, pp. 2601-2613.

Chernysheva, M.A. and Maydanik, Y.F. (2008), Numerical Simulation of Transient Heat and Mass Transfer in a Cylindrical Evaporator of a Loop Heat Pipe, *Int. J. Heat Mass Transfer*, Vol. 51, pp. 4204-4215.

Chhabra, R. and Richardson, J. (2008), *Non-Newtonian Flow and Applied Rheology: Engineering Applications*, 2nd Edition, Butterworth-Heinemann, U.K.

Chi, S.W. (1976), *Heat Pipe Theory and Practice: A Sourcebook*, Hemisphere Publishing

Chisholm, D. (1967), A Theoretical Basis for the Lockhart-Martinelli Correlation for Two-Phase Flow, *International Journal of Heat and Mass Transfer*, Vol. 10, pp. 1767-1778.

Choudhury, D. and Patankar, S.V. (1988), Combined Forced and Free Laminar Convection in the Entrance Region of an Inclined Isothermal Tube, *J. Heat Transfer, Trans. ASME*, Vol. 110, pp. 901-909.

Chu, C.I, Wu., S.C, Chen, P.L., and Chen, Y.M. (2004), Design of Miniature Loop Heat Pipe, *Heat Transfer—Asian Research*, Vol. 33, pp. 42-52.

Civan, .F., (2011), *Porous Media Transport Phenomena*, John Wiley and Sons, USA.

Clark, M.M., (2009), *Transport Modeling for Environmental Engineers and Scientists,* 2nd Edition,Wiley-Interscience, New Jersey, U.S.A.

Colebrook, C.F. (1939), Turbulent Flow in Pipes, with Particular Reference to the Transition Region between the Smooth and Rough Pipe Laws, *Journal of the Institution of Civil Engineers*, Vol. 11, pp. 133-156.

Coleman, J.W. and Garimella, S. (2003), Two-Phase Flow Regimes in Round, Square, and Rectangular Tubes During Condensation of Refrigerant R134a", *International Journal of Refrigeration*, Vol. 26, pp. 117-128.

Collier, J.G. (1972), *Convection Boiling and Condensation*, McGraw-Hill, London.

Crapiste, G.H., Rotstein, E., and Whitaker, S. (1973), General Closure Scheme for the Method of Volume Averaging, *Chemical Engineering Science*, Vol. 41, pp. 227-235.

Crowe, C.T. (2006), *Multiphase Flow Handbook*, Taylor & Francis, Boca Raton, Florida.

Curr, R.M., Sharma, D., and Tatchell, D.G. (1972), Numerical Predictions of Some Three-Dimensional Boundary Layers in Ducts, *Comp. Methods Appl. Mech. Eng.*, Vol. 1, pp. 143-158.

Currie, I.G. (2003), *Fundamental Mechanics of Fluids*, 3rd Ed., McGraw-Hill, New York.

Daungthongsuk, W. and Wongwises, S. (2007), A Critical Review of Convective Heat Transfer of Nanofluids, *Renewable and Sustainable Energy Reviews*, Vol. 11, pp. 797-817.

Davidson, P., (2004), *Turbulence: An Introduction for Scientists and Engineers*, Oxford University Press, U.K.

de Gennes, P.G. (1985), Wetting: Statics and Dynamics, *Review of Modern Physics,* Vol. 57, pp. 827-863.

Del Giudice, S., Strada, M. and Comini, G. (1981), Three-Dimensional Laminar Flow in Ducts, *Num. Heat Transfer*, Vol. 4, pp. 215-228.

Demidov, A.S. and Yatsenko, E.S. (1994), Investigation of Heat and Mass Transfer in the Evaporation Zone of a Heat Pipe Operating by the 'Inverted Meniscus' Principle, *Int. J. Heat and Mass Transfer*, Vol. 37, pp. 2155-2163.

Dobson, M.K. (1994), *Heat Transfer and Flow Regimes During Condensation in Horizontal Tubes,* Ph.D. Thesis, Department of Mechanical and Industrial Engineering, University of Illinois at Urbana-Champaign.

Dobson, M.K. and Chato, J.C. (1998), Condensation in Smooth Horizontal Tubes, *ASME Journal of Heat Transfer*, Vol. 120, pp. 193-213.

Drew, D.A. (1983), Mathematical Modeling of Two-Phase Flow, *Annual Review of Fluid Mechanics*, Vol. 15, pp. 261-291.

Dukler, A.E., Wicks, M., and Cleveland, R.G. (1964), Frictional Pressure Drop in Two-Phase Flow, *AIChE J.*, Vol. 10, pp. 44-51.

Dul'nev, G.N. (1965), Heat Transfer Through Solid Disperse Systems, *Journal of Engineering Physics,* Vol. 9, pp. 275-279.

Dullien, F.A.L. (1992), *Porous Media: Fluid Transport and Pore Structure*, 2nd Edition, Academic Press, San Diego.

Dunn, P. and Reay, D.A. (1982), *Heat Pipes*, 3rd Edition, Pergamon Press Ltd, New York.

Durbin, P. and Pettersson-Reif, B. (2010), Statistical Theory and Modeling for Turbulent Flow, 2nd Edition, John Wiley, New York.

Eckert, E.R.G. and Drake, R.M. (1971), *Analysis of Heat and Mass Transfer*, McGraw-Hill, New York.

El-Hajal, J., Thome, J.R. and Cavallini, A. (2003), Condensation in Horizontal Tubes, Part 1: Two-Phase Flow Pattern Map. *Int. J. Heat Mass Transfer*, Vol. 46, pp. 3349–3363.

Elias, S.R., Stubley, G.D. and Raithby, G.D. (1997), An Adaptive Agglomeration Method for Additive Correction Multigrid, *Int. J. Num. Methods in Eng.*, Vol. 40, pp. 887-903.

Faghri, A. (1995), *Heat Pipe Science and Technology*, Taylor & Francis, Washington, DC.

Ferziger, J.H. and Peric, M. (1999), *Computational Methods for Fluid Dynamics*, 2nd Edition, Springer, New York.

Figus, C., Le Bray, Y., Bories, S., and Prat, M. (1999), Heat and Mass Transfer with Phase Change in a Porous Structure Partially Heated: Continuum Model and Pore Network Simulations, *Int. J. Heat Mass Transfer*, Vol. 42, pp. 2557-2569.

Fleming, D.P. and Sparrow, E.M. (1969), Flow in the Hydrodynamic Entrance Region of Ducts of Arbitrary Cross-Section, *J. Heat Transfer, Trans. ASME*, Vol. 91, pp. 345-354.

Fox, R.F. and McDonald, A. (1998), *Introduction to Fluid Mechanics*, 5th Edition, John Wiley, New York.

Freeden, W., Nashed, M. and Sonar, T. (2010), *Handbook of Geomathematics*, Springer, USA.

Gaul, L., Kogl, M. and Wagner, M. (2003), *Boundary Element Methods for Engineers and Scientists*, Springer, Berlin, Germany.

Ghajar, A.J. (2005), Non-Boiling Heat Transfer in Gas-Liquid Flow in Pipes – A Tutorial, *J. Brazilian Society of Mechanical Sciences and Engineering*, Vol. 27, pp. 46-73.

Ghajar, M. and Darabi, J. (2005), Numerical Modeling of Evaporator Surface Temperature of a Micro Loop Heat Pipe at Steady-State Condition, *J. Micromech. Microeng.*, Vol. 15, pp. 1963-1971.

Ghajar, M., Darabi, J., and Crews, N. (2005), A Hybrid CFD-Mathematical Model for Simulation of a MEMS Loop Heat Pipe for Electronics Cooling Applications, *J. Micromechanics and Microelectronics*, Vol. 15, pp. 313-321.

Gnielinski, V. (1976), New Equations for Heat and Mass Transfer in Turbulent Pipe and Channel Flow, *International Chemical Engineering*, Vol. 16, pp. 359-367.

Gnielinski, V. (1983), Forced Convection in Ducts, in *Heat Exchanger Design Handbook*, E.U. Sclünder (Editor), Hemisphere, New York, pp. 2.5.1-2.5.3.

Goldstein, R.J. and Kreid, D.K. (1967), Measurements of Laminar Flow Development in a Square Duct Using Laser-Doppler Flowmeter, *J. Appl. Mechanics*, Vol. 34, pp. 813-818.

Goncharov, K.A., Golovin, O.A. and Kolesnikov, V.A. (2000), Multi-Evaporator Loop Heat Pipe, *American Institute of Physics Conference Proceedings 504,* M.S. El-Genk (Editor), American Institute of Physics, New York, pp. 778-784.

Gorring, R.L. and Churchill, S.W. (1961), Thermal Conductivity of Heterogeneous Materials, *Chemical Engineering Progress*, Vol. 57, pp. 53-59.

Gresho, P.M. and Sani, R.L. (2000), *Incompressible Flow and the Finite Element Method: Volume 2, Isothermal Laminar Flow*, John Wiley, New York.

Griffith, P. (1985), Two-Phase Flow, in *Handbook of Heat Transfer Fundamentals*, 2nd Edition, W.M. Rohsenow, J.P. Hartnett, and E.N. Ganic (Editors), Chapter 13, pp. 1-41.

Gusarov, A. and Kovalev, E., (2009), Model of Thermal Conductivity in Powder Beds, *Physical Review B,* Vol. 80, pp. 1-15.

Hadley, G.R. (1986), Thermal Conductivity of Packed Metal Powders, *International Journal of Heat and Mass Transfer,* Vol. 29, pp. 909-920.

Harlow, F.H. and Welch, J.E. (1965), Numerical Calculation of Time-Dependent Viscous Incompressible Flow of Fluid with Free Surface, *Physics of Fluids*, Vol. 8, pp. 2182-2189.

Hinze, J.O. (1975), *Turbulence*, 2nd Edition, McGraw-Hill, New York.

Hoang, T., & Ku, J. (2005). Mathematical Modeling of Loop Heat Pipes with Multiple Evaporators and Multiple Condensers. *3rd International Energy Conversion Engineering Conference* (pp. 1-11). American Institute of Aeronautics and Astronautics.

Hsu, C. T. (2000), Heat Conduction in Porous Media, in *Handbook of Porous Media*, K. Vafai and M. Dekker (Editors), Chapter 4, pp. 171-200.

Hubbert, M.K. (1956), Darcy Law and the Field Equations of the Flow of Underground Fluids, *Transactions AIME*, Vol. 207, pp. 222-239.

Hwang, G.J., Cheng, Y.C., and Ng, M.L. (1993), Developing laminar flow and heat transfer in a square duct with one-walled injection and suction, *Int. J. Heat Mass Transfer*, Vol. 36, pp. 2429-2440.

Incropera, F.P. and DeWitt, D.P. (2002), *Fundamentals of Heat and Mass Transfer*, 5th Edition, John Wiley, New York.

Irvine, T.F. and Hartnett, J.P., (1964 – 2004), *Advances in Heat Transfer*, Vols. 1 – 38, Academic Press, New York.

Ishii, M., and Hibiki, T., (2010), *Thermo-Fluid Dynamics of Two-Phase Flow*, 2nd Edition, Springer, USA.

ISO 4022: *Permeable Sintered Metal Materials - Determination of Fluid Permeability*, 1987-10-01.

Jaluria, Y. and Torrance, K.E. (2003), *Computational Heat Transfer*, 2nd Edition, Taylor and Francis, Washington D.C.

Jaster, H. and Kosky, P.G. (1976), Condensation Heat Transfer in a Mixed Flow Regime, *International Journal of Heat and Mass Transfer*, Vol. 19, pp. 95-99.

Jesuthasan, N., Atabaki, N. and Baliga, B.R. (2008), Modeling of Multiphase Thermofluid Phenomena in Segmented Network Simulations of Loop Heat Pipes, *Proc. Fifth International Conference on Transport Phenomena in Multiphase Systems (HEAT 2008)*, Vol. 2, pp. 335-342, Bialystok, Poland, June 30 – July 3.

Jesuthasan, N. and Baliga, B.R. (2009a), Steady-State Segmented Thermofluid Network Simulations of a Loop Heat Pipe Operating with Four Different Working Fluids, *Proc. ASME Summer Heat Transfer Conference*, Paper # HT2009-88411, pp. 1-10, San Francisco, July 19-23.

Jesuthasan, N. and Baliga, B.R., (2009b), A Numerical Method for Three-Dimensional Parabolic Flow and Heat Transfer in Straight Ducts of Irregular Cross Section, *J. Computational Thermal Sciences,* Vol. 1, pp.259-288.

Jesuthasan, N. and Baliga, B.R. (2010), Modeling laminar fluid flows in rectangular vapor grooves of evaporators used in loop heat pipes, *Proceedings of ASME 2010 3rd Joint US-European Fluids Engineering Summer Meeting and 8th International Conference on Nanochannels, Microchannels, and Minichannels (FEDSM2010-ICNMM2010)*, pp. 1-10, August 1-5.

Jothiprasad, G., Mavriplis, D.J., and Caughey, D.A. (2003), Higher-Order Time Integration Schemes for the Unsteady Navier-Stokes Equations on Unstructured Grids, *J. Comp. Physics*, Vol. 191, pp. 542-566.

Kakac, S., Shah, R.K. and Aung, W. (1987), *Handbook of Single-Phase Convective Heat Transfer*, John Wiley, New York.

Karniadakis, G. and Sherwin, S.J. (2005), *Spectral/hp Element Method for Computational Fluid Dynamics*, 2nd Edition, Oxford University Press, Oxford, U.K.

Kaviany, M. (1999), *Principles of Heat Transfer in Porous Media*, 2nd Edition, Springer Verlag, New York.

Kaviany, M. (2001), *Principles of Convective Heat Transfer*, 2nd Edition, Mechanical Engineering Series, Springer-Verlag, New York.

Kaya, T. and Hoang, T.T. (1999), Mathematical Modeling of Loop Heat Pipes and Experimental Validation, *AIAA Journal of Thermophysics and Heat Transfer,* Vol. 13, pp. 314-320.

Kaya, T. and Ku, J. (2003), Thermal Operational Characteristics of a Small-Loop Heat Pipe, *AIAA Journal of Thermophysics and Heat Transfer,* Vol. 17, pp. 464-470.

Kaya, T. and Goldak, J. (2008), Numerical Analysis of Heat and Mass Transfer in the Capillary Structure of a Loop Heat Pipe, *Int. J. Heat and Mass Transfer*, Vol. 49, pp. 3211-3220.

Kays, W.M. and Crawford, M.E. (1993), *Convective Heat and Mass Transfer*, 3rd Edition, McGraw-Hill, New York.

Kays, W.M. and London, A.L. (1984), *Compact Heat Exchangers, 3rd ed*., McGraw-Hill, New York.

Kays, W.M. and Perkins, H.C. (1973), Forced Convection, Internal Flow in Ducts, in *Handbook of Heat Transfer*, W.M. Rohsenow, and J.P. Hartnett (Editors), Section 7, pp. 7-1 to 7-193.

Khandlikar, S.G., Shoji, M. and Dhir, V.K. (1999), *Handbook of Phase Change: Boiling and Condensation*, Taylor & Francis, New York.

Kim, J. and Ghajar, A.J. (2006), A General Heat Transfer Correlation for Non-Boiling Gas–Liquid Flow with Different Flow Patterns in Horizontal Pipes. *Int. J. Multiphase Flow*, Vol. 32, pp. 447–465.

Kinney, R.B. (1968), Fully Developed Frictional and Heat-Transfer Characteristics of Laminar Flow in Porous Tubes, *Int. J. Heat Mass Transfer*, Vol. 11, pp. 1393-1401.

Kleinstreuer, C. (2003), *Two-Phase Flow: Theory and Applications*, Taylor & Francis, New York.

Klinkenberg, L.J. (1941), The Permeability of Porous Media to Liquids and Gases, Drilling and Production Practice, American Petroleum Inst., pp. 200–213

Kolev, N., (2007), *Multiphase Flow Dynamics: Fundamentals*, Vol. 1, 3rd Edition, Springer, USA.

Ku, J. (1998), Capillary Pumped Loops with Multiple Parallel Starter Pumps, A*erospace Engineering*, Vol. 18, pp. 45-50.

Ku, J. (1999), Operating Characteristics of Loop Heat Pipes, *Proceedings of 29th International Conference on Environmental System*, USA, 1999, SAE Paper No. 1999-01-2007.

Ku, J. (2003), High Frequency Low Amplitude Temperature Oscillations in Loop Heat Pipe Operation, *International Conference On Environmental Systems, SAE 2003-01-2387*, Vancouver, BC, CANADA.

Ku, J. and Leidenfrost, W. (1981), Laminar Flow in a Porous Tube with Uniform Mass Injection, *Ingenieur-Archiv*, Vol. 51, pp. 111-126.

Ku, J. and Rodriguez, J.I. (2003), Low Frequency High Amplitude Temperature Oscillations in Loop Heat Pipe Operation, *International Conference On Environmental Systems, SAE 2003-01-2386*, Vancouver, BC, CANADA.

Ku, J., Hoang, T. and O'Connell, T. (2009), Mathematical Modeling of a Miniature Loop Heat Pipe With Two Evaporators and Two Condensers, *ASME 2009 Heat Transfer Summer Conference collocated with the InterPACK09 and 3rd Energy Sustainability Conferences (HT2009*) July 19–23, 2009 , San Francisco, California, USA.

Kunii, D. and Smith, J.M. (1960), Heat Transfer Characteristics of Porous Rocks, *J. American Institute of Chemical Engineers*, Vol. 6, pp. 71-78.

Kunz, H.R., Langston L.S., Hilton B.H., Wyde S.S. and Nashick G.H. (1967), *Vapor-Chamber Fin Studies: Transport Properties and Boiling Characteristics of Wicks*, NASA Contract Report, NASA-CR-812.

Landau, L.D. and Lifshitz, E.M. (1987), *Fluid Mechanics*, Translated from the Russian edition by J.B. Sykes and W.H. Reid, Pergamon Press, Oxford, U.K.

Launay, S. and Vallée, M., (2011), State-of-the-art experimental studies on loop heat pipes, *Frontiers in Heat Pipes (FHP)*, Vol. 2, pp. 1-27.

Launay, S., Sartre, V. and Bonjour, J. (2007a), Parametric Analysis of Loop Heat Pipe Operation: A Literature Review, *International Journal of Thermal Sciences*, Vol. 46, pp. 621-636.

Launay, S., Platel, V., Dutour, S. and Joly, J. (2007b), Transient Modeling of Loop Heat Pipes for the Oscillating Behavior Study, *J. Thermophysics and Heat Transfer*, Vol. 21, pp. 487-495

Launder, B.E. and Sandham, N.D. (2002), *Closure Strategies for Turbulent and Transitional Flow*, Cambridge University Press, Cambridge, U.K.

Lee, H.J., Liu, D.Y., Alyousef, Y. and Yao., S. (2010), Generalized Two-Phase Pressure Drop and Heat Transfer Correlations in Evaporative Micro/Minichannels, *Journal of Heat Transfer*, Vol. 132, pp. 1-9

Lehner, K. (1979), A Derivation of the Field Equations for Slow Viscous Flow Through a Porous Medium, *Ind. Eng. Chem. Fundam*., Vol. 18, p. 41-45.

Leonard, B.P. (1979), A Stable and Accurate Convective Modelling Procedure Based on Quadratic Upstream Interpolation, Computational Methods in Applied Mechanics and Engineering, Vol. 19, pp. 59-98.

Leonard, B.P. (1997), Bounded Higher-Order Upwind Multidimensional Finite-Volume Convection-Diffusion Algorithms, in *Advances in Numerical Heat Transfer*, W.J. Minkowycz and E.M. Sparrow (Editors), Vol. 1, Chapter 1, pp. 1-57, Taylor & Francis, New York.

Leong, K.C., Liu, C.Y. and Lu, G.Q. (1997), Characterization of Sintered Copper Wicks Used in Heat Pipes, *Journal of Porous Materials*, Vol. 4, pp. 303-308.

Leong, K.C., Liu, C.Y., and Sun, K.H. (1996), Vapor Pressure Distribution of a Flat Plate Heat Pipe, *Int. Comm. Heat Mass Transfer*, Vol. 23, pp. 789-797.

Levy, S. (1999), *Two-Phase Flow in Complex Systems*, John Wiley, New York.

Li, J. and Peterson, G.P. (2011), 3D Heat Transfer Analysis in a Loop Heat Pipe Evaporator with Fully Saturated Wick, *Int. J. of Heat and Mass Transfer*, Vol. 54, pp. 564-574.

Li, J., Wang, D. and Peterson G.P. (2010), Experimental Studies on a High Performance Compact Loop Heat Pipe with a Square Flat Evaporator, *Applied Thermal Engineering*, Vol. 30, pp. 741 - 752.

Li, Z.G., Huai, X.L., Tao, Y.J. and Chen, H.Z. (2007), Effects of Thermal Property Variations on the Liquid Flow and Heat Transfer in Microchannel Heat Sinks, *Appl. Thermal Eng.*, Vol. 27, pp. 2803-2814.

Linstrom, P.J. and Mallard, W.G., Eds., 2005, *NIST Chemistry WebBook, NIST Standard Reference Database Number 69*, National Institute of Standards and Technology, Gaithersburg MD, 20899 (http://webbook.nist.gov).

Liu, J.T., Peng, X.F. and Yan, W.M. (2007), Numerical Study of Fluid Flow and Heat Transfer in Microchannel Cooling Passages, *Int. J. Heat Mass Transfer*, Vol. 50, pp. 1855-1864.

Lockhart, R.W. and Martinelli, R.C. (1949), Proposed Correlation of Data for Isothermal Two-Phase, Two-Component Flow in Pipes, *Chem. Eng. Progress*, Vol. 45, pp. 39-48.

Loosveldt, H., Lafhaj, Z. and Skoczylas, F. (2002), Experimental Study of Gas and Liquid Permeability of a Motar, Cement and Concrete Research, Vol. 32, pp. 1357-1363.

Mandhane, J.M., Gregory, G.A. and Aziz, K. (1974), A Flow Pattern Map for Gas-Liquid Flow in Horizontal Pipes, *International Journal of Multiphase Flow*, Vol. 1, pp. 537-553.

Mandhane, J.M., Gregory, G.A., and Aziz, K. (1977), Critical Evaluation of Friction Pressure-Drop Prediction Methods for Gas-Liquid Flow in Horizontal Pipelines, *Journal of Petroleum Technology*, Vol. 29, pp. 1348-1358.

Mantel, W.J. and Chang W.S. (1991), Effective Thermal Conductivity of Sintered Metal Fibers, *AIAA Journal of Thermophysics and Heat Transfer,* Vol. 5, pp. 545-549.

Masson, C., Saabas, H.J. and Baliga, B.R. (1994), Co-Located Equal-Order Control-Volume Finite Element Method for Two-Dimensional Axisymmetric Incompressible Flow, *Int. J. Num. Methods in Fluids*, Vol. 18, pp. 1-26.

Maxwell, J.C. (1954), *A Treatise on Electricity and Magnetism*, 3rd Edition, Vol. 1, Dover Publications, New York, (reprinted; original printed by Oxford University Press in 1891).

Maydanik, Y.F. (2005), Loop Heat Pipes, *Applied Thermal Engineering*, Vol. 25, pp. 635-657.

Maydanik, Y.F., Vershinin, S.V., Pastukhov, V.G. and Fried S. (2010), Loop Heat Pipes for Cooling Systems of Servers, *IEEE Transactions on Components and Packaging Technologies*, Vol. 33, pp. 416-423.

Mell, P. and Grance, T. (2011), The NIST Definition of Cloud Computing (Draft), *Special Publication* 800-145, National Institute of Standards and Technology, U.S. Department of Commerce.

Minkowycz, W.J. and Sparrow, E.M. (1997), *Advances in Numerical Heat Transfer,* Vol. 1, Taylor and Francis, Washington D.C., pp. 3373-3385.

Minkowycz, W.J. and Sparrow, E.M. (2000), *Advances in Numerical Heat Transfer,* Vol. 2, Taylor & Francis, Washington D.C.

Minkowycz, W.J., Haji-Sheikh, A. and Vafai, K. (1999), On Departure from Local Equilibrium in Porous Media Due to Rapidly Changing Heat Source: The Sparrow Number, *International Journal of Heat and Mass Transfer*, Vol. 42, pp. 3373-3385.

Minkowycz, W.J., Sparrow, E.M., and Murthy, J.Y. (2006), *Handbook of Numerical Heat Transfer*, 2nd Edition, John Wiley, New York.

Mo, S., Hu, P., Cao, J., Chen, Z., Fan, H. and Yu, F. (2006), Effective Thermal Conductivity of Moist Porous Sintered Nickel Material, *Int. J. of Thermophysics*, Vol. 27, pp. 304-313.

Montillet, A., Akkari, E. and Comiti, J. (2007), About a Correlating Equation for Predicting Pressure Drops Through Packed Beds of Spheres in a Large Range of Reynolds Numbers, *Chemical Engng. and Processing,* Vol. 46, pp. 329-333.

Morini, G.L. (2004), Single-Phase Convective Heat Transfer in Microchannels: A Review of Experimental Results, *Int. J. Thermal Sciences*, Vol. 43, pp. 631-651.

Munson, B., Young, D., Okiishi, T., Huebsch, W. (2008), Fundamentals of Fluid Mechanics, 6th Edition, John Wiley, New York.

Nagano, H., Ku, J. (2006), Testing of a Miniature Loop Heat Pipe with Multiple Evaporators and Multiple Condensers for Space Applications, *Proceedings of the 8th International Heat Pipe Symposium*, pp.204-209.

Nesreddine, H., Galanis, N. and Nguyen, C.T. (1997), Variable-Property Effects in Laminar Aiding and Opposing Mixed Convection of Air in Vertical Tubes, *Num. Heat Transfer: Part A - Applications*, Vol. 31, pp. 53-69.

Ng, E.Y.K. and Tan, S.T. (2004), Computation of Three-Dimensional Developing Pressure-Driven Flow in a Microchannel with EDL effect, *Num. Heat Transfer: Part A – Applications*, Vol. 45, pp. 1013-1027.

Nield, D. and Bejan, A., (2006), *Convection in Porous Media*, 3rd Ed. Springer, USA.

Nikitkin, M. and Cullimore, B. (1998), CPL and LHP Technologies: What Are the Differences, What Are the Similarities?, *Proc. SAE, 28th International Conference on Environmental Systems, SAE-98-1587*, Danvers, MA.

Ochoa-Tapia, J.A. and Whitaker, S. (1995), Momentum Transfer at the Boundary Between a Porous Medium and a Homogeneous Fluid I: Theoretical Development, *Int. J. Heat Mass Transfer*, Vol. 38, pp. 2635-2646.

Ochterbeck, J.M. and Peterson, G.P. (1997), Modeling of Heat Transfer in Heat Pipes, in *Modeling of Engineering Heat Transfer Phenomena*, B. Sundén and M. Faghri (Editors), Computational Mechanics Publications, Southampton, UK and Boston, USA, Vol. 2, Chapter 7, pp. 175-212.

Ofuchi, K. and Kunii, D. (1965), Heat-Transfer Characteristics of Packed Beds with Stagnant Fluids, *International Journal of Heat and Mass Transfer*, Vol. 8, pp. 749-757.

Ogniewicz, Y. and Yovanovich, M.M. (1978), Effective Conductivity of Liquid-Saturated Porous Beds of Spheres: Basic Cell Model with Constriction, *Progress in Astronautics and Aeronautics*, Vol. 60, pp. 209-228.

Ong., C. and Thome, J.R. (2011), Macro-to-Microchannel Transition in Two-Phase Flow: Part 1 – Two-Phase Flow Patterns and Film Thickness Measurements, *Experimental Thermal and Fluid Science*, Vol. 35, pp. 37–47.

Ould Didi, M.B., Kattan, N. and Thome, J.R. (2002), Prediction of Two-Phase Pressure Gradients of Refrigerants in Horizontal Tubes, *International Journal of Refrigeration*, Vol. 25, pp. 935-947.

Patankar, S.V. (1980), *Numerical Heat Transfer and Fluid Flow*, McGraw-Hill, New York.

Patankar, S.V. and Baliga, B.R. (1978), A New Finite-Difference Scheme for Parabolic Differential Equations, *Num. Heat Transfer*, Vol. 1, pp. 27-37.

Patankar, S.V. and Spalding, D.B. (1972), A Calculation Procedure for Heat, Mass and Momentum Transfer in Three-Dimensional Parabolic Flows, *Int. J. Heat Mass Transfer*, Vol. 15, pp. 1787-1806.

Patankar, S.V., Ramadhyani, S. and Sparrow, E.M. (1978), Effect of Circumferentially Non-Uniform Heating on Laminar Combined Convection in a Horizontal Tube, *J. Heat Transfer, Trans. ASME*, Vol. 100, pp. 63-70.

Pederson, R.J. and Kinney, R.B. (1971), Entrance-Region Heat Transfer for Laminar Flow in Porous Tubes, *Int. J. Heat Mass Transfer*, Vol. 14 pp. 159-161.

Peng, X.F. and Petersen, G.P. (1996), Convective Heat Transfer and Flow Friction for Water Flow in Microchannel Structures, *Int. J. Heat Mass Transfer*, Vol. 39, pp. 2599-2608.

Peterson, G.P. (1994), *An Introduction to Heat Pipes. Modeling, Testing, and Applications,* John Wiley, New York.

Peterson, G.P. and Fletcher L.S. (1987), Effective Thermal Conductivity of Sintered Heat Pipes Wicks, *AIAA Journal of Thermophysics and Heat Transfer,* Vol. 1, pp. 343-347.

Petrasch, J., Schrader, B., Wyss, P. and Stenfeld, A. (2008), Tomography-Based Determination of the Effective Thermal Conductivity of Fluid-Saturated Reticulate Porous Ceramics, *ASME Journal of Heat Transfer*, Vol. 130, pp. 1-10.

Peyret, R. (2002), *Spectral Methods for Incompressible Viscous Flow*, Springer, Berlin, Germany.

Pope, S.B. (2000), *Turbulent flows*, Cambridge University Press, Cambridge, U.K.

Prakash, C. and Patankar, S.V. (1985), A Control-Volume-Based Finite-Element Method for Solving the Navier-Stokes Equations Using Equal-Order Velocity-Pressure Interpolation, *Num. Heat Transfer*, Vol. 8, pp. 259-280.

Prasad, V., Kladias, N., Bandopadhaya, A. and Tian, Q. (1989), Evaluation of Correlations for Stagnant Thermal Conductivity of Liquid-Saturated Porous Beds of Spheres, *International Journal of Heat and Mass Transfer*, Vol. 32, pp. 1793-1796.

Pratap, V.S. and Spalding, D.B. (1976), Fluid Flow and Heat Transfer in Three-Dimensional Duct Flows, *Int. J. Heat Mass Transfer*, Vol. 19, pp. 1183-1188.

Quibén, J.M. and Thome, J.R. (2007), Flow Pattren based Two-Phase Frictional Pressure Drop Model for Horrizontal Tubes. Part I: Diabatic and Adiabatic Experimental Study, *Int. Journal of Heat and Fluid Flow*, Vol. 28, pp. 1049 - 1059.

Quibén, J.M. and Thome, J.R. (2007), Flow Pattern based Two-Phase Frictional Pressure Drop Model for Horrizontal Tubes. Part II: New Phenomenological Model, *Int. Journal of Heat and Fluid Flow*, Vol. 28, pp. 1060 - 1072.

Raithby, G. (1971), Laminar Heat Transfer in the Thermal Entrance Region of Circular Tubes and Two-Dimensional Rectangular Ducts with Wall Suction and Injection, *Int. J. Heat Mass Transfer*, Vol. 14, pp. 223-243.

Raithby, G.D. and Knudsen, D.C. (1974), Hydrodynamic Development in a Duct with Suction and Blowing, *J. Appl. Mechanics*, Vol. 41, pp. 896-902.

Raithby, G.D. (1976), Skew Upstream Difference Schemes for Problems Involving Fluid Flow, *Comput. Methods Appl. Mech. Eng.*, Vol. 9, pp. 153-164.

Reddy, J.N. and Gartling, D.K. (2000), *The Finite Element Method in Heat Transfer and Fluid Dynamics*, 2nd Edition, CRC Press, Boca Raton.

Ren, C. (2011), Parametric Effects on Heat Transfer in Loop Heat Pipe's Wick, *Int. J. Heat Mass Transfer*, Vol. 54, pp. 3987-3999.

Ren, C., Wu, Q.S., and Hu, M.B. (2007), Heat Transfer with Flow and Evaporation in Loop Heat Pipe's Wick at Low or Moderate Heat Fluxes, *Int. J. Heat Mass Transfer*, Vol. 50, pp. 2296-2308.

Rhee, S.J. and Edwards, D.K. (1981), Laminar Entrance Flow in a Flat Plate Duct with Asymmetric Suction and Heating, *Numerical Heat Transfer, Part B: Fundamentals*, Vol. 4, pp. 85-100.

Rhie, C.M. and Chow, W.L. (1983), Numerical Study of the Turbulent Flow Past an Airfoil With Trailing Edge Separation, *AIAA Journal*, Vol. 21, pp. 1525-1532.

Richardson L.F. (1910), The Approximate Arithmetical Solution by Finite Differences of Physical Problems Involving Differential Equations with Application to a Masonry Dam, *Transc. Royal Society of London, Series A*, Vol. 210, pp. 307-357.

Roache, P.J. (1998) *Fundamental of Computational Fluid Dynamics*, Hermosa Publishers, Albuquerque, New Mexico.

Roberts, D.W. and Forester, C.K. (1979), Parabolic Procedure for Flows in Ducts of Arbitrary Cross-Section, *AIAA J.*, Vol. 17, pp. 33-40.

Rohsenow, W.M., (1985), Condensation- Part 1: Film Condensation, in *Handbook of Heat Transfer Fundamentals*, 2nd Edition, W.M. Rohsenow, J.P. Hartnett, and E.N. Ganic (Editors), Chapter 11, pp. 1-36.

Rohsenow, W.M., Harnett, J.P. and Cho, Y.I. (1998), *Handbook of Heat Transfer*, 3rd Edition, McGraw-Hill, New York.

Rose, J.W. (1998), Condensation Heat Transfer Fundamentals, *Institution of Chemical Engineers (Trans IChemE)*, Vol. 76, Part A, pp. 143-152.

Rouhani, S.Z. and Sohal, M.S. (1983), Two-Phase Flow Patterns: A Review of Research Results, *Progress in Nuclear Energy*, Vol. 11, pp. 219-259.

Saabas, H.J. and Baliga, B.R. (1994), A Co-Located Equal-Order Control-Volume Finite Element Method for Multidimensional, Incompressible Fluid flow – Part I: Formulation, *Num. Heat Transfer, Part B*, Vol. 26, pp. 381-407.

Sangani, A.S. and Acrivos, A. (1983), The Effective Conductivity of a Periodic Array of Spheres, *Proceedings of the Royal Society of London*, Vol. A386, pp. 263-275.

Scheidegger, A.E. (1974), *The Physics of Flow Through Porous Media,* 3rd Edition, University of Toronto Press.

Schneider, G.E. and Raw, M.J. (1986), A Skewed Positive Influence Coefficient Upwind Procedure for Control-Volume-Based Finite Element Convection-Diffusion Computation, *Num. Heat Transfer*, Vol. 9, pp. 1-26.

Sebben, S. and Baliga, B.R. (1995), Some Extensions of Tridiagonal and Pentadiagonal Matrix Algorithms, *Num. Heat Transfer, Part B*, Vol. 28, pp. 323-351.

Shah, R.K. and London, A.L. (1978), Laminar Flow Forced Convection in Ducts, *Advances in Heat Transfer, Supplement 1*, Academic Press, New York.

Shah, R.K. and London, A.L. (1978), *Laminar Flow Forced Convection in Ducts*, Advances in Heat Transfer, Supplement 1, Academic Press, New York.

Silverstein, C.C. (1992), *Design and Technology of Heat Pipes for Cooling and Heat Exchange,* Hemisphere Publishing Corporation, Taylor & Francis, Washington D.C.

Singh, B.S., Dybbs A. and Lyman F.A. (1973), Experimental Study of the Effective Thermal Conductivity of Liquid Saturated Sintered Fiber Metal Wicks, *International Journal of Heat and Mass Transfer,* Vol. 16, pp. 145-155.

Singh, R., Akbarzadeh, A., Dixon, C. and Mochizuku, M. (2009), Theoretical Modelling of Miniature Loop Heat Pipe, *Heat Mass Transfer*, Vol. 46, pp. 209-224.

Singh, R., Akbarzadeh, A., Dixon, C., Mochizuku, M. and Riehl, R.R. (2007), Miniature Loop Heat Pipe with Flat Evaporator for Cooling Computer CPU, *IEEE Transactions on Components and Packaging Technologies*, Vol. 30, pp. 42-49.

Slattery, J.C. (1981), *Momentum, Energy and Mass Transfer in Continua*, Krieger, Malabar.

Smirnov, H., (2009), *Transport Phenomena in Capillary-Porous Structures and Heat Pipes*, Taylor& Francis, Boca Raton, FL.

Soliman, H.M. (1982), On the Annular-to-Wavy Flow Pattern Transition during Condensation Inside Horizontal Tubes, *Canadian Journal of Chemical Engineering*, Vol. 60, pp. 457-481.

Soliman, H.M. (1986), The Mist-Annular Transition During Condensation and Its Influence on the Heat Transfer Mechanism, *International Journal of Multiphase Flow*, Vol. 12, pp. 277-288.

Soliman, M.M., Graumann, D.W. and Berenson, P.J. (1970), Effective Thermal Conductivity of Dry and Liquid-Saturated Sintered Fiber Metal Wicks, *ASME Paper 70HT/SpT-40*.

Spalding, D.B. (1972), A Novel Finite-Difference Formulation for Differential Expressions Involving Both First and Second Derivatives, *Int. J. Num. Methods in Eng.*, Vol. 4, pp. 551-559.

Sparrow, E.M. and Patankar, S.V. (1977), Relationships Among Boundary Conditions and Nusselt Numbers for Thermally Developed Duct Flows, *ASME Journal of Heat Transfer*, Vol. 99, pp. 483-485.

Stenger, F.J. (1966), Experimental Study of Water-Filled Capillary Pumped Heat Transfer Loops, NASA TMX-1310.

Stepanov, V.G., Volyak, L.D. and Tarlakov Y.V. (1977), Wetting Contact Angles of Certain Systems, *Journal of Engineering Physics and Thermophysics,* Vol. 32, pp. 1000-1003.

Taitel, Y. and Dukler, A.E. (1976), A Model for Predicting Flow Regime Transitions in Horizontal and Near Horizontal Gas-Liquid Flow, *AIChE Journal*, Vol. 22, pp. 47-55.

Tannehill, J.C., Anderson, D.A., and Pletcher, R.H. (1997), *Computational Fluid Mechanics and Heat Transfer*, 2nd Edition, Taylor and Francis, Washington D.C.

Tavman, I.H. (1996), Effective Thermal Conductivity of Granular Porous Materials, *International Communications in Heat and Mass Transfer*, Vol. 23, pp. 169-176.

Taylor, G. (1956), Fluid Flow in Regions Bounded by Porous Surfaces, *Proc. Royal Soc. London, Series A, Mathematical and Physical Sciences*, Vol. 234, pp. 456-475.

Tennekes, H. and Lumley, J.L. (1972), *A First Course in Turbulence*, MIT Press, Cambridge, MA.

Thome, J.R. (2003), On Recent Advances in Modeling of Two-Phase Flow and Heat Transfer, *Heat Transfer Engineering*, Vol. 24, pp. 46-59.

Thompson, B.R., Maynes, D. and Webb, B.W. (2005), Characterization of the Hydrodynamically Developing Flow in a Microtube using MTV, *J. Fluids Eng., Trans. ASME*, Vol. 127, pp. 1003-1012.

Tien, C.L. and Rohani, A.R. (1974), Analysis of the Effects of Vapor Pressure Drop on Heat Pipe Performance, *Int. J. Heat Mass Transfer*, Vol. 17, pp. 61-67.

Tong, L.S. and Tang, Y.S. (1997), *Boiling Heat Transfer and Two-Phase Flow*, Taylor & Francis, Washington D.C.

Trishchenko, A.P. and Garand L. (2011), Canadian Polar Communication and Weather (PCW) Satellite System: New Capabilities for Mapping Arctic Snow and Ice Dynamics from Highly Elliptic Orbit, *6th EARSeL Workshop Cryosphere, Hydrology and Climate Interactions*, University of Berne, Switzerland, 7 February.

Tritton, D.J. (1988), *Physical Fluid Dynamics*, 2nd Edition, Oxford University Press, Oxford, U.K.

Tsotsas, E. and Martin, H. (1987), Thermal Conductivity of Packed Beds: A Review, *Chemical Engineering Progress,* Vol. 22, pp. 19-37.

Vadász, P. (2008), Emerging Topics in Heat and Mass Transfer in Porous Media: From Bioengineering and Microelectronics to Nanotechnology, Published by Springer Science.

Vafai, K. (2005), *Handbook of Porous Media,* 2nd Edition, Published by CRC Press, Taylor & Francis, New York.

Van Sant, J.H. and Malet, J.R. (1975), Thermal Conductivity of Some Heat Pipe Wicks, *Letters in Heat and Mass Transfer*, Vol. 2, pp. 199-206.

Vasiliev, L., Lossouarn, D., Romestant, C., Alexandre, A. and Bertin, Y. (2009), Loop Heat Pipe for Cooling of High-Power Electronic Components, *International Journal of Heat and Mass Transfer*, Vol. 52, pp. 301–308.

Venditti, D. and Baliga, B.R. (1998), An h-Adaptive Strategy for CVFEM Simulations of Viscous Incompressible Flow, *CFD 98: Proc. 6th Ann. Conf. CFD Society of Canada*, Part VIII, pp. 65-70, Quebec City, Quebec, Canada.

Vissersa, J., Hoebenb, M., Lavenb, J., Claessensa, H. and Cramers, C. (2000), Hydrodynamic Aspects of Slurry Packing Processes in Microcolumn Liquid Chromatography, *Journal of Chromatography A*, Vol. 883, pp. 11–25.

Vlassov, V. and Riehl, R. (2008), Mathematical Model of a Loop Heat Pipe with Cylindrical Evaporator and Integrated Reservoir, *Applied Thermal Eng*., Vol. 28, pp. 942–954.

Wallis, G. (1969), *One-Dimensional Two-Phase Flow*, McGraw-Hill, New York.

Wang, B.X. and Peng, X.F. (1994), Experimental Investigation on Liquid Forced-Convection Heat Transfer through Microchannels, *Int. J. Heat Mass Transfer*, Vol. 37, pp. 73-82.

Wang, G., Mishkinis, D., and Nikanpour, D. (2008), Capillary Heat Loop Technology: Space Applications and Recent Canadian Activities, *Applied Thermal Engineering*, Vol. 28, pp. 284-303.

Webb, R.L. and Zhang, M. (1998), Heat Transfer and Friction in Small Diameter Channels, *Microscale Thermophysical Engineering*, Vol. 2, pp. 189-202.

Wendt, J., Anderson, J., (2009), Computational Fluid Dynamics: An Introduction, 3rd Edition, Springer, USA

Whalley, P.B. (1996), *Two-Phase Flow and Heat Transfer*, Oxford University Press, Oxford, U.K.

Whitaker, S. (1999), *The Method of Volume Averaging*, Kluwer Academic Publishers, Dordrecht, The Netherlands.

White, F.M. (1991), *Viscous Fluid Flow*, 2nd Edition, McGraw-Hill, New York.

Wilcox, D. (1993), *Turbulence Modeling for CFD*, 2nd Edition, DCW Industries, La Canada, California.

Wirsch, P.J. and Thomas S.K. (1996), Performance Characteristics of a Stainless Steel/Ammonia Loop Heat Pipe, *AIAA Journal of Thermophysics and Heat Transfer*, Vol. 10, pp. 326-333.

Wrenn, K. R., Krein, S. J., Hoang, T. T. and Allen, R. D. (1999), Verification of a Transient Loop Heat Pipe Model, *SAE International, Paper 1999-01-2010*, July 1999.

Yu, X., Zhang, L., Zhou, E., and Feng, Q., (2011), Heat Transfer of an IGBT Module Integrated With a Vapor Chamber, J. of Electronic Packaging, 133, pp. 1-6.

Yuan, J., Rokni, M., and Sunden, B. (2001), Simulation of Fully Developed Laminar Heat and Mass Transfer in Fuel Cell Ducts with Different Cross-Sections, *Int. J. Heat Mass Transfer*, Vol. 44, pp. 4047-4058.

Yuan, S.W. and Finkelstein, A.B. (1958), Heat Transfer in Laminar Pipe Flow with Uniform Coolant Injection, Jet Propulsion, Vol. 28, pp. 178-181.

Yun, S., Wolf, D., and Kroliczek, E. (1999), "Design and Test Results of Multi-Evaporator Loop Heat Pipes", SAE-99-01-2051, *Proc. SAE, ASME, AIAA, et al. 29th International Conference on Environmental Systems*, Denver, Co, July 12-15.

Zienkiewicz, O.C. and Taylor, R.L. (2000), *Finite Element Method: Volume 2, Fluid Dynamics*, 5th Edition, Butterworth-Heinemann, Elsevier, New York.

Zimberck, W., Slavik, G., Cennamo, J., Kang, S., Yun, J., and Kroliczek, E. (2008), Loop Heat Pipe Technology for Cooling Computer Servers, Proc. 11th Intersociety Conference on Thermal and Thermomechanical Phenomena in Electronic Systems (ITHERM 2008), Paper # ITHERM2008-4544248, pp. 19-25, Orlando, FL, May 28-31.

Zivi, S.M. (1964), Estimation of Steady-State Steam Void-Fraction by Means of the Principle of Minimum Entropy Production, *ASME Journal of Heat Transfer*, Vol. 86, pp. 247-252.